SOIL PERFORMANCE FOR LARGE SCALE SOIL-PIPELINE TESTS

A Dissertation

Presented to the Faculty of the Graduate School

of Cornell University

In Partial Fulfillment of the Requirements for the Degree of

Doctor of Philosophy

by

Nathaniel A. Olson

May 2009

SOIL PERFORMANCE FOR LARGE SCALE SOIL-PIPELINE TESTS

Nathaniel A. Olson, Ph. D.

Cornell University 2009

The strength and dilation properties of dry and partially saturated sand at peak and critical state are measured and compared in terms of the matric suction measured for partially saturated sand. Techniques are developed for the movement, placement, compaction and measurement of large quantities of soil with tight control of water content, w, and dry unit weight, γ_{dry}. Tactile pressure sensors are used to measure pipe-soil interaction stresses reliably.

Direct shear (DS) tests performed on three different glacio-fluvial sands with DS box dimensions of 60, 100 and 300 mm show that the conventional 60 mm apparatus produces results that are consistently higher in terms of peak strength and dilatency than those of the larger boxes. Based on an evaluation of the test results, a modified 100 mm apparatus, consistent with the design proposed by Lings and Dietz (2004), is recommended for future DS testing. This DS apparatus gives high quality data, and is validated through favorable comparison with flow rules relating strength and dilation at peak to critical state strength.

The desorption soil water retention curve (SWRC) measured with Tempe cells is used to predict an adsorption SWRC, which compares favorably with tensiometer measurements. The effects of matric suction on the peak angle of shear resistance and dilatency are quantified by comparing DS test results for dry and partially saturated

sand of identical composition and γ_{dry}. Apparent cohesion at peak stress is found to be dependent on γ_{dry} for partially saturated sand, and is related to increased dilatency. It appears that matric suction increases the interference among the sand particles, thus increasing the work against volumetric expansion during shear failure.

Methods of soil placement, compaction and measurement for large scale tests are shown. The mean values of w and γ_{dry} for tests with up to 320 measurements taken are shown to have 95% confidence intervals of 0.04 – 0.10% and 0.07 – 0.12 kN/m^3, respectively. A comparison of nuclear gage and Selig density scoop measurements of γ_{dry} shows that the density scoop overestimates γ_{dry} for dry sand, and is in favorable agreement with γ_{dry} determined with the nuclear gage for partially saturated sand. A comparison of nuclear gage and ASTM D2216 (ASTM, 2003d) methods for measuring w shows that the nuclear gage systematically underestimates w in the soil mass and is less precise than the ASTM method.

Tactile pressure sensors are shown to be suitably accurate and versatile for measurement of normal stresses in large-scale laboratory testing. A two-layer system of Teflon® sheets is shown to be effective in protecting the sensors from shear stress effects, and methods for sensor calibration and measurement are proposed for minimizing time-rate of loading and creep effects.

BIOGRAPHICAL SKETCH

Nathaniel was born in Philadelphia, PA and raised in Ithaca, NY. After graduating from Trumansburg High School, he attended Cornell University where he graduated with a Bachelor of Science degree in Civil Engineering in May 2005. Nathaniel continued at Cornell University to pursue his doctoral degree in the School of Civil and Environmental Engineering at Cornell, under the assistance of the George E. Brown, Jr. Network for Earthquake Engineering Simulation program of the National Science Foundation. Nathaniel spends his free time with his wife Brianna Bamford Olson (Cornell University B.A. 2007, M.P.A. 2009) and two loving dogs, Murphy and Molly.

To my family

ACKNOWLEDGMENTS

First and foremost, I must express the deepest thanks and gratitude to the co-chair of my Special Committee, Professor Thomas D. O'Rourke. His support, patience, and knowledge were vital to my success as a graduate student at Cornell University. I appreciate the patience with which he guided me through long months of direct shear tests, tactile pressure sensor analyses, and thesis writing. I could not have accomplished this without him. I must also thank Professor Harry Stewart for inviting me to work as a graduate student on the NEES project, and for his encouragement and guidance in the early months of investigation. He was very helpful when learning to place, compact and measure soil, and taught me to develop a sense for target soil conditions of water content and dry unit weight. I thank my other committee members, Wilkins Aquino and Mircea Grigoriu, for their guidance in my studies, and for the excellent courses I was able to take from them while at Cornell University. In this regard, I also thank Professors Ken Hover and Fred H. Kulhawy.

I was privileged to share an office with Jeremiah Jezerski and Dr. Sami Akbas during their years as graduate students at Cornell. I thank Jai Jung, Javier Perez, Cesar Chan and John Grillo for their friendship and support. Jeremiah's support and help was a great lift throughout my time as a graduate student, and we spent countless hours placing, compacting, and measuring sand in the lab. I also sincerely thank him for being the best man at my wedding, and for the great friendship we still share.

Financial support for my graduate tuition and stipend from the George E. Brown, Jr. Network for Earthquake Engineering Simulation (NEES) Program of the

National Science Foundation (NSF) under Grant No. CMS-0421142 was vital, in addition to the excellent facilities supplied by Cornell University and the Department of Civil and Environmental Engineering.

The staff of the Harry E. Bovay Jr. Civil Infrastructure Laboratory Complex were infinitely helpful, especially Tim Bond, who has been a friend for my eight years as an undergraduate and graduate student at Cornell University, and helped me develop as a student, lab worker, and citizen. Mr. Bond, Joe Chipalowsky, Qinge Ma, Dave Ash, Cameron Willkens, and Brett Sheldon all provided excellent support and technological expertise. The experience of Michael Palmer, Lee Virtue, Scott Jones, Keith Kesner, Steve Carino, John Davis, Paul Charles and Tim Brock were enormously helpful in designing and fabricating test equipment and performing large scale tests. I also thank the administration of the Department of Civil and Environmental Engineering, including but not limited to Patty Apgar, Tania Sharpsteen, Maureen Letteer, Christine Day and Jeanette Little. Undergraduate lab technicians Desi Bluiett, Elizabeth Crowley, Jessica Fuller, Gavin Graeper, Will Graeper, Matthew Kibbee, Ting Lin, Nicholas Palumbo, Ben Schmidt and Seneca Thomas, were extremely enthusiastic and I appreciate their hard work with the research.

Mr. Robert Schindelbeck of the Department of Crop and Soil Sciences devoted a great deal of his time and expertise to my research. He donated tensiometers and showed us how to use them properly in our large scale tests. He also invited me to use his laboratory to test our soil in his Tempe cells, and showed us how to interpret the data. John Hunt of the Cornell Center for Materials Research patiently taught me to use his microscopes to capture images for this work.

The large scale tests were performed in conjunction with centrifuge scale tests at Rensselaer Polytechnic Institute. I appreciate the work of Professors Michael O'Rourke, Mike Symans, and Tarek Abdoun and Drs. Da Ha and Xiaojian (Jerry) Xie. Professor Kenichi Soga and graduate student Dilan Robert of Cambridge University provided valuable data on the properties of our large scale test soil in dry and partially saturated conditions.

Completing my degree would not have been possible without the love and support of my family. My parents, Nancy Lorr and Randy Olson, brother Tom Olson, and grandparents Joan Lorr, Lorraine Sorrel and Billie Olson have provided love and financial support for which I am extremely grateful. My in-laws, Bronwen Bamford, Ben Bamford and Ian Bamford, gave financial support and encouragement. Finally, I thank my wife and best friend, Brianna, for her patience and love during this process. I spent many late nights in the lab instead of at home, and she always encouraged me to keep up the hard work. I miss Quimby the hedgehog very much, but Murphy and Molly, our two Standard Schnauzers, are excellent companions and always know how to brighten my day.

TABLE OF CONTENTS

LIST OF FIGURES

LIST OF TABLES

LIST OF ABBREVIATIONS

2-D	large scale box for plane strain conditions
3-D	large scale box for strike-slip displacement
ASTM	American Society for Testing and Materials
BSI	British Standards Institute
CU	Cornell University
DCDT	direct current displacement transducers
DS	direct shear
EHS	Cornell University Department of Environmental Health and Safety
HDPE	high density polyethylene
IDC	initial drying curve
LVDT	linear variable differential transformer
MDC	main drying curve
MWC	main wetting curve
NEES	George E. Brown, Jr. Network for Earthquake Engineering Simulation
NYSDOT	New York State Department of Transportation
PGD	permanent ground deformation
RPI	Rensselaer Polytechnic Institute
SP	poorly graded sand
SWRC	soil water retention curve

LIST OF SYMBOLS

ARABIC SYMBOLS

a_1	SWRC curve fitting parameter
A_{eq}	equivalent A-coefficient for DS test
A_f	A-coefficient for triaxial test
b_i	SWRC curve fitting parameter
b_w	SWRC curve fitting parameter
B	direct shear box inside width
c	soil cohesion (y-intercept in plot of τ_p vs σ_N)
c_{ds}	c measured from DS test
c_{ps}	c in plane strain parameters
c_i	SWRC curve fitting parameter
$c_{indirect}$	c measured by indirect method
c_w	SWRC curve fitting parameter
C	center of Mohr Circle
C_c	coefficient of curvature
C_u	coefficient of uniformity
C_s	cohesion force of soil
CI	95% two-tailed confidence interval
COV	coefficient of variation
d_i	SWRC curve fitting parameter
d_w	SWRC curve fitting parameter
D	pipeline outside diameter
D_{10}	particle diameter at which 10% of particles are smaller
D_{30}	particle diameter at which 30% of particles are smaller

D_{50}	median particle size
D_{60}	particle diameter at which 60% of particles are smaller
D_{max}	maximum particle size
D_M	depth of nuclear gage measurement
D_{SL}	distance between MDC and MWC on semilogarithmic scale
f	frictional force between soil and pipeline per unit length
F_N	normal force
F_S	shear force
g	gap separation between upper and lower DS frame
g_{front}	gap at a given point during the DS test at the front edge of the soil
G_S	specific gravity
H	direct shear box inside height
H_c	depth to center of pipeline
H_{tip}	depth to center of tensiometer porous cup
H_s	height of unsupported vertical soil wall
H_D	Shore D hardness
i_{ax}	angle of repose as determined by sand cone
j	number of pressure node on tactile pressure sensor
J	number of pressure sensor nodes around pipe surface per unit length
L	direct shear box inside length
m_1	SWRC curve fitting parameter
M_{water}	weight of water
n	number of data points
n_1	SWRC curve fitting parameter
O	intersection of x- and y-axis
p	two-tailed probability

p_1	pipe pressure per unit length of pipeline
$(p_m)_j$	measured pressure at the j-th pressure sensor node
P_h	net force acting on pipeline in transverse horizontal direction
r^2	coefficient of determination
R	radius of Mohr Circle
R_1	radius of to outside wall of pipeline
R_s	resultant soil force
R_{SL}	slope ratio between MDC and MWC on semilogarithmic scale
S	degree of saturation
S_D	standard deviation
S_j	arc length associated with j-th pressure sensor node
t	two-tailed t-value at p = 0.05
t_1	time 1 during creep < t_2
t_2	time 2 during creep > t_1
t_{DS}	thickness of simple shear zone in DS test
u_a	vacuum pressure in airspace above water column in tensiometer
u_m	matric suction (vacuum pressure) in partially saturated soil
u_r	matric suction at residual water content
v_x	relative horizontal displacement between upper and lower DS frame
v_y	vertical displacement of top plate in DS test
$(v_y)_{corrected}$	DS top plate vertical displacement, corrected for extrusion
$(v_y)_{measured}$	DS top plate average measured vertical displacement
$\dot{v}_x$	increment of horizontal displacement in DS test
V_{soil}	volume of soil in calibration box
V_{total}	volume of soil sample before drying
V_w	volume of water in soil sample or graduated cylinder

V_v	volume of voids in a soil sample
w	gravimetric water content
w_{sat}	w at total saturation
w_u	w at wet limit state with air entrapment
W_{dry}	weight of the soil sample before oven drying
W_s	weight of soil wedge
W_{soil}	weight of soil in calibration box
W_{wet}	weight of the soil sample after oven drying
X	value on x-axis
Y	value on y-axis
z	water column height in tensiometer or manometer

GREEK SYMBOLS

α	slope of regression through top of Mohr Circles
α_{creep}	creep coefficient
γ_{dry}	soil dry unit weight
$\gamma_{dry\text{-}gage}$	γ_{dry} measured by nuclear gage
$\gamma_{dry\text{-}grav}$	γ_{dry} by weight-volume relationships
γ_{total}	soil wet unit weight
$\gamma_{w\text{-}soil}$	weight of water per unit volume of soil
γ_{yx}	horizontal soil shear strain in the simple shear zone in DS test
δ_{SI}	direct shear friction angle on a surface interface
Δp_1	change in measured pressure
Δu	change in pore water pressure for triaxial test
ε_{yy}	vertical soil strain in the simple shear zone in DS test
θ	circumferential angle around the pipe

θ_j	angle defining orientation of $(p_m)_j$
θ_w	volumetric water content
σ	stress
σ_1	major principal stress
σ_1	minor principal stress
σ_N	normal stress
σ_{ps}	normal stress on the plane strain failure envelope
τ	shear stress
τ_{SI}	shear stress on a surface interface
τ_{ps}	shear stress on the plane strain failure envelope
ϕ_{crit}	critical state friction angle
ϕ_{ds}	direct shear friction angle
$\phi_{ds\text{-}ld}$	large displacement direct shear friction angle
ϕ_{ps}	plane strain friction angle
ψ	dilation angle

SUFFIXES

‘	superscript indicating effective stress parameters
dry	subscript indicating dry conditions
ds	subscript indicating direct shear stress parameters
p	subscript indicating value of a parameter at peak state in DS test
ps	subscript indicating plane strain stress parameters
p.sat	subscript indicating partially saturated conditions

CHAPTER 1

INTRODUCTION

1.1 Background

Large-scale soil-structure interaction tests require characterization of soil behavior in terms of strength and stress-strain properties. Such tests involve movement, placement, compaction and measurement of large quantities of soil. The properties of the test soil need to be assessed with respect to representative unit weights, water content, and strength throughout the soil mass. Finally, large-scale tests involve measurement and evaluation of soil pressures generated between soil and structure during the interaction testing.

One of the most significant trends in geotechnical earthquake engineering has been the implementation of large-scale testing facilities for soil-structure interaction, such as those at the Japanese National Research Institute for Earth Science and Disaster Prevention that have been used to characterize soil-pile interaction during liquefaction (Tokomatsu and Suzuki, 2004) and the large-scale split box experiments at the George E. Brown, Jr. Network for Earthquake Engineering Simulation (NEES) equipment site at Cornell University (Palmer et al., 2006; O'Rourke and Bonneau, 2007). The large-scale facilities allow for physical modeling of soil-structure interaction at full scale so that conditions in the field can be simulated reliably under laboratory control, with detailed characterization and measurements of soil and structure response.

It has long been recognized that the most serious damage to underground pipelines during an earthquake is caused by permanent ground deformation, or PGD (Hamada and O'Rourke, 1992; O'Rourke, 1998; O'Rourke and Liu, 1999]. It is not possible to model with accuracy the soil displacement patterns at all potentially vulnerable locations. In fact, studies of ground deformation patterns associated with surface faulting have shown complex patterns of ground rupture and distributed deformation even for strike slip faults (Bray et al., 1994; Lazarte et al., 1994). It is possible, nevertheless, to set an upper bound on deformation effects by simplifying spatially distributed PGD as movement concentrated along planes of soil failure. Detailed studies of fault deformation disclose that abrupt soil rupture and offsets are indeed recurrent patterns of deformation (Bray et al., 1994). Accordingly, they establish a baseline with which to evaluate soil-pipeline interaction under large ground deformation.

Split-box testing has the capability of imposing abrupt soil displacements on buried pipelines consistent with PGD effects at fault crossings and the margins of lateral spreads and landslides. Relative displacement between the pipeline and soil is generated along a moveable interface between two test basins, or boxes, containing soil and the buried pipeline. The pipeline is buried in soil that is placed, compacted and measured according to field construction practice. The scale of the experimental boxes is selected based on computational modeling and previous test experience in an effort to minimize the effect that the boundaries of the test facility have on the soil-structure interaction.

This work addresses key issues related to large scale testing, including characterization of dry and partially saturated sand properties, preparation and control of large volumes of soil, and assessment of soil-structure interaction forces, which are reviewed under the subheadings that follow:

1.1.1 Dry Soil Strength Characterization

The direct shear (DS) test is among the oldest and most widely used methods for measuring the strength of soils, and consists of a rigid split container that allows the soil sample to be subjected to an increasing shear displacement on its mid-height horizontal plane. Many studies have been performed to determine the angle of shearing resistance of sand with the DS test, beginning with a primitive shear box used in 1846 by Alexandre Collin (Skempton, 1949). In 1932 Casagrande used a horizontal shear box with increasing load, while in 1936 Gilroy pioneered the displacement controlled DS apparatus (Matthews, 1988). The constant rate of displacement shear box, discussed extensively in the 1952 American Society for Testing and Materials (ASTM) Symposium on Direct Shear Testing of Soils (ASTM, 1953) is still used today, and is referred to as the conventional DS apparatus in the current study. The procedure for performing DS tests with the conventional apparatus was standardized by ASTM D 3080 (ASTM, 2003e) and British Standards Institute (BSI) 1377-7 (BSI, 1990).

Many modifications have been attempted to minimize error associated with boundary conditions in the DS test. Hvorslev (1939) noted that upper frame had a tendency to ride over the sample, and was subject to rotations. Wernick (1979) recorded counter-rotation of the load pad and upper frame. Some researchers have

attempted to restrain upper frame rotation (Shibuya et al., 1997; Takada, 1993; Wernick, 1977). Other studies sought to limit upper frame and load pad rotations by modifying the mechanism of load transfer to the system or securing the load pad to the upper frame before testing (Jewell and Wroth, 1987; Jewell, 1989). Dietz (2000) constructed a winged DS apparatus, where load was applied to the upper frame through a pair of yokes ("wings") attached to the midpoints of the upper frame's sidewalls. Load was applied coincident with the central horizontal plane through roller bearings, so that vertical restraint would not be imposed and external moments would be eliminated. This device had the benefit of well defined geometry and forces acting on the DS box and specimen, and data gathered with the device was found to correspond well with flow rules (Lings and Dietz, 2004).

A number of researchers have investigated the effects of DS box dimensions on shear strength determination. It has been observed (Cerato and Lutenegger, 2006; Dietz, 2000; Parsons, 1936) that small box dimension to particle size ratios lead to boundary constraints on DS behavior and overestimation of strength and dilation parameters, while large ratios lead to progressive failure and underestimation of the same parameters. A friction angle decrease of up to 10° has been measured for an increase in DS box length, L, from 60 to 300 mm (Cerato and Lutenegger, 2006). Additionally, increases in L led to decreasing rate of strain softening and increasing vertical displacements (Dietz, 2000; Palmiera and Milligan, 1989).

The American DS standard, ASTM D 3080 (ASTM, 2003e), recommends a minimum L of 50 mm, or ten times the maximum particle diameter, D_{max}, a minimum thickness, H, of 6 D_{max}, or at least 12 mm, and a minimum L/H ratio of two. The British DS standard, BSI 1377-7 (BSI, 1990), recommends that H/D_{max} be greater than

ten. Jewell and Wroth (1987) stated that a ratio of L over median particle diameter, D_{50}, of 50 – 300 was likely to give good DS results, while Scarpelli and Wood (1982) suggest a L/D_{50} ratio of 100.

The DS test does not provide a peak stress state at maximum obliquity with respect to the Mohr circle, i.e. it does not represent a point on the Mohr circle of stress that is tangent to the Mohr-Coulomb failure surface. Constitutive laws that utilize the Mohr-Coulomb failure surface are readily available in software, such as ABAQUS and FLAC. They require specification of the maximum obliquity effective friction angle, ϕ'_{ps}, for plane strain problems of soil-structure interaction.

Lings and Dietz (2004) outlined the parameters measurable in a DS test as the effective DS friction angle, ϕ'_{ds}, and the dilation angle, ψ. At peak state, the parameters are referred to as $\phi'_{ds\text{-}p}$ and ψ_p, respectively, while at critical state, ϕ'_{ds} is called $\phi'_{ds\text{-}ld}$, and the dilation angle approaches zero. As shown by Jewell and Wroth (1987), the horizontal direction, bisecting the DS specimen at its mid-height, is a plane of zero linear extension. As shown by Cole (1967) and Stroud (1971), the Mohr circles of stress and incremental strain coincide, so there is co-axiality. Davis (1968) gave an equation linking $\phi'_{ds\text{-}p}$ to $\phi'_{ps\text{-}p}$ using ψ, assuming zero extension and co-axiality. Taylor (1948), Rowe (1962, 1969) and Bolton (1986) all provided flow rules linking large displacement strength to peak strength in a DS test, given a known value of ψ. Stroud (1971), Jewell (1989) and Lings and Dietz (2004) showed that these flow rules were useful in evaluating the consistency of DS data.

Many researchers have used the DS apparatus to evaluate the frictional resistance at soil-structure interfaces. Trautmann and O'Rourke (1983) tested

interfaces between dry sand and materials used in his large-scale test basin (Formica and glass) using a conventional DS apparatus. O'Rourke et al. (1990) investigated interface direct shear behavior between dry sand and polymers using the conventional DS apparatus, while Lings and Dietz (2005) used the modified DS apparatus to test dry sand-steel interfaces.

1.1.2 Partially Saturated Soil Characterization

Soil moisture was first investigated for agricultural purposes (Buckingham, 1907). Significant research has been performed on the characterization of partially saturated soil in the last half-century, as summarized by Fredlund (2006). Bishop et al. (1960) measured the pore-water and pore-air pressures of partially saturated soils with high air entry ceramic disks. Fredlund and Morgenstern (1976) characterized the behavior of partially saturated soil, and later research combined volume change and shear strength for partially saturated soil in elasto-plastic models (Alonso et al., 1990; Wheeler and Sivakumar, 1995; Blatz and Graham, 2003). Fredlund (2000, 2002, 2006) discussed the challenges of the development of partially saturated soil mechanics and the solutions available for the implementation of partially saturated soil mechanics into geotechnical engineering practice.

Central to the characterization of partially saturated soil is the measurement and incorporation of the effects of matric suction on the strength properties of partially saturated media. The methods for measuring soil suction were detailed by Schofield (1935). Terzaghi (1943) discussed negative pore water pressures in relation to capillarity and drainage. The relationship between water content and matric suction has long been studied in the field of soil science. Livingston (1908) and Gardner et al.

(1922) measured matric suction using a device similar to the type of modern tensiometer used today in soil science research (Dane and Topp, 2002). Tempe cells commonly are used in soil science and geotechnical engineering (ASTM, 2008a; Dane and Topp, 2002) to develop soil water retention curves (SWRCs), which are related to the particle size distribution of a soil as well as the weight-volume properties (Fredlund et al., 1997; Fredlund et al., 2000).

Equations to represent the SWRC have been proposed (Brooks and Corey, 1964; Fredlund and Xing, 1994; van Genuchten, 1980). The point on the SWRC most useful to the current study is the residual state, which is defined by a residual water content and a residual matric suction. A qualitative definition of the residual state is the water content at which the water goes from being held within the soil primarily by capillary action to water held primarily by absorptive forces (Sillers, 1997). Various quantitative definitions of residual state have been proposed (Brooks and Corey, 1964; Lebedeff, 1927; van Genuchten, 1980; van Genuchten et al., 1991), but it has been pointed out that measured residual water contents are more a function of the instrumentation used to measure the parameter than an actual physical constant (Nitao and Bear, 1996). A graphical construction method was presented by Vanapalli et al. (1998) to define quantitatively the residual state, using the Fredlund and Xing (1994) equation for the SWRC.

The water retention properties of a soil are hysteretic, meaning that they behave differently in wetting (adsorption) than drying (desorption). Different methods of measurement result in different SWRCs, as discussed by Klausner (1991). Numerous physically- and empirically-based hysteresis models for the SWRC have been proposed, from Everett (1954, 1955) to Feng and Fredlund (1999). Pham et al.

(2005) evaluated 28 different physical and empirical models using 34 different soils in laboratory testing, and developed their own model, based on a simplified version of the Feng and Fredlund (1999) model.

1.1.3 Measurement of Soil Properties for Large Scale Tests

Previous studies at Cornell University (Trautmann and O'Rourke, 1983; Turner, 2004) used a 1.2 m x 2.4 m x 1.2 m wooden box to place and compact dry and partially saturated sand around buried pipelines, which were then displaced relative to the sand to induce soil-structure interaction forces. Large-scale testing of ground rupture effects on steel gas distribution pipelines with 90° elbows were performed at Cornell University in collaboration with Tokyo Gas, Ltd. (Yoshisaki et al., 2001). The experimental setup involved the largest full-scale replication of ground deformation effects on pipelines ever performed at that time in the laboratory, involving a split test basin with up to 65 metric tons of partially saturated sand and a buried pipeline subjected to 1 m of offset along a strike-slip fault.

Evaluation of dry unit weight, γ_{dry}, of the sand placed and compacted for large scale tests is critical to the selection of an appropriate friction angle and shear strength. Trautmann et al. (1985) measured γ_{dry} for dry sand using the Selig Density Scoop (Selig, 1962, Selig and Ladd, 1973), which was modified to increase the base plate dimensions and add scissor arms. Turner (2004) used the density scoop to measure γ_{dry} for dry and partially saturated sand, using lead block weights placed on the base plate to improve the repeatability of the device. With proper technique and calibration, the density scoop was found to provide suitable measurements of soil unit

weight, although taking many measurements with the scoop is time- and labor-intensive.

The nuclear gage has long been the industry standard for measurement of asphalt, concrete, and soil backfill unit weight for roadway and geotechnical construction (Mamlouk, 1988; NYSDOT, 2007). Servais (1990) calibrated the nuclear gage on calibration blocks of known unit weight and water content. Jameson (1985a and 1985b) and Mamlouk (1988) showed that the nuclear gage must be recalibrated for each new material. Cassaro et al. (2000) calibrated a nuclear gage over a wide range of densities and materials. The procedures for calibration and efficient use of the nuclear gage to measure the unit weight of soil and the weight of water present in a soil are given by ASTM D6938 (ASTM, 2008b).

1.1.4 Assessment of Soil-Structure Interaction Pressures

Soil-structure interaction forces in large scale tests have been measured conventionally by load cells external to the soil and embedded test pipe (Trautmann and O'Rourke, 1983; Turner, 2004). The current research involves soil-structure interaction tests where the pressures and forces produced by soil-structure interaction are not easily measureable externally, and must be measured at the pipe-soil interface. Conventional soil stress cells, such as those used by Yoshizaki (2002), typically register stresses that are either low or high relative to actual soil stresses as a function of stress cell stiffness, size and aspect ratio (thickness-to-length ratio), cell placement procedures, and other factors (Kohl et al., 1989; Dunnicliff, 1988; Weiler and Kulhawy, 1982; Selig, 1964). Because tactile pressure sensors are thin, wide and

flexible, they possess favorable characteristics with respect to aspect ratio and stiffness.

A tactile pressure sensor is an array of small sensors, referred to as sensels, embedded in a polymeric sheet or pad, that measure the distribution of normal stresses associated with externally applied loads. Paikowsky and Hajduk (1997) reported on a comprehensive series of sensor tests in granular media, concluding that the device provided normal stress measurements in granular soil to a good degree of accuracy. The sensors have also been applied to measure the vertical stress under model strip footings (Paikowsky et al., 2000), vertical stress distribution due to arching during trap door experiments in granular material (Paikowsky et al., 2003), vertical stress distribution beneath a conical pile of sand (Paikowsky et al., 2006) and vertical pressures transmitted by railroad tracks (Stith, 2005). Paikowsky and coworkers developed a calibration device for applying controlled granular material pressure to tactile pressure sensors (Paikowsky and Hajduk, 1997) and investigated the effects of soil grain size relative to sensel dimensions on sensor measurements (Paikowsky et al., 2006).

1.2 Objectives

The goals of this work are to investigate comprehensively the factors affecting soil performance for soil-pipeline interaction. Methods of determining appropriate material properties for dry and partially saturated sand are shown and compared with previous research. Procedures for placing and measuring soil for large scale tests of soil-pipeline interaction are described and evaluated, and techniques for assessment of the soil-pipeline interaction force are shown. Sample interpretations of large scale

data are given. The goals of the thesis are addressed by focusing on four objectives as described briefly in the following sections.

1.2.1 Dry Soil Strength Characterization

The properties of dry sand are investigated, starting with physical characteristics of three different glacio-fluvial materials. The design and application of the DS apparatus are explored, starting with conventional procedures and including an analysis of key variables, such as modified DS specimen boundary conditions and changes in DS specimen dimensions. Systematic testing is performed to characterize DS sand strength and critical state properties of the three glacio-fluvial materials. DS strength parameters are converted to plane strain strength parameters. Flow rules are used to evaluate the relationship between peak and critical state strength and dilation properties.

1.2.2 Partially Saturated Soil Characterization

The properties of partially saturated sand are investigated using a variety of techniques. Matric suction is measured for large-scale tests of soil-pipeline interaction using tensiometers. Tempe cells are used to define SWRCs for partially saturated sand at a variety of γ_{dry}. The hysteresis and residual state of partially saturated sand is evaluated to compare measurements of matric suction by the tensiometer and the Tempe cell. Direct shear tests are performed on partially saturated sand to develop a Mohr Coulomb model for soil behavior, and the measured parameters are evaluated using modified flow rules. DS strength parameters are converted to plane strain. Dry and partially saturated sand properties are compared at the same γ_{dry}. The effect of

matric suction on the cohesion, strength, and dilation of partially saturated soil is investigated.

1.2.3 Measurement of Soil Properties for Large Scale Tests

The nuclear gage and density scoop are calibrated for dry and partially saturated sand. Performance of the nuclear gage is assessed with respect to measurement depth, time duration, wall proximity, and location in the test box. A statistical framework is established for the quantitative determination of different sources of measurement variability. The preparation, placement and compaction of dry and partially saturated soil to target water content and γ_{dry} for large scale tests are discussed. Results from large scale tests are presented and evaluated, and the nuclear gage and density scoop are directly compared, using measurements from the calibration box and large scale tests.

1.2.4 Assessment of Soil-Structure Interaction Pressures

Tactile pressure sensors are calibrated and prepared for large scale soil-structure interaction tests. Methods for minimizing the effects of shear on sensor measurements are discussed, and the efficacy of these methods are demonstrated by laboratory experiments. The time-dependent characteristics of the sensors are evaluated, and recommendations are provided for measurements that account for time dependent effects. Tactile pressure sensor measurements in response to vertical loading and unloading are used to verify the sensor calibration. Lateral loads on full-scale pipelines affected by large horizontal ground movements are measured by tactile

pressure sensors according to a procedure developed by O'Rourke et al. (2008) and compared with independent measurements of the loads.

1.3 Scope

The work is divided into six chapters, the first of which provides background and objectives of the study. Chapter 2 reviews the DS apparatus and soil strength properties obtained with the equipment. A modified DS box is described, which was used to measure the DS and plane strain properties of three dry glacio-fluvial sands. Chapter 3 presents the matric suction and DS properties of partially saturated sand. The strength and dilation of dry and partially saturated sand are compared, and the differences are explained in terms of matric suction. Chapter 4 discusses the placement of soil for large scale tests and the measurement of properties for dry and partially saturated sand. The bias and precision of two different measurement devices for dry unit weight are compared by examining data from calibration and large scale tests. Chapter 5 provides an assessment of tactile pressure sensors for geotechnical applications. They are calibrated and protected from shear effects to produce accurate, repeatable results. The tactile pressure sensor response is validated with vertical loading, and tactile pressure sensors are shown to provide lateral force vs displacement measurements that compare favorably with those obtained independently with load cells. The final chapter summarizes the research findings and presents conclusions pertaining to the work. It also provides recommendations for future research.

CHAPTER 2

DIRECT SHEAR CHARACTERISTICS OF DRY GLACIO-FLUVIAL SAND

2.1 Introduction

This chapter discusses the characteristics of dry sands used in large-scale ground rupture tests of buried pipelines at the NEES facility at Cornell University (CU) (Palmer et al., 2006, O'Rourke et al., 2008). Centrifuge tests at Rensselaer Polytechnic Institute (RPI) were performed for comparison with the large-scale tests (Ha et al., 2008). To promote similitude between the large-scale tests at CU and centrifuge tests at RPI, a fraction of the RMS graded sand, referred to in this chapter as RMS uniform sand, was obtained from the RMS graded sand by screening out all particles larger than 0.475 mm (#40 sieve) and smaller than 0.075 mm (#200 sieve). A third sand, used in previous large scale testing at Cornell University by Trautmann and O'Rourke (1983) and Turner (2004), is referred to as Cornell Filter Sand (CU Filter).

To learn about the characteristics of the three sands, particle size distributions were made, microscope analysis was performed, and direct shear (DS) data were collected and analyzed. DS tests were performed using two types of DS apparatus with DS specimens of three different sizes. The influence of gap separation between the two halves of the DS box was investigated, as was the influence of edging to constrain the soil at the shear plane. DS box dimensions were compared to investigate the influence of specimen length and height relative to the grain size parameters of the

material used. DS tests were run over a range of dry unit weights and normal stresses to investigate the influence of these parameters on the strength and dilation characteristics of each of the three sands. The relation between soil strength and dilation was evaluated though comparison with theoretical models of soil behavior.

2.2 Description of Sand

The large-scale experimental soil is a crushed, washed, glacio-fluvial sand, consisting of particles mostly passing the 6.3 mm (1/4 in.) sieve. The sand is produced by RMS Gravel, Dryden, NY, and meets the New York State Department of Transportation specification for sand backfill (NYSDOT, 2008). This soil, referred to in this chapter as RMS graded sand, was used in previous large-scale testing at Cornell University (Turner, 2004; Yoshizaki, 2002).

This chapter also presents test results for Cornell Filter (CU Filter) sand. As described by Trautmann and O'Rourke (1983), CU Filter sand is a clean, subangular glacio-fluvial sand. The material was produced by W.F. Saunders & Sons, Nedrow, NY. A petrographic analysis showed 20% quartz, 40% limestone, 20% siltstone, and 10% quartzite in addition to traces of other constituents.

2.2.1 Particle Size Distributions

Particle size distributions performed on RMS graded sand, RMS uniform sand and CU Filter sand are shown in Figure 2.1. The analyses were performed in accordance with ASTM D422 (2003a). RMS graded sand is composed of washed

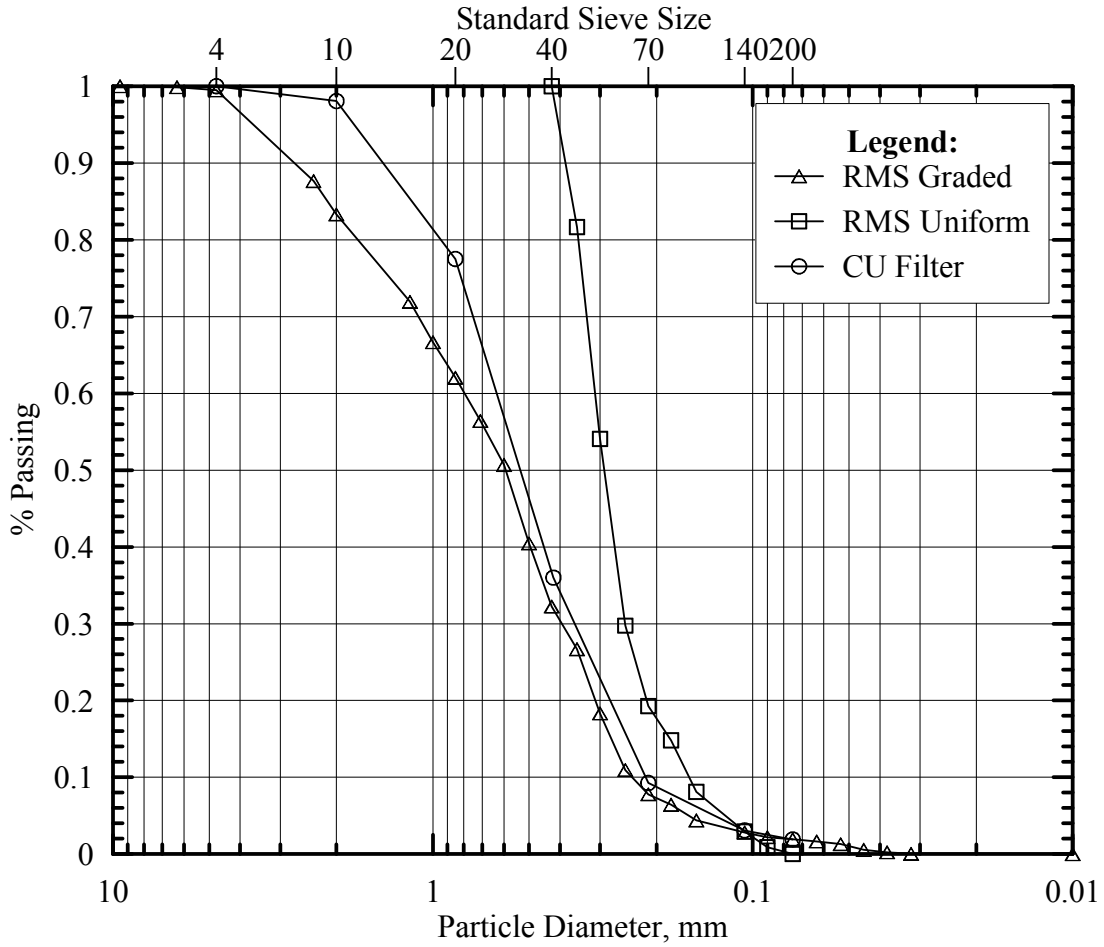

Figure 2.1 Particle size distributions for RMS graded, RMS uniform and CU Filter sand

crushed stone fragments ranging in diameter from particles passing the #450 sieve (0.032 mm) to those retained on the ¼ in. sieve (6.3 mm). The mean grain size, D_{50}, for the soil is 0.59 mm, the coefficient of curvature, C_c is 0.83, and the coefficient of uniformity, C_u, is 3.35.

RMS uniform sand was obtained by removing all particles retained on the #40 sieve and passing the #200 sieve. The resulting sand has particles ranging in diameter from 0.075 mm to 0.425 mm and has D_{50} = 0.29 mm, C_c = 1.27, and C_u = 1.97. Both

RMS graded and RMS uniform sand are classified as poorly graded sand (SP) according to the Unified Classification System. Atterberg limit tests performed on the fines fraction of RMS graded sand in accordance with ASTM D4318 (2003f) indicate negligible plasticity. This is consistent with the manufacturing process, whereby the sand was washed, removing all clay and silt particles.

Table 2.1 shows the particle size distribution parameters, angularity, and mineralogy for RMS graded and RMS uniform sand. Table 2.2 shows the grading parameters for RMS graded, RMS uniform and CU Filter sand. CU Filter sand was analyzed by Turner (2004), and his particle size distribution is used in the figures and tables in this section. Generally, CU Filter sand has a particle size distribution between the RMS graded and RMS uniform sand, and is also classified as poorly graded sand. It has a greater C_u than RMS uniform sand but less than RMS graded sand. Its C_c parameter is approximately identical to RMS uniform sand, and greater than RMS graded sand.

2.2.2 Microscope Analysis

RMS graded sand, sorted by particle size, was examined by microscope, to show an approximate composition of 71% by volume of siltstone, fine-grained sandstone, shale, and limestone fragments, and 29% quartz grains. The fraction of the RMS uniform sand was also examined by microscope to show 44% rock fragments and 56% quartz grains. The smaller particles are more quartzitic and rounded, and larger particles are composed primarily of rock fragments (shale, siltstone, and sandstone) and are more angular. RMS graded sand is shown in Figure 2.2, with an

Table 2.1 Physical characteristics of RMS graded and RMS uniform sand

Standard Sieve Size	Sieve Opening (mm)	Retained (RMS graded)	Retained (RMS uniform)
4	4.750	0.5%	0.0%
10	2.000	16.2%	0.0%
20	0.850	21.3%	0.0%
40	0.425	29.8%	0.0%
70	0.212	24.5%	80.7%
140	0.105	5.0%	16.3%
200	0.075	0.9%	2.9%
PAN		1.9%	0.0%

Standard Sieve Size	Angularity			Quartz
	Angular	Sub-angular	Sub-rounded	
4	65-70%	20-25%	5-15%	0%
10	65-70%	20-25%	5-15%	5%
20	65-70%	20-25%	5-15%	10%
40	70-80%		10-20%	30%
70	75-80%		20-25%	55%
140	75-80%		20-25%	65%
200	75-80%		20-25%	80%
PAN	Rock Flour			80%
Notes:	1. Particles are shale, siltstone, and sandstone			
	2. Particles look clastic, not crystalline			
	3. Atterberg limit tests indicate negligible plasticity			

Table 2.2 Grading characteristics for RMS graded, RMS uniform, and CU Filter sands

Soil Name	D_{10}	D_{30}	D_{50}	D_{60}	C_c	C_u
RMS graded	0.24	0.40	0.59	0.80	0.83	3.35
RMS uniform	0.16	0.25	0.29	0.31	1.27	1.97
CU Filter	0.23	0.42	0.53	0.61	1.26	2.65

inset of particles passing the #20 sieve (0.85 mm) but retained on the #40 sieve (0.425 mm), corresponding to D_{50} for RMS graded sand. RMS uniform sand is shown in Figure 2.3, with an inset of particles passing the #40 sieve (0.425 mm) but retained on the #70 sieve (0.212 mm), corresponding to D_{50} for RMS uniform sand. Notable in these images is the greater angularity of larger particles in comparison with smaller particles, consistent with a crushed material. CU Filter sand is shown in Figure 2.4, with an inset of particles passing the #20 sieve (0.85 mm) but retained on the #40 sieve (0.425 mm), corresponding to D_{50} for CU Filter sand.

Previously performed petrographic analysis on RMS graded sand indicated 45% limestone fragments, 18% quartz grains, 16% siltstone fragments, traces of other constituents, and a specific gravity of 2.71 (Yoshizaki, 2002). These analyses are consistent with the microscope-assisted analysis reported above. A particle size distribution obtained by Turner (2004), who also performed DS tests on dry RMS graded sand, shows a particle size distribution nearly identical to the one for RMS graded sand by this study.

2.2.3 Angle of Repose

The angle of repose for the experimental sands was first investigated using a procedure proposed by Santamarina and Cho (2001) whereby a square box with clear plastic sides is half filled with sand. The box is tilted 90° to one side, and then slowly brought back to its original position, allowing the sand particles to form a slope within the box at the angle of repose. This method was found to give inconsistent results. For the RMS graded sand in particular, the formation of the sand slope led to

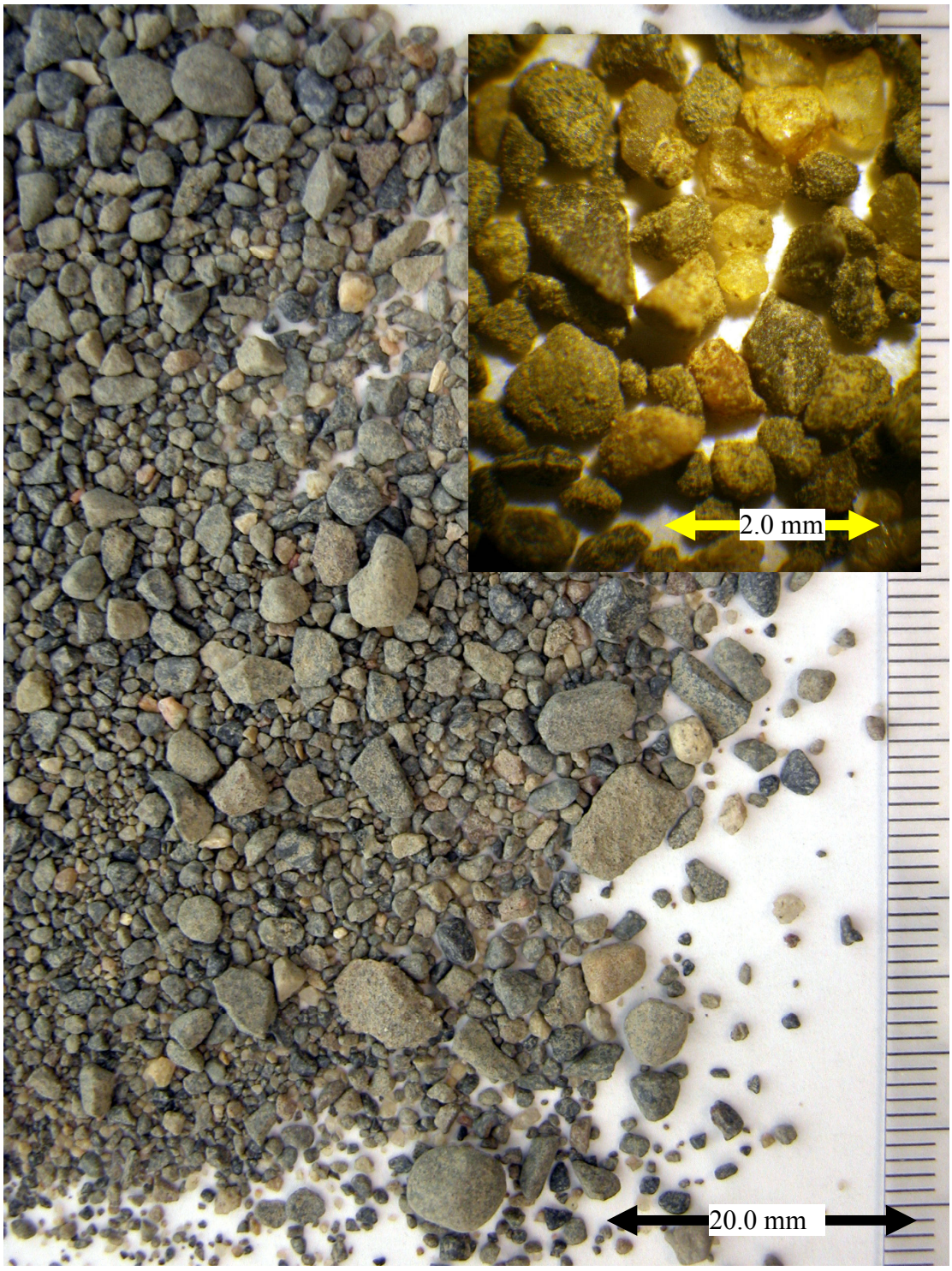

Figure 2.2 Photo of RMS graded sand with inset of sand with particle diameter between 0.425 – 0.85 mm

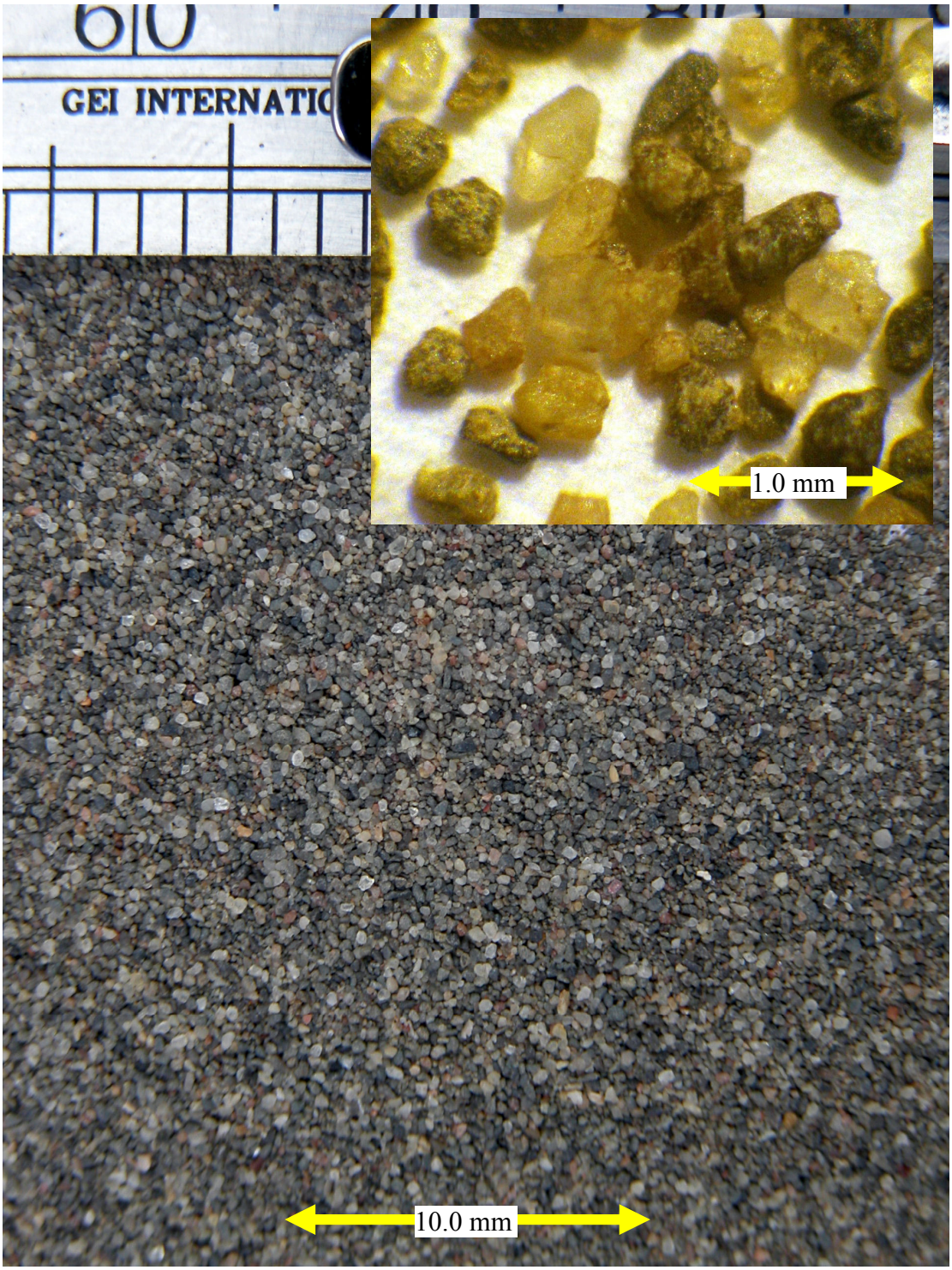

Figure 2.3 Photo of RMS uniform sand with inset of sand with particle diameter between 0.212 – 0.425 mm

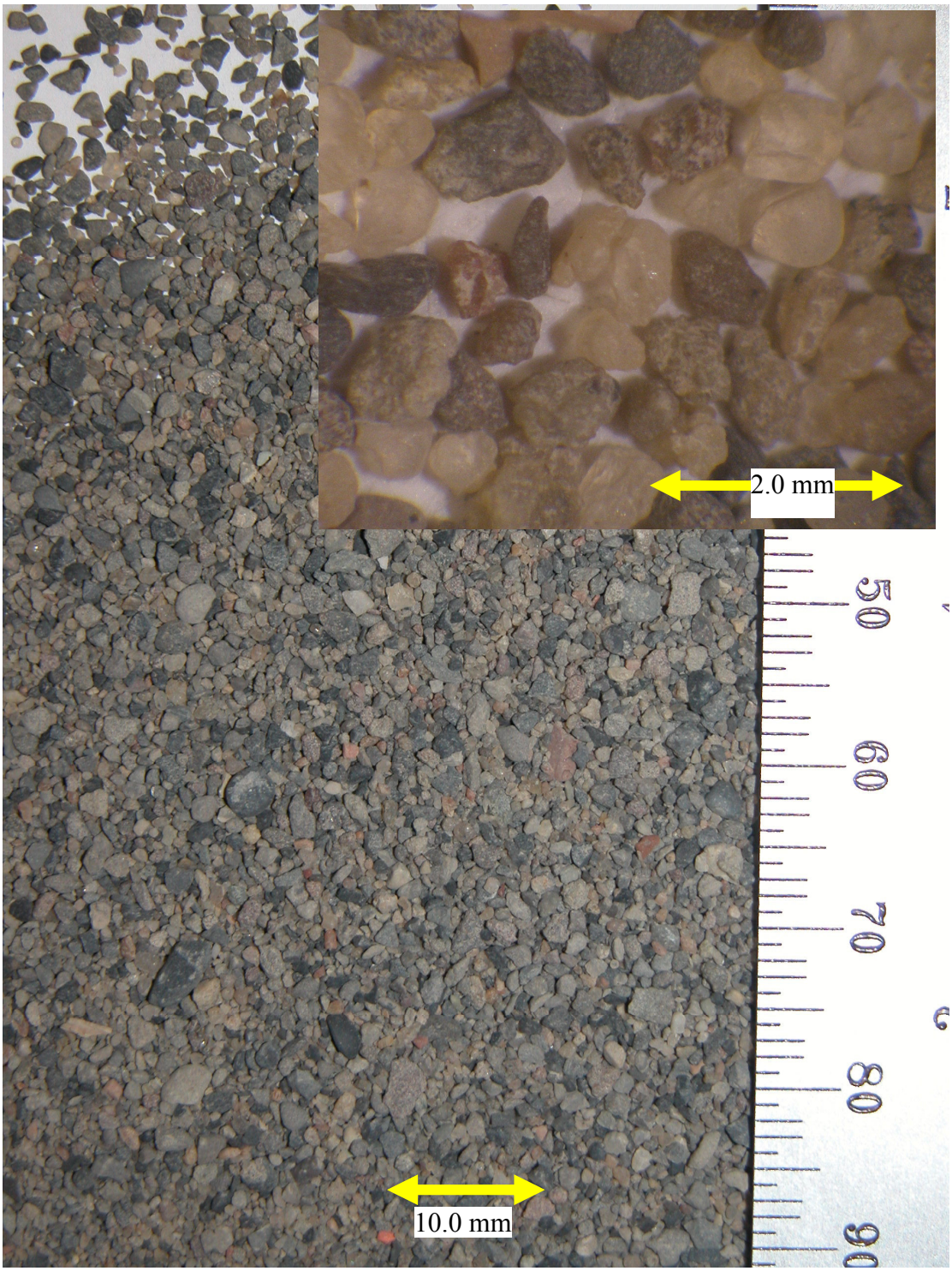

Figure 2.4 Photo of CU Filter sand with inset of sand with particle diameter between 0.425 – 0.85 mm

segregation of the larger particle sizes as they rolled down the slope over the smaller particles, so that the slope was not composed of a representative mixture of grain sizes. The degree of segregation was variable with each test, leading to inconsistent results.

Miura et al. (1997) developed a 75 mm diameter pedestal-ring apparatus to produce sand cones for measurement of the angle of repose of dry sands. Dietz (2000) found that the angle of repose of dry sand was a good estimator for the critical friction angle, and called the parameter the axisymmetric angle of repose, using the symbol $i_{ax.}$. The sand is placed by pouring from a funnel, starting with the funnel directly on the bottom of the pedestal and raising the funnel as slowly as possible. Keeping the soil drop height to the minimum ensures that the soil is placed at the lightest possible dry unit weight (γ_{dry}). Soil is poured from the funnel until the base of the cone reaches the edge of the outer ring, at which point the funnel is held in place as the remaining sand slowly flows over the cone. The shims are removed and the outer ring is slowly lowered to the bottom of the pedestal. The sides of the resulting sand cone on the pedestal is oriented at the angle of repose with respect to the horizontal. Figures 2.5a through 2.5d show the procedure in a series of photos. Multiple repetitions of the sand cone test were performed for each of the three sands, and histograms of i_{ax} are shown in Figure 2.6. Figures 2.7 shows photographs of typical sand cones formed using RMS uniform, RMS graded, and CU Filter sand. RMS graded and CU Filter sands are subject to particle segregation, which tends to decrease i_{ax} measured using the sand cone.

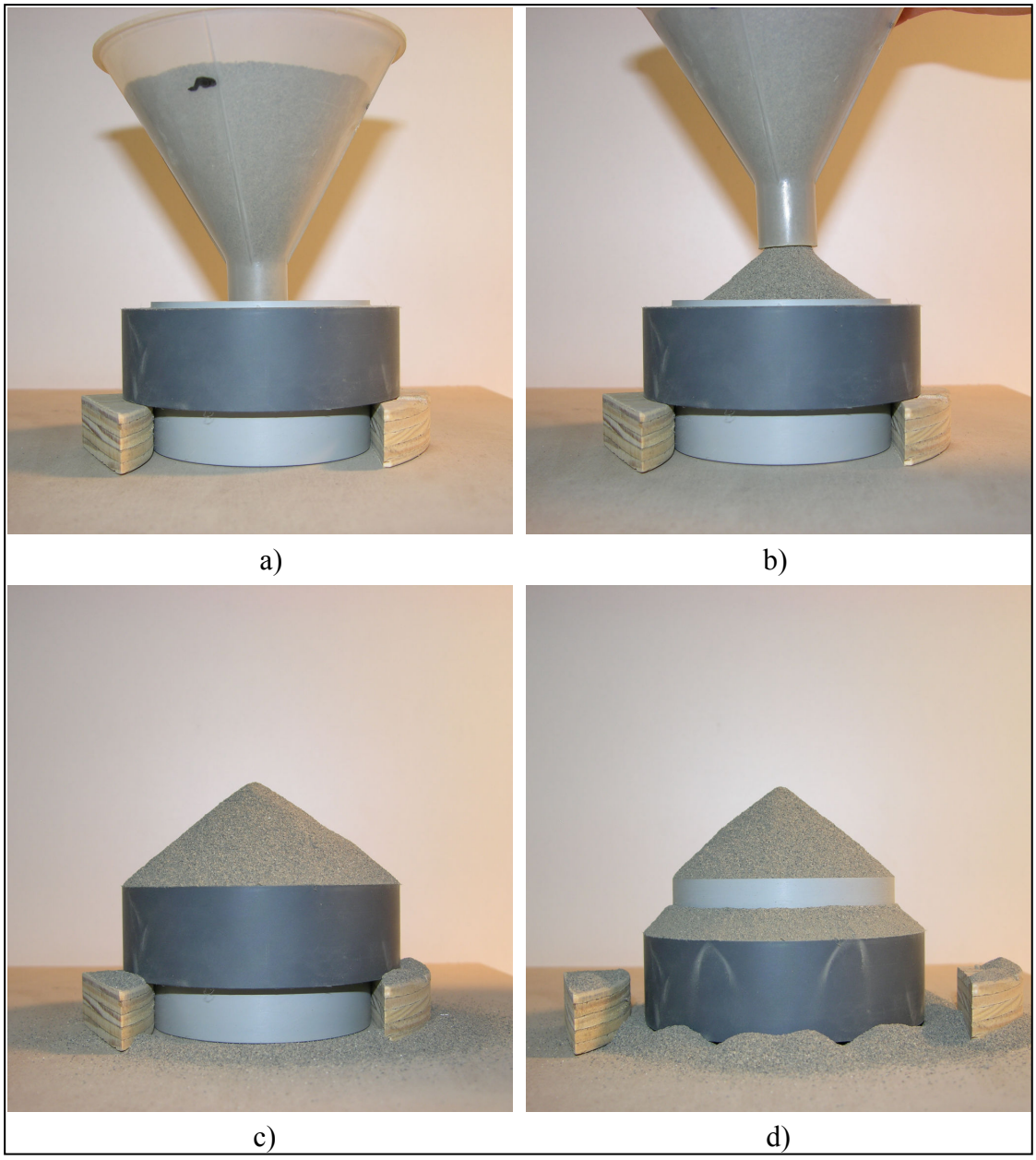

Figure 2.5 Photographs of sand cone angle of repose procedure: a) Funnel resting on pedestal b) Funnel lifted up slowly to release sand c) Sand cone to edge of outer ring d) Outer ring lowered slowly to expose sand cone on pedestal

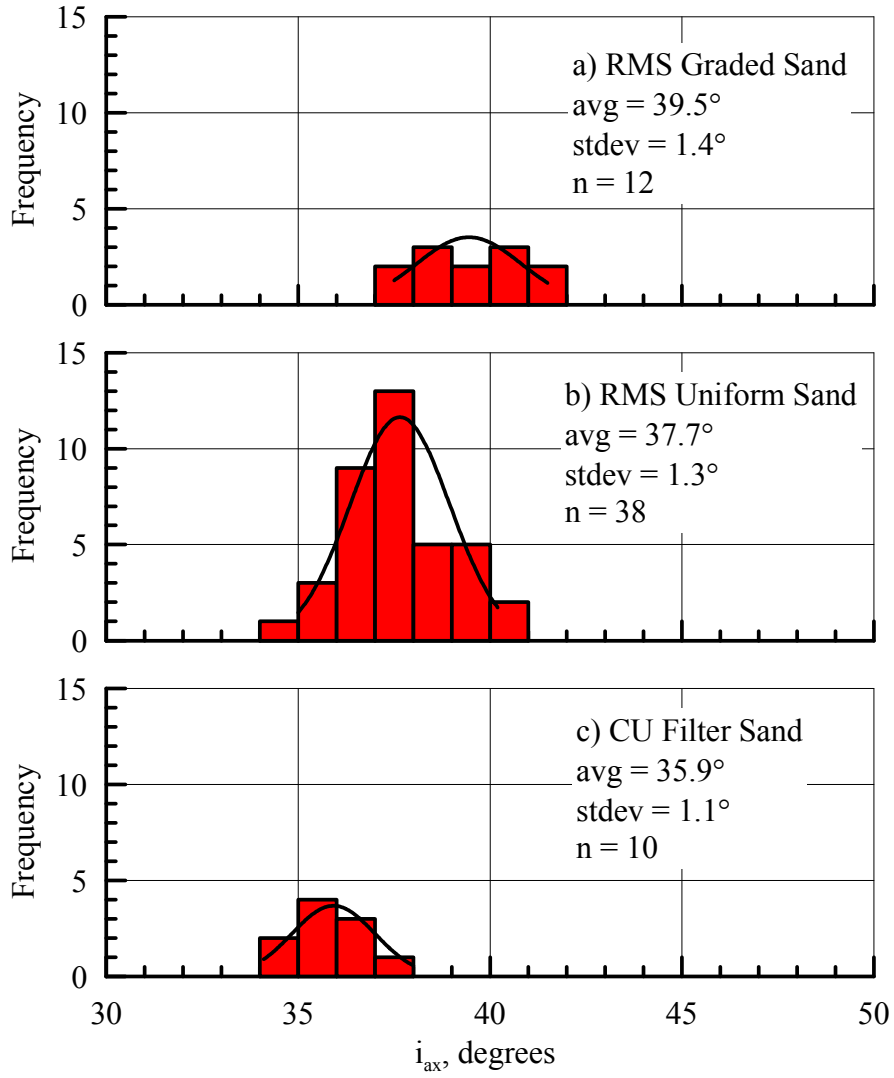

Figure 2.6 Histograms of axisymmetric angle of repose for the three test soils showing data gathered using the sand cone

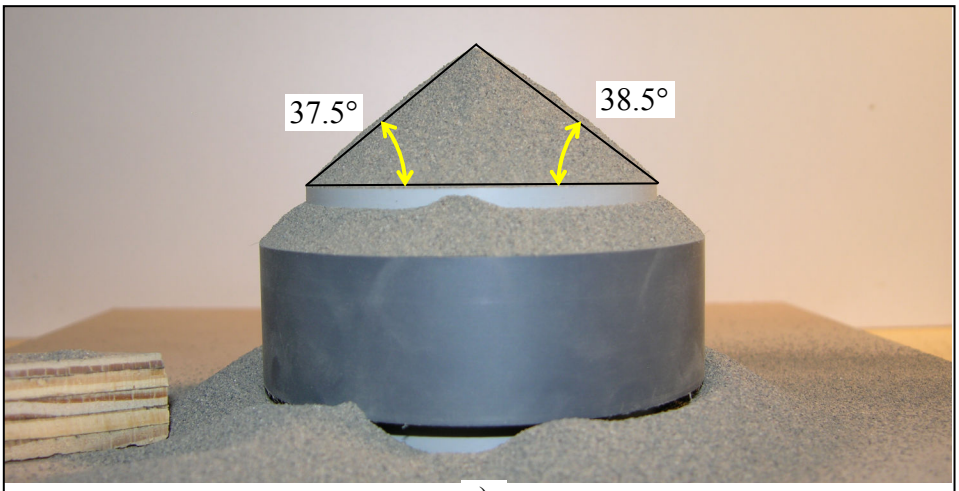

a)

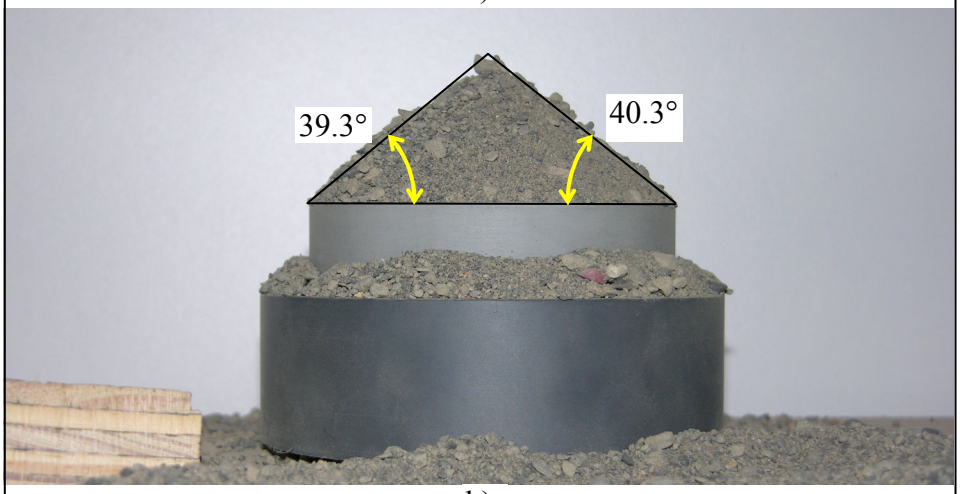

b)

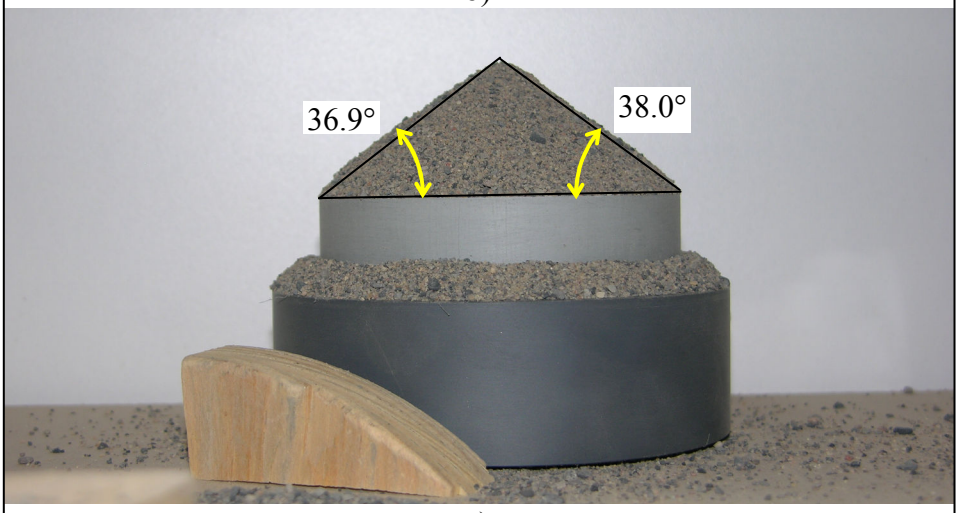

c)

Figure 2.7 Sand cones a) RMS uniform sand b) RMS graded sand c) CU Filter sand

2.3 Direct Shear Relationships

Mohr circles of incremental strain and stress, suitable for characterizing dry RMS graded and RMS uniform sand, are shown in Figures 2.8a and 2.8b, respectively. As described by Lings and Dietz (2004), the four parameters measurable from a DS test are the effective direct shear friction angle, ϕ'_{ds} (also known as $\phi'_{ds\text{-}p}$ at peak), the dilation angle, ψ (ψ_p at peak), the effective plane strain friction angle, ϕ'_{ps} ($\phi'_{ps\text{-}p}$ at peak), and the critical state effective plane strain friction angle, ϕ'_{crit}. ϕ'_{ds} is obtained from measurements of effective shear stress, τ' (τ'_p at peak), and effective normal stress, σ' (called σ'_N for convenience), on the shear plane using

$$\tan\phi'_{ds} = \frac{\tau'_p}{\sigma'_N} \tag{2.1}$$

ψ is obtained from the change of vertical soil displacement, v_y, relative to the horizontal displacement, v_x, between the upper and lower boxes of the DS test apparatus, using

$$\tan\psi = \frac{-d\varepsilon_{yy}}{d\gamma_{yx}} = \frac{dv_y / t_{DS}}{dv_x / t_{DS}} = \frac{dv_y}{dv_x} \tag{2.2}$$

which assumes all dilation occurs within a simple shear zone of thickness, t_{DS}, where ε_{yy} is the vertical soil strain in the simple shear zone, and γ_{yx} is the horizontal soil shear strain in the simple shear zone.

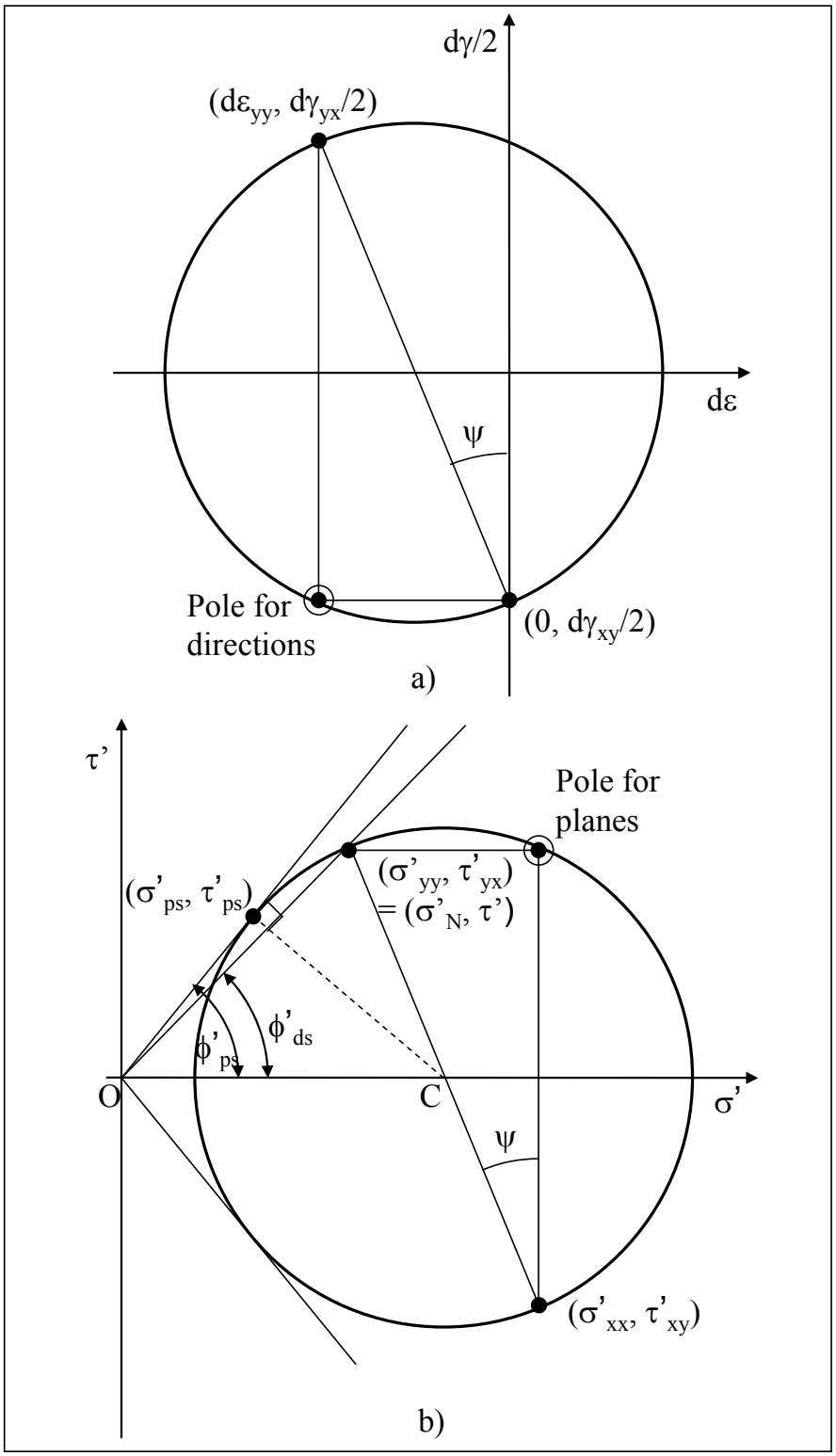

Figure 2.8 Mohr's circles for a) Incremental strain and b) Stress (after Lings and Dietz, 2004)

At large horizontal displacement, ϕ'_{ds} reaches a constant value independent of initial pre-shear γ_{dry}, called the large displacement direct shear friction angle ($\phi'_{ds\text{-}ld}$). The critical state occurs when the sand is displaced at constant strength and volume. ϕ'_{ps}, which describes conditions of maximum stress obliquity in the soil, can be written as

$$\tan\phi'_{ps} = \frac{\tau'_{ps}}{\sigma'_{ps}} \tag{2.3}$$

where τ'_{ps} and σ'_{ps} are the effective shear and normal stresses, respectively, on the plane strain failure envelope. Many researchers (Bishop, 1950; Bolton, 1986; Dietz, 2000; Lings and Dietz, 2004; Houlsby, 1991; Jewell, 1989; Taylor, 1948; Shibuya et al., 1997; Stroud, 1971; Wroth, 1958) claim that $\phi'_{ds\text{-}ld}$ is reached in the DS test at ϕ'_{ps} equal to ϕ'_{crit}.

As discussed by Lings and Dietz (2004), work by Cole (1967), Stroud (1971), and Dyer (1986) show that at peak strength, there is co-axiality, meaning that the principal axes of stress and incremental strain coincide, as is the case in Figure 2.8. The horizontal axis is a direction of zero linear incremental strain (zero extension). Assuming co-axiality, the dilation angle enables the Mohr's circle of stress to be constructed from the measured values of τ'_{p}, and σ'_{N}. Davis (1968) first derived the equation linking the parameters shown in Figure 2.8b

$$\tan\phi'_{ds} = \frac{\cos\psi \sin\phi'_{ps}}{1-\sin\psi \sin\phi_{ps}} \tag{2.4}$$

which at the critical state ($\psi = 0$) becomes

$$\tan \phi'_{ds} = \sin \phi'_{crit} \quad (2.5)$$

2.4 Direct Shear Apparatus

Over 700 DS tests were performed to quantify the DS behavior of RMS graded, RMS uniform and CU Filter sand. The DS test apparatus induces relative displacement between the upper and lower rigid halves of the DS box on a horizontal surface that is initially square. The tests were performed using DS testing apparatus with upper and lower frames with nominal interior horizontal dimensions of 1) 60 mm x 60 mm, 2) 100 mm x 100 mm, and 3) 300 mm x 300 mm, referred to as the 60 mm, 100 mm, and 300 mm test boxes, respectively.

2.4.1 Direct Shear Testing Using Conventional Apparatus

The 60 mm DS tests were performed using a conventional Wykeham-Farrance DS testing apparatus powered with a Drayton 1 rpm Type RQR electric motor, connected by a drive chain to a worm drive unit. The data acquisition system consisted of a National Instruments NI cDAQ-9172 chassis, two Tektronix CPS250 Triple Output power supplies, and an IBM Lenovo LE-1150 computer system.

A schematic of the conventional DS apparatus is shown in Figure 2.9a, a free body diagram of shear and normal forces is shown in Figure 2.9b, and schematics of the DS box are shown in Figures 2.9c and 2.9d. A photograph of the 60 mm DS box is shown in Figure 2.10a. Horizontal force was measured using a Data Instruments JP200 load cell with a capacity of 0.89 kN in compression or tension, and horizontal

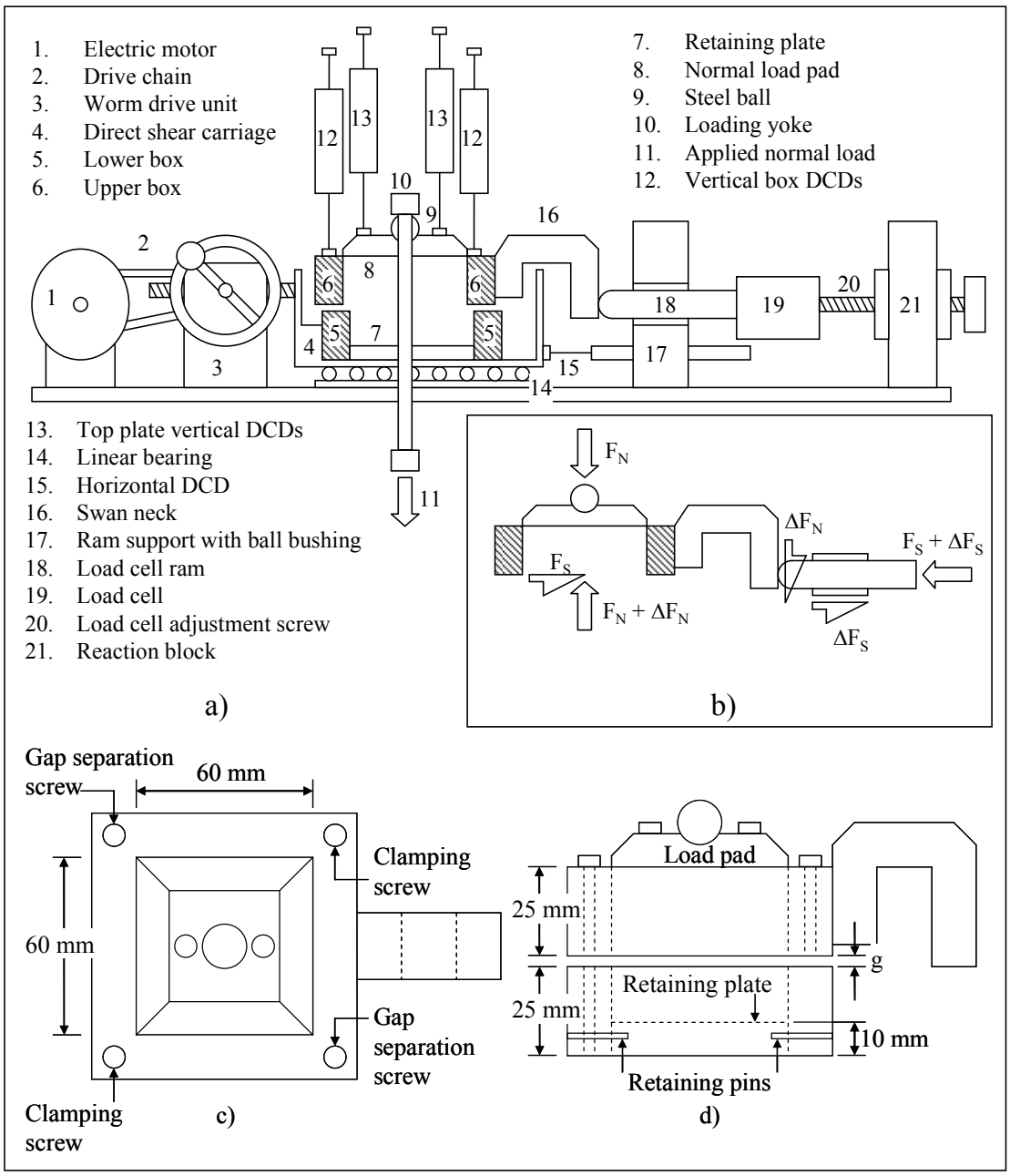

Figure 2.9 a) Schematic of conventional DS apparatus b) Free-body diagram of 60 mm box c) Plan view of 60 mm box d) Elevation view of 60 mm box

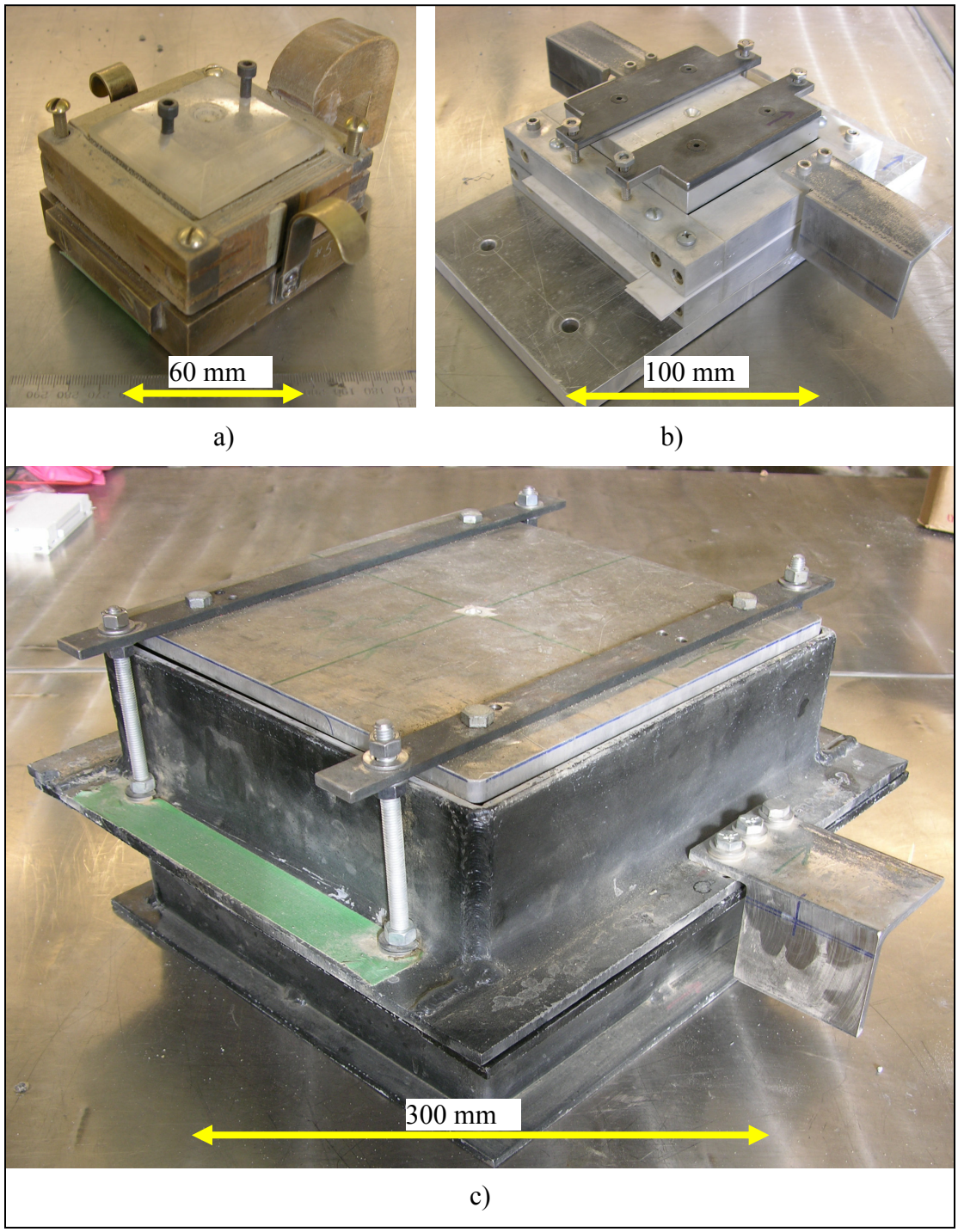

Figure 2.10 a) 60 mm conventional DS box b) 100 mm winged DS box with locking top plate c) 300 mm winged DS box with locking top plate

displacement measured with a Trans-Tek Model 0336 linear variable differential transformer (LVDT) with a range of ± 13 mm. A steel ball and plastic top plate distributed σ'_N evenly to the soil from weights applied through a loading yoke, and vertical displacement and tilt of the top plate were measured using two Schaevitz Type 200 direct current displacement transducers (DCDTs) with a range of ± 6 mm. Vertical displacement and tilt of the upper frame were measured using a third Schaevitz Type 200 DCDT and a Trans-Tek 0243-000 D-93 DCDT with a range of ± 18 mm. Horizontal force transfer at the interface between the load cell ram and ram support was minimized with a ball bushing, and assumed to be negligible.

The 60 mm DS box had nominal inside dimensions of 60 x 60 x 42 mm, with a conventional brass lower box and an upper box machined from maple wood, held together at opposite corners by a pair of machine screws, called "clamping screws" (see Figure 2.9c). The wooden upper frame weighed 0.9 N in comparison with the 13.0 kN brass upper frame available from commercial DS testing equipment suppliers. This wooden upper frame, also used with previous research at CU (Trautmann and O'Rourke, 1983; O'Rourke and Druschel, 1989; Turner, 2004), minimized the vertical load transferred to the soil failure plane by the upper DS frame, reducing uncertainties in the calculation of σ'_N on the soil specimen. The use of the lightweight upper frame also conformed to the ASTM specifications, which specify that "the weight of the top shear box should be less than 1 percent of the applied normal force" (ASTM, 2003e). Since the average applied normal load was 79.1 N for the majority of tests, the upper frame accounted for 1.2% of the total normal load on the shear plane for these tests. For all tests, the weight of the upper frame was accounted for in the calculation of σ'_N on the shear plane, since the vertical DCDTs monitoring the upper frame showed that it did not contact the lower frame, and therefore all normal force from the weight of

the upper frame was transferred though the soil at the shear plane. Self weight of the soil above the shear plane, weight of the top plate, steel centering ball, and loading yoke, and weight of the DCDT central cores were also accounted for in the calculation of σ'_N. A pair of retaining plates (6.4 and 3.4 mm thick) were supported on pins attached to the bottom shear box to ensure a consistent soil specimen volume from test to test, and to retain the soil for specimen weight measurements after each test.

A problem with the conventional DS apparatus is the connection between the load cell ram and the swan neck of the upper DS frame. Since the load cell ram cannot displace vertically, there is a tendency for vertical normal load transfer at this connection during testing of a dilative soil specimen. This load transfer applies an unknown additional normal load to the soil specimen, as well as increases the shear friction between the ball bushing and the load cell ram. Both of these problems create uncertainties in the assumed normal and shear stresses applied to the soil specimen, creating a potential for increased variability in a DS testing program.

In the conventional apparatus, the top plate is free to rotate, because there is no mechanism to lock the plate to the upper frame as there is in the modified apparatus. The top plate therefore tends to rotate forward, causing soil specimen disturbance and measurement uncertainties. The top plate rotation is most pronounced at large horizontal displacements, causing uncertainties in the measurement of $\phi'_{ds\text{-}ld}$.

2.4.2 Soil Specimen Preparation and Testing Using Conventional Apparatus

Great care was taken in the preparation of soil to the proper γ_{dry}. Each 60 mm test required about 3.9 N of sand. Soil was placed in the DS box in two lifts, making

sure that the lift boundary was far enough from the shear plane (typically 3 – 5 mm) that an artificial plane of weakness was not created near the shear plane, which would affect test results. Loose soil was placed in the DS box using a special teaspoon with the handle bent at 90º to the spoon. Soil could be placed with the bent spoon with very little disturbance to obtain low γ_{dry}. Dense soil was placed using a teaspoon, leveled, and compacted using a 59 x 59 mm plate and a specially designed hammer consisting of a 2.7 N steel rod falling down a 25 mm diameter, 300 mm long PVC pipe. Compaction effort was controlled by the number of times the rod was dropped onto the plate. For the second lift, a compaction collar was placed on the upper frame to maintain a consistent horizontal confinement of the soil specimen during placement and compaction. Soil was leveled to the top of the box using a straightedge, and loose soil was cleared from the top and sides of the box using a small brush.

After the top plate and yoke were assembled, the vertical DCDTs were put in place and adjusted to be at the center of their range, and their initial values were recorded. Normal load was applied to the specimen by placing weights on the loading yoke, and vertical displacement of the top plate and upper frame were recorded by the DCDT measurements. For tests run with the "gap screw method", gap screws were advanced clockwise 1 full turn to separate the upper and lower box and then removed, fix screws were removed, and the final pretest vertical displacement of the top plate and upper frame were recorded. For tests performed using the "Teflon strip method", the strips were removed, fix screws removed, and final pretest vertical displacement of the upper frame recorded. Initial volume of the soil specimen was calculated using the average of measurements from the top plate DCDTs, assuming that the change in height of the top plate was identical to the change in height of the soil specimen. The separation between the top and bottom DS frames, or gap, was assumed to equal the

vertical displacement of the upper frame, measured by the upper frame DCDTs. Pretest values for horizontal load and displacement were recorded, and the load cell position was adjusted to make contact with the loading arm of the upper frame. The data acquisition program was restarted, the motor started, and the upper frame displaced at a rate of 0.62 mm/minute. After a shear force peak was reached, the test was stopped and the DCDTs and normal load were removed. After each test, the DS box and soil specimen were weighed to calculate the γ_{dry} of the specimen.

2.4.3 Direct Shear Testing Using Modified Apparatus

The 100 mm and 300 mm DS tests were performed using a custom fabricated winged DS testing apparatus, called the modified DS apparatus. Photographs of the 60 mm, 100 mm and 300 mm DS boxes are shown in Figure 2.10a, b and c. A photo of the 100 mm apparatus is shown in Figure 2.11b, a schematic is shown in Figure 2.12, a free body diagram of shear and normal forces is shown in Figure 2.13a, and plan and elevation views of the DS box are shown in Figures 2.13b and 2.13c.

Horizontal displacement of the lower DS box frame was powered with a Baldor L3406M electric motor connected through a Zero-Max JK1 variable speed gearbox with an output of 0 to 400 rpm to a Soiltest CF410 worm drive actuator by a V-belt and pulleys. The data acquisition system consisted of a National Instruments SCXI chassis with two 1520 cards and a National Instruments PXI 1050 computer system. Horizontal force was measured using a pair of Data Instruments JP1000 load cells with a capacity of 4.44 kN each in compression or tension, and horizontal displacement measured with a Trans-Tek 0245-0000 DCDT with a range of ±50 mm.

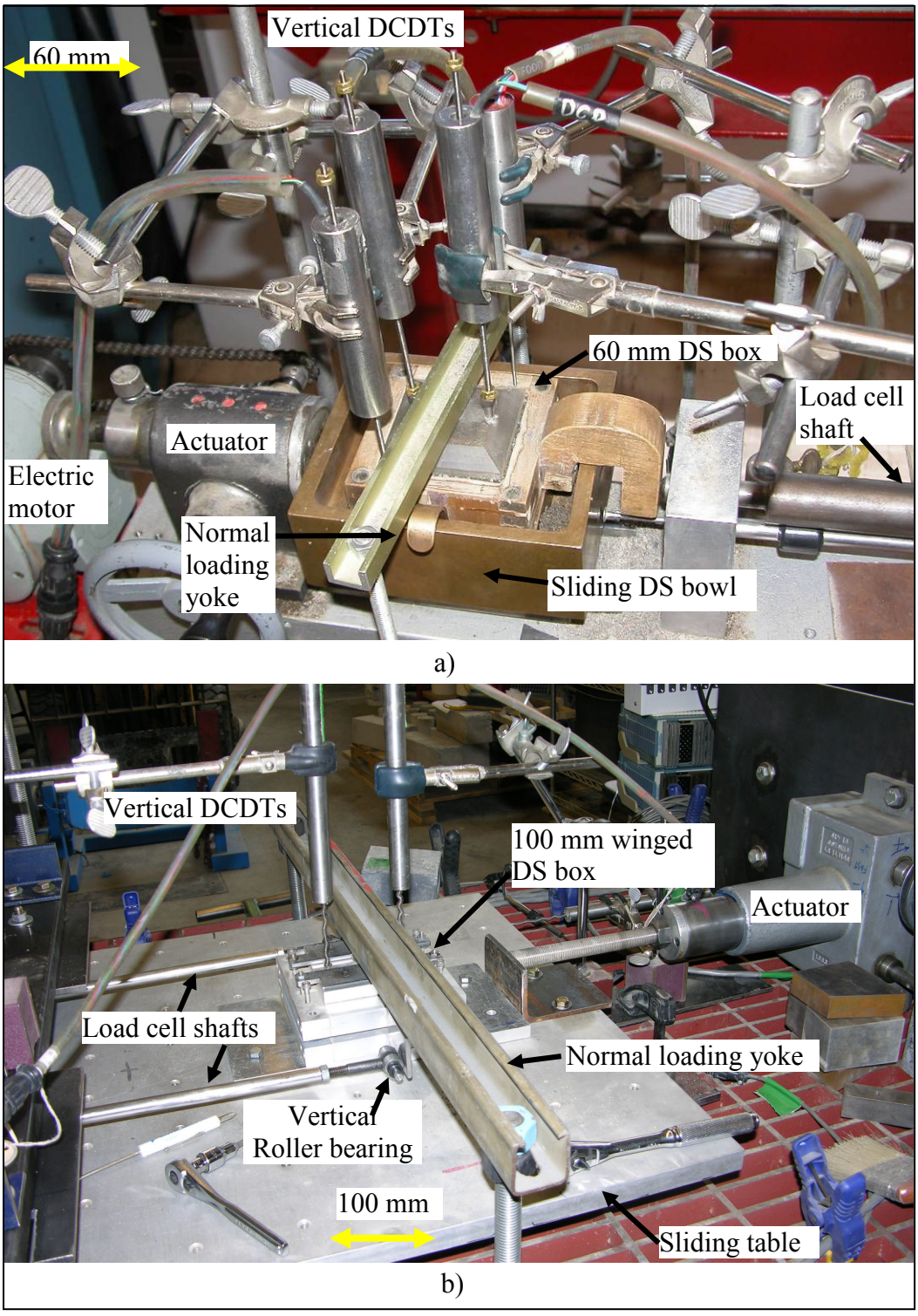

Figure 2.11 a) Photo of 60 mm box in conventional DS apparatus b) Photo of 100 mm box in modified DS apparatus

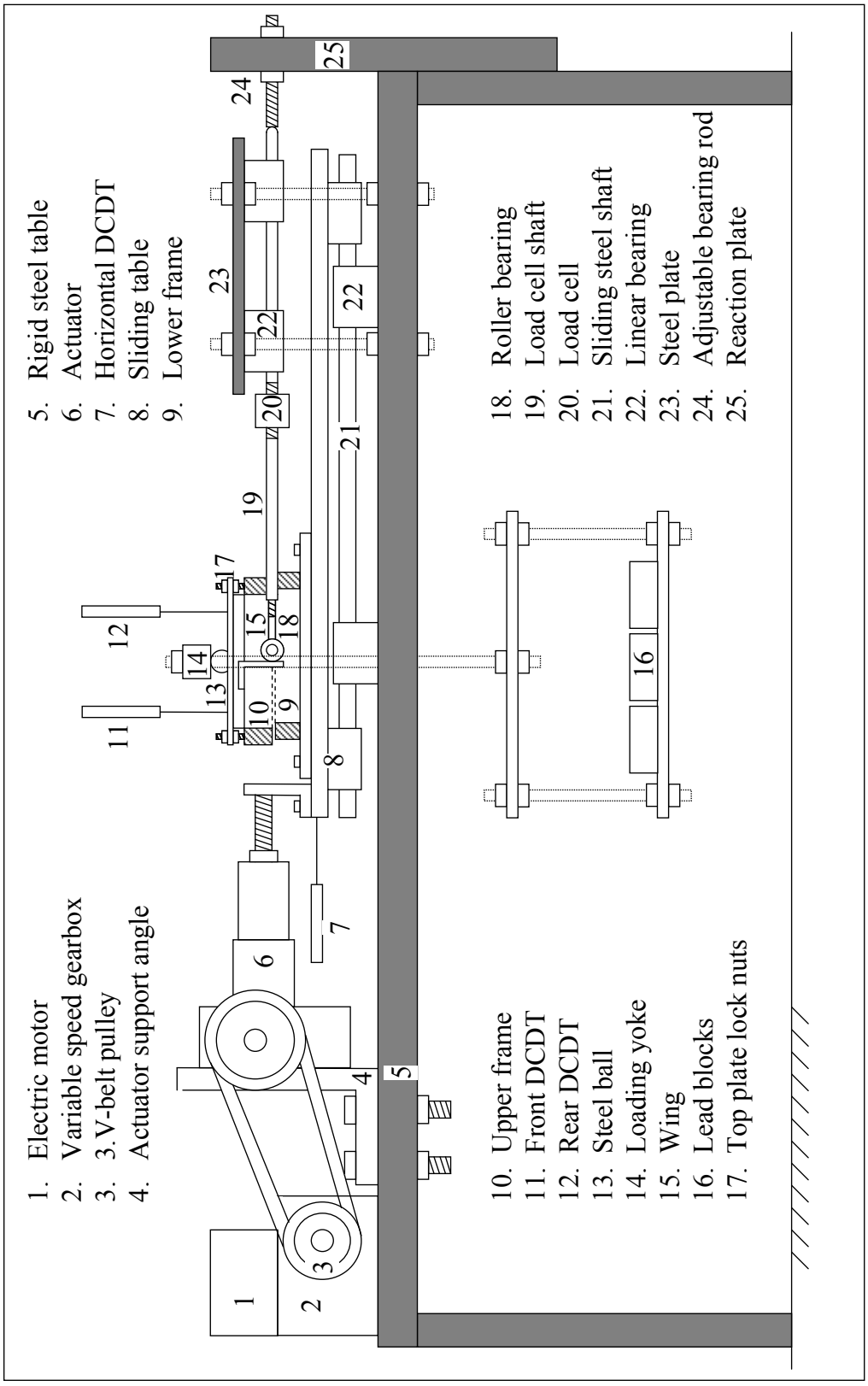

Figure 2.12 Schematic of modified DS apparatus

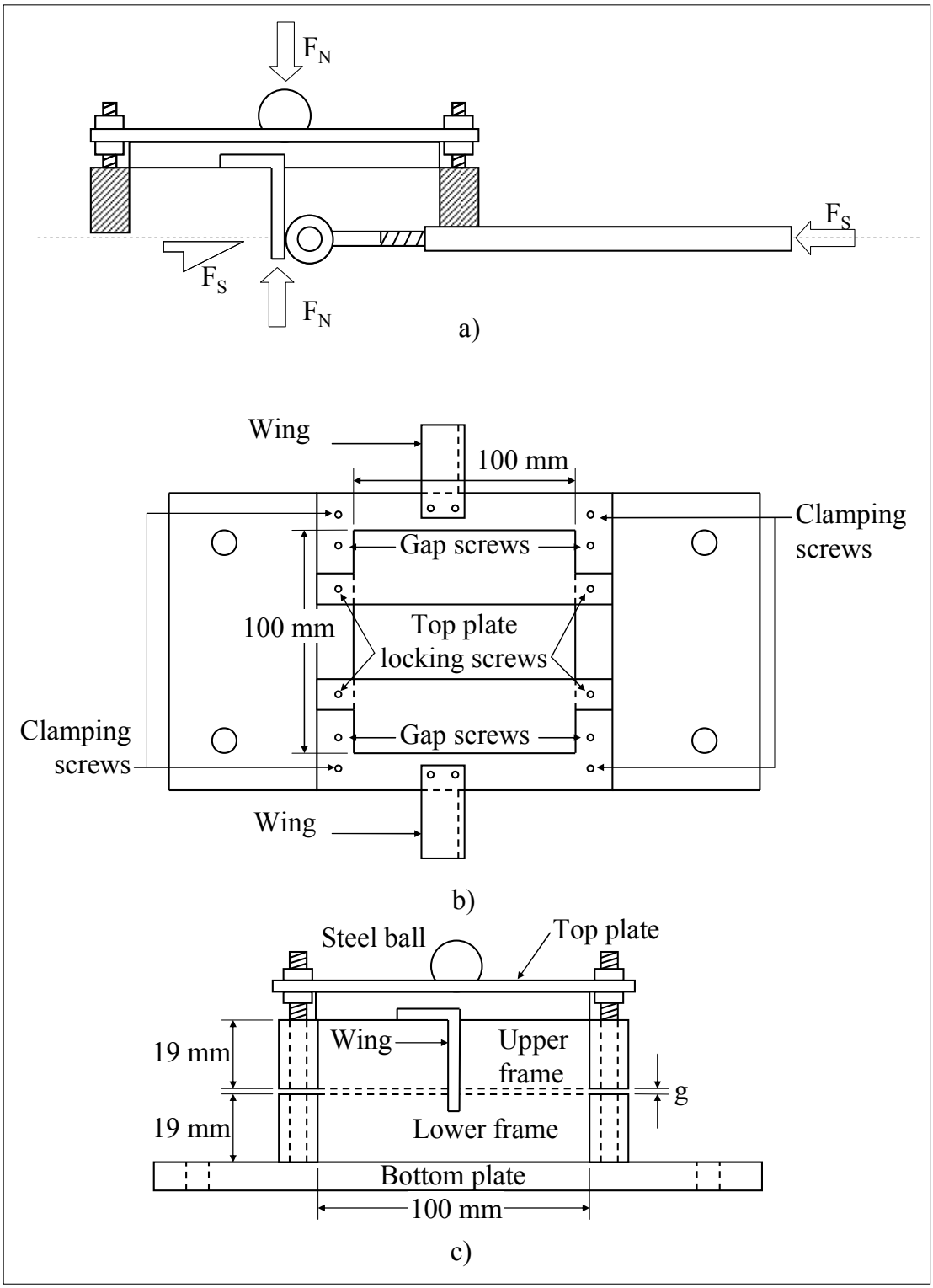

Figure 2.13 Schematics of 100 mm DS box a) Free body diagram b) Plan view c) Elevation view

A 610 mm by 914 mm by 25 mm aluminum plate on linear bearings allowed a total horizontal displacement of 120 mm. The lower DS frame was bolted to this sliding plate prior to testing.

A steel ball and aluminum top plate distributed σ'_N evenly to the soil from weights applied through a loading yoke, and vertical displacement and tilt of the top plate were measured using two Trans-Tek 0245-0000 DCDTs with a range of ± 50 mm. Because the upper frame was locked to the top plate prior to testing, there was equal rigid body displacement and rotation of both. Horizontal load cells were supported on stainless steel shafts gliding on linear bearings, but were placed before the linear bearings so as to eliminate the risk of horizontal force dissipation due to friction in the linear bearings. The load cells transferred horizontal load to the upper DS box frame through frictionless rollers bearing on polished vertical wings, which allowed free vertical displacement of the upper frame and eliminated the risk of additional vertical normal force being applied to the DS specimen during testing. The upper box wings and frictionless vertical rollers, based on a design by Lings and Dietz (2004), were the most important modification to the conventional apparatus, but the unique interior dimensions of the 100 mm box were also responsible for the improved ability to rapidly obtain high quality, repeatable DS test data.

The 100 mm DS box had nominal interior dimensions of 100 x 100 x 39 mm, with upper and lower frames machined from Alloy 6061 aluminum with a nominal height of 19 mm each, fastened with stainless steel machine screws. The use of aluminum allowed for a lightweight and corrosion-free upper frame, minimizing the risk of uncertainty in the calculation of normal load on the specimen shear plane. The upper frame weighed 10.4 N, which was 4.6% of the normal load at the typical normal

stress of 22 kPa. However, the displacement of the upper frame was monitored during the test, and tests during which the upper and lower frame contacted were discarded to eliminate uncertainty in the σ'_N applied to the soil shear plane.

The lower frame was screwed to a 13 mm x 150 mm x 250 mm rigid aluminum bottom plate which was bolted to the sliding table. The upper and lower frames were held together at the four corners by machine screws (10-32 English thread size), called "clamping screws" (see Figure 2.11c). The upper frame was also fitted with four threaded holes for the use of gap screws, whereby the screws would be extended to a specific distance below the upper frame for the placement of soil in the box, and retracted after the application of normal load but prior to testing. Since split rubber edging was not used for the majority of 100 mm tests, the gap screws were not used, and were replaced by 0.5 mm thick Teflon strips. The number of Teflon strips varied according to the gap between the upper and lower frame required for the particular test, but the strips covered the entire perimeter of the DS plane, so that soil could not escape the fixed specimen volume prior to removal of the strips.

For all tests, the weight of the upper frame was accounted for in the calculation of σ'_N on the shear plane, since the vertical DCDTs monitoring the upper frame showed that the upper frame did not contact the bottom box, and therefore all normal force from the weight of the upper frame was transferred though the soil at the shear plane. Self weight of the soil above the shear plane, weight of the top plate, steel centering ball, and loading yoke, and weight of the DCDT central cores were also accounted for in the calculation of σ'_N. The vertical displacement of the top plate was recorded before and after the application of normal load and the removal of Teflon strips to determine the change in soil specimen volume.

The 300 mm DS box (with nominal interior dimensions of 300 mm x 300 mm x 200 mm) was built from welded steel angles with leg thickness of 8 mm. The lower frame was welded to a 6 mm thick steel bottom plate, which was fastened to the sliding table with bolted steel clips. The upper and lower frames were held together with C-clamps instead of clamping screws, and the gap was preset with Teflon strips. The upper frame was locked to the 13 mm thick aluminum top plate after application of normal load and before testing. A more robust loading yoke was used to apply the σ'_N = 22 kPa to the specimen, as more load was needed to apply the same σ'_N to the larger area shear plane of the 300 mm DS box relative to the 100 mm DS box. All other components of the DS apparatus were similar as for 100 mm DS testing. Figures 2.14a and 2.14b show the 300 mm shear box during testing.

In the modified DS apparatus for both the 100 mm and 300 mm DS tests, the upper frame tends to rotate forward, with the front of the upper frame displacing downward while the rear of the upper frame displaces upward. Dietz (2000) explains that although the cause of the rotation is difficult to ascertain, a possible explanation is the triangular distribution of soil pressure on the rear wall of the upper frame of the shear box. Such a distribution, measured by Palmeira & Milligan (1989) and Paikowsky et al (1996) using load cells and pressure sensors, would induce a moment that causes the upper frame to rotate forward. A second explanation discussed by Dietz is the loss of soil at the front of the DS box, which (as discussed later in this chapter) causes a forward rotation of the upper frame. Although Dietz reduced rotation of the upper frame by applying external moments, he pointed out that the true cause of the rotations remained hidden and that further research is needed to fully clarify the mechanical performance of the equipment.

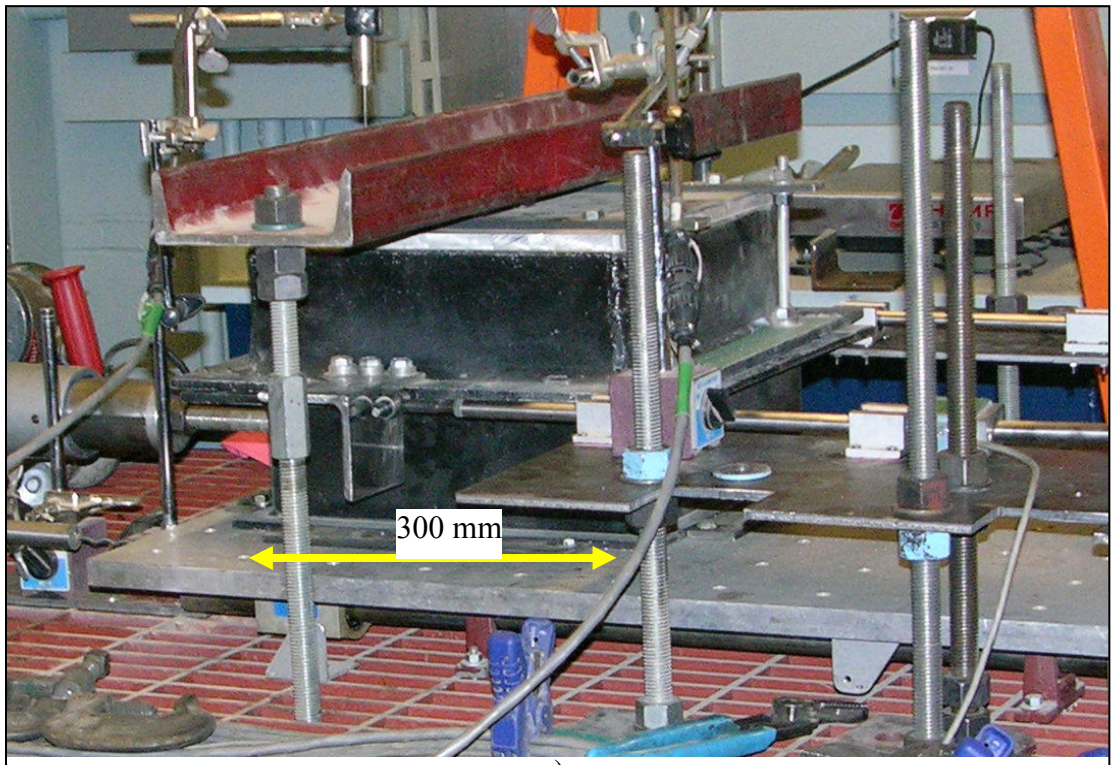

a)

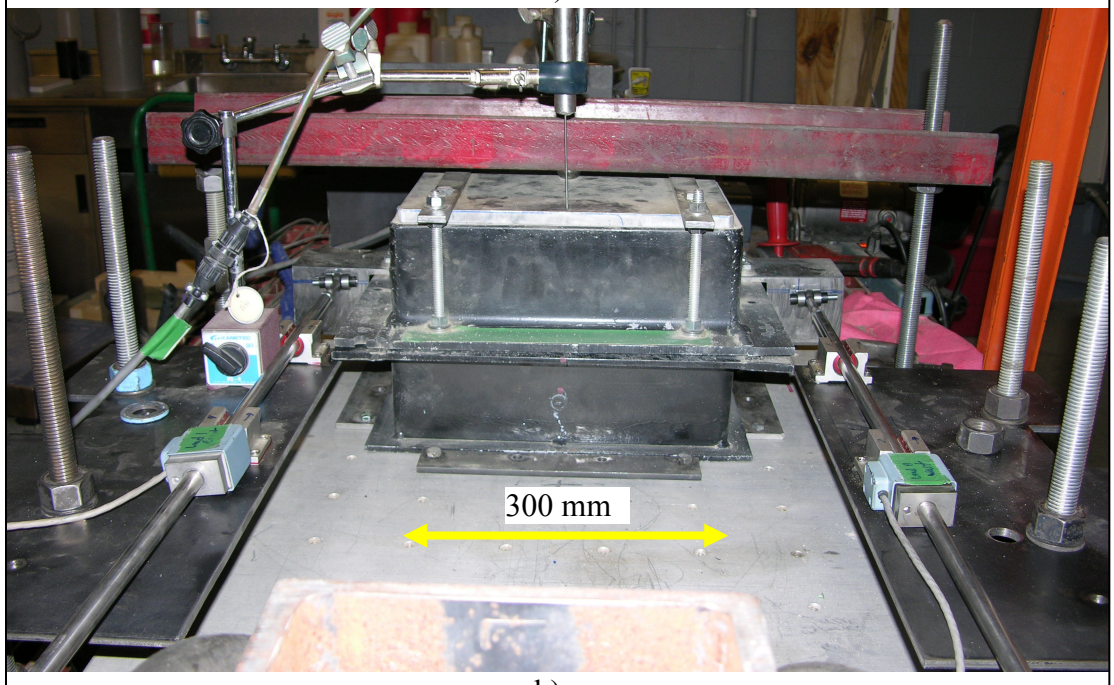

b)

Figure 2.14 300 mm DS box during testing a) Side view b) Rear view

2.4.4 Soil Specimen Preparation and Testing Using Modified Apparatus

Each 100 mm test required about 7 N of sand, while each 300 mm test required approximately 300 N of sand. The procedure was nearly identical for the different box sizes, but the weight of the larger box required that it be transported to and from the sliding table using an overhead A-frame crane with a 8.9 kN chain hoist. For typical dry or partially saturated sand tests using either box, soil was placed in the DS box in three even lifts, weighed on the scale, of 2.5 N each, for uniformity in compactive effort per lift, and thus improved consistency between tests.

For dry sand having a low unit weight, soil was placed in the DS box in a single lift using a funnel to minimize drop height. For slightly denser specimens, soil was poured in a single lift from a scoop from a 20 – 100 mm drop height, depending on the required γ_{dry}. Dense soil was placed in 3 uniform lifts, which were leveled and compacted using a 98 mm by 98 mm steel plate and a specially designed hammer consisting of a 2.7 N steel rod dropped down a 25 mm diameter, 300 mm long PVC pipe, just as with the 60 mm box. Although compaction effort was varied by the number of times the rod was dropped onto the plate, there was not a strong relationship between compaction effort and γ_{dry}. For instance, a compaction effort of 50 kN-m/m^3 achieved by drop hammer resulted in soil prepared to γ_{dry} = 16.2 – 17.8 kN/m^3. γ_{dry} for dense dry sand was better controlled by vibration, which was achieved by tapping the sides and top of the DS box a specified number of times (low-energy vibration), or placing the DS box on a vibrating table (γ_{dry} was difficult to control with the vibrating table, so high-energy vibration was only used for the densest specimens). A combination of the drop hammer and low-energy vibration methods was found to be the most consistent method of controlling γ_{dry}, but the total applied energy per unit

volume was not quantifiable. For the 300 mm box, soil was manually tamped using 100 mm by 100 mm wooden block, varying the number of tamps per layer to achieve different γ_{dry}.

Partially saturated sand was placed in 3 uniform lifts, which were leveled and compacted using a 98 mm by 98 mm steel plate and a specially designed hammer consisting of a 2.7 N steel rod dropped down a 25 mm diameter, 300 mm long PVC pipe. Compaction effort was controlled by the number of times the rod was dropped onto the plate and was dependent on energy applied, where loose sand (15.0 kN/m^3) required 50 kN-m/m^3 of energy, medium sand (15.8 kN/m^3) required 150 kN-m/m3 of energy, and dense sand (16.5 kN/m^3) required 250 kN-m/m^3 of energy.

For the final lift, a compaction collar was placed on the upper frame to maintain a consistent horizontal confinement of the soil specimen during placement and compaction. After compaction, the compaction collar was removed, and the soil surface was leveled to the top of the box using a straightedge, and areas of particle gouge were filled in, tamped down, and re-leveled. Loose soil particles were cleared from the top and sides of the box with a small brush, using the straightedge as a screen to prevent disturbance of the soil surface. The DS box and specimen were then weighed, the top plate was installed, and locking nuts screwed onto their threaded rods.

The DS box was placed on the sliding table (using the chain hoist for the large box) and secured to the table with bolts, and the actuator adjusted until it was almost touching the bearing plate. Vertical DCDTs were placed to be at the center of their calibrated range, and zeros were taken and recorded. Normal load was applied,

clamping screws removed, top plate nuts tightened, Teflon strips removed, and the sliding table pulled to contact with the actuator to ensure no initial load was applied to the horizontal load cells. The data acquisition program was started, the motor started, and the actuator was advanced at a rate preset using the variable gearbox of 3.9 mm/minute. The test was run until a large displacement condition of constant force and no change in vertical displacement was reached, usually at a horizontal displacement of 15 to 20% of the specimen length. The test setup was disassembled and the actuator retracted using an electric drill with a V-belt pulley attachment. For DS tests on partially saturated sand, samples were taken for the determination of soil specimen water content.

2.5 Effect of Gap Size

Lings and Dietz (2004) and Shibuya et al. (1997) showed that an increase in gap size resulted in a decrease in ϕ'_{ds-p} and ψ_p for dry sand at the same γ_{dry}. To characterize the influence of gap size on the DS parameters of RMS graded and RMS uniform sand, 100 mm tests were performed with and without edging for gaps from 0 to 7 mm using 0 to 14 0.5 mm thick Teflon strips.

2.5.1 Effect of Gap Size on RMS Graded Sand

Figure 2.15 shows the influence of gap distance, g, on DS parameters for dry RMS graded sand using the 100 mm box with no edging. Eleven tests were performed with gaps from 0 to 7 mm. Soil specimens were prepared to an average γ_{dry} of 17.6 kN/m^3, with a standard deviation of 0.2 kN/m^3. The parameters, ϕ'_{ds-p}, ψ_p, and ϕ'_{ds-ld},

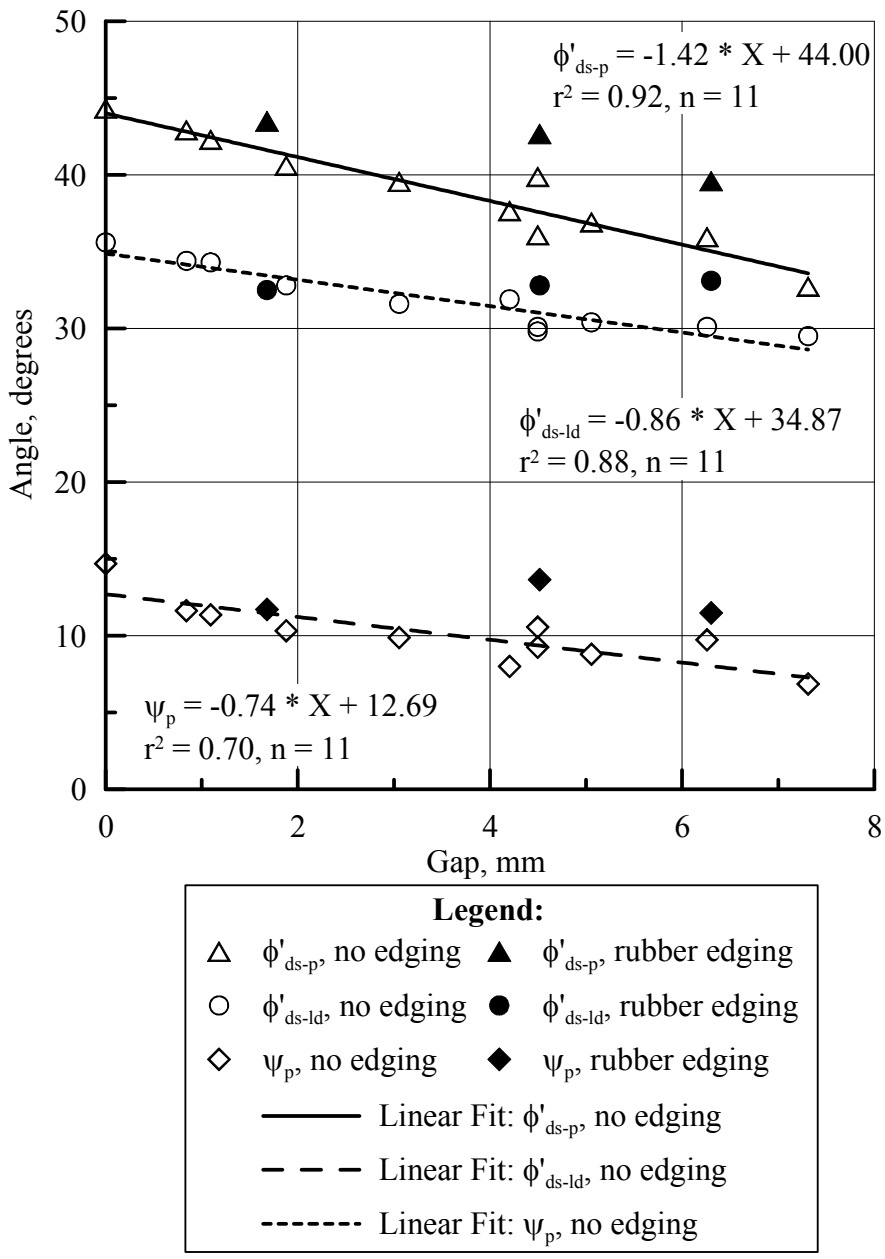

Figure 2.15 ϕ'_{ds-p}, ϕ'_{ds-ld}, and ψ_p vs gap distance for dry RMS graded sand in the 100 mm box at an average γ_{dry} = 17.6 kN/m^3 with a standard deviation = 0.2 kN/m^3

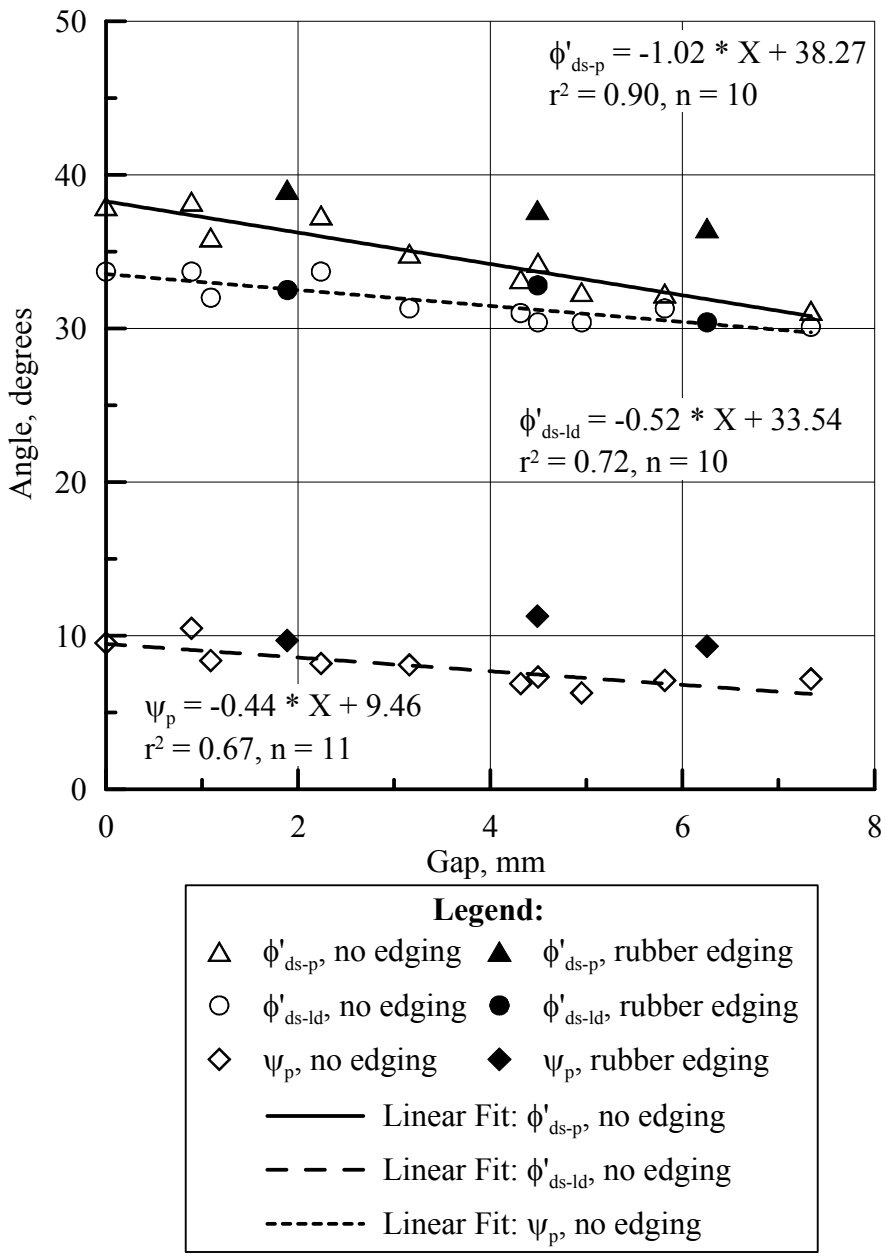

Figure 2.16 ϕ'_{ds-p}, ϕ'_{ds-ld}, and ψ_p vs gap distance for dry RMS uniform sand in the 100 mm box at an average γ_{dry} = 15.5 kN/m^{3}with a standard deviation = 0.2 kN/m^3

were all found to decrease with increasing gap distance. The strongest relationship was with $\phi'_{ds\text{-}p}$, which increased from 32.7° to 44.3° from the largest gap to the smallest gap. The coefficient of determination, or r^2, for the linear regression was strong, 0.92. The parameter $\phi'_{ds\text{-}ld}$ increased over the same range from 29.5 to 39.6° with an r^2 of 0.88. The parameter ψ_p was more weakly correlated with gap distance, increasing over the range from 6.8 to 14.7 with an r^2 of 0.70.

2.5.2 Effect of Gap Size on RMS Uniform Sand

Figure 2.16 shows the influence of gap distance, g, on DS parameters for dry RMS uniform sand using the 100 mm box with no edging. Ten tests were performed with gaps from 0 to 7 mm. Soil specimens were prepared to an average γ_{dry} of 15.5 kN/m^3, with a standard deviation of 0.2 kN/m^3. The parameters, $\phi'_{ds\text{-}p}$, ψ_p, and $\phi'_{ds\text{-}ld}$, were all found to decrease with increasing gap distance, but relationships between the parameters were generally weaker than for RMS graded sand. The strongest relationship was again with $\phi'_{ds\text{-}p}$, which increased from 31.2° to 38.3° from the largest gap to the smallest gap. The coefficient of determination, or r^2, for the relationship was strong, 0.90. The parameter $\phi'_{ds\text{-}ld}$ increased over the same range from 30.4 to 33.7° with an r^2 of 0.72. The parameter ψ_p was more weakly correlated with gap distance, increasing over the range from 6.3 to 10.5 with an r^2 of 0.67.

2.5.3 Effect of Edging

Dietz (2000) employed 1 mm thick split rubber edging in all tests using the modified DS apparatus. In this work, the split rubber edging was 0.8 mm Silicone rubber (McMaster Carr product code 93755K23, Hardness = 50A, tensile strength =

33.5 kPa, density = 1490 kg/m^3, orange-red color) with adhesive backing. Dietz (2000) and Shibuya et al. (1997) both used silicone grease to apply the edging to the DS box, but this process was found to be inconsistent with respect to results and time consuming, so that adhesive-backed edging was used instead. The edging was applied to all four walls of the upper and lower frame, but not to the top or bottom plates. The upper frame edging was extended across the gap to prevent the extrusion of soil during shear, and adhesive was removed from all exposed rubber surfaces to reduce the risk of shear load transfer between the upper and lower frame. Figure 2.17 shows a photo of the 100 mm box with split rubber edging.

To evaluate the influence of gap distance when split rubber edging was used, three tests were performed for both RMS graded and RMS uniform sand at gaps of approximately 2, 4, and 6 mm. The results of these tests are shown in Figures 2.15 and 2.16 along with tests performed with no edging. As can be seen, tests with edging consistently give higher values of $\phi'_{ds\text{-}p}$, $\phi'_{ds\text{-}ld}$, and ψ_p than tests at the same gap distance without split rubber edging, although the influence of edging diminishes at smaller gaps.

Many variables must be taken into consideration when selecting a gap separation to use for DS tests. Small gaps do not provide sufficient separation for a shear surface to develop in an unimpeded way through the specimen, while large gaps result in significant deterioration and loss of soil during shear, unless restrained by edging. The optimum gap configuration found by Dietz (2000) was a 4 mm gap with split rubber edging. The current study found that this configuration gives nearly the same strength and dilation values as a gap of 1 mm with no edging. A 1 mm gap is

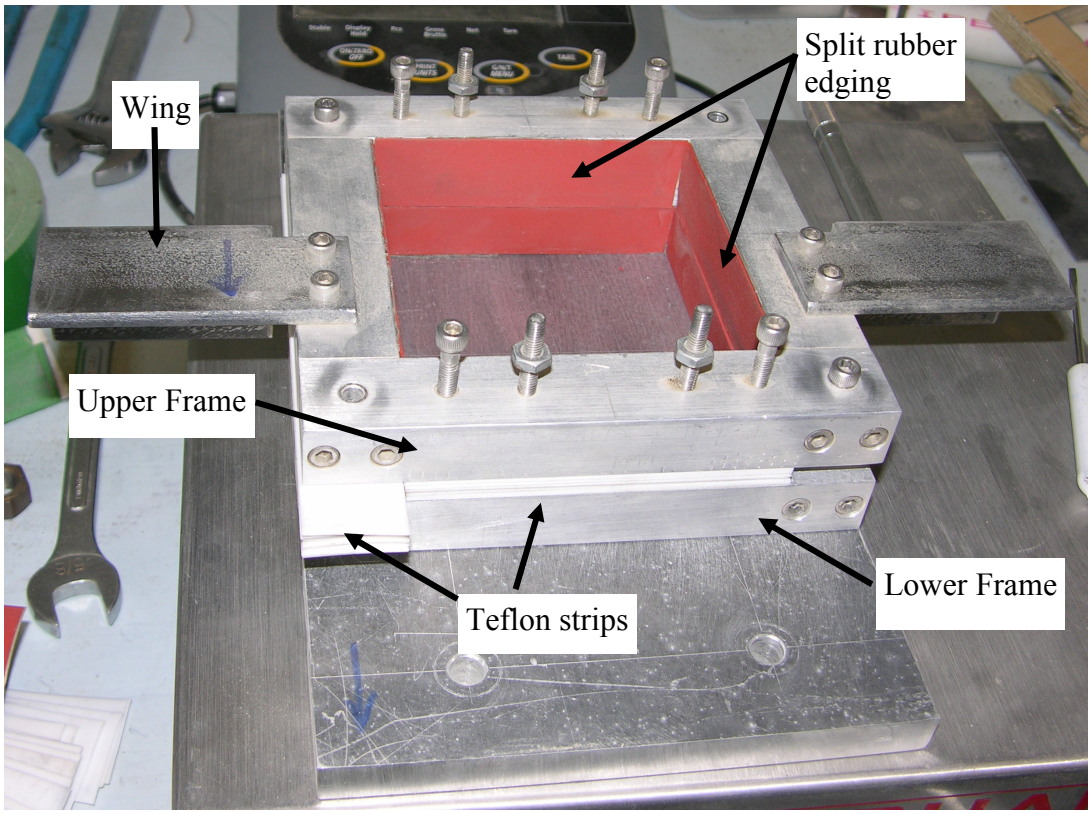

Figure 2.17 100 mm box with split rubber edging

close to D_{50} for RMS graded sand, 0.59 mm, and to the ASTM recommended value of 0.64 mm (ASTM, 2003e). The standard also indicates that the gap should be increased to accommodate soil with larger particles, implying that the increase to a 1 mm gap is better suited for the RMS graded sand and CU Filter sand, both which contain particle sizes considerably larger than D_{50} (see Figure 2.1). Finally, the difference in DS parameters between a 0.5 and 1 mm gap is consistent with the scatter in the data, indicating that while RMS uniform sand would be satisfied by a gap of 0.5 mm, Since there is no significant disadvantage in choosing the 1 mm gap for RMS uniform sand, the gap size of 1 mm was chosen as the standard for all the different sands in this study. A 1 mm gap is sufficiently small that soil loosening and deterioration does not occur in the separation between the upper and lower boxes, and sufficiently large that

measurements of peak shear strength and dilation are not amplified by constraints imposed by the testing apparatus.

2.5.4 Sample Extrusion

When no edging is used, the DS sample is subject to loss of soil during shear displacement referred to as extrusion. Dietz (2000) described this phenomenon as a "systematic process by which every increment of shear displacement is associated with a uniform extrusion volume. When a substantial opening is implemented between the shear box frames prior to testing, an increment of shear displacement brings with it the extrusion of the portion of the sample immediately beneath the upper frame and adjacent to its end wall by the rear wall's cutting action." (p. 69)

Dietz proposed correcting for extrusion by accounting for the additional volume created during shear to obtain the corrected vertical top plate displacement, $(v_y)_{corrected}$, using the formula

$$\left(v_y\right)_{corrected} = \left(v_y\right)_{measured} + \sum \frac{g_{front}\dot{v}_x}{B} \tag{2.6}$$

where $(v_y)_{measured}$ is the average measured vertical top plate displacement, B is the sample width, $\dot{v}_x$ is an increment of shear displacement, g_{front} was taken to be the gap between the upper and lower frame at a given point during the test at the front edge of the soil. Dietz found that this adjustment led to more consistent DS data, especially at large displacements where neglecting extrusion results in measurements that indicate a continuing loss of volume. Tests performed in this study corroborate Dietz's findings in that correcting for extrusion resulted in more consistent DS data and a better means

of identifying behavior at zero volume change along the shear plane. In general, using this adjustment for extrusion at a 1 mm gap resulted in only a small increase in ψ_p of about 0.5 – 0.7° for dry 100 mm tests on RMS graded sand. All sample vertical displacement and dilation angles reported in this work (excluding tests with split rubber edging) are calculated using adjusted values for vertical top plate displacement, which will be referred to simply as v_y.

2.6 Effect of Box Dimension

To explore the difference in DS behavior as a function of box length (L), tests performed with a 60 mm box in the conventional apparatus were compared with 100 mm box and 300 mm box tests performed in the modified apparatus. Figures 2.18 through 2.23 show the influence of box length on different DS parameters for RMS graded sand. All tests were run with no edging and a 1 mm gap. Box height was investigated for the 300 mm box using sample heights (H) of 75 mm, 110 mm, and 200 mm. H/L ratio was found to have no significant influence on DS strength and dilation using the 300 mm box, so all data gathered with the 300 mm box are shown, regardless of H.

It was observed that sand placed at low γ_{dry} ($\leq$15.6 kN/m^3 for RMS graded sand, $\leq$13.2 kN/m^3 for RMS uniform sand) did not show a clear peak stress and were contractive throughout the entire test. The trend of the data at these densities differs markedly from the linear trend at higher unit weights, and so were not included in the linear regression fits to the data.

Figure 2.18 shows $\phi'_{ds\text{-}p}$ vs γ_{dry} for RMS graded sand. In general, the regression line for the 60 mm box is 4° to 6° higher than the 100 mm box and 6° – 7° higher than the 300 mm box. The 100 mm box trend line has a coefficient of determination (r^2) of 0.98, slightly stronger than the values of 0.90 and 0.89 for the 60 mm and 300 mm box, giving an indication of the improved consistency of data gathered using the 100 mm box relative to the 60 mm and 300 mm boxes. Figure 2.19 shows ψ_p vs γ_{dry} for RMS graded sand. The 60 mm line is 3 – 7° higher than the 100 mm and 300 mm box lines, which are statistically indistinguishable from each other. The trend lines all have strong r^2 values, with the 100 mm box slightly stronger, at 0.94 than the other boxes, at 0.91. Figure 2.20 shows $\phi'_{ds\text{-}ld}$ vs γ_{dry} for RMS graded sand. The linear fits, not shown in the figure, had low r^2, indicating that there was not a strong dependence of the parameter on γ_{dry}. Instead, lines of zero slope are drawn on the figure, indicating the average $\phi'_{ds\text{-}ld}$ for the three boxes. The 60 mm box has the highest average $\phi'_{ds\text{-}ld}$, then the 300 mm box, and the 100 mm box the lowest average line.

Shown in Figure 2.21 is $\phi'_{ds\text{-}p}$ vs γ_{dry} for RMS uniform sand. The linear regression fit for 60 mm data is about 2-3° higher than the 100 mm data, and 4° higher than the 300 mm data. The r^2 for the 100 mm box is strongest, at 0.98, the 300 mm box r^2 is 0.89, and the 60 mm box has significantly greater scatter, at $r^2 = 0.82$. Figure 2.22 shows ψ_p vs γ_{dry}. At the lower range of γ_{dry}, the linear fit trend lines merge, but separate at the higher range of γ_{dry}, with the 60 mm box 2° higher than the 100 mm box and 3° higher than the 300 mm box. r^2 is very strong, 0.99, for the 100 mm box, and weaker, 0.88 for the 60 mm box and 0.82 for the 300 mm box. $\phi'_{ds\text{-}ld}$ vs γ_{dry} is shown in Figure 2.23. Lines of average $\phi'_{ds\text{-}ld}$ are very close to one another, with the

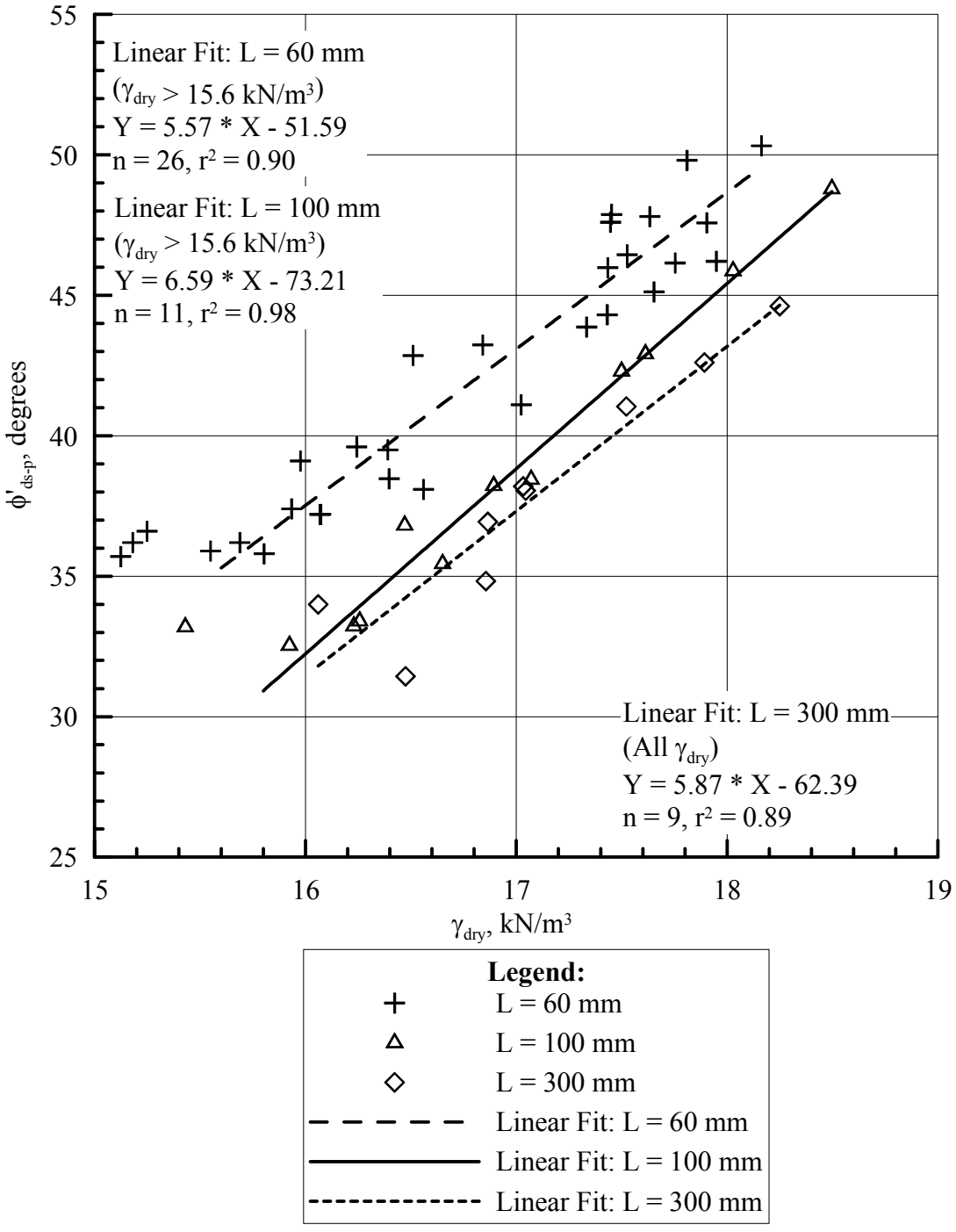

Figure 2.18 ϕ'_{ds-p} vs γ_{dry} for three different box sizes with RMS graded sand

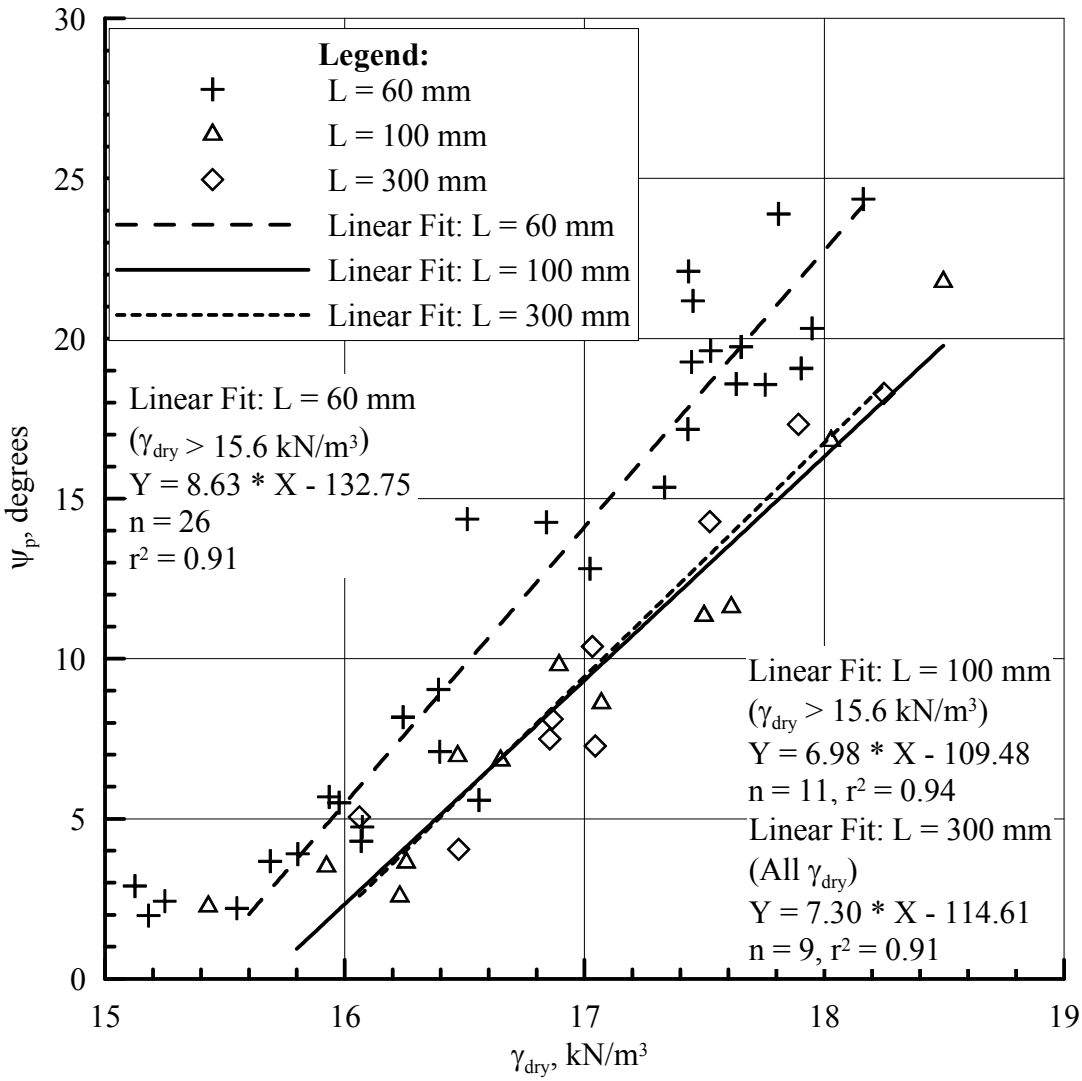

Figure 2.19 ψ_p vs γ_{dry} for three different box sizes with RMS graded sand

100 mm box higher, at 33.0°, than the 300 mm box, at 32.5° and the 60 mm box, at 32.4°.

For the purposes of comparing data gathered using the three different boxes, relevant parameters are shown in Table 2.3. In general, there appears to be a stronger influence of box length on RMS graded sand data than that of RMS uniform sand.

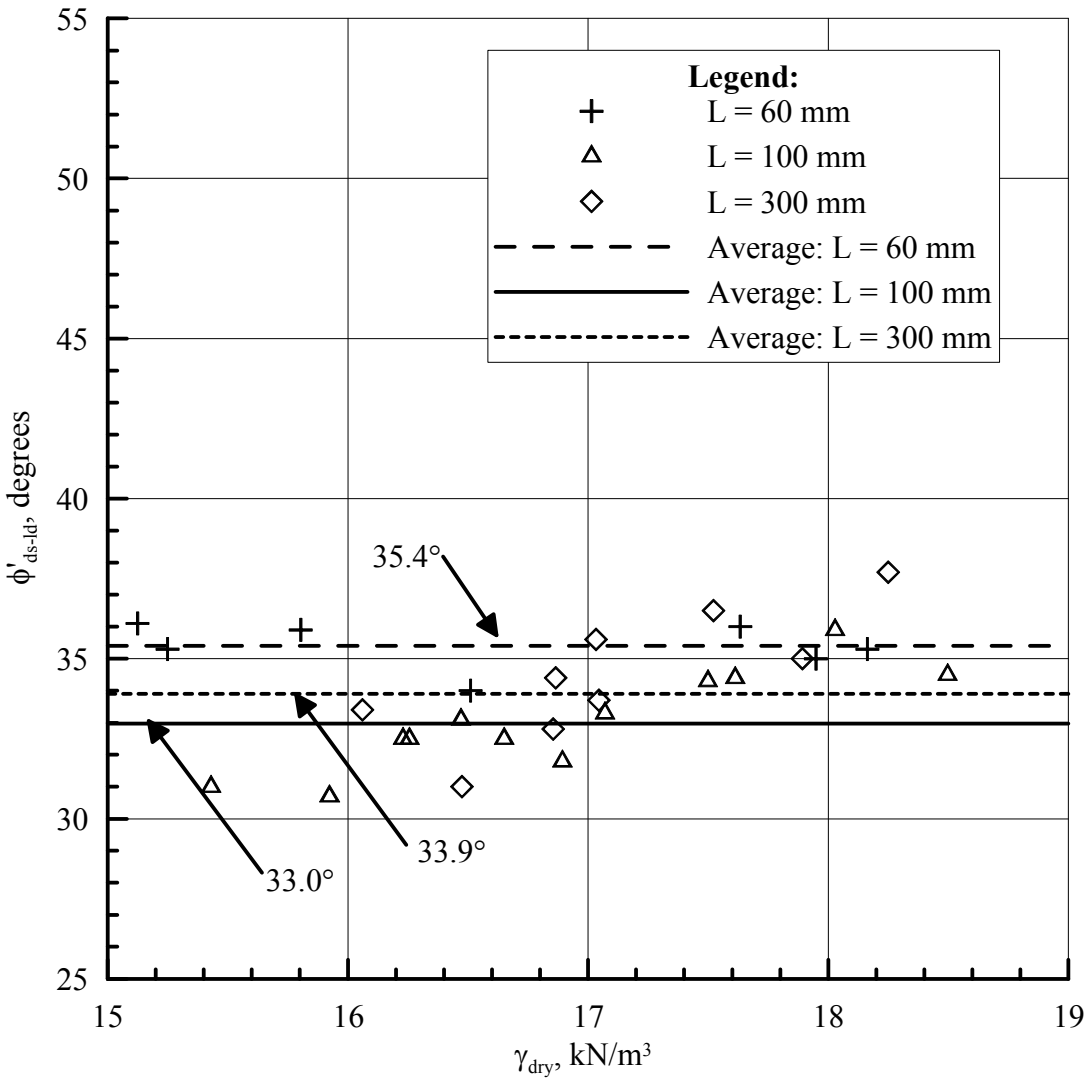

Figure 2.20 $\phi'_{ds\text{-}ld}$ vs γ_{dry} for three different box sizes with RMS graded sand

Comparisons for CU Filter sand are not shown because it is difficult to determine whether the differences between the 60 mm box and 100 mm box data are due to a change in box length or a change in normal stress. For RMS graded sand, there is a 4° to 6° decrease in $\phi'_{ds\text{-}p}$ at a given γ_{dry} from the 60 mm to the 100 mm data, compared with a 2 – 3° decrease for RMS uniform sand. There is a 6 – 7° decrease in $\phi'_{ds\text{-}p}$ at a given γ_{dry} from the 60 mm to the 300 mm data for RMS graded sand, compared with a

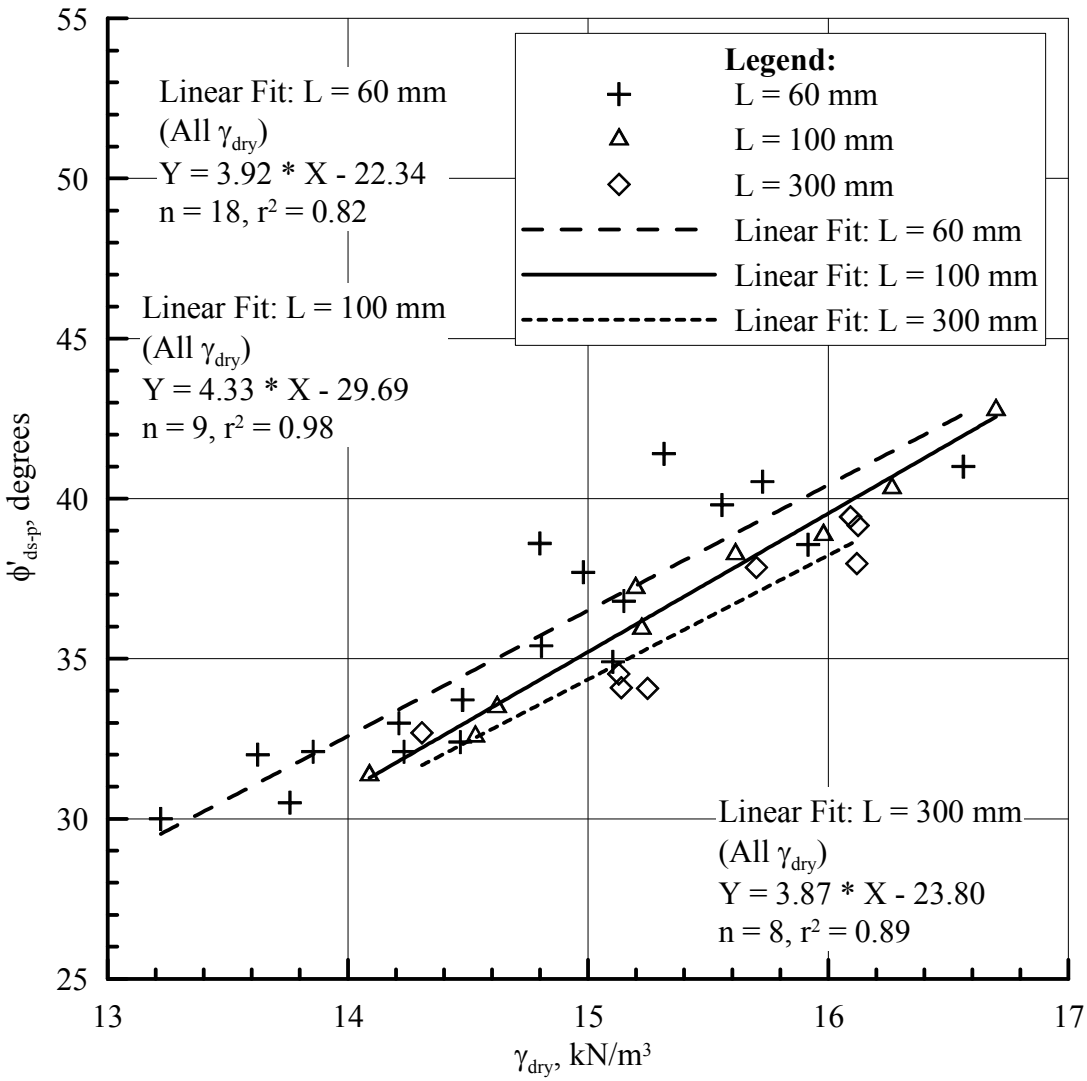

Figure 2.21 $\phi'_{ds\text{-}p}$ vs γ_{dry} for three different box sizes with RMS uniform sand

4° decrease for RMS uniform sand. Similarly, there are greater decreases in ψ_p and $\phi'_{ds\text{-}ld}$ at given values of γ_{dry} for RMS graded than for RMS uniform sand, for a given increase in box length. For ψ_p, there is a 3 – 7° decrease from the 60 mm data to both the 100 mm and 300 mm data for RMS graded sand, compared with a 2° or 3° decrease for the same data with RMS uniform sand. For $\phi'_{ds\text{-}ld}$, there is no significant difference between the three boxes for RMS uniform sand, while for RMS graded sand, the 60 mm box shows greater $\phi'_{ds\text{-}ld}$ than the 100 mm box or the 300 mm box.

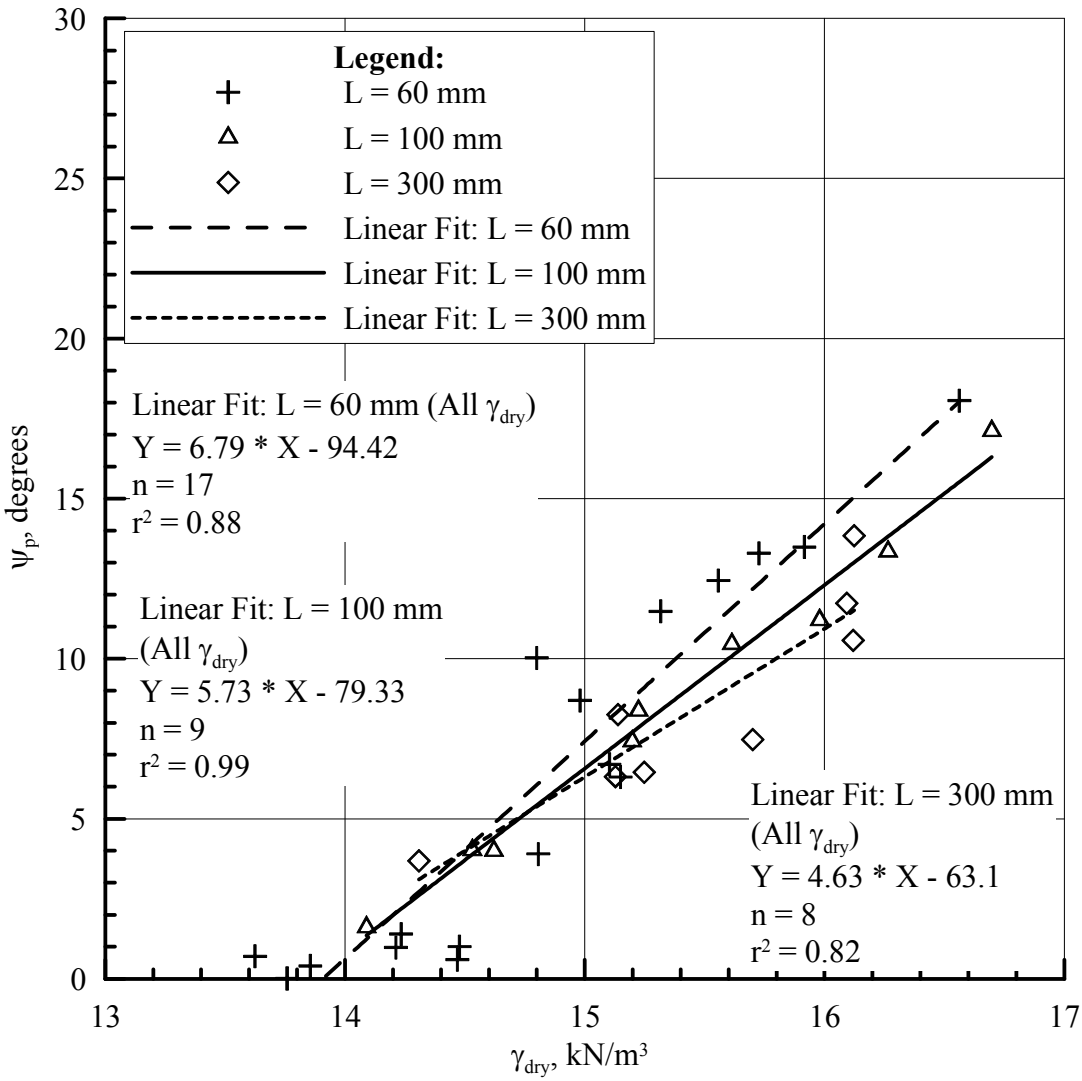

Figure 2.22 ψ_p vs γ_{dry} for three different box sizes with RMS uniform sand

As can also be seen in the table, the 100 mm data generally shows stronger linear relationships than the 60 mm or 300 mm data. This improvement in statistical goodness of fit is attributable to the modified DS apparatus (as compared to the conventional DS apparatus), and the use of a direct DS box with dimensions more conducive to larger particle sizes. The ASTM standard (ASTM, 2003e) specifies an L/D_{max} ratio of at least 10, which for RMS graded sand is not satisfied by the 60 mm

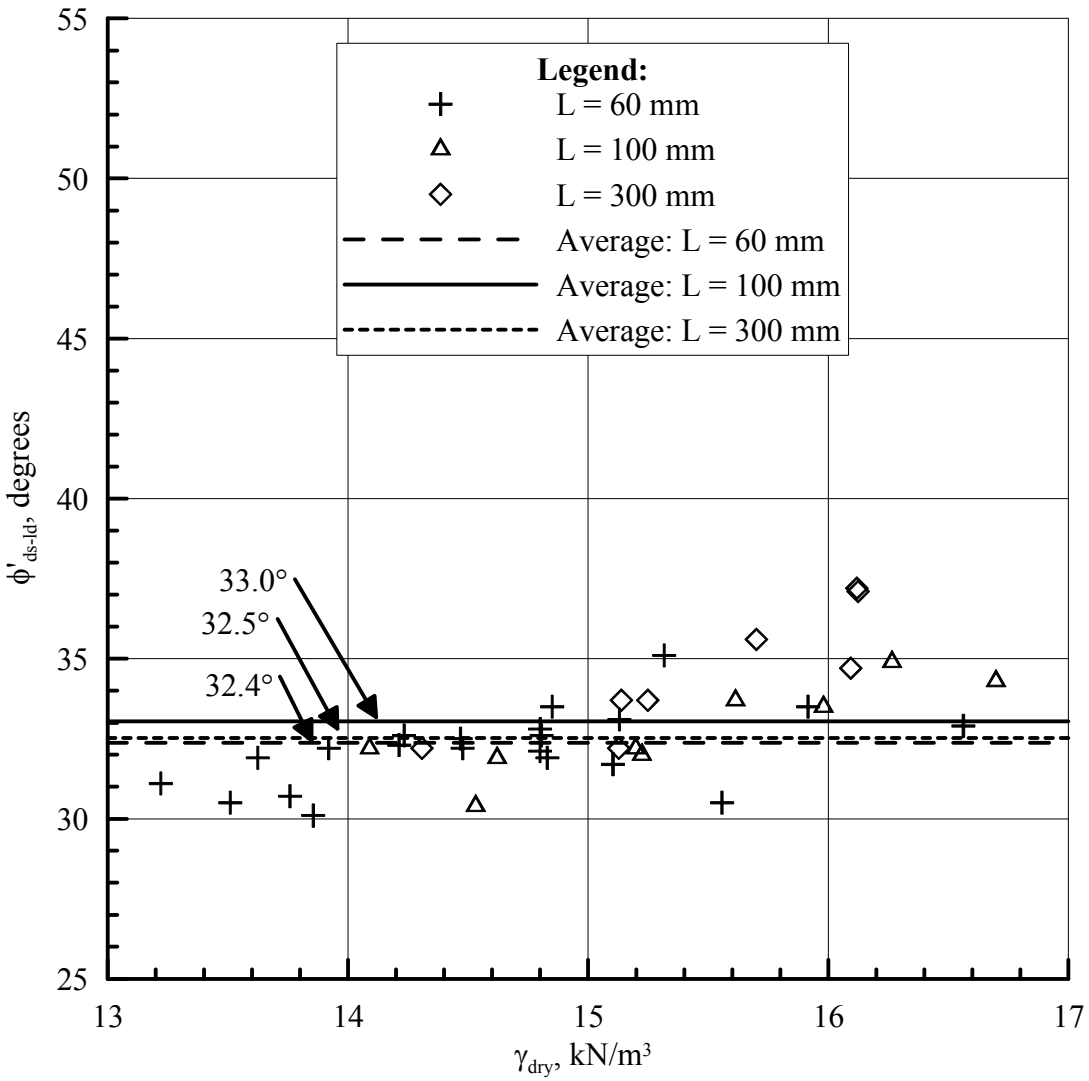

Figure 2.23 $\phi'_{ds\text{-}ld}$ vs γ_{dry} for three different box sizes with RMS uniform sand

box, but is satisfied by the 100 mm and 300 mm boxes. Jewell and Wroth (1987) affirmed that the scale of the DS box relative to D_{50} has an influence on boundary conditions, and recommended that L/D_{50} should be between 50 and 300, a ratio satisfied by the 60 mm box. However, they tested sand with a C_u of 1.2, which is more uniform than either the RMS graded or RMS uniform sand, which have C_u values of 3.4 and 2.0, respectively. It is likely that the larger particles in the soil

Table 2.3 Influence of box length on various DS parameters

Parameter	Statistic	60 mm	100 mm	300 mm
a) RMS graded Sand				
ϕ'_{ds-p}	Change from 60 mm trend	N/A	-(4 – 6°)	-(6 – 7°)
	r^2	0.90	0.98	0.89
ψ_p	Change from 60 mm trend	N/A	-(3 – 7°)	-(3 – 7°)
	r^2	0.91	0.94	0.91
ϕ'_{ds-ld}	Change from 60 mm trend	N/A	-2.4°	-1.5°
	r^2	N/A	N/A	N/A
b) RMS uniform Sand				
ϕ'_{ds-p}	Change from 60 mm trend	N/A	-(2 – 3°)	-4°
	r^2	0.82	0.98	0.89
ψ_p	Change from 60 mm trend	N/A	-2°	-3°
	r^2	0.88	0.99	0.82
ϕ'_{ds-ld}	Change from 60 mm trend	N/A	+0.6°	+0.1°
	r^2	N/A	N/A	N/A

matrix of the RMS graded and CU Filter sands affect the boundary conditions for the 60 mm box, and that the larger 100 mm and 300 mm boxes are better able to accommodate the larger particles to provide a more representative measure of the actual DS test parameters.

Given the favorable characteristics of the 100 mm box, this apparatus with no edging and a 1 mm gap was used to acquire the data presented and described in the following sections.

2.7 Peak Stress Envelopes

Figure 2.24 shows plots of τ'_P vs σ'_N at average γ_{dry} of 15.8 and 16.5 kN/m^3. The data show that the ϕ'_{ds-p} for dry RMS graded sand is consistent over σ'_N of 2.1 to 98.9 kPa. As can be seen, there is no cohesion for dry RMS graded sand. Figure 2.25

shows plots of τ'_{ps} vs σ'_{ps} for the same data as presented in Figure 2.24. The data points were converted from DS parameters to plane strain parameters using Equation 2.4, using values of ψ_p measured for each individual test. Trautmann and O'Rourke (1983) and Turner (2004) showed that ϕ'_{ds-p} of CU Filter sand was constant over a range of σ'_N from 6 - 35 kPa at an average γ_{dry} of 17.8 kN/m^3. Using the peak stress envelopes presented by Trautmann and O'Rourke (1983) and Turner (2004) for CU Filter sand and envelopes shown here for RMS graded sand, it can be seen that all three sands have linear Mohr-Coulomb envelopes.

Figure 2.26 shows DS strength and dilation parameters as a function of σ'_N for dry RMS graded sand at γ_{dry} = 15.8 and 16.5 kN/m^3. Figure 2.26a shows ϕ'_{ds-p} vs σ'_N. The average ϕ'_{ds-p} is represented with a line, with the higher γ_{dry} having an average ϕ'_{ds-p} of 36.6° and the lower γ_{dry} having an average ϕ'_{ds-p} of 32.7°. If a linear regression is fit to the data for γ_{dry} = 15.8 kN/m^3, the resulting slope is not statistically significant at a probability of 95%. However, if the potential outlier corresponding to σ'_N = 8.0 kPa is removed, the resulting linear regression is statistically significant at a probabilility of 95%. This linear regression is shown on the plot, and has r^2 = 0.66. According to the regression, ϕ'_{ds-p} increases from 32.5° to 33.7° as σ'_N increases from 2.1 to 98.9 kPa. This range of ϕ'_{ds-p} is comparable with the slope of the τ'_P vs σ'_N curve in Figure 2.24, which shows ϕ'_{ds-p} = 33.5° for the full range of σ'_N.

Figure 2.26b shows ϕ'_{ds-ld} vs σ'_N. Although ϕ'_{ds-ld} appears to increase slightly with increasing σ'_N there is no significant relationship between the variables. Linear regressions of the data, not shown in the figure, have r^2 less than 0.60 for both sets of γ_{dry}. There is an increase in ϕ'_{ds-ld} between the two data sets at different γ_{dry}, with an

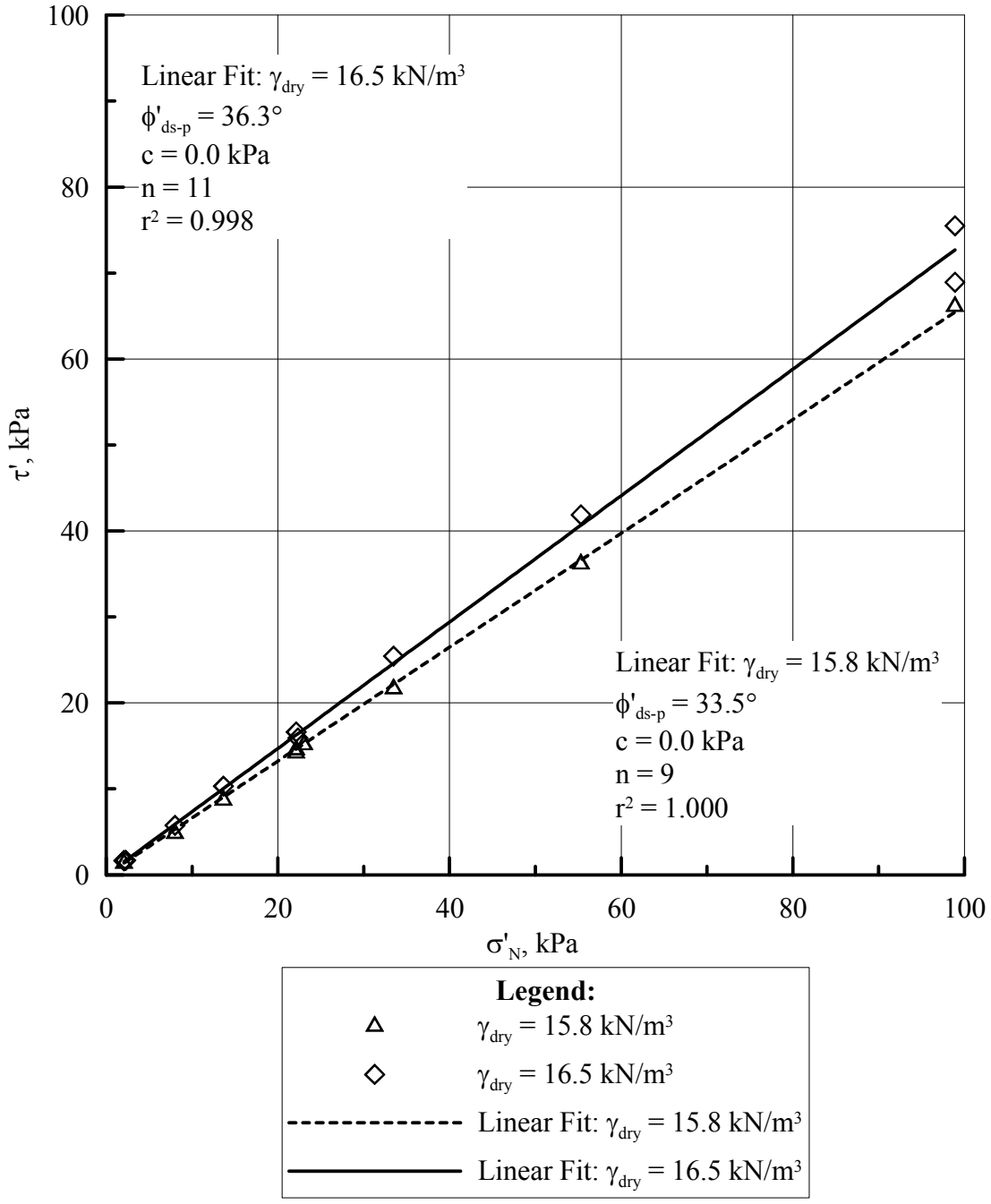

Figure 2.24 τ' vs σ'_N for dry RMS graded sand

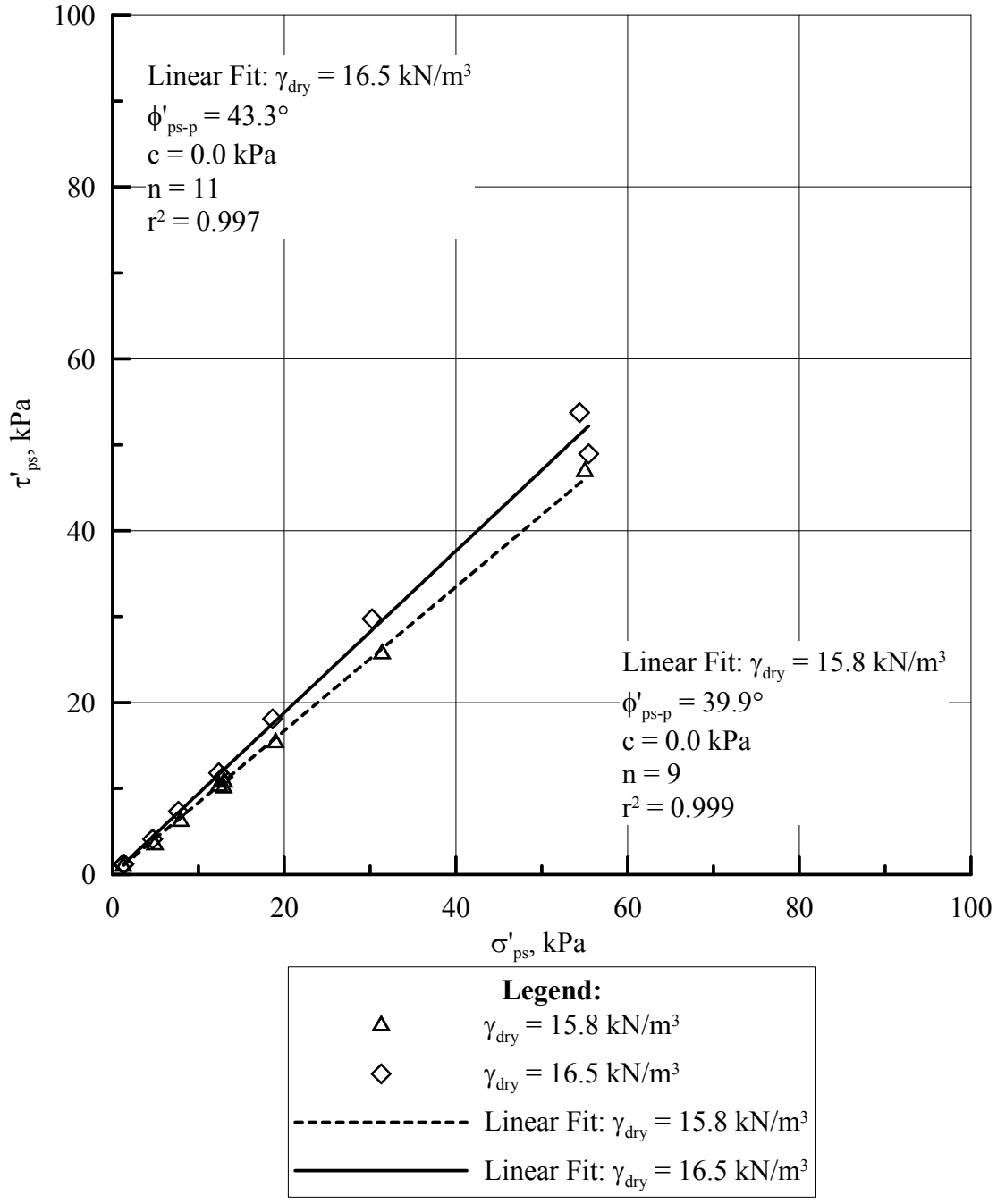

Figure 2.25 τ'_{ps} vs σ'_{ps} for dry RMS graded sand

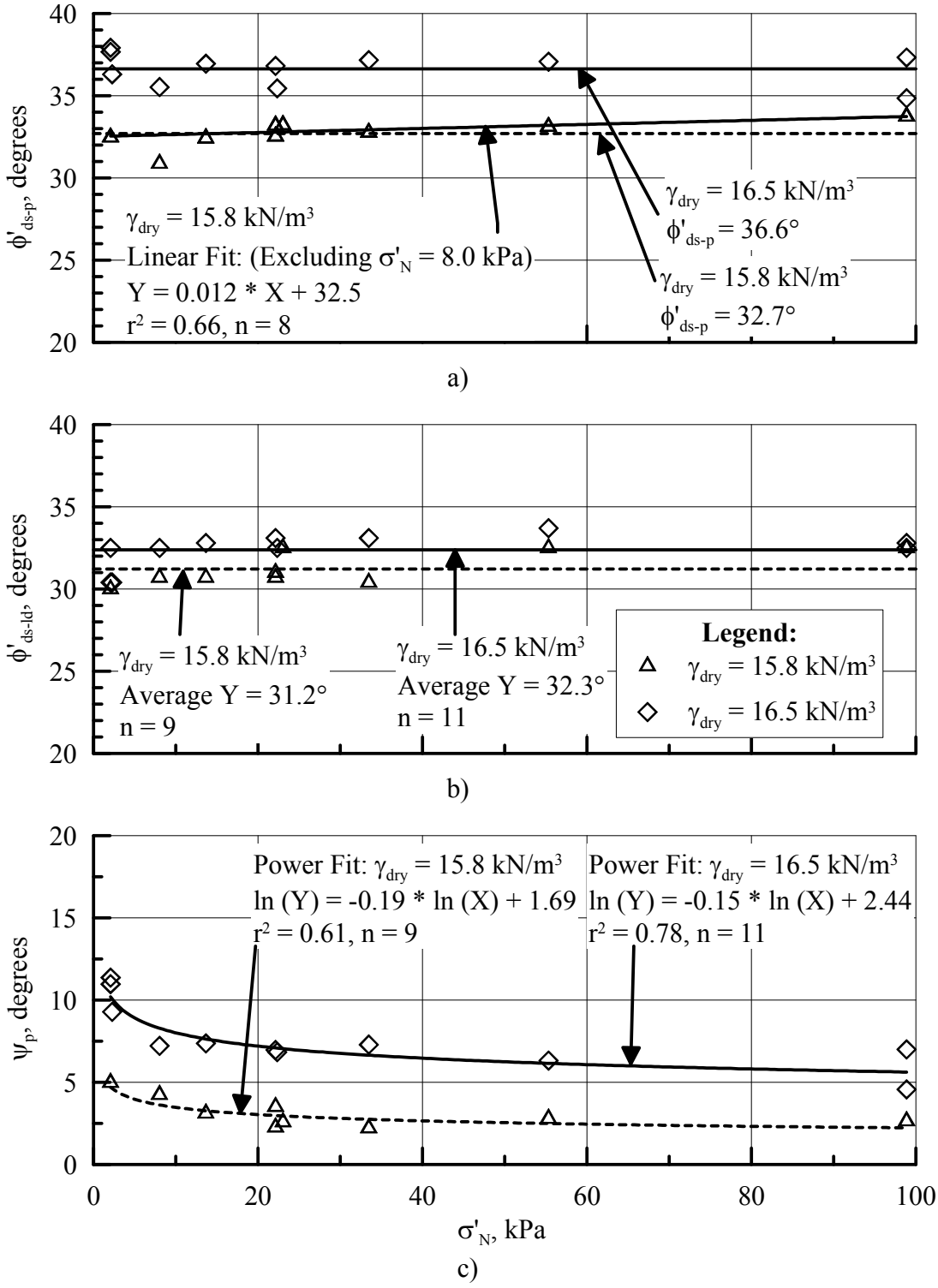

Figure 2.26 DS parameters vs σ'_N for dry RMS graded sand a) ϕ'_{ds-p} vs σ'_N b) ϕ'_{ds-ld} vs σ'_N c) ψ_p vs σ'_N

average of 31.2° for γ_{dry} = 15.8 kN/m^3 and 32.3° for γ_{dry} = 16.5 kN/m^3. Figure 2.26c shows ψ_p vs σ'_N. Over the range of σ'_N included in the Mohr-Coulomb envelopes, ψ_p decreases from 4.8° to 2.2° for the lower γ_{dry}, and 10.3° to 5.6° for the higher γ_{dry}, respectively, as σ'_N increases from 2.1 to 98.9 kPa. Power curve regressions fitted to the data show moderate r^2, 0.61, for the lower γ_{dry}, and a stronger r^2, 0.78, for the higher γ_{dry}.

2.8 Direct Shear Strength and Dilation Characteristics for RMS Graded Sand

Shown in Figure 2.27 are plots of $\phi'_{ds\text{-}p}$, ψ_p, and $\phi'_{ds\text{-}ld}$ vs γ_{dry} for dry RMS graded sand. The data in the figure pertain to $\gamma_{dry} \geq$ 15.9 kN/m^3. The linear regressions for $\phi'_{ds\text{-}p}$ and ψ_p have strong r^2 of 0.98 and 0.94, respectively. Because $\phi'_{ds\text{-}ld}$ represents a critical state in which the particles have been deformed with no further change in structure or volume change, it is regarded as being independent of initial dry unit weight. Accordingly, an average value of $\phi'_{ds\text{-}ld}$ has been plotted in Figure 2.27, which represents the best measured estimate of constant $\phi'_{ds\text{-}ld}$. The data, however, show a linearly increasing trend of $\phi'_{ds\text{-}ld}$ vs γ_{dry} and a linear regression has been fit to the data, with an r^2 of 0.78. It can be shown that the slope of the line is significantly different from zero at a 90% level of probability, but not at the 95% level.

Figure 2.28 shows histograms of ϕ'_{crit} for RMS graded sand determined by DS tests and the sand cone method. Values of ϕ'_{crit} were evaluated from $\phi'_{ds\text{-}ld}$ with the 100 mm box for a 1 mm gap and no edging and a 2 – 6 mm gap with split rubber edging. The relationship between ϕ'_{crit} and $\phi'_{ds\text{-}ld}$ given by Equation 2.5 was used to

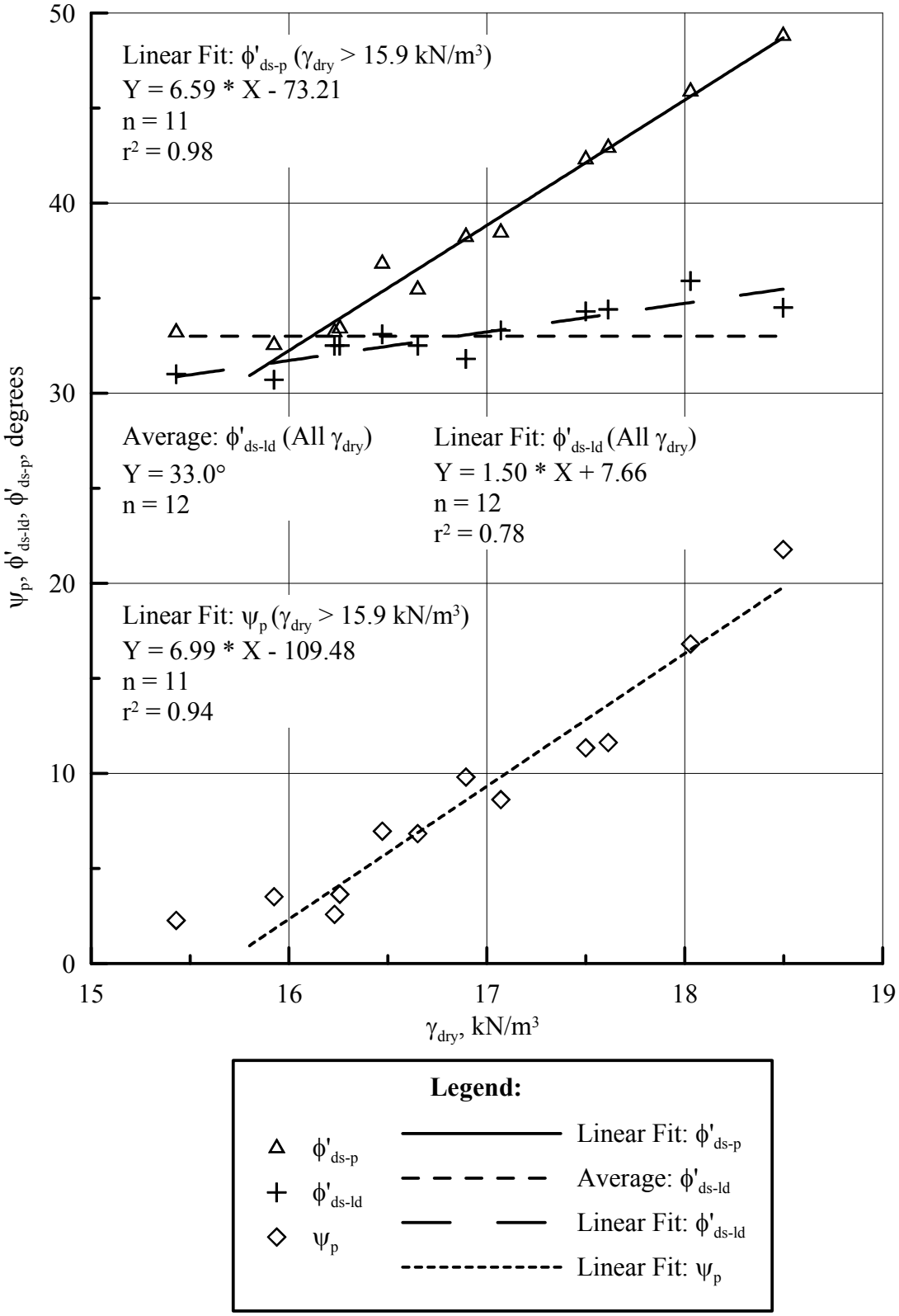

Figure 2.27 ϕ'_{ds-p}, ϕ'_{ds-ld} and ψ_p vs γ_{dry} for dry RMS graded sand

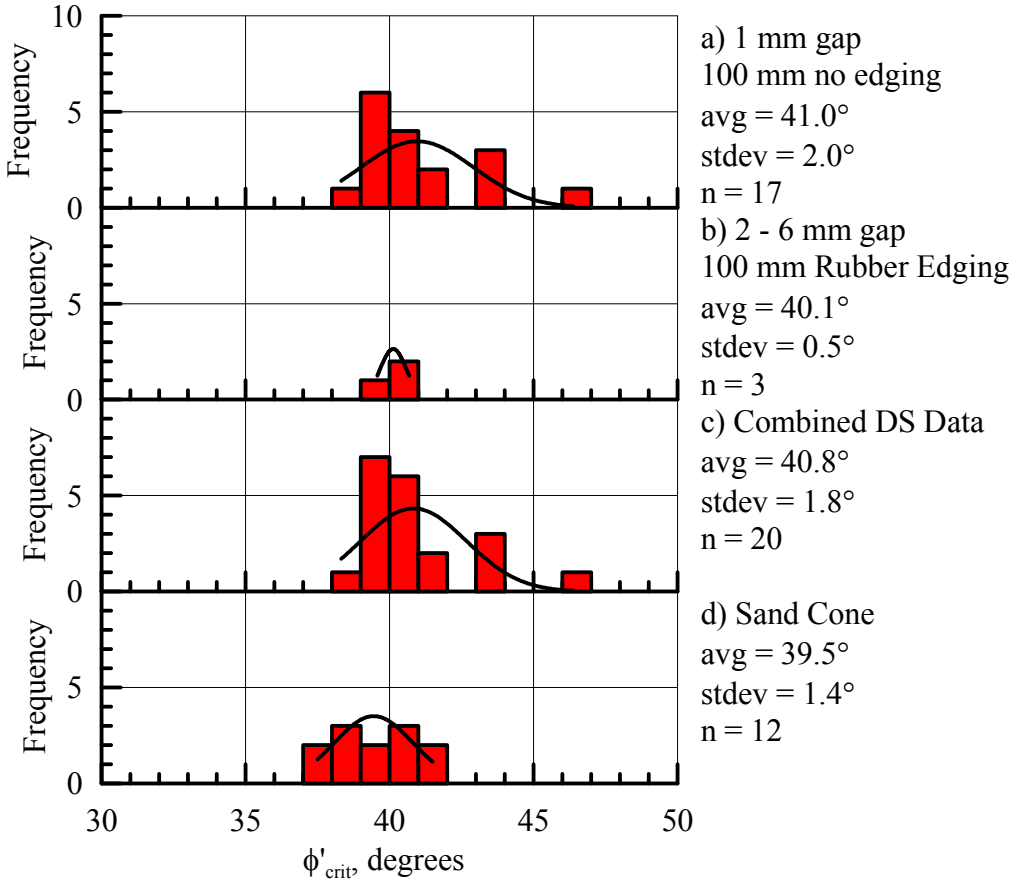

Figure 2.28 Histograms of ϕ'_{crit} for dry RMS graded sand using different methods

estimate ϕ'_{crit} from the DS data. Figure 2.28c shows a histogram of the combined data from Figures 2.28a and 2.28 b. The normal distribution fit has a mean of 40.8° and a standard deviation of 1.8°. The histogram of twelve data points gathered for dry RMS graded sand using the sand cone (shown earlier in Figure 2.6a) is shown again in Figure 2.28d for reference. The normal distribution has a mean of 39.5° and a standard deviation of 1.4°. The mean from Figure 2.28c of ϕ'_{crit} = 40.8° corresponds (using Equation 2.5) to $\phi'_{ds\text{-}ld}$ = 33.2°, which is slightly higher than the average$\phi'_{ds\text{-}ld}$ = 32.3° for γ_{dry} = 15.8 kN/m^3 from Figure 2.26b.

Various flow rules have been proposed for relating shear stress with volume change. As discussed by Lings and Dietz (2004), these flow rules in particular have been referenced extensively in the technical literature. The oldest was proposed by Taylor (1948) as

$$\tan \phi'_{ds} = \sin \phi'_{crit} + \tan \psi \tag{2.7}$$

Rowe's flow rules (1962, 1969) can be expressed as

$$\sin \phi'_{ps} = \frac{\sin \phi'_{crit} + \sin \psi}{1 + \sin \phi'_{crit} \sin \psi} \tag{2.8}$$

Bolton (1986) presented an empirical flow rule, based on a "saw tooth" simplification of the DS surface as

$$\phi'_{ps} = \phi'_{crit} + 0.8\psi \tag{2.9}$$

Combining Davis's relation (Equation 2.4) with Rowe's flow rule (Equation 2.8), Lings and Dietz (2004) obtained

$$\tan \phi'_{ds} = \frac{\sin \phi'_{crit} + \sin \psi}{\cos \psi} \tag{2.10}$$

Similarly, combining Davis's relation (Equation 2.4) with Bolton's flow rule (Equation 2.9) gives

$$\tan \phi'_{ds} = \frac{\cos \psi \sin\left(\phi'_{crit} + 0.8\psi\right)}{1 - \sin \psi \sin\left(\phi'_{crit} + 0.8\psi\right)} \tag{2.11}$$

Plotted in Figures 2.29a and 2.29b is $\phi'_{ds\text{-}p}$ vs ψ_p for dry RMS graded sand. The σ'_N shown in the figure ranges from 13.7 – 98.9 kPa. Also shown in Figures 2.29a and 2.29b are curves representing the flow rules defined in Equations 2.7, 2.10, and 2.11. The flow rules shown Figure 2.29a use ϕ'_{crit} as presented by the histogram in Figure 2.28c, for the average of the "combined data", where the mean $\phi'_{crit} = 40.8°$. The flow rules shown in Figure 2.29b, in contrast, use a linearly increasing ϕ'_{crit} as presented in the regression of the $\phi'_{ds\text{-}ld}$ vs $\phi'_{ds\text{-}p}$ data shown in Figure 2.27. The flow rules in Figure 2.29b provide a better fit to the experimental data.

2.9 Direct Shear Strength and Dilation Characteristics for RMS Uniform Sand

Shown in Figure 2.30 are plots of $\phi'_{ds\text{-}p}$, ψ_p, and $\phi'_{ds\text{-}ld}$ vs γ_{dry} for dry RMS uniform sand. The linear regressions for $\phi'_{ds\text{-}p}$ and ψ_p have strong r^2 of 0.98 and 0.99, respectively. The mean value of $\phi'_{ds\text{-}ld}$ is plotted as a constant value with respect to the data. Also shown in the figure is a linear regression for $\phi'_{ds\text{-}ld}$ vs γ_{dry}, which has a statistically significant slope at a probability of 95%.

Figure 2.31 shows histograms of ϕ'_{crit} for RMS uniform sand determined by DS tests and the sand cone method. Values of ϕ'_{crit} are evaluated from $\phi'_{ds\text{-}ld}$ with the 100 mm test apparatus for a 1 mm gap and no edging (shown in Figure 2.31a) and a -4 - 5 mm gap with split rubber edging (shown in Figure 2.31b), as well as the 60 mm test apparatus with a 1 mm gap without edging (shown in Figure 2.31c). Test data from the 60 mm box were used for RMS uniform sand because the particle sizes of the specimen were sufficiently small that the 60 mm device was in compliance with the

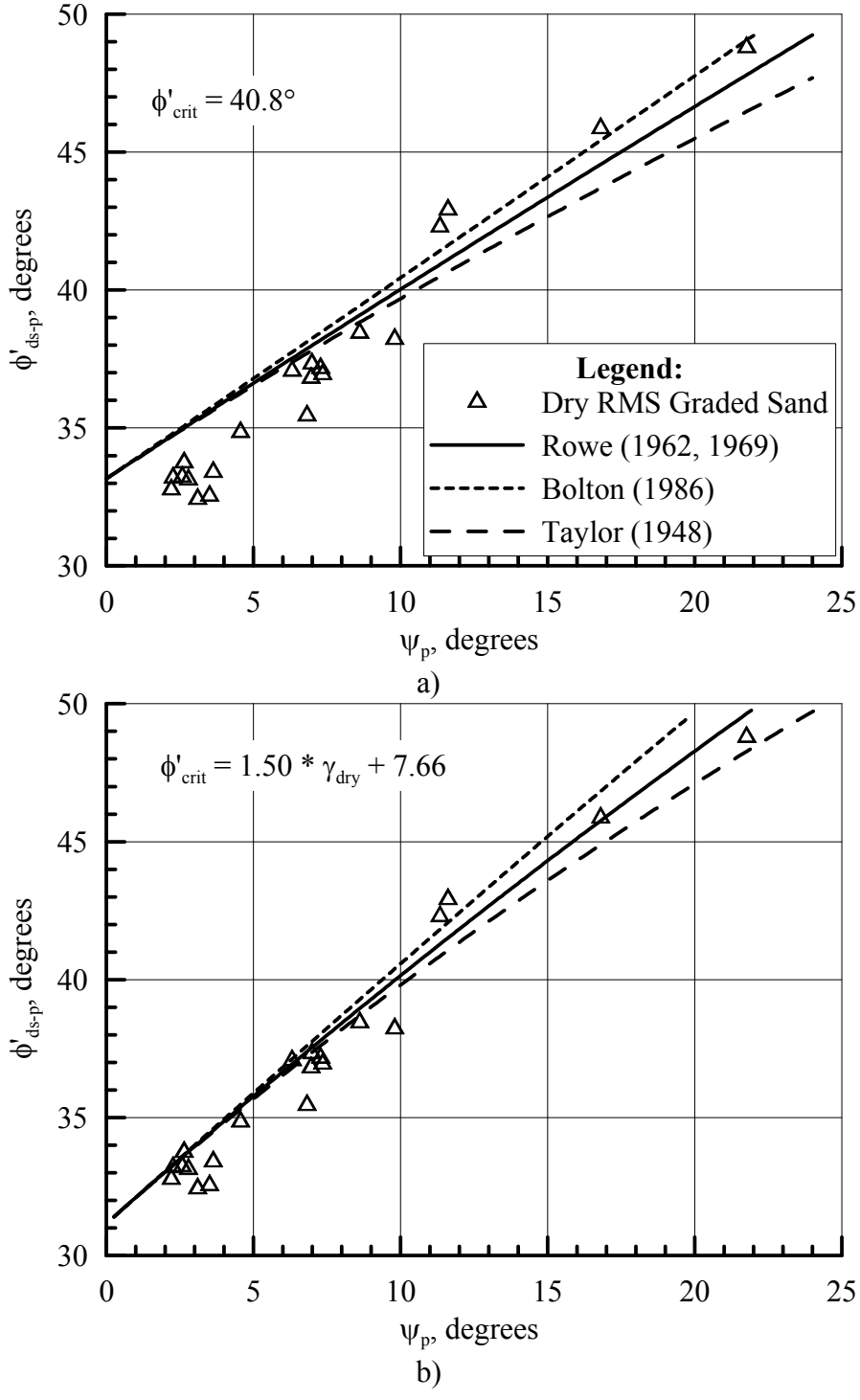

Figure 2.29 Plots of ϕ'_{ds-p} vs ψ_p and flow rules for RMS graded sand a) Using constant ϕ'_{crit} b) Using ϕ'_{crit} linearly dependent on γ_{dry}

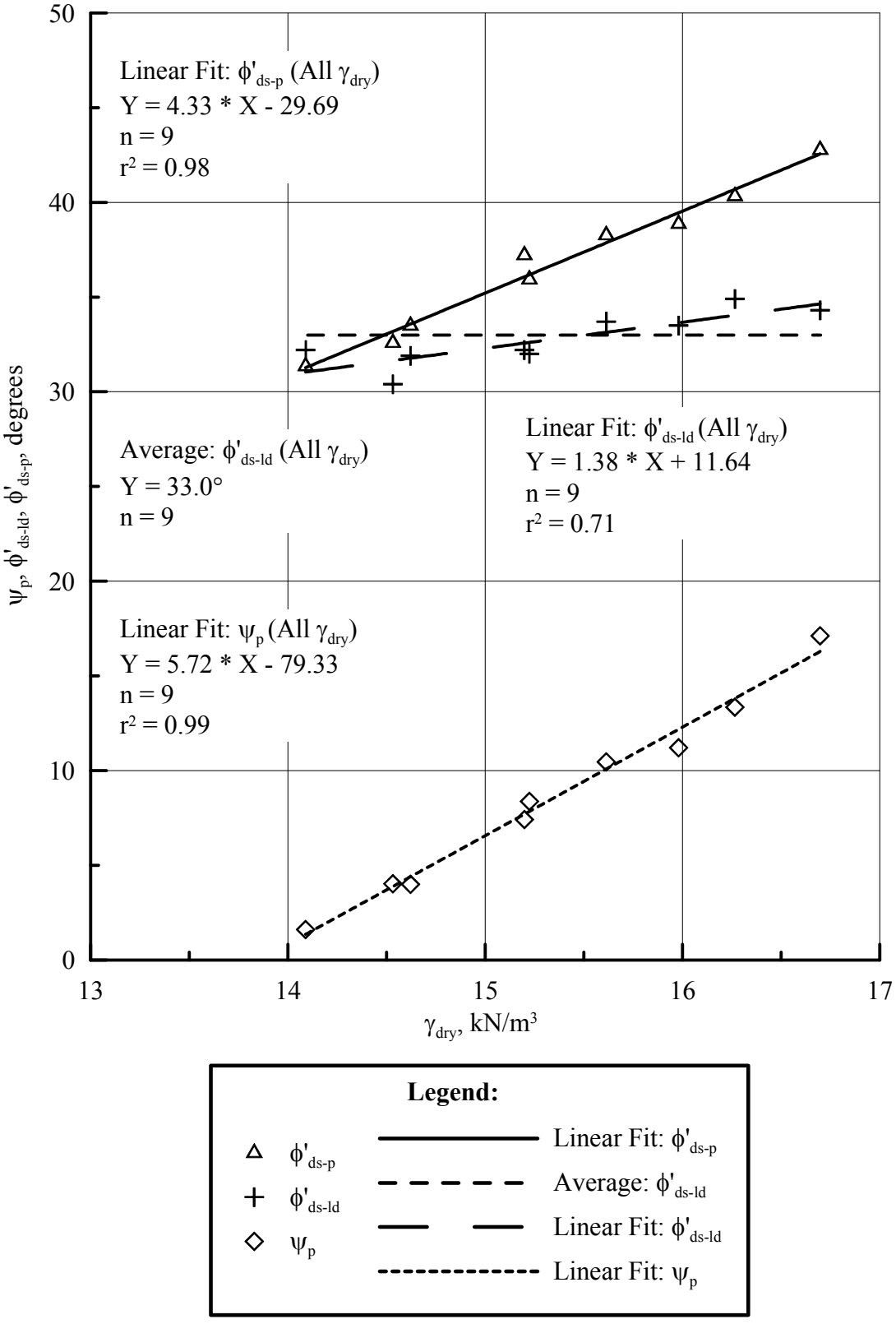

Figure 2.30 $\phi'_{ds\text{-}p}$, $\phi'_{ds\text{-}ld}$ and ψ_p vs γ_{dry} for dry RMS uniform sand

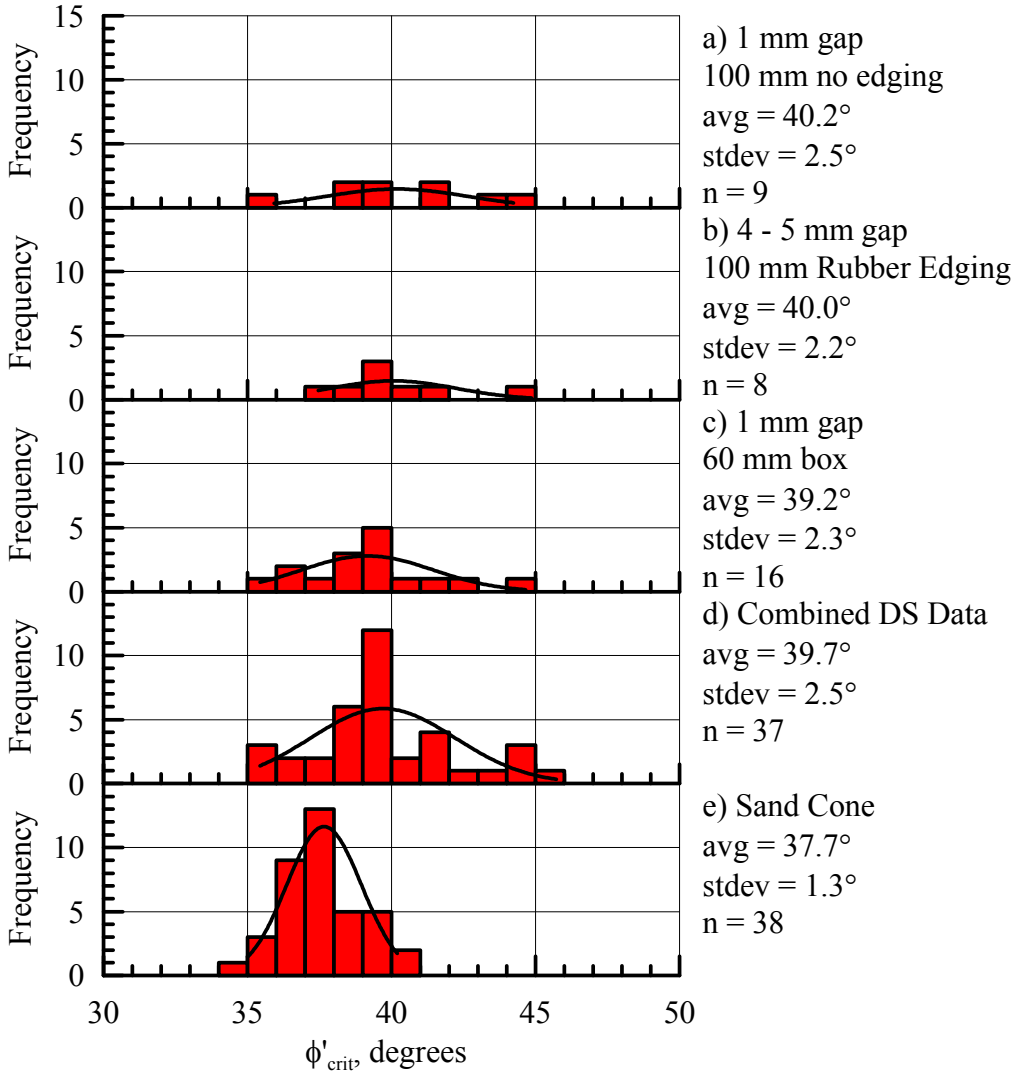

Figure 2.31 Histograms of ϕ'_{crit} for dry RMS uniform sand using different methods

ratio of box dimension to maximum particle size recommended for accurate test results by the ASTM standard (ASTM, 2003e). The combined DS data from tests on RMS uniform sand are shown in Figure 2.31d. Figure 2.31e presents a histogram of 38 data points for ϕ'_{crit} using the sand cone (shown earlier in Figure 2.6b). A normal distribution was fit to the data, with a mean of 37.7° and a standard deviation of 1.3°.

Plotted in Figure 2.32 is $\phi'_{ds\text{-}p}$ vs ψ_p for dry RMS uniform sand using the 100 mm box with no edging and a 1 mm gap at a σ'_N = 22.3 kPa. Also shown in Figure 2.32 are curves representing the flow rules defined in Equations 2.7, 2.10, and 2.11. The flow rules shown in Figure 2.32a use the mean ϕ'_{crit} from sand cone data shown in Figure 2.31e. The flow rules shown in Figure 2.32b use ϕ'_{crit} as presented by the histogram in Figure 2.31d, for the average of the "combined data", where ϕ'_{crit} is assumed constant with respect to γ_{dry} at 39.7°. The flow rules for ϕ'_{crit} = 37.7° fit the data better than those for ϕ'_{crit} = 39.7°.

2.10 Direct Shear Strength and Dilation Characteristics for CU Filter Sand

Shown in Figure 2.33 are plots of $\phi'_{ds\text{-}p}$, ψ_p, and $\phi'_{ds\text{-}ld}$ vs γ_{dry} for dry CU Filter sand. The linear regressions for $\phi'_{ds\text{-}p}$ and ψ_p have strong r^2 of 0.89. The mean value of $\phi'_{ds\text{-}ld}$ is plotted as a constant value with respect to the data. Statistical analysis on the slope of the regression line fit to the $\phi'_{ds\text{-}ld}$ vs γ_{dry} data yielded a confidence of less than 90%, and the line is not shown on the figure.

Figure 2.34 shows histograms of ϕ'_{crit} for CU Filter sand determined by DS tests and the sand cone method. Values of ϕ'_{crit} are evaluated from $\phi'_{ds\text{-}ld}$ with the 100 mm test apparatus for a 1 mm gap and no edging, shown in Figure 2.31a. The normal distribution fit has a mean of 38.6° and a standard deviation of 0.8°. The histogram of ten data points gathered for dry CU Filter sand using the sand cone (shown earlier in Figure 2.6c) is shown again in Figure 2.34b for reference. The normal distribution fit has a mean of 35.9° and a standard deviation of 1.1°. The histograms for the DS data and the sand cone data for CU Filter sand are both well behaved, with smaller standard

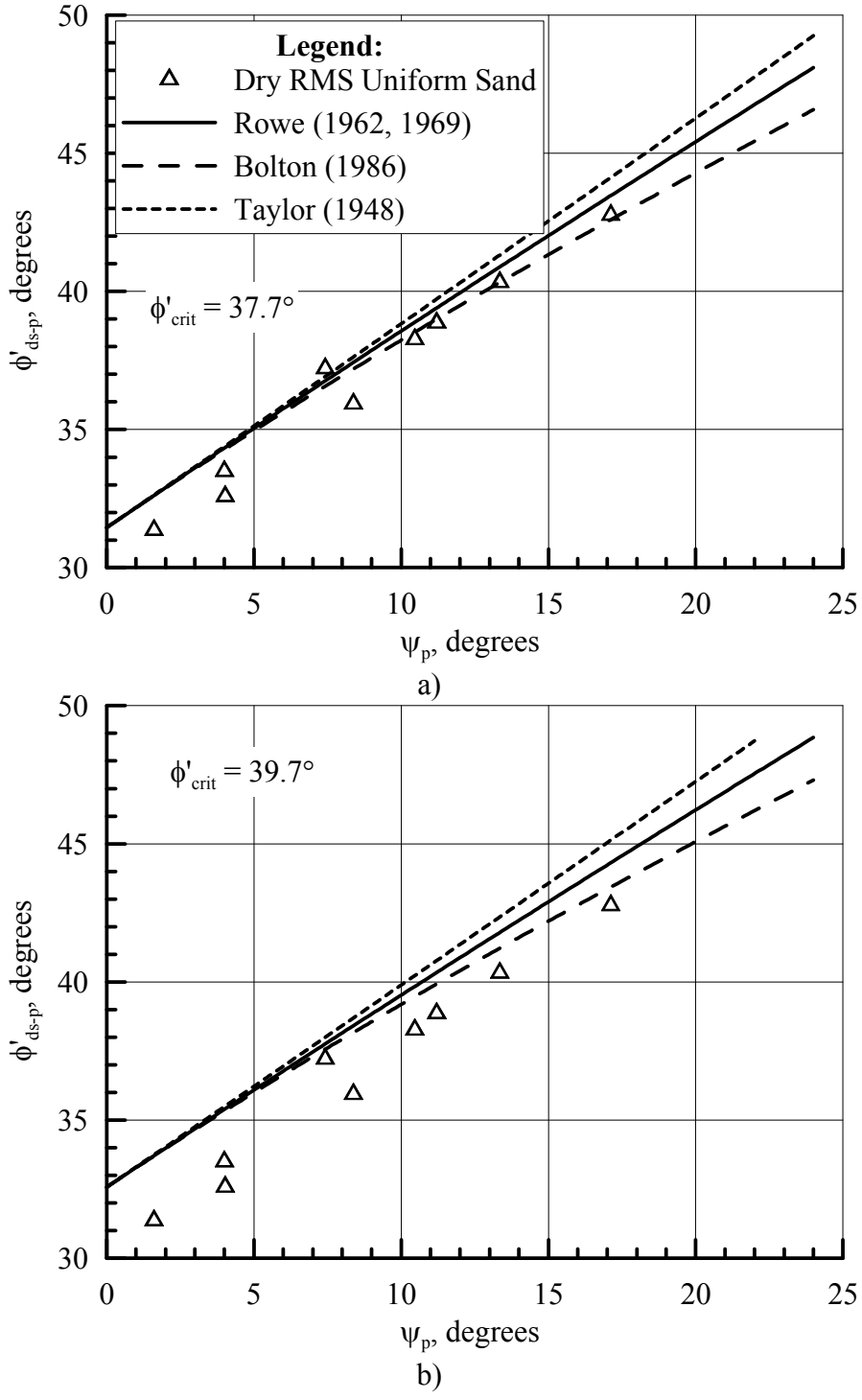

Figure 2.32 Plots of $\phi'_{ds\text{-}p}$ vs ψ_p and flow rules for RMS uniform sand using a) Average ϕ'_{crit} from sand cone data b) Constant ϕ'_{crit} from large displacement DS data

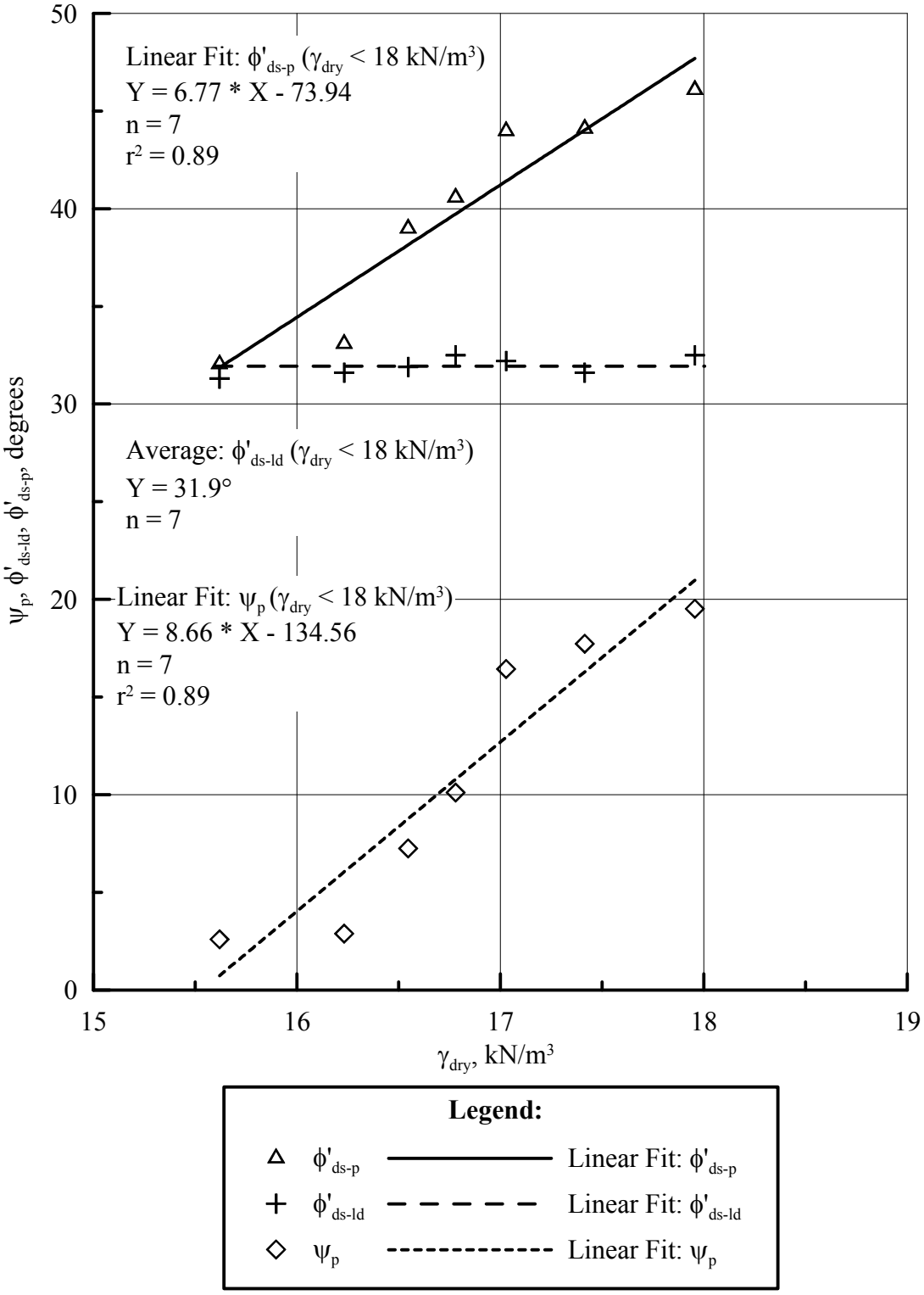

Figure 2.33 ϕ'_{ds-p}, ϕ'_{ds-ld} and ψ_p vs γ_{dry} for dry CU Filter sand

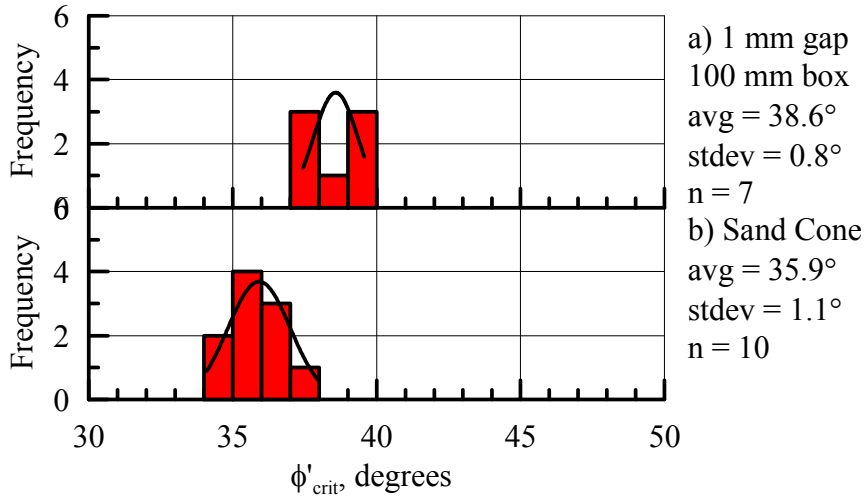

Figure 2.34 Histograms of ϕ'_{crit} for dry CU Filter sand gathered using different methods

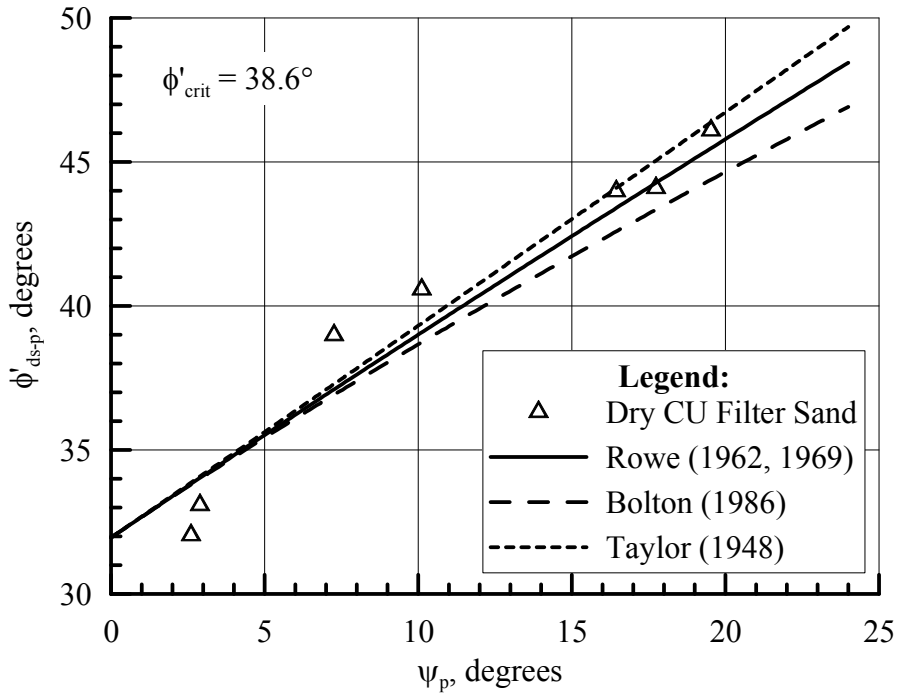

Figure 2.35 Plots of ϕ'_{ds-p} vs ψ_p and flow rules for CU Filter sand using constant ϕ'_{crit} from large displacement DS data

deviations than found for the other sands. This may be related to the finding, stated previously, that $\phi'_{ds\text{-}ld}$ is not statistically dependent on γ_{dry} for this test material.

Plotted in Figure 2.35 is $\phi'_{ds\text{-}p}$ vs ψ_p for dry CU Filter sand using the 100 mm box with no edging and a 1 mm gap at a σ'_N = 22.3 kPa. Also shown in Figure 2.35 are curves representing the flow rules defined in Equations 2.7, 2.10, and 2.11. The flow rules use ϕ'_{crit} as presented by the histogram in Figure 2.34a, for the average of the 100 mm data, where ϕ'_{crit} is assumed constant at 38.6°. The flow rules appear to represent the $\phi'_{ds\text{-}p}$ vs ψ_p data well.

2.11 300 mm Direct Shear Box

Shown in Figure 2.36a is a histogram of ϕ'_{crit} for dry RMS graded sand using tests run with the 300 mm box. Figure 2.36b shows the histogram of combined ϕ'_{crit} data for dry RMS graded sand, also shown in Figure 2.28c. The normal distribution fit to the 300 mm box data has a higher mean and a greater standard deviation than the combined DS data. Shown in Figure 2.37a is a histogram of ϕ'_{crit} for dry RMS uniform sand using tests run with the 300 mm box. Figure 2.37b shows the histogram of combined ϕ'_{crit} data for dry RMS uniform sand, also shown in Figure 2.31d. The normal distribution fit to the 300 mm box data again has a higher mean and a greater standard deviation than the combined DS data.

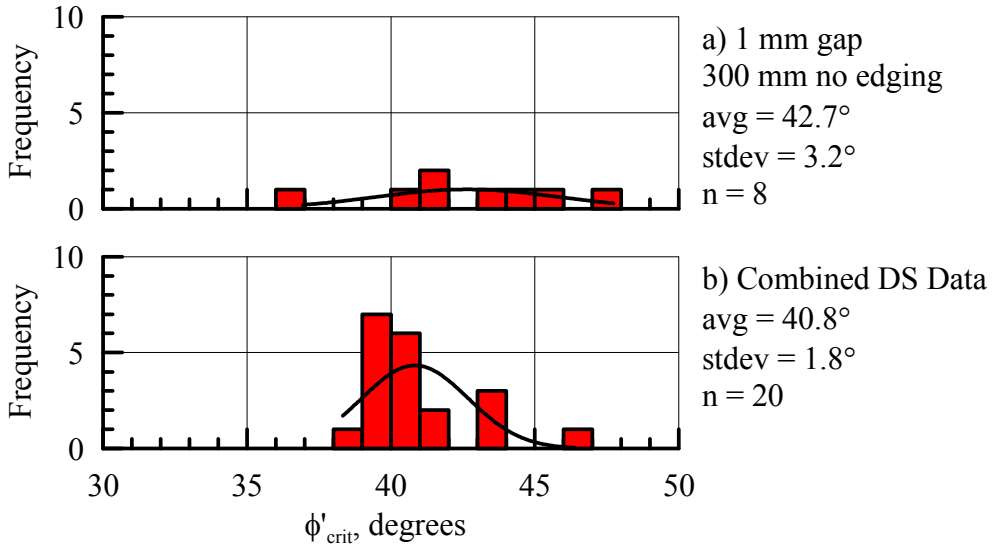

Figure 2.36 Histograms of ϕ'_{crit} for dry RMS graded sand a) Using 300 mm box b) Combined data from Figure 2.27c

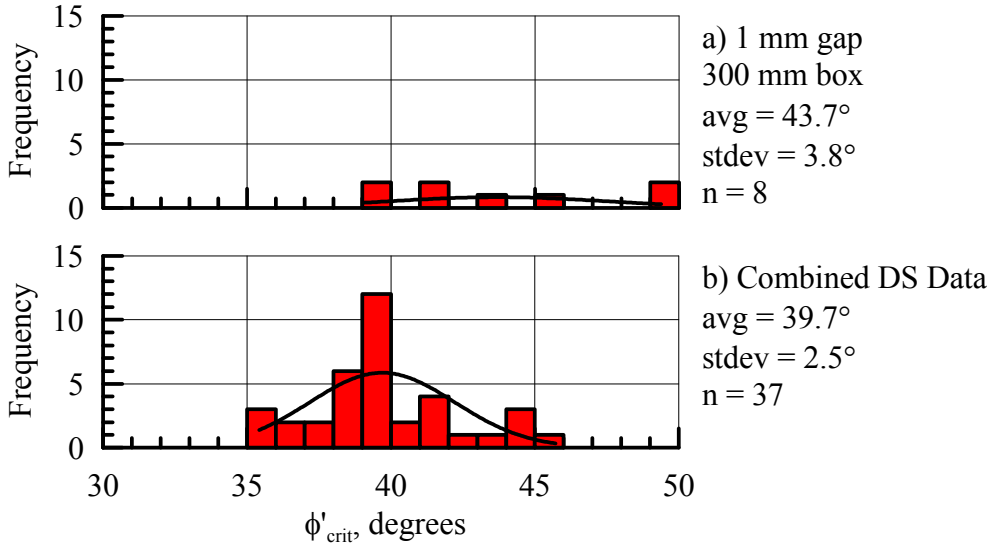

Figure 2.37 Histograms of ϕ'_{crit} for dry RMS uniform sand a) Using 300 mm box b) Combined data from Figure 2.30d

It is not clear why there is a higher mean and greater variability for ϕ'_{crit} as estimated from tests with the 300 mm test apparatus. Although great care was taken during the fabrication of the 300 mm DS device, the precision of machining in the large box could not achieve the same level of precision as that for the smaller boxes. As a result the separation between upper and lower frames in the 300 mm device was more variable than that of the smaller boxes. Moreover, the weight of the 300 mm upper frame was approximately 7% of the normal force applied to the specimens, compared with 1.2% and 4.6% associated with the 60 mm and 100 mm upper frames, respectively. It may be that the combination of higher percentage weight of the upper frame and greater variation in gap thickness associated with the 300 mm device are reflected in the higher mean and bias of the data.

CHAPTER 3

DIRECT SHEAR AND MATRIC SUCTION CHARACTERISTICS OF PARTIALLY SATURATED GLACIO-FLUVIAL SAND

3.1 Introduction

Partially saturated sand is different from saturated or dry sand in that it generates negative pore water pressure due to matric suction, u_m. The presence of u_m has the effect of increasing the effective stress and inducing apparent cohesion in the soil, thereby increasing the soil shear strength and dilatency for a given σ_N and γ_{dry}. Large scale tests were performed using partially saturated RMS graded sand to simulate partially saturated soil, which is typical of most pipeline installations. Since RMS graded sand naturally drains to a gravimetric water content, w, of 4 – 6%, DS tests were run for these conditions to explore the effect of changing w within this range. Unless otherwise noted, the 100 mm box and improved DS apparatus discussed previously were used for all tests in this chapter, with a typical gap of 1 mm and no edging.

Soil water retention curves (SWRCs) on individual soil specimens were performed with Tempe cells, and tensiometer measurements were taken during large scale tests to generate relationships between w and u_m. The SWRCs were used to define the residual u_m and w associated with the range of γ_{dry} used in the large-scale tests. A relationship was derived to compute the u_m associated with the difference in strength between DS tests on dry and partially saturated sand at the same γ_{dry}. This

value was shown to compare well with the direct measurements of u_m using the Tempe cells and tensiometers.

3.2 Matric Suction Measurement

According to the Soil Science Society of America (SSSA), soil water matric potential, or matric suction, u_m, is the amount of work per unit volume to transport reversibly and isothermally an infinitesimal quantity of water from a specified source to a specified destination (SSSA, 1997). It is always a negative value (measured for this study in kPa of vacuum pressure) in partially saturated soil because the energy required to overcome the absorptive and capillary forces is equal and opposite to the matric potential. The Tempe cell, discussed in ASTM D6836 (ASTM, 2008a), was used to develop SWRCs, while tensiometers, discussed by Dane and Topp (2002), were used to measure u_m in situ during large scale tests. Measurements were compared with published results for similar soils, and important water retention properties such as residual water content are estimated from the SWRCs.

3.2.1 Tensiometer

Tensiometers, fabricated by the Cornell University Department of Crop and Soil Sciences, were used to measure u_m beneath the soil surface during large scale tests. Energy equilibrium between the tensiometer and the surrounding soil is achieved through water movement across a porous cup in the direction of decreasing matric potential.

A typical tensiometer is shown in Fig. 3.1a. Each tensiometer consisted of a porous ceramic cup with a pore size of 2.5 μm attached to a 600 mm long PVC pipe with 19 mm outside diameter and capped with a serum septum stopper. The porous cup was saturated with de-aired water, and the device is filled with the same water to 20 - 30 mm beneath the stopper. To install a tensiometer in the soil, a hole was bored to a depth 50 cm below the desired porous cup depth, a small handful of soil was sprinkled into the hole. The tensiometer was placed in the hole and gently pushed down and rotated to make a good bond between the soil and the porous cup. The tensiometer was allowed to sit in the soil for an hour to develop a state of equilibrium between the matric potential in the soil and the matric potential at the bottom of the porous cup.

Figure 3.1b shows a tensiometer (left) equipped with a septum stopper. Measurements of vacuum pressure were made with a handheld Tensimeter measurement device which has a small needle that punctures the septum stopper. The Tensimeter measurement device was manufactured by Soil Measurement Systems, Tuscon, Arizona. The septum stopper reseals when the needle is removed, preserving the internal pressure in the airspace at the top of the tensiometer. The tensiometer on the right in Figure 3.2b is fitted with a pressure transducer, which is connected to a computer data acquisition system.

Suction measurements must be corrected for the weight of the water column in the tensiometer. For a water column height, z, (1000 mm, for example) as measured from the water surface to porous cup center, a value of (1000 mm)(9.81 kN/m^3) = 9.81 kPa, must be added to vacuum pressure measured with the Tensimeter in the airspace

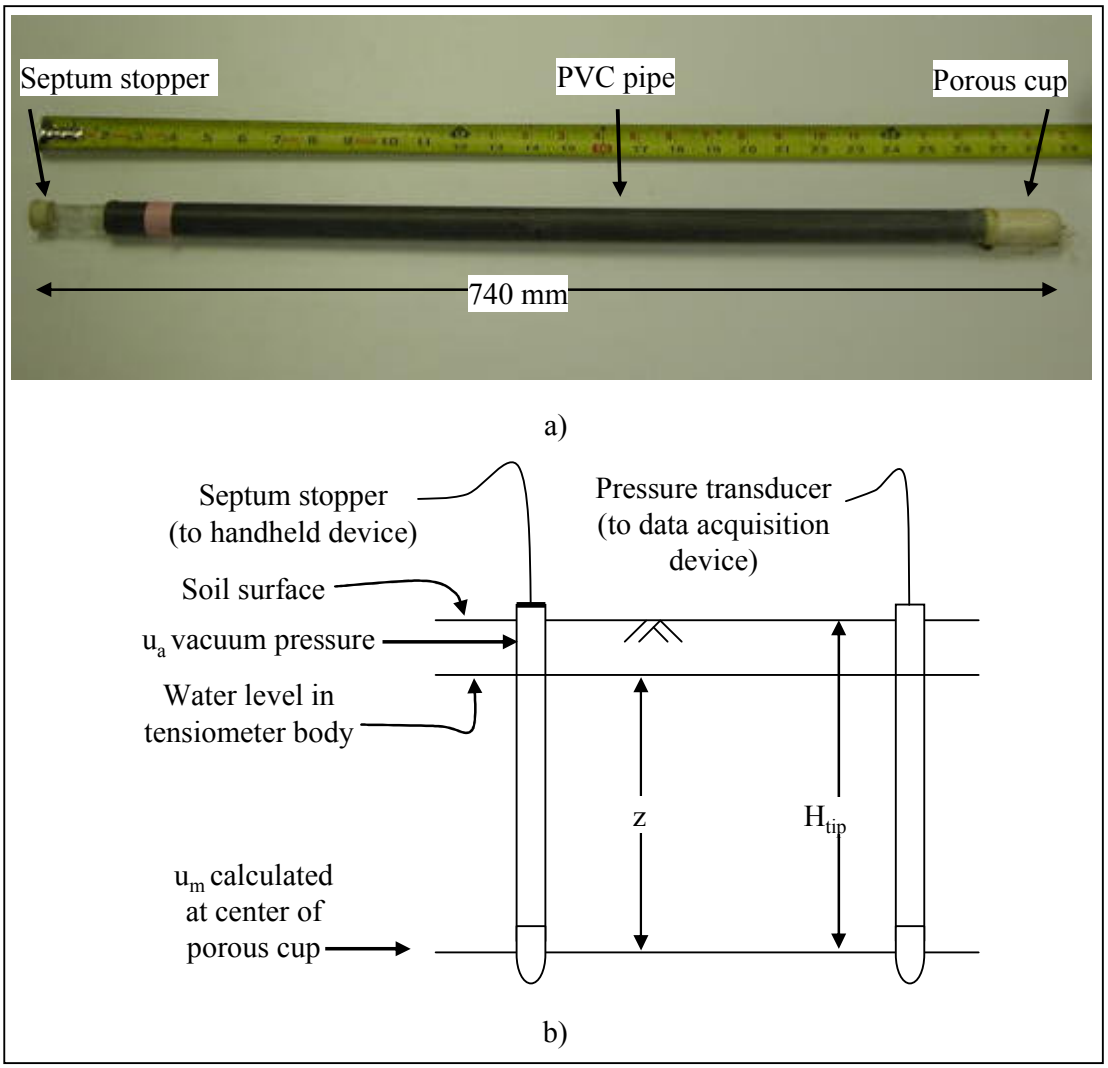

Figure 3.1 a) Photo of tensiometer b) Schematic of tensiometer (Not to scale)

above the water column, u_a, to obtain the matric suction, u_m. Matric suction at the center of the tensiometer porous cup, u_m, is calculated, using a conversion factor of 1 mm water pressure head = 0.00981 kPa, by the following equation:

$$u_m = u_a + 0.00981z \tag{3.1}$$

Table 3.1 Summary of u_m for large-scale tests

Test	u_m, kPa	w, %	γ_{dry}, kN/m^3	H_{tip}, mm	D, mm	H_c, mm
2D 10	5.1	3.7	16.0	430	120	660
2D 11	4.5	4.9	16.5	280	120	660
	3.0			200		
3D 6	3.5	4.6	15.8	150	400	1120
	2.5			150		

Tensiometers were used in two 2-D large-scale ground rupture tests and one 3-D strike-slip compression test. Table 3.1 shows measurements of u_m and tensiometer porous cup depth, H_{tip}, for the three tests, as well as values of γ_{dry}, w, and test geometry. Gravimetric water content, or w, is calculated as

$$w = \frac{W_{wet} - W_{dry}}{W_{dry}} \tag{3.2}$$

where W_{wet} and W_{dry} are the weights of the soil before and after oven drying, respectively. The tests, as discussed later in Chapter 4, were prepared to obtain γ_{dry} of 15.8 through 16.5 kN/m^3, with w from 3.7 to 4.9%. H_{tip} varies from 150 – 430 mm. As can be seen in the figure, one tensiometer was installed in the soil for test 2-D 10 and two tensiometers each were installed in the soil for tests 2-D 11 and 3-D 6. Values of u_m before the initiation of displacement were measured between 2.5 – 5.1 kPa. All tensiometers were monitored continuously during pipe displacement and/or strike-slip offset, and there was found to be no significant change in u_m during the tests.

3.2.2 Tempe Cell Apparatus

The Tempe cell was used to obtain SWRCs (plots of w vs u_m), which are unique for a particular material prepared to a particular unit weight. In essence, a SWRC is a series of equilibrium stages in which applied u_m is in balance with w. The relationship between water content and matric suction is hysteretic in that the soil will behave differently in adsorption (wetting) than desorption (drying). Tempe cells fabricated by Dept. of Crop and Soil Sciences at Cornell University were used to determine SWRCs for RMS graded sand. Photographs of a Tempe cell are presented in Figures 3.2a and b, and a schematic of the device is shown in Figure 3.2c.

The Tempe cell provided the SWRC by desorption (drying), in accordance with "Method B" from ASTM D6836 (ASTM, 2008a). Initially dry soil was compacted into a specimen ring on top of a mesh sheet, weighed, and placed in a flat-bottomed bowl. Water was slowly poured into the bowl over a period of ten minutes to saturate the soil sample from the bottom up, driving air upward from the soil specimen. Tap water was used to saturate the soil specimen. After a saturation period of three hours, the sample was quickly and carefully weighed to determine its water content, and then was placed into the Tempe cell on top of a double thickness of saturated filter paper (see Fig. 3.2b). The filter paper had an air entry suction of 100 kPa, well beyond the maximum pressure applied in the current study. The Tempe cell was sealed at the top, and pressure was applied to the cell through a tube, and measured by a mercury manometer. As the soil equilibrated to the new applied pressure, water was removed from the soil voids by suction and collected in a graduated cylinder. The water content associated with the applied matric suction was

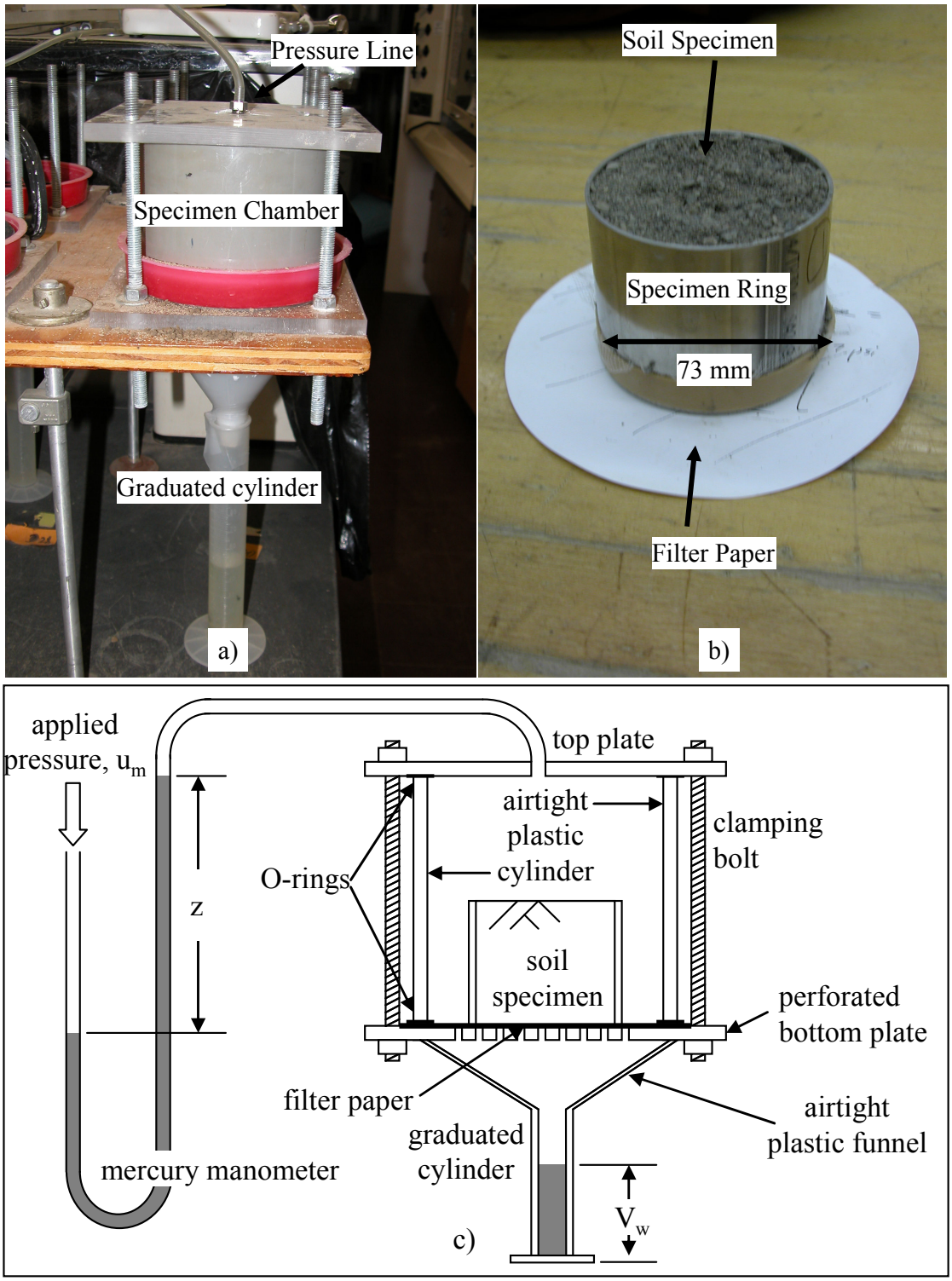

Figure 3.2 a) Photo of Tempe cell b) Photo of soil specimen c) Schematic of Tempe cell (Not to scale)

calculated by measuring the amount of water collected in the graduated cylinder over the 24 hour equilibration period. The remaining pressure steps were applied to the chamber and the soil was given 24 hours to equilibrate to the applied pressure for each successive point on the SWRC. The final water content was measured by drying the soil specimen in an oven.

3.2.3 Soil Water Retention Curve

Figure 3.3a shows a plot of w vs u_m for three tests on RMS graded sand at different γ_{dry}. There is a significant influence of γ_{dry} for low applied suctions, but the influence is less pronounced at greater values of u_m. Also shown in Figure 3.3a are (w, u_m) data points measured with tensiometers during large scale tests. These data fall at a lower w than the SWRCs for reasons that will be explained later. Also explained later is the procedure for calculating residual w, which is shown to be 4 – 6% for these SWRCs.

Volumetric water content, θ_w, and degree of saturation, S, are defined as

$$\theta_w = \frac{V_w}{V_{total}} \tag{3.3}$$

$$S = \frac{V_w}{V_v} \tag{3.4}$$

where V_{total} is the volume of the soil sample before drying, V_w is the volume of water, and V_v is the volume of voids in a soil sample. Figure 3.3b shows a plot of θ_w vs u_m for the same three retention curves as shown in Figure 3.3a with the addition of a retention curve for a similar sand measured by Singh et al. (2006).

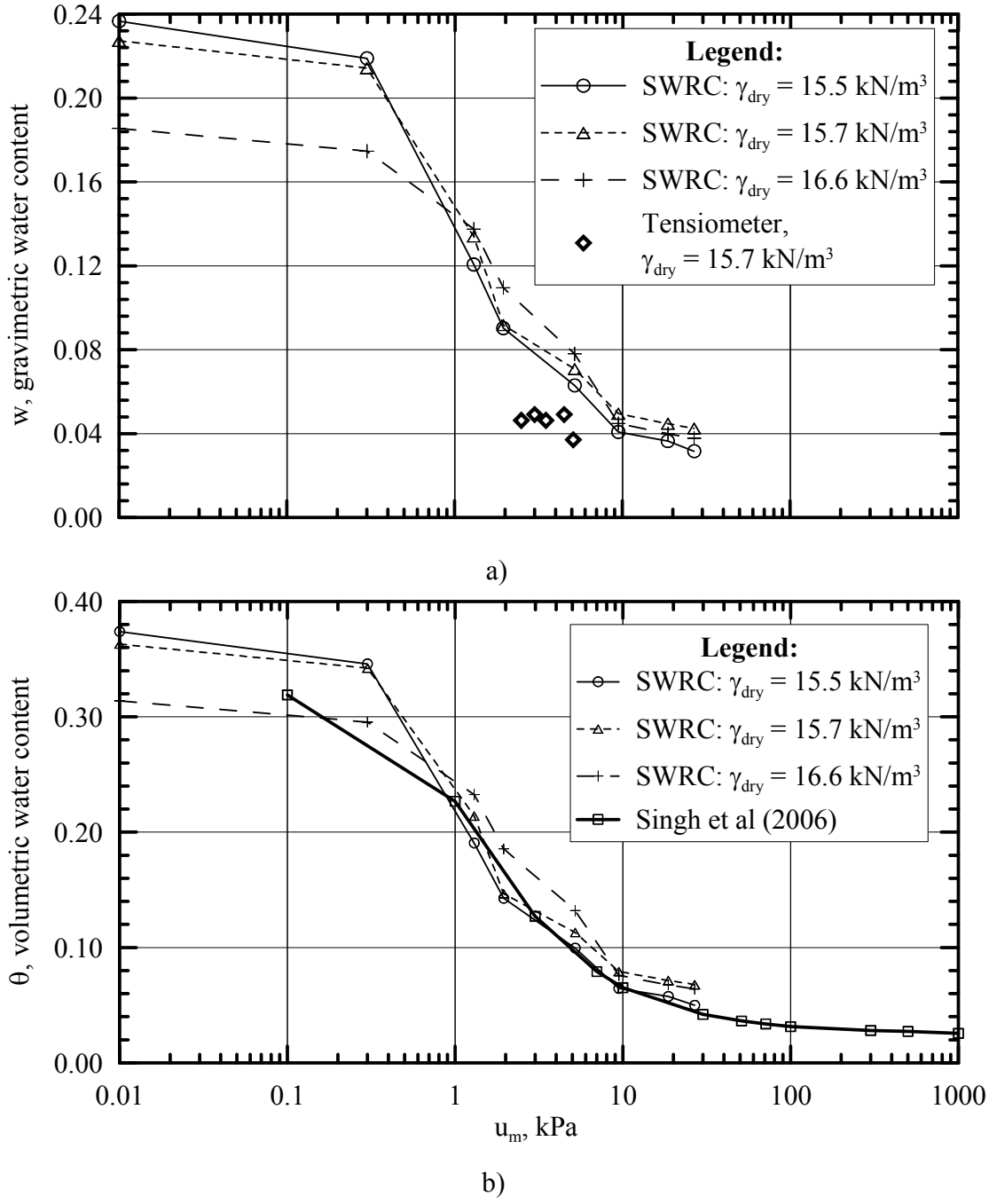

Figure 3.3 a) w vs u_m for RMS graded sand with SWRCs by desorption and in situ measurements b) θ vs u_m for RMS graded sand and similar sand (by desorption)

The soil used by Singh et al. had D_{10} = 0.17 mm and D_{60} = 0.64 mm, which compare closely with D_{10} = 0.24 mm and D_{60} = 0.80 mm for RMS graded sand. As can be seen in the figure, the SWRC reported by Singh et al. (2006) plots very closely to the SWRC for RMS graded sand.

Fredlund and Xing (1994) derived an equation for representing the SWRC from known (w, u_m) data, defined as

$$w = \frac{w_{sat}}{\left\{\ln\left[e + \left(u_m / a_1\right)^{n_1}\right]\right\}^{m_1}} \left\{\frac{-\ln\left(1 + u_m / u_r\right)}{\ln\left[1 + \left(1000000 / u_r\right)\right]} + 1\right\} \qquad (3.5)$$

where a_1, m_1, and n_1 are parameters used to fit the function to the w vs u_m data, w_{sat} is the saturated w, and u_r is the value of matric suction at residual w.

Figure 3.4a compares for RMS graded sand the SWRC computed with Eqn. 3.5 and the SWRC measured with the Tempe cell. Microsoft Excel's Solver function was used to minimize the error between the actual data points and the SWRC that was fit to the data using Eqn. 3.5. The constants used in the curve fit and data points obtained for soil samples at other γ_{dry} (not shown in Figs. 3.3 or 3.4) are provided in Table 3.2.

Vanapalli et al. (1998) identified key points on the SWRC and developed methods for calculating them, including the air-entry and residual suctions shown in Fig. 3.4b. The SWRC for RMS graded sand at 15.7 kN/m^3 is plotted in the figure, and the constructions recommended by Vanapalli et al. are drawn relative to the SWRC.

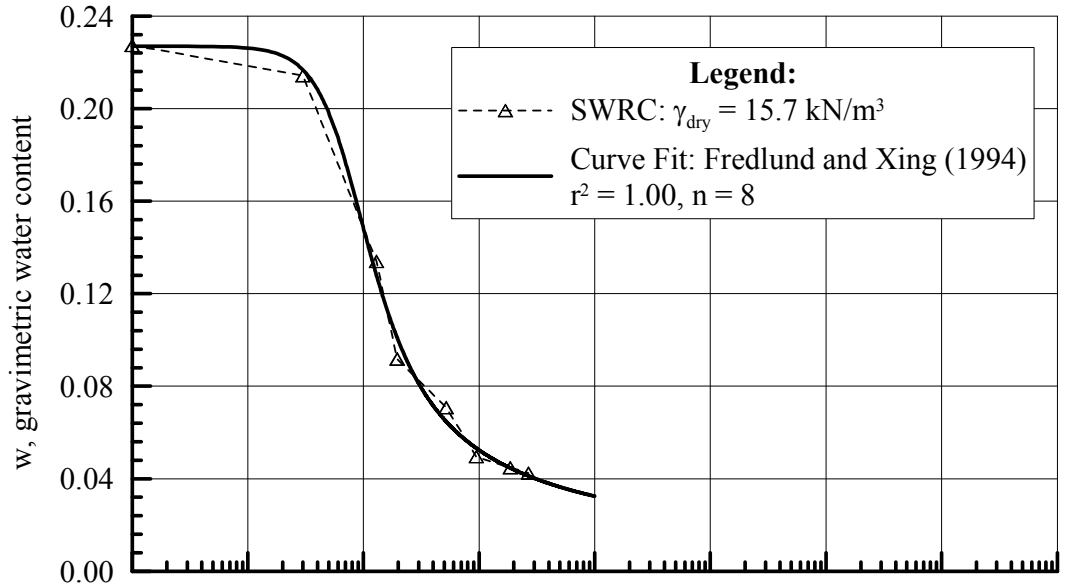

a)

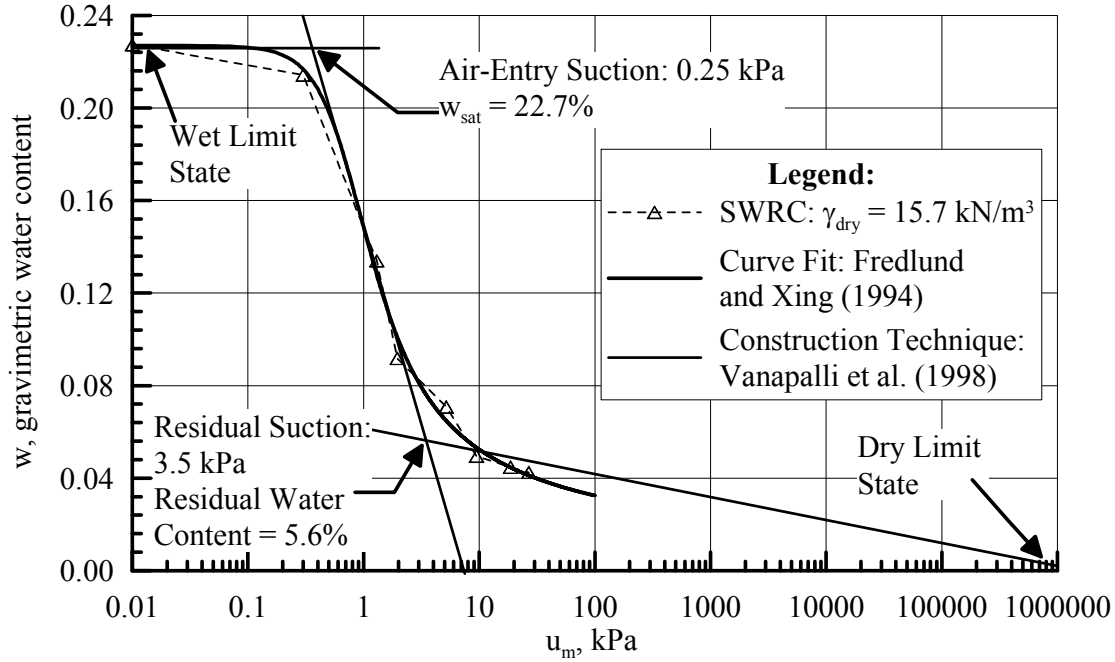

b)

Figure 3.4 w vs u_m for RMS graded sand a) Curve fit to SWRC b) Graphical determination of water retention parameters

Table 3.2 Curve fitting parameters for SWRCs on RMS graded sand

γ_{dry}, kN/m^3	w_{sat}	a_1	n_1	m_1	r^2
14.9	25.3%	0.62	1.58	0.89	0.9999
15.2	24.8%	0.61	1.57	1.10	0.9999
15.5	23.7%	0.60	2.04	0.96	0.9999
15.5	22.9%	0.74	1.83	0.97	0.9997
15.5	20.9%	0.86	3.42	0.62	0.9998
15.6	23.4%	0.63	2.30	0.70	0.9998
15.7	22.7%	0.64	2.34	0.79	0.9999
16.6	18.6%	1.23	1.40	1.14	0.9998

The dry limit state (w = 0%, S = 0%) is defined at 1,000,000 kPa, and the wet limit state is 0 kPa at 100% saturation. According to Vanapalli et al., the residual water content is estimated by a secant line drawn from the dry limit state through a point on the best fit curve one logarithmic cycle past the inflection point. The air-entry pressure, 0.25 kPa, corresponds to a water column height of 25 mm, or the maximum soil height at which RMS graded sand can maintain a saturated state. The residual state, 3.5 kPa, corresponds to a water column height of 350 mm required to evacuate water from enough pores to reach a residual w of approximately 5.6%. It should be noted that the Vanapalli et al. construction provides only an approximation of the residual water content and suction. In this case the residual w estimated by Vanapalli et al. compares reasonably well with w = 4 – 5%, which was found to be the water content to which RMS graded sand drained when moistened in preparation for large scale tests.

3.2.4 Hysteresis in the Soil Water Retention Curve

The relationship between w and u_m is hysteretic, so that different values of (w, u_m) will be measured depending on the initial water content of the soil sample. As

discussed by Klausner (1991), a SWRC developed by desorption will give a higher w at a given u_m than will a SWRC developed by adsorption because of 1) irregularities in the cross-sections of the void passages or the "ink-bottle" effect (Haines, 1930), 2) contact angle being greater in an advancing meniscus than in a receding meniscus, 3) entrapped air, which has a different volume when the soil suction is increasing or decreasing, and 4) thixotropic regain or aging due to the wetting and drying history of the soil. As the measurement of a complete set of hysteretic SWRCs is very difficult, it is desirable to predict them from a known SWRC, which can be measured in the laboratory. Pham et al. (2005) developed equations to represent the limit SWRCs for sands based on a known SWRC and key soil properties. The relations presented by Pham et al. were for a θ_w vs u_m relationship, but are adapted here for a w vs u_m relationship.

Pham et al. (2005) proposed equations for the initial drying curve (IDC), main drying curve (MDC) and main wetting curve (MWC), all three of which can be predicted by knowing either the IDC or MDC. The IDC, MDC, and MWC, respectively, are written as

$$w_1(u_m) = \frac{w_{sat} b_i + c_i (u_m)^{d_i}}{b_i + (u_m)^{d_i}} \tag{3.6}$$

$$w_d(u_m) = \frac{w_u b_i + c_i (u_m)^{d_i}}{b_i + (u_m)^{d_i}} \tag{3.7}$$

$$w_w(u_m) = \frac{w_u b_w + c_w (u_m)^{d_w}}{b_w + (u_m)^{d_w}} \tag{3.8}$$

where w_{sat} = w at the wet limit state on the SWRC (see Fig. 3.4b) and b_i, c_i, and d_i are curve-fitting parameters specific to each SWRC, calculated using Microsoft

Solver. As calculated using Eqn. 3.4, $w_u = 0.88\ w_s$ for RMS graded sand, indicating 12% initial air entrapment in the soil specimen. This value is consistent with the observation by Pham et al. that 10-15% air entrapment by volume is common for soil in wetting. As high pressure was not used to initially saturate the soil, not all air was forced from the voids, possibly causing the initial air entrapment in the soil specimens.

As presented by Pham et al. (2005), the curve fitting parameters b_w, c_w, and d_w used in Eqn. 3.8 are calculated using the relations

$$c_w = c_i \tag{3.9}$$

$$b_w = \left[\frac{b_i}{\left(10^{D_{SL}}\right)^{d_i}} \right]^{\frac{1}{R_{SL}}} \tag{3.10}$$

$$d_w = \frac{d_i}{R_{SL}} \tag{3.11}$$

where D_{SL} and R_{SL} are the distance and slope ratio between the MDC and MWC on a semilogarithmic scale, defined as 0.35 and 1.0, respectively, for compacted sand.

Figure 3.5 shows a plot of w vs u_m, comparing Tempe cell and tensiometer measurements for partially saturated RMS graded sand at $\gamma_{dry} = 15.7$ kN/m^3 with Eqns. 3.6, 3.7 and 3.8. The MDC (Eqn. 3.7) shown in the figure was calculated using Microsoft Solver to fit the data obtained with the Tempe cell, and the IDC (3.6) and MWC (3.8) were calculated from Eqn. 3.7 using the equations presented above. The data obtained with the tensiometers are the same data shown in Table 3.1 and Fig. 3.3a, and plots closely to the MWC.

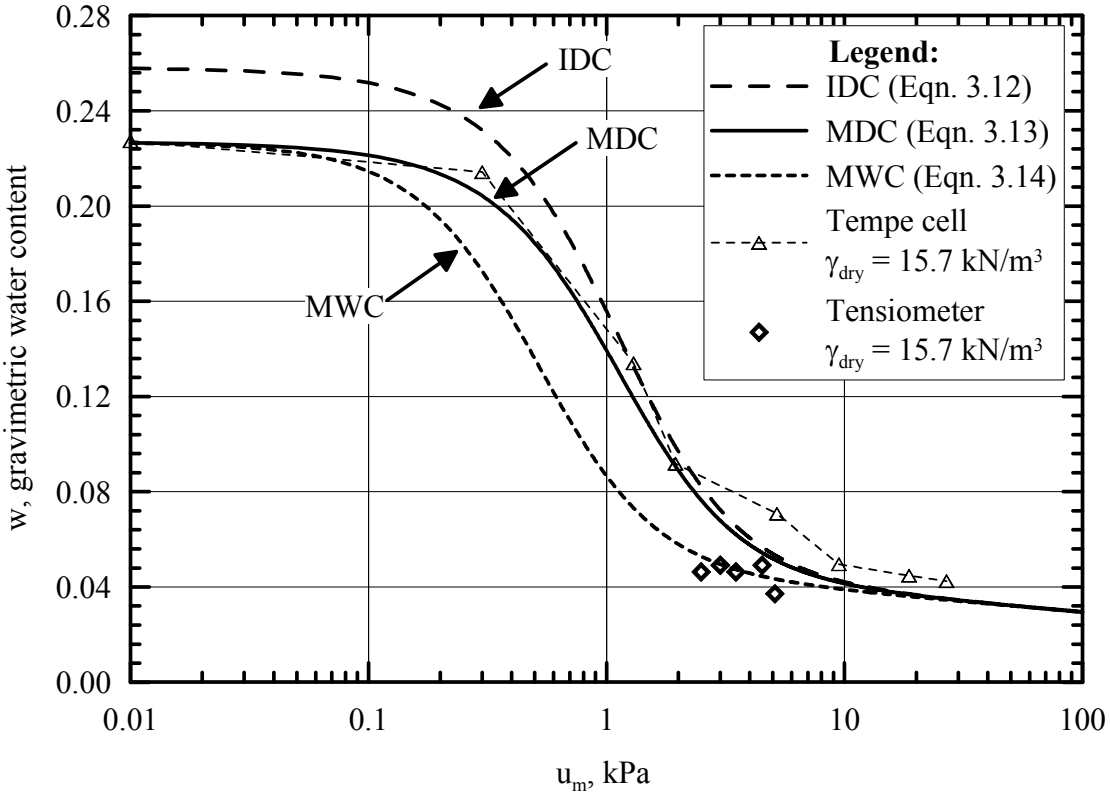

Figure 3.5 w vs u_m for RMS graded sand compared with boundary SWRCs and tensiometer measurements

As explained previously, tensiometers operate by equilibrating the vacuum pressure in the airspace at the top of the water column with the matric suction present in the soil. To induce a vacuum pressure in the airspace, water must be transported from the tensiometer across the porous cup into the surrounding soil, with the soil providing the matric potential necessary for the water transport. This suction of water is analogous to the process by which an SWRC is obtained by adsorption, where water is also transported into the soil by suction. The MWC in Fig. 3.5 is the idealized representation of an adsorption SWRC, and lines up very well with the (w, u_m) data obtained by the tensiometer. This indicates consistency between (w, u_m) relationships obtained by the tensiometer and the Tempe cell.

3.3 Direct Shear Relationships for Partially Saturated Sand

Figure 3.6a shows DS and plane strain Mohr-Coulomb stress parameters for partially saturated sand. The DS and plane strain friction angles at peak state, ϕ_{ds-p} and ϕ_{ps-p}, account for cohesion, according to the following expressions:

$$\tan\phi_{ds-p} = \frac{\tau_p - c_{ds}}{\sigma_N} \tag{3.12}$$

$$\tan\phi_{ps-p} = \frac{\tau_{ps} - c_{ps}}{\sigma_{ps}} \tag{3.13}$$

It should be noted that ϕ_{ds-p} is a total stress parameter, and that σ_N, τ_p, σ_{ps}, and τ_{ps} are expressed in terms of total stress. In the DS tests on partially saturated soil, pore water pressure was not measured explicitly. The dilation angle, ψ_p, is defined from DS tests on partially saturated sand in the same way as for dry sand.

As discussed in Chapter 2, it has been shown for DS tests on dry sand that there is co-axiality of incremental strain and stress at peak strength, meaning that the principal axes of stress and incremental strain coincide (see Figure 2.8a and b). Moreover, the horizontal plane of the DS device for both dry and partially saturated sand is a direction of zero linear incremental strain (zero extension).

It is assumed that the co-axiality of incremental strain and stress applies for the partially saturated sand of this study. Given the low values of suction measured for the test sand, it is likely that the relative orientations of stress and incremental strain are not materially different than those for dry sand. Moreover, it will be shown later

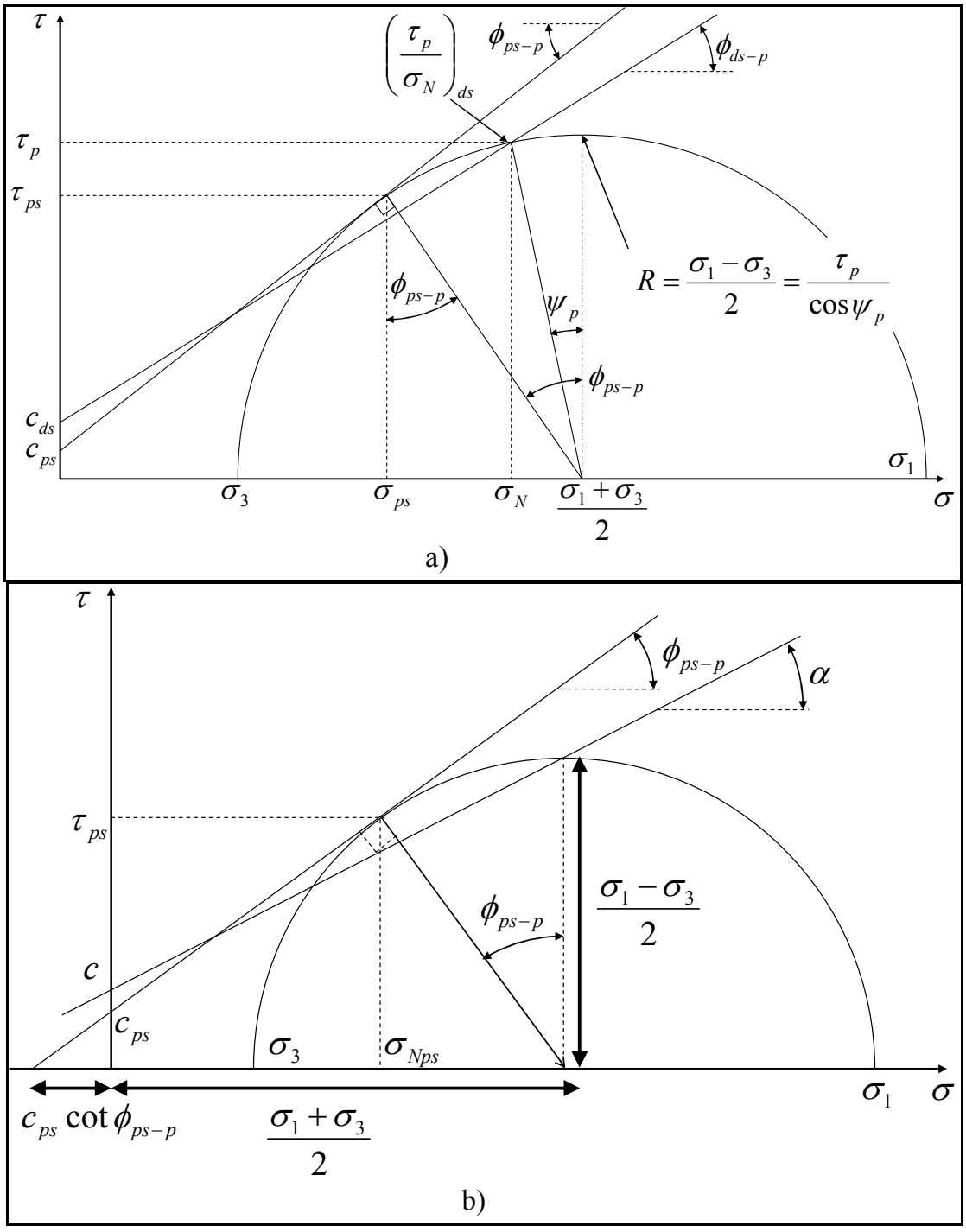

Figure 3.6 Mohr coulomb stress parameters for a c - ϕ material (Not to scale) a) Representation of DS parameters b) Regression through top of Mohr circle

that strength and volume change characteristics evaluated on the premise of coaxiality provide results that support a rational mechanics-based explanation of observed behavior and are consistent on a comparative basis with the properties of dry sand.

Given that the DS test failure plane coincides with zero extension and that stress and incremental strain are co-axial, an equation can be derived (see Appendix A) that is similar to Eqn. 2.4 in Chapter 2, of the form

$$\sin\phi_{ps-p} = \frac{\dfrac{\tau_p}{\sigma_N}}{\left[1 + \dfrac{\tau_p}{\sigma_N}\tan\psi_p + \dfrac{c_{ps}\cot\phi_{ps}}{\sigma_N}\right]\cos\psi_p} \tag{3.14}$$

It should be noted that Eqn. 3.20 reduces to Eqn. 2.4 in Chapter 2 for zero cohesion, as is the case for dry sand.

Figure 3.6a shows τ vs σ for a partially saturated sand with c and ϕ. From this figure it can be seen that the center and top of the Mohr circle of stress is related to $\left(\tau_p / \sigma_N\right)$ through ψ_p, such that

$$\frac{\sigma_1 + \sigma_3}{2} = \sigma_N + \tau_p \tan\psi_p \tag{3.15}$$

$$\frac{\sigma_1 - \sigma_3}{2} = \frac{\tau_p}{\cos\psi_p} \tag{3.16}$$

Therefore, we can construct the Mohr circle of stress at peak strength using Eqns. 3.15 and 3.16 for the DS data. If we develop a linear regression for $\left(\sigma_1 + \sigma_3\right)/2$ (the center of the Mohr circle) and $\left(\sigma_1 - \sigma_3\right)/2$ (the radius of the Mohr circle) from the DS data,

we get a plot with intercept = c and slope = tanα, as shown in Fig. 3.6b. The plane strain failure envelope for maximum obliquity is also shown in Fig. 3.6b. It can be shown by simple trigonometry that

$$\frac{\sigma_1 - \sigma_3}{2} = c + \frac{\sigma_1 + \sigma_3}{2}\tan\alpha \tag{3.17}$$

$$\frac{\sigma_1 - \sigma_3}{2} = c_{ps}\cos\phi_{ps-p} + \frac{\sigma_1 + \sigma_3}{2}\sin\phi_{ps-p} \tag{3.18}$$

The radius of the Mohr circle, $(\sigma_1 - \sigma_3)/2$, is simultaneously satisfied by Eqns. 3.17 and 3.18 if and only if

$$c_{ps} = \frac{c}{\cos\phi_{ps-p}} \tag{3.19}$$

$$\phi_{ps-p} = \sin^{-1}(\tan\alpha) \tag{3.20}$$

Hence, Eqns. 3.19 and 3.20 give the parameters that represent the plain strain failure envelope from data plotted in accordance with Eqns. 3.15 and 3.16.

3.4 Direct Shear Strength Envelopes for Partially Saturated Sand

Figure 3.7 shows plots of τ_p vs σ_N at average γ_{dry} = 15.8 and 16.5 kN/m^3. The data show that $\phi_{ds\text{-}p}$ and c_{ds} for partially saturated RMS graded sand at w = 4 – 5% is consistent over σ_N of 2.1 to 98.9 kPa. Both $\phi_{ds\text{-}p}$ and c_{ds} increase as γ_{dry} increases from 15.8 to 16.5 kN/m^3. Figure 3.8 shows plots of τ vs σ_N at large displacement at average γ_{dry} = 15.8 and 16.5 kN/m^3. The data show that $\phi_{ds\text{-}ld}$ is consistent over σ_N = 2.1 to 98.9 kPa, and c_{ds} is not significantly different from zero at large displacement. Both

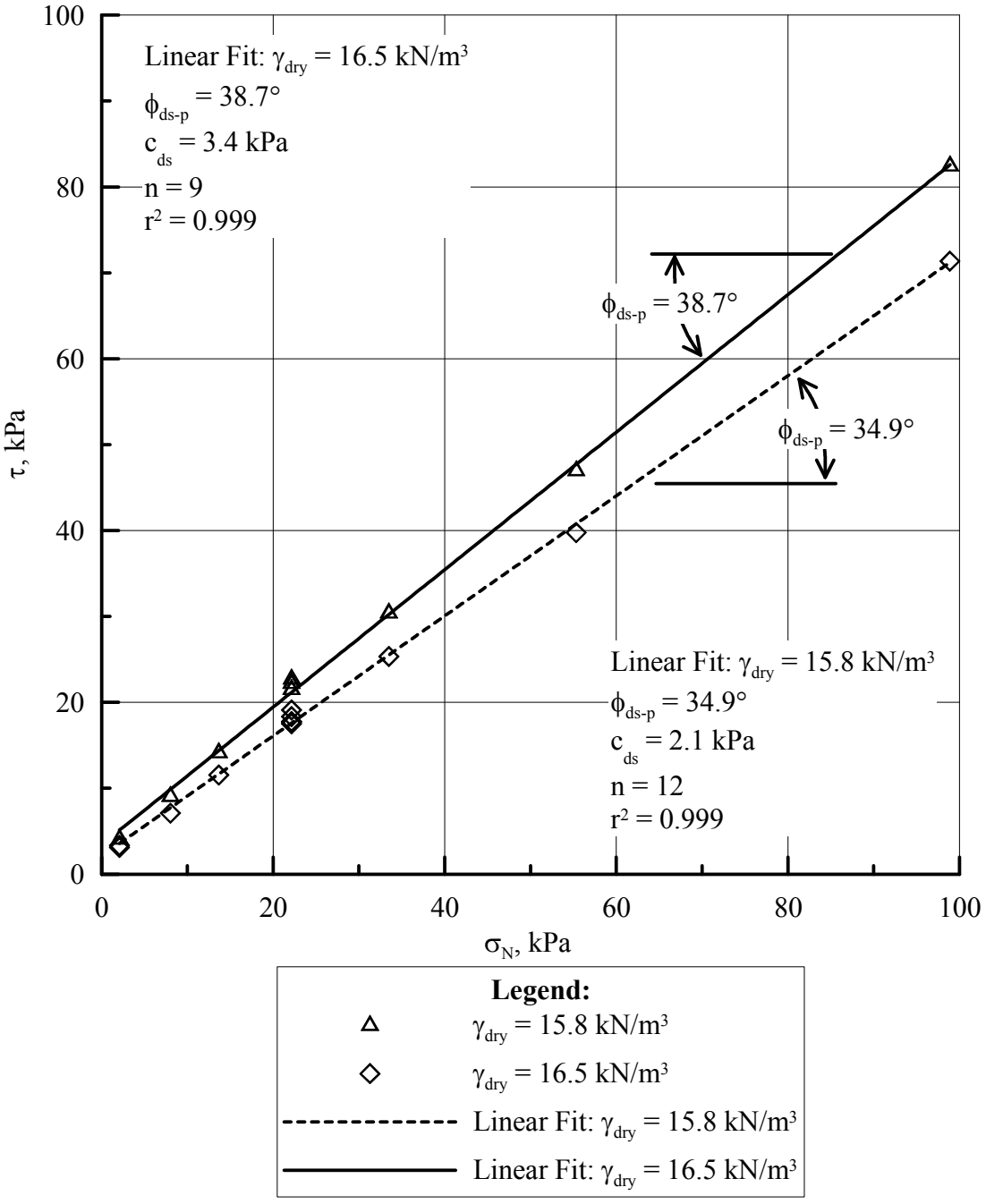

Figure 3.7 τ vs σ_N for partially saturated RMS graded sand at w = 4 – 5% at peak strength

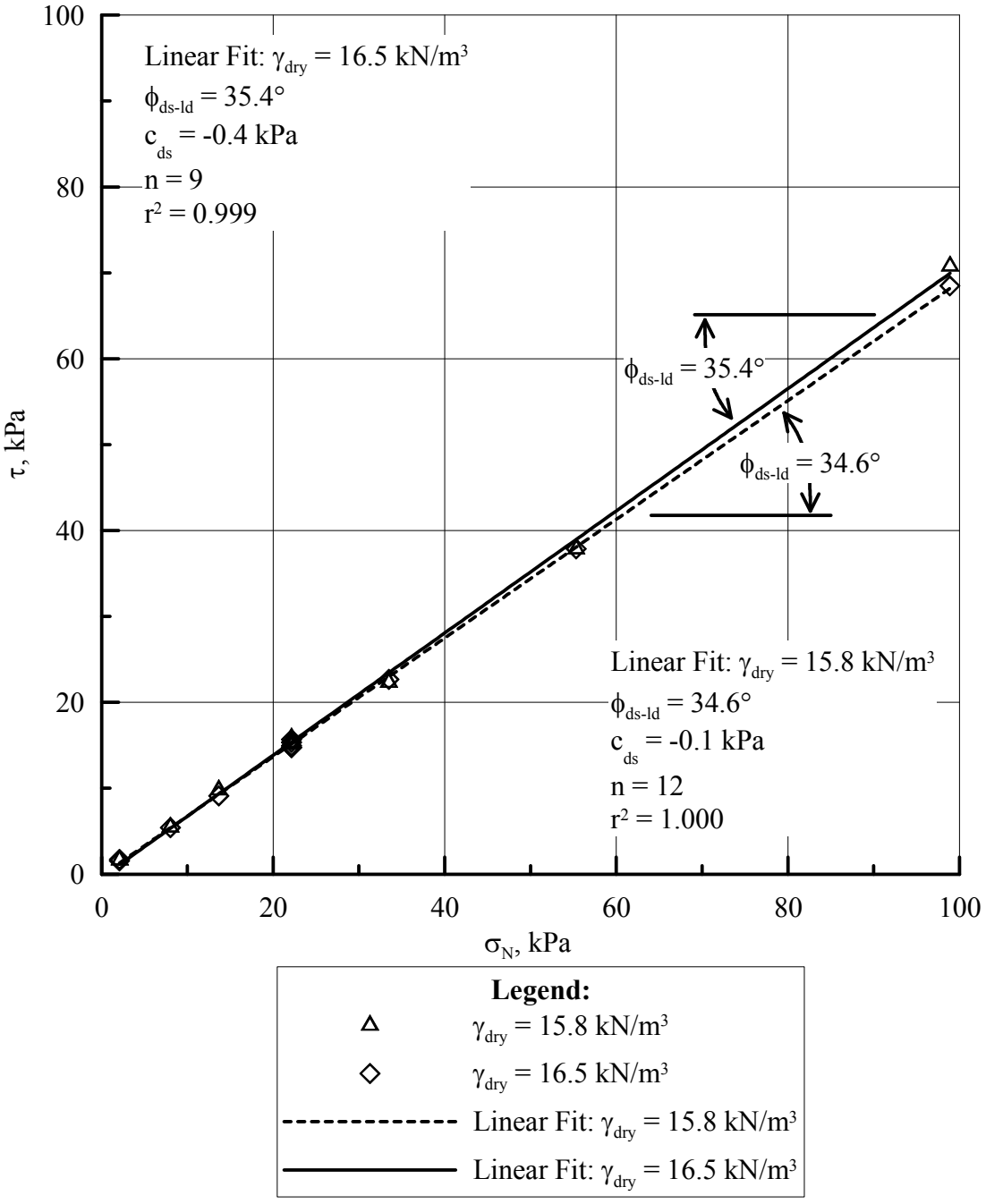

Figure 3.8 τ vs σ_N for partially saturated RMS graded sand at w = 4 – 5% at large displacement

$\phi_{ds\text{-}ld}$ and c_{ds} do not appear to be influenced by a change in γ_{dry} from 15.8 to 16.5 kN/m^3. If c_{ds} is forced to be zero in Fig. 3.8, the slope of the DS envelope is virtually unchanged, at 34.5 and 35.2°, respectively, at average γ_{dry} = 15.8 and 16.5 kN/m^3.

Figure 3.9 shows plots of $(\sigma_1 - \sigma_3)/2$ vs $(\sigma_1 + \sigma_3)/2$ for partially saturated RMS graded sand with γ_{dry} = 15.8 kN/m^3. A linear regression fit to the data gives a line with a slope of α = 34.3° and an intercept of c = 0.9 kPa. Using Eqns. 3.19 and 3.20, the plane strain envelope at maximum obliquity can be calculated from c and α, and is also plotted on Fig. 3.9. This line has $\phi_{ps\text{-}p}$ = 43.0° and c_{ps} = 1.2 kPa.

Figure 3.10 shows plots of $(\sigma_1 - \sigma_3)/2$ vs $(\sigma_1 + \sigma_3)/2$ for partially saturated RMS graded sand with γ_{dry} = 16.5 kN/m^3. A linear regression fit to the data gives a line with a slope of α = 36.1° and an intercept of c = 1.7 kPa. Again using Eqns. 3.19 and 3.20, the plane strain envelope at maximum obliquity is calculated from c and α, and is plotted on Fig. 3.10. This line has $\phi_{ps\text{-}p}$ = 46.7° and c_{ps} = 2.4 kPa.

Also shown on Figs 3.9 and 3.10 are the Mohr's circles corresponding to the DS data shown in Fig. 3.8. As can be seen in the figures, the α – c envelope is a good fit to the ($(\sigma_1 - \sigma_3)/2$, $(\sigma_1 + \sigma_3)/2$) data, and the $\phi_{ps\text{-}p}$ and c_{ps} envelope is a good approximation for the plane strain envelope at maximum obliquity, as it passes closely to the tangent point of each Mohr's circle. As with $\phi_{ds\text{-}p}$ and c_{ds}, $\phi_{ps\text{-}p}$ and c_{ps} are assumed to be constant over σ_N = 2.1 to 98.9 kPa.

Figure 3.11a shows $\phi_{ds\text{-}p}$ vs σ_N for partially saturated RMS graded sand at γ_{dry} = 15.8 kN/m^3. The $\phi_{ds\text{-}p}$ component of a ($\phi_{ds\text{-}p}$, σ_N) pair represents the slope of a line

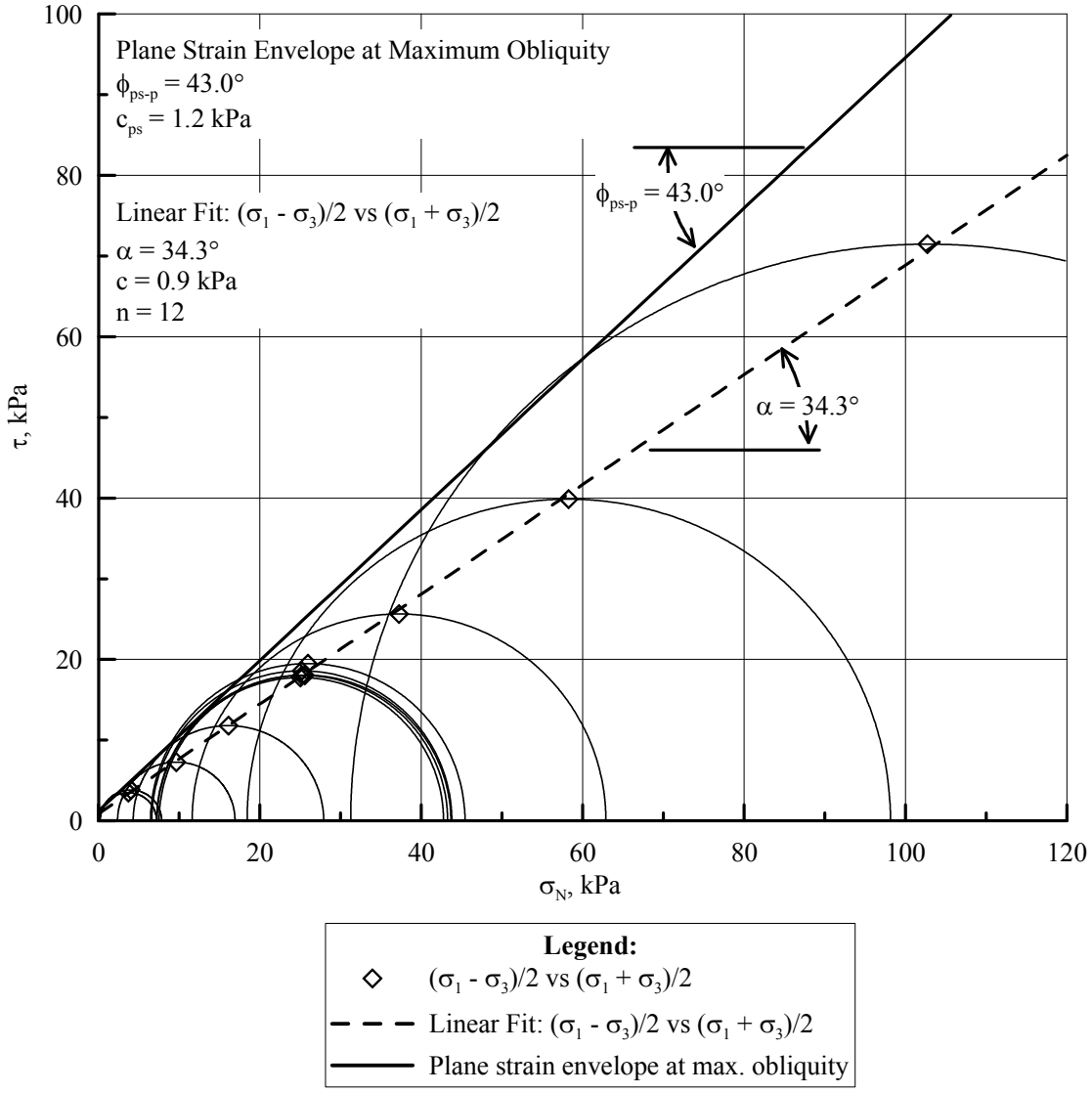

Figure 3.9 τ vs σ_N for partially saturated RMS graded sand at peak strength, γ_{dry}= 15.8 kN/m^3

starting at the y-intercept, c_{ds} = 2.1 kPa, and drawn through a given (τ_p, σ_N) point in Fig. 3.7. The line ϕ_{ds-p} = 34.9° represents the slope of the linear regression fit to the (τ_p, σ_N) data in Fig. 3.7. As can be seen, the (ϕ_{ds-p}, σ_N) data are well represented by the ϕ_{ds-p} = 34.9° line for σ_N > 15 kPa, but fall below the line below 15 kPa. Figure

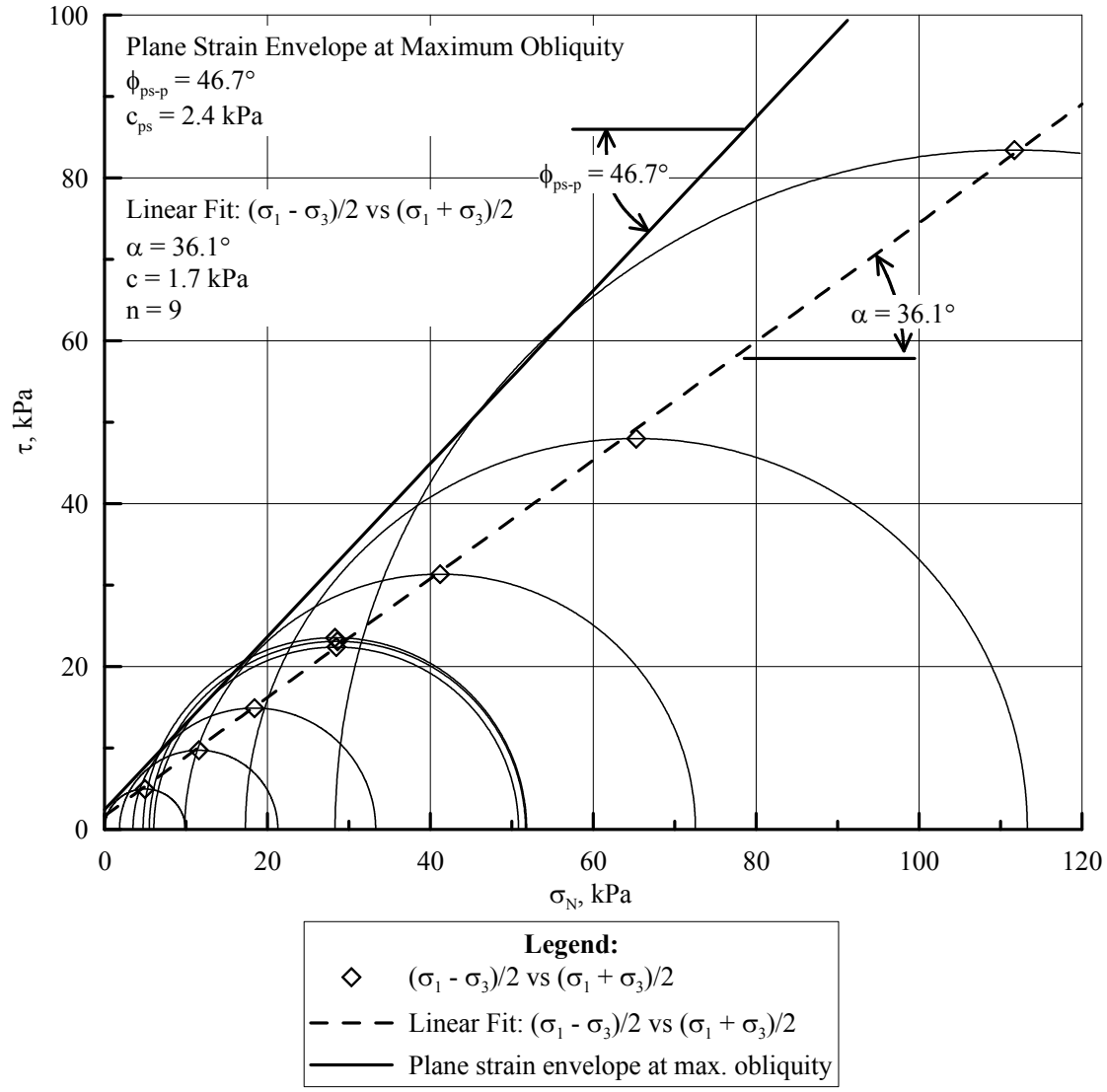

Figure 3.10 τ vs σ_N for partially saturated RMS graded sand at peak strength, γ_{dry}= 16.5 kN/m^3

3.11a also shows ϕ_{ds-p} vs σ_N for partially saturated RMS graded sand at γ_{dry} = 16.5 kN/m^3. The ϕ_{ds-p} component of a (ϕ_{ds-p}, σ_N) pair assumes c_{ds} = 3.4 kPa, and the ϕ_{ds-p} = 38.7° line represents the slope of the linear regression fit to the (τ_p, σ_N) data, both as presented for γ_{dry} = 16.5 kN/m^3 in Fig. 3.7. As with the lower γ_{dry}, the (ϕ_{ds-p}, σ_N) data

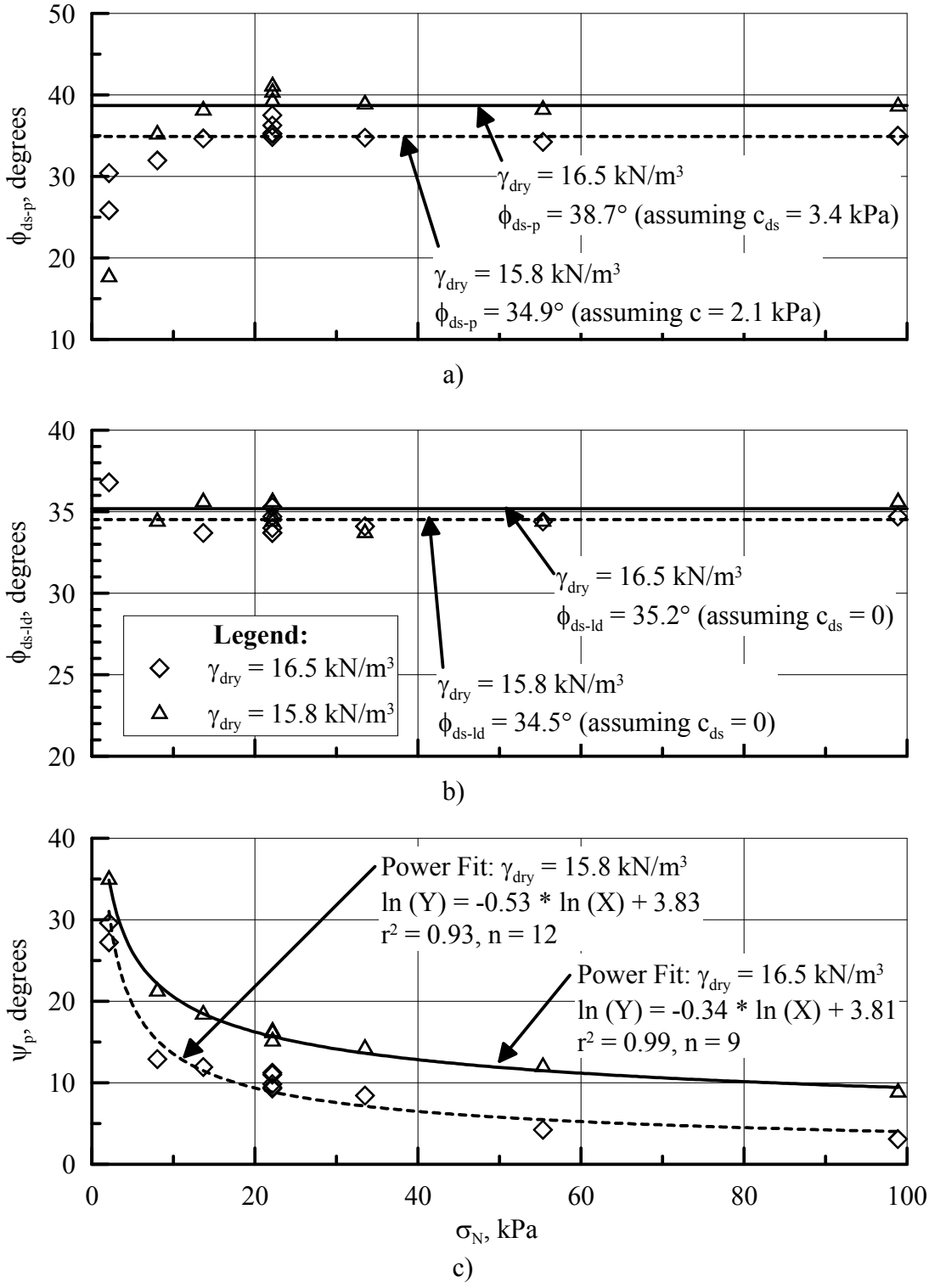

Figure 3.11 Strength parameters as a function of σ_N a) ϕ_{ds-p} vs σ_N b) ϕ_{ds-ld} vs σ_N c) ψ_p vs σ_N

are well represented by the $\phi_{ds\text{-}p} = 38.7°$ line for $\sigma_N > 15$ kPa, but fall below the line for $\sigma_N < 15$ kPa.

Figure 3.11b shows $\phi_{ds\text{-}ld}$ vs σ_N for partially saturated RMS graded sand at $\gamma_{dry} = 15.8$ kN/m^3. The $\phi_{ds\text{-}ld}$ component of a ($\phi_{ds\text{-}ld}$, σ_N) pair represents the slope of a line starting at (0, 0) and drawn through a given (τ, σ_N) point in Fig. 3.8. The line $\phi_{ds\text{-}ld} = 34.5°$ represents the slope of the linear regression fit to the (τ, σ_N) data in Fig. 3.8 and forced to have a cohesion of $c_{ds} = 0.0$ kPa. Figure 3.11b also shows $\phi_{ds\text{-}ld}$ vs σ_N for partially saturated RMS graded sand at $\gamma_{dry} = 16.5$ kN/m^3. The $\phi_{ds\text{-}ld}$ component of a ($\phi_{ds\text{-}ld}$, σ_N) pair represents the slope of a line starting at (0, 0) and drawn through a given (τ, σ_N) point in Fig. 3.8. The line $\phi_{ds\text{-}ld} = 35.2°$ represents the slope of the linear regression fit to the (τ, σ_N) data at $\gamma_{dry} = 16.5$ kN/m^3 in Fig. 3.8 and forced to have a cohesion of $c_{ds} = 0.0$ kPa. As can be seen in Fig. 3.11b, the ($\phi_{ds\text{-}ld}$, σ_N) data are well represented by lines of constant $\phi_{ds\text{-}ld}$ at all levels of σ_N, and there is very little difference between $\phi_{ds\text{-}ld}$ at the two different levels of γ_{dry}.

Figure 3.11c shows ψ_p vs σ_N for partially saturated RMS graded sand at $\gamma_{dry} = 15.8$ kN/m^3 and at $\gamma_{dry} = 16.5$ kN/m^3. As can be seen, ψ_p decreases from 30° to 5° for the lower level of γ_{dry} as σ_N increases from 2.1 to 98.9 kPa. The (ψ_p, σ_N) data is well represented by a Power regression ($r^2 = 0.93$), indicating that the data will appear to decrease linearly with increasing σ_N when plotted on a log-log scale. For the higher level of γ_{dry}, ψ_p decreases from 35° to 10° as σ_N increases from 2.1 to 98.9 kPa. A Power curve regression fit to the (ψ_p, σ_N) data again shows a strong $r^2 = 0.99$.

3.5 Direct Shear Strength and Dilation Characteristics for Partially Saturated RMS Graded Sand Using 100 mm Box

Figure 3.12 plots $\phi_{ds\text{-}p}$, $\phi_{ds\text{-}ld}$, and ψ_p vs γ_{dry} for partially saturated sand at w = 4 – 5%, and σ_N = 22 kPa. All tests for this figure were performed using the 100mm box with a 1 mm gap and no edging, as discussed in Chapter 2. As noted in the figure, ($\phi_{ds\text{-}p}$, γ_{dry}) data are plotted assuming c_{ds} = 2.1 kPa for γ_{dry} < 16.0 kN/m^3 and c_{ds} = 3.4 kPa for γ_{dry} > 16.0 kN/m^3. There is a strong relationship between $\phi_{ds\text{-}p}$ and γ_{dry} (r^2 = 0.88) and the linear regression is plotted through the data. ($\phi_{ds\text{-}ld}$, γ_{dry}) data are plotted assuming c_{ds} = 0 kPa for all γ_{dry}, as shown in Fig. 3.8. There is no statistically significant relationship between $\phi_{ds\text{-}ld}$ and γ_{dry} (r^2 = 0.13 for a linear regression, not shown in Fig. 3.12) so line is drawn through the data at $\phi_{ds\text{-}ld}$ = 34.6°, representing the average value of $\phi_{ds\text{-}ld}$ for the 13 ($\phi_{ds\text{-}ld}$, γ_{dry}) data points shown in the figure. There is a strong linear relationship between ψ_p and γ_{dry} (r^2 = 0.91), and the regression and (ψ_p, γ_{dry}) data points are plotted in Fig. 3.12.

Modifying the flow rules, which were presented in Chapter 2, to account for the additional cohesion present in partially saturated RMS graded sand results in the equivalent flow rules for partially saturated sand, as follows. For the flow rule equivalent to that proposed by Taylor (1948):

$$\tan\phi_{ds} + \frac{c_{ds}}{\sigma_N} = \sin(\phi_{crit}) + \tan\psi \tag{3.21}$$

For the flow rule equivalent to that proposed by Rowe (1962, 1969):

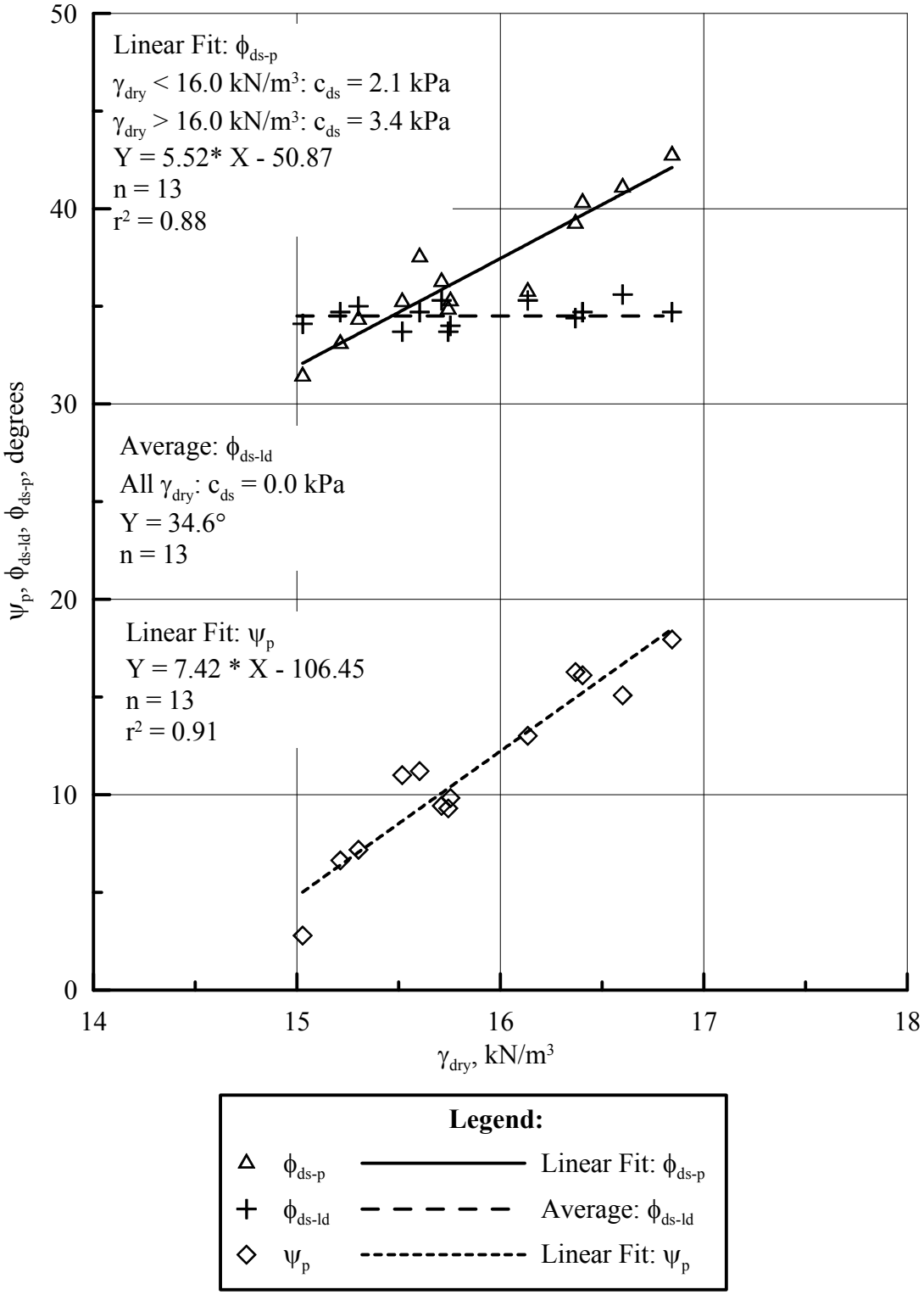

Figure 3.12 ϕ_{ds-p}, ϕ_{ds-ld} and ψ_p vs γ_{dry} for partially saturated RMS graded sand, σ_N = 22 kPa

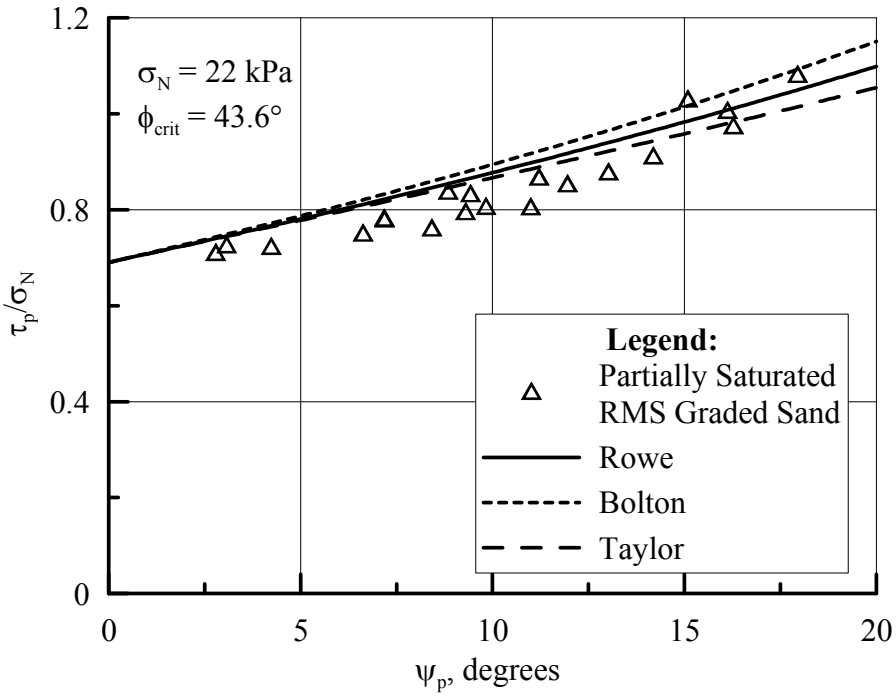

Figure 3.13 τ_p/σ_N vs ψ_p and equivalent flow rules for partially saturated RMS graded sand

$$\tan\phi_{ds} + \frac{c_{ds}}{\sigma_N} = \frac{\sin(\phi_{crit}) + \sin\psi}{\cos\psi} \tag{3.22}$$

For the flow rule equivalent to that proposed by Bolton (1986):

$$\tan\phi_{ds} + \frac{c_{ds}}{\sigma_N} = \frac{\cos\psi \sin(\phi_{crit} + 0.8\psi)}{1 - \sin\psi(\sin\phi_{crit} + 0.8\psi)} \tag{3.23}$$

DS data, represented in terms of τ_p/σ_N, are plotted vs ψ_p in Fig. 3.15. Equivalent Taylor, Rowe, and Bolton flow rules are also plotted in the figure. Since no cohesion was observed in DS tests for partially saturated RMS graded sand at large displacements, ϕ_{crit} can be calculated from $\phi_{ds\text{-}ld}$ using Eqn. 2.5 in Chapter 2 for use in Eqns. 3.21, 3.22 and 3.23. Selecting the average $\phi_{ds\text{-}ld}$ = 34.6° from Fig. 3.12, ϕ_{crit} =

43.6° using Eqn. 2.5 from Chapter 2. As can be seen in Fig. 3.13, the data corresponds well with the flow rules for partially saturated RMS graded sand at σ_N = 22 kPa.

3.6 Partially Saturated Sand-Polymer Interface Direct Shear Behavior using 60 mm Box

O'Rourke et al. (1990) and Trautmann and O'Rourke (1983) found that the peak direct shear interface friction angle, δ_{SI}, for a dry sand-polymer interface was linearly related to $\phi'_{ds\text{-}p}$, and could be defined based on the soil γ_{dry} and the hardness of the polymer defining the interface, using the relation

$$\tan \delta_{SI} = \frac{\tau'_{SI}}{\sigma'_N} \tag{3.24}$$

where all shear is assumed to take place along the interface, and cohesion is neglected. O'Rourke et al. (1990) related the peak direct shear interface friction angle to the Shore D Hardness, H_D, of the interface polymer using the equation

$$\frac{\delta_{SI}}{\phi'_{ds-p}} = -0.0088 H_D + 1.15 \tag{3.25}$$

Figure 3.14 shows plots of $\phi_{ds\text{-}p}$ vs γ_{dry} for partially saturated RMS graded sand and δ_{SI} vs γ_{dry} for a partially saturated RMS graded sand – polymer interface. All tests were performed using the 60 mm DS box in the conventional DS apparatus (see Chapter 2) with a polymer interface specimen bonded to a plywood insert in the lower

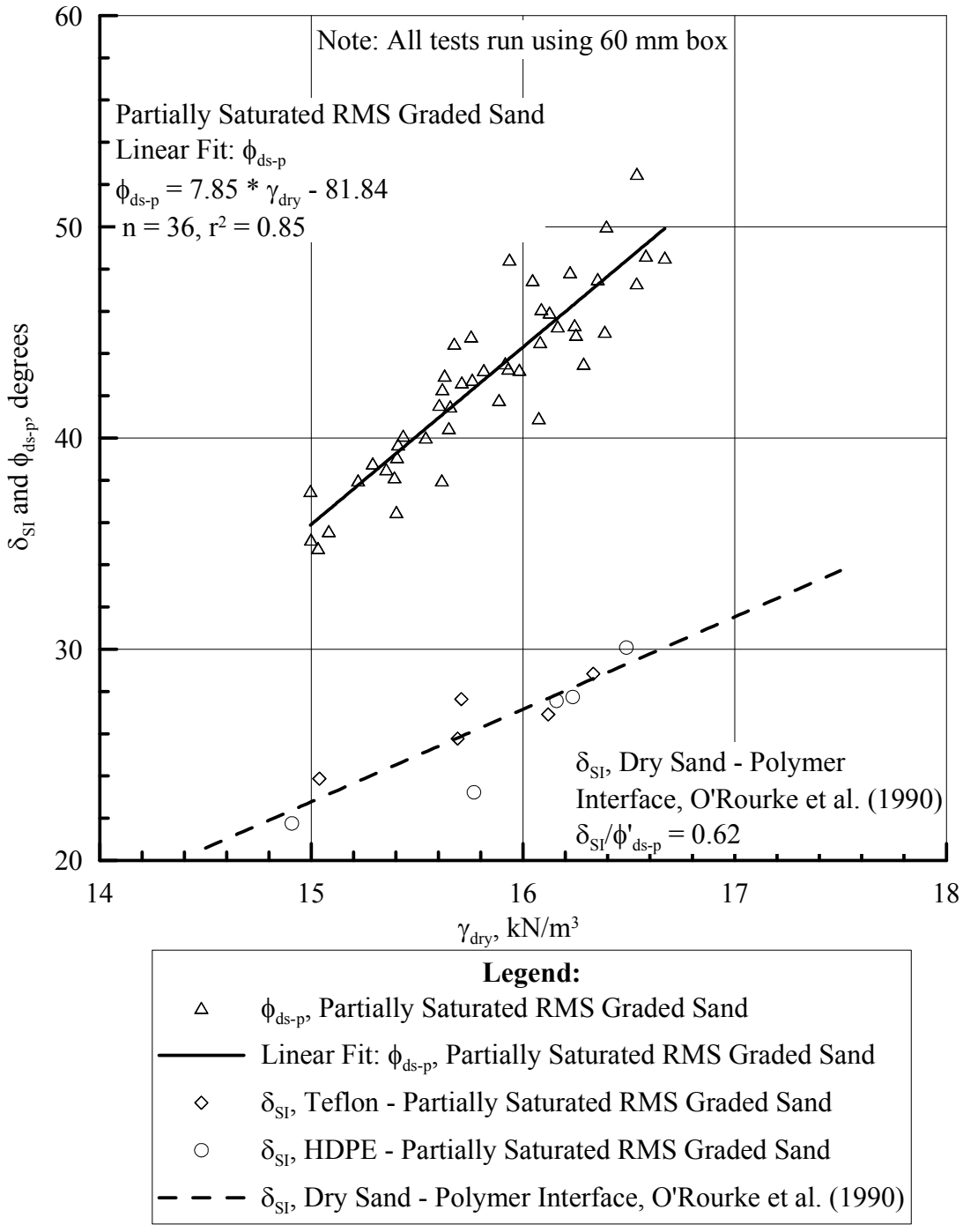

Figure 3.14 Plot of ϕ_{ds-p} and δ_{SI} vs γ_{dry} for a partially saturated RMS graded sand - polymer interface

DS frame. The interfaces tested, Teflon and HDPE, were found to have Shore D Hardness values between 58 and 60, corresponding to $\delta_{SI}/\phi'_{ds\text{-}p}$ values of 0.64 and 0.62. The Teflon specimen used was identical to a thin covering used to protect tactile force sensors installed on pipes during large scale tests from damage due to shear, puncture, and moisture damage (See Chapter 5). The HDPE specimen was one of the specimens used in the O'Rourke et al. (1990) study, and was milled from an HDPE pipeline similar to the pipes used in the current large scale testing, lending continuity to the two interface testing programs. A line representing $\delta_{SI}/\phi'_{ds\text{-}p} = 0.62$ is plotted in Figure 3.14, showing that the O'Rourke et al. (1990) relationship is indistinguishable from data measured for a partially saturated RMS graded sand – polymer interface using HDPE and Teflon.

3.7 Comparison of Dry and Partially Saturated RMS Graded Sand

Figures 3.15 and 3.16 show τ_p vs τ'_p and σ_N vs σ'_N for dry and partially saturated RMS graded sand at average γ_{dry} = 15.8 and 16.5 kN/m^3, respectively. The data presented have standard deviations of γ_{dry} = 0.12 – 0.28 kN/m^3. For dry sand, w = 0%, and for partially saturated sand, w = 3.9% - 5.0%. All tests were prepared using the same method with the same applied energy, and thus the same soil fabric was achieved (see Chapter 2 for description of DS specimen preparation procedure). There was some variation of soil γ_{dry} over the range of applied σ_N due to vertical compression of the soil specimen when normal load was applied. For tests at the lowest values of σ_N, there was little compression of the sample compared to tests at the highest values of σ_N. The variation in γ_{dry} was 5%. All tests were performed using the 100 mm box with a 1 mm gap and no edging.

Fig. 3.15 shows that at an average γ_{dry} = 15.8 kN/m^3, partially saturated RMS graded sand has a value of c_{ds} that is 2.1 kPa and a value of $\phi_{ds\text{-}p}$ that is 1.4° greater than dry RMS graded sand. Fig. 3.16 shows that at an average γ_{dry} = 16.5 kN/m^3, c_{ds} is 3.4 kPa greater and $\phi_{ds\text{-}p}$ is 2.4° greater for partially saturated RMS graded sand than for dry RMS graded sand.

Figure 3.17 shows strength and dilation parameters vs γ_{dry} for dry and partially saturated RMS graded sand. All data in this figure have been shown previously in this chapter or in Chapter 2, but are grouped here for convenience. It can be seen that at a given γ_{dry}, partially saturated RMS graded sand has an approximate 10° and 5° increase in $\phi_{ds\text{-}p}$ and ψ_p, respectively, in comparison to dry RMS graded sand.

Chapter 2 presented flow rules, used to define relationships between different strength and dilation parameters for dry sand (see Eqns. 2.7 – 2.9). Previously in Chapter 3, equivalent flow rules were proposed for partially saturated sand (see Eqns. 3.21 – 3.23). To define a relationship between dry and partially saturated sand, the Taylor flow rule is considered (given by Eqn. 2.7 in Chapter 2 for dry sand and Eqn. 3.21 in the current chapter for partially saturated sand). Assuming that $[\tau/\sigma_N]_{p.sat.}$ and $[\tau/\sigma_N]_{dry}$ are the stress ratios representing the total strength of a dry and partially saturated sand, respectively, Eqns. 2.7 and 3.21 can be written at peak state, respectively, as

$$\left[\frac{\tau_p}{\sigma_N}\right]_{dry} = \tan\phi'_{ds-p} = \sin\phi'_{crit} + \tan\left(\psi_p\right)_{dry} \tag{3.26}$$

$$\left[\frac{\tau_p}{\sigma_N}\right]_{p.sat.} = \tan\phi_{ds-p} + \frac{c_{ds}}{\sigma_N} = \sin\phi_{crit} + \tan\left(\psi_p\right)_{p.sat.} \tag{3.27}$$

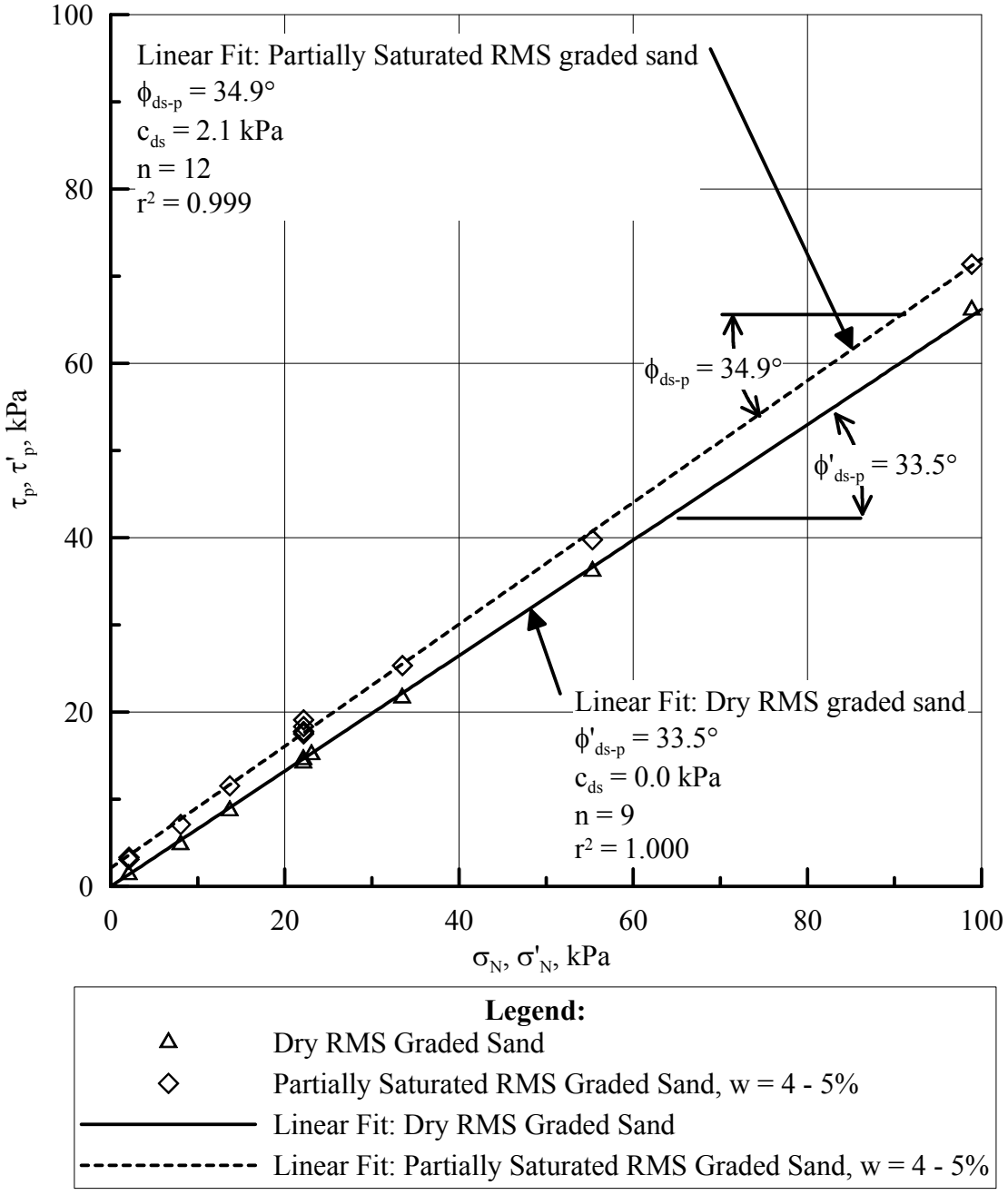

Figure 3.15 τ_p vs σ_N and τ'_p vs σ'_N for dry and partially saturated RMS graded sand at γ_{dry} = 15.8 kN/m^3

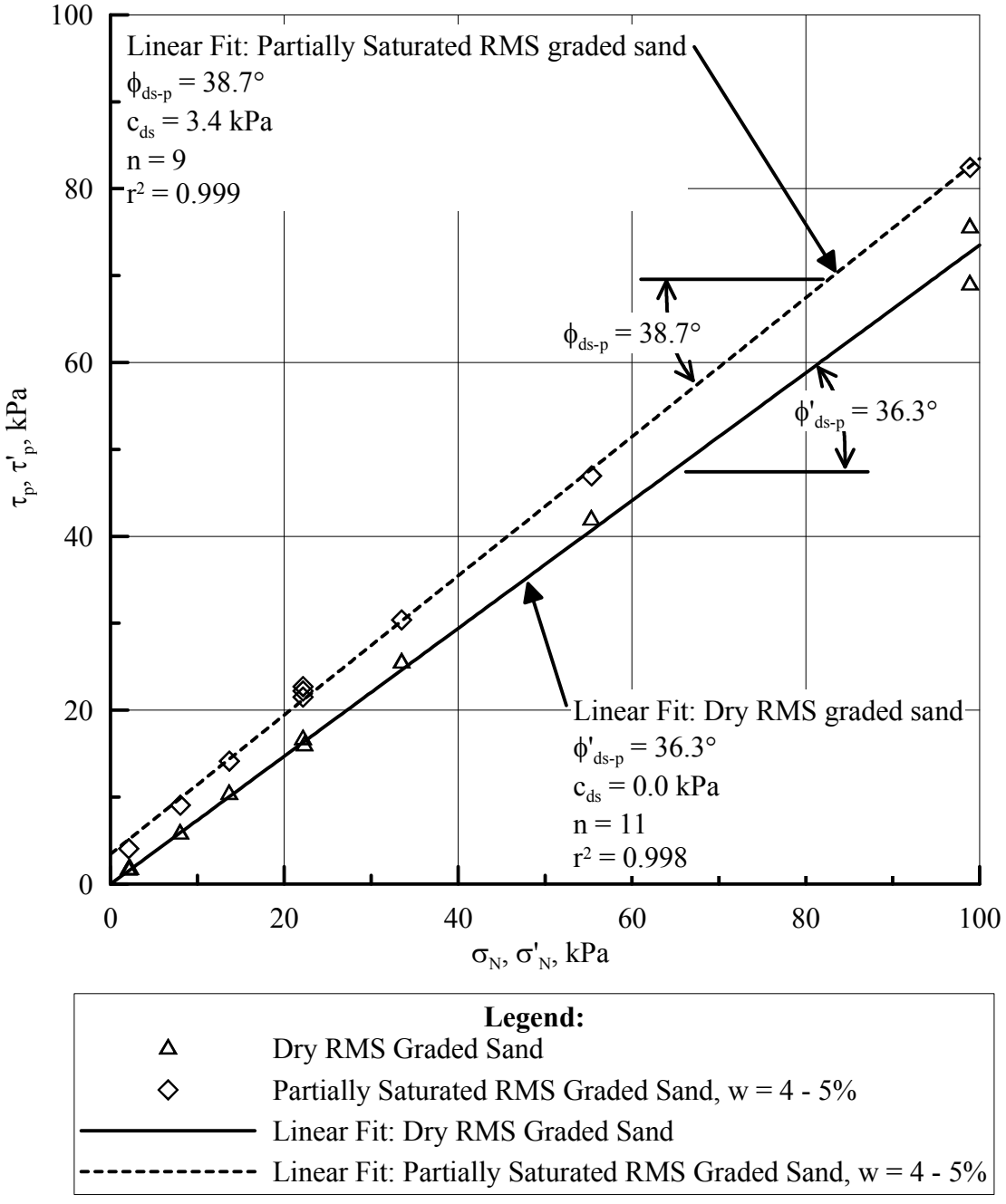

Figure 3.16 τ_p vs σ_N and τ'_p vs σ'_N for dry and partially saturated RMS graded sand at γ_{dry} = 16.5 kN/m^3

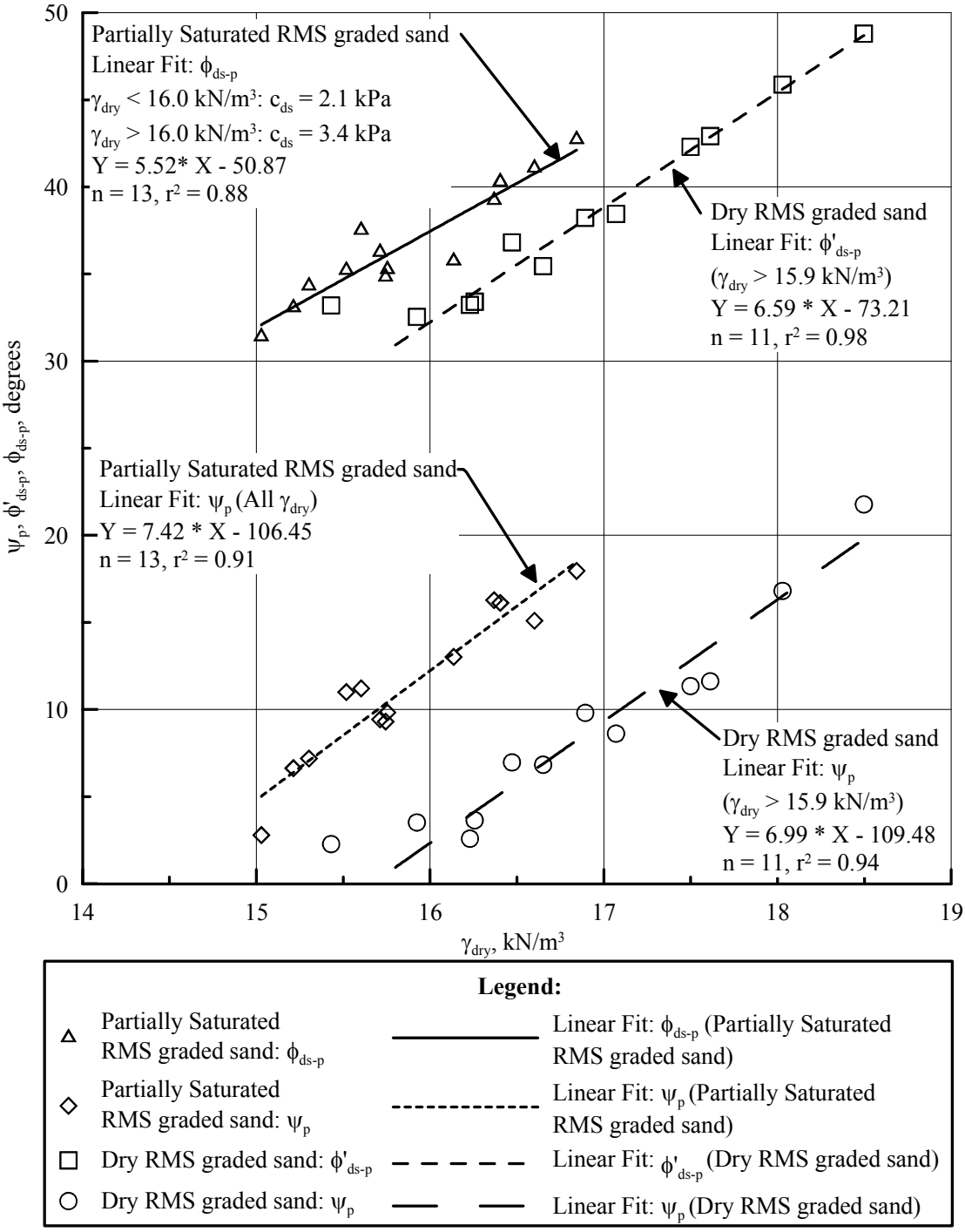

Figure 3.17 ψ_p, ϕ'_{ds-p}, ϕ_{ds-p} vs γ_{dry} for dry and partially saturated RMS graded sand

Table 3.3 Comparison of tangents of DS strength parameters for dry and partially saturated RMS graded sand

γ_{dry}, kN/m^3	Dry RMS Graded Sand	Partially Saturated RMS Graded Sand	Difference, (P.Sat. - Dry)
	$\tan\phi'_{ds\text{-}p} - \sin\phi'_{crit}$	$\tan\phi_{ds\text{-}p} - \sin\phi_{crit}$	
15.8	tan(33.5°) - sin(41.0°)	tan(34.9°) - sin(43.6°)	+0.00
	0.01	0.01	
16.5	tan(36.3°) - sin(41.0°)	tan(38.7°) - sin(43.6°)	+0.03
	0.08	0.11	

Table 3.3 shows a comparison of peak and large displacement strength parameters for dry and partially saturated RMS graded sand at two different levels of γ_{dry}. Peak and critical state parameters are selected from Figs. 3.7 and 3.13 (for partially saturated RMS graded sand) and from Figs. 2.24 and 2.28 in Chapter 2. Please note that ϕ_{crit} is constant with respect to γ_{dry}. For a given γ_{dry}, the table shows the increase from $\sin(\phi_{crit})$ to $\tan(\phi_{ds\text{-}p})$ for both dry and partially saturated RMS graded sand. As can be seen in the table, the increase for dry RMS graded sand is virtually identical to the increase of the partially saturated material. If $[\tan(\phi_{ds\text{-}p}) - \sin(\phi_{crit})]$ for dry sand is taken to be equivalent to $[\tan(\phi_{ds\text{-}p}) - \sin(\phi_{crit})]$ for partially saturated sand, Eqns. 3.26 and 3.27 can be combined to give the relationship

$$\frac{c_{ds}}{\sigma_N} = \tan\left(\psi_p\right)_{p.sat} - \tan\left(\psi_p\right)_{dry} \tag{3.28}$$

which shows that the increase in dilatency between dry and partially saturated sand is equal to the normalized cohesion, c_{ds}/σ_N.

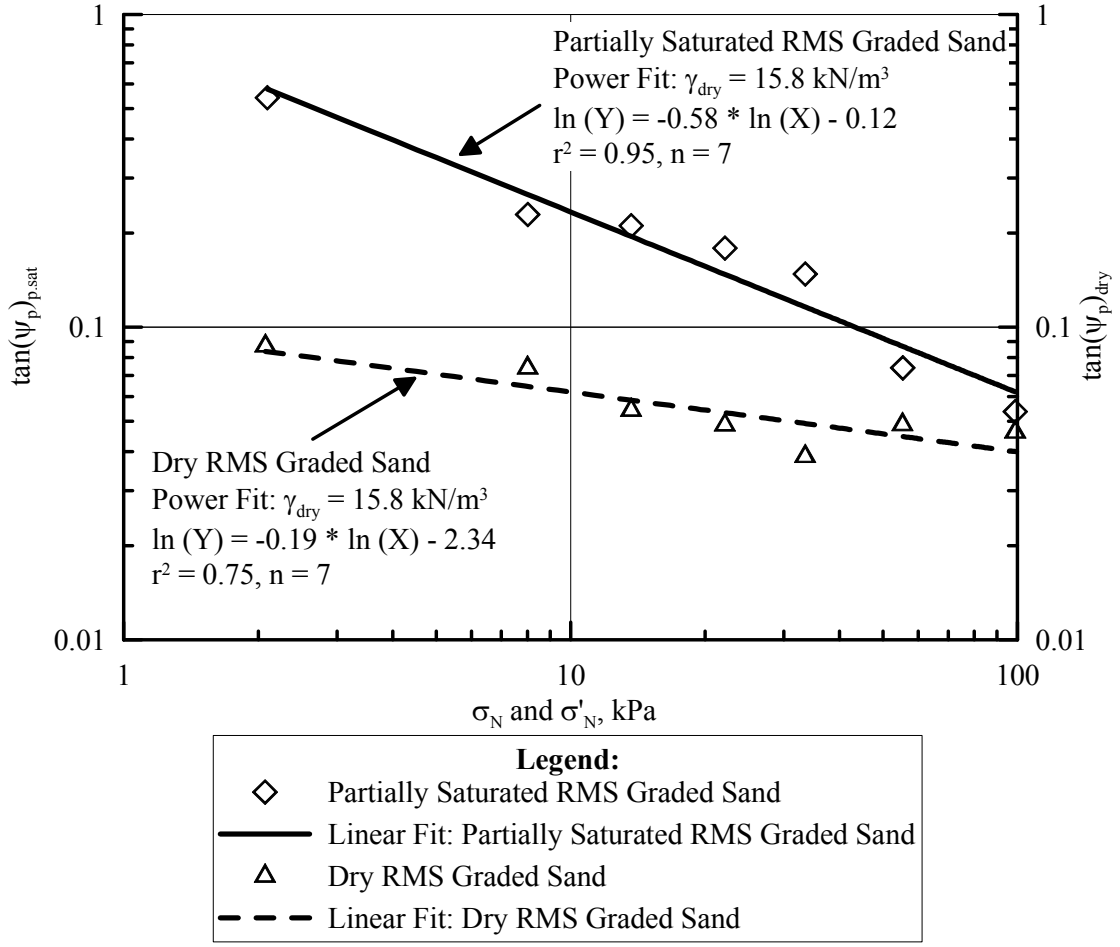

Figure 3.18 $\tan(\psi_p)_{p.sat}$ vs σ_N and $\tan(\psi_p)_{dry}$ vs σ'_N for RMS graded sand at γ_{dry} = 15.8 kN/m^3

Figure 3.18 shows $\tan(\psi_p)$ vs σ'_N for dry RMS graded sand at γ_{dry} = 15.8 kN/m^3. The plot shows the same data as presented in Chapter 2 for dry RMS graded sand. Also shown is $\tan(\psi_p)$ vs σ_N for partially saturated RMS graded sand at the same γ_{dry}. When there was more than one test run at a given σ_N for either the dry or partially saturated material, the average ψ_p of all tests at that σ_N was plotted in the figure, so that there are only seven distinct data points for each curve. Linear regressions are plotted for both data sets.

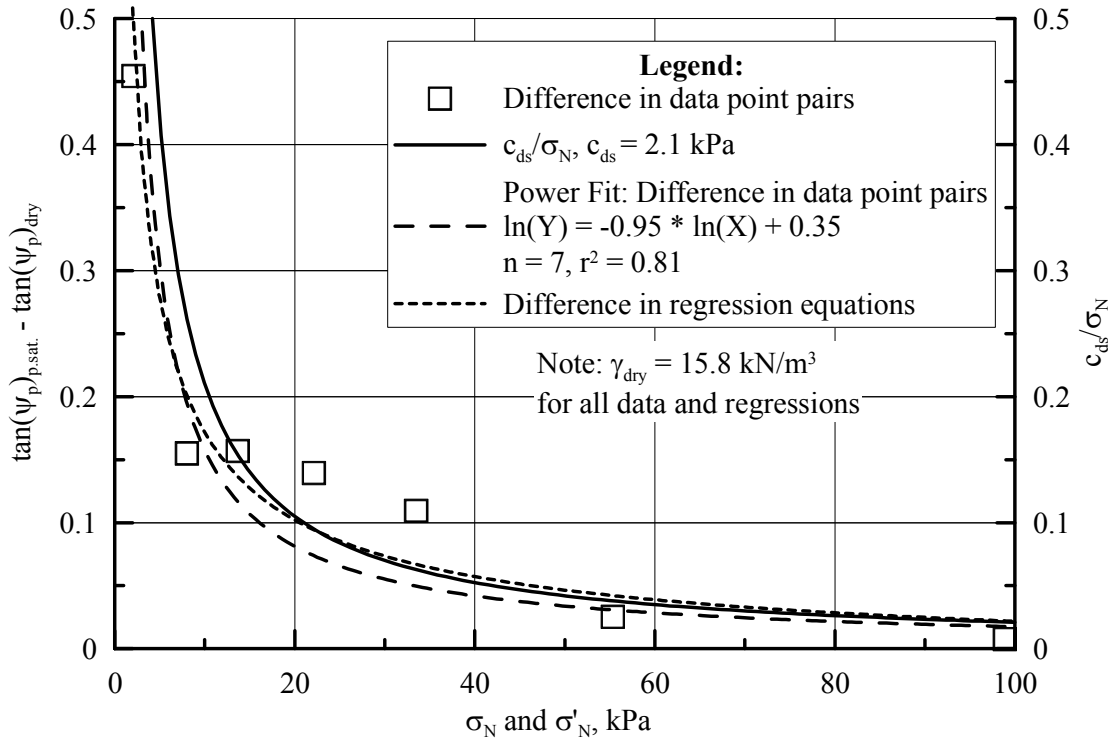

Figure 3.19 $[\tan(\psi_p)_{p.sat} - \tan(\psi_p)_{dry}]$ and c/σ_N vs σ_N and σ'_N for RMS graded sand at γ_{dry} = 15.8 kN/m^3

In Figure 3.19, showing $\tan(\psi_p)$ vs σ_N for γ_{dry} = 15.8 kN/m^{3}the $\tan(\psi_p)$ value for dry RMS graded sand (called $\tan(\psi_p)_{dry}$) is subtracted from the corresponding $\tan(\psi_p)$ value for partially saturated RMS graded sand (called $\tan(\psi_p)_{p.sat}$), and is plotted as $[\tan(\psi_p)_{p.sat} - \tan(\psi_p)_{dry}]$ vs σ_N. This value is plotted in Fig. 3.19 as the "Difference in data point pairs", and is fit with a Power regression, which has r^2 = 0.81. For comparison, a separate curve is plotted in Fig. 3.19, representing the difference between the power fits for partially saturated and dry RMS graded sand shown in Fig. 3.18. Also plotted in Fig. 3.19 is c_{ds}/σ_N vs σ_N for c_{ds} = 2.1 kPa, corresponding to the value measured for partially saturated RMS graded sand at γ_{dry} = 15.8 kN/m^3.

Figure 3.20 shows $\tan(\psi_p)$ vs σ'_N for dry and partially saturated RMS graded sand at γ_{dry} = 16.5 kN/m^3. The plot shows the same data as presented in Chapter 2 for dry RMS graded sand and previously in this chapter for partially saturated RMS graded sand. As with Fig. 3.18, when there was more than one test run at a given σ_N for either the dry or partially saturated material, the average ψ_p of all tests at that σ_N was plotted in the figure, so that there are only seven distinct data points for each curve. Linear regressions are plotted for both data sets.

In Figure 3.21, showing $\tan(\psi_p)$ vs σ_N for γ_{dry} = 16.5 kN/m^3, the $\tan(\psi_p)$ value for dry RMS graded sand (called $\tan(\psi_p)_{dry}$) is subtracted from the corresponding $\tan(\psi_p)$ value for partially saturated RMS graded sand (called $\tan(\psi_p)_{p.sat}$), and is plotted as $[\tan(\psi_p)_{p.sat} - \tan(\psi_p)_{dry}]$ vs σ_N. This value is plotted in Fig. 3.21 as the "Difference in data point pairs", and is fit with a Power regression, which has r^2 = 1.00. For comparison, a separate curve is plotted in Fig. 3.21, representing the difference between the power regressions for partially saturated and dry RMS graded sand shown in Fig. 3.20. Also plotted in Fig. 3.21 is c_{ds}/σ_N vs σ_N for c_{ds} = 3.4 kPa, corresponding to the value measured for partially saturated RMS graded sand at γ_{dry} = 16.5 kN/m^3.

As can be seen in Figs. 3.19 and 3.21, the data and the three different curves are statistically indistinguishable for σ_N > 15 kPa, showing that the difference in $\tan(\psi_p)$ for dry and partially saturated RMS sand is well represented by the c_{ds}/σ_N ratio at both γ_{dry} = 15.8 and 16.5 kN/m^3. It can be concluded therefore that the cohesion associated with partially saturated RMS graded sand is related to increased dilatency. It appears that suction increases the interference among the sand particles, thus

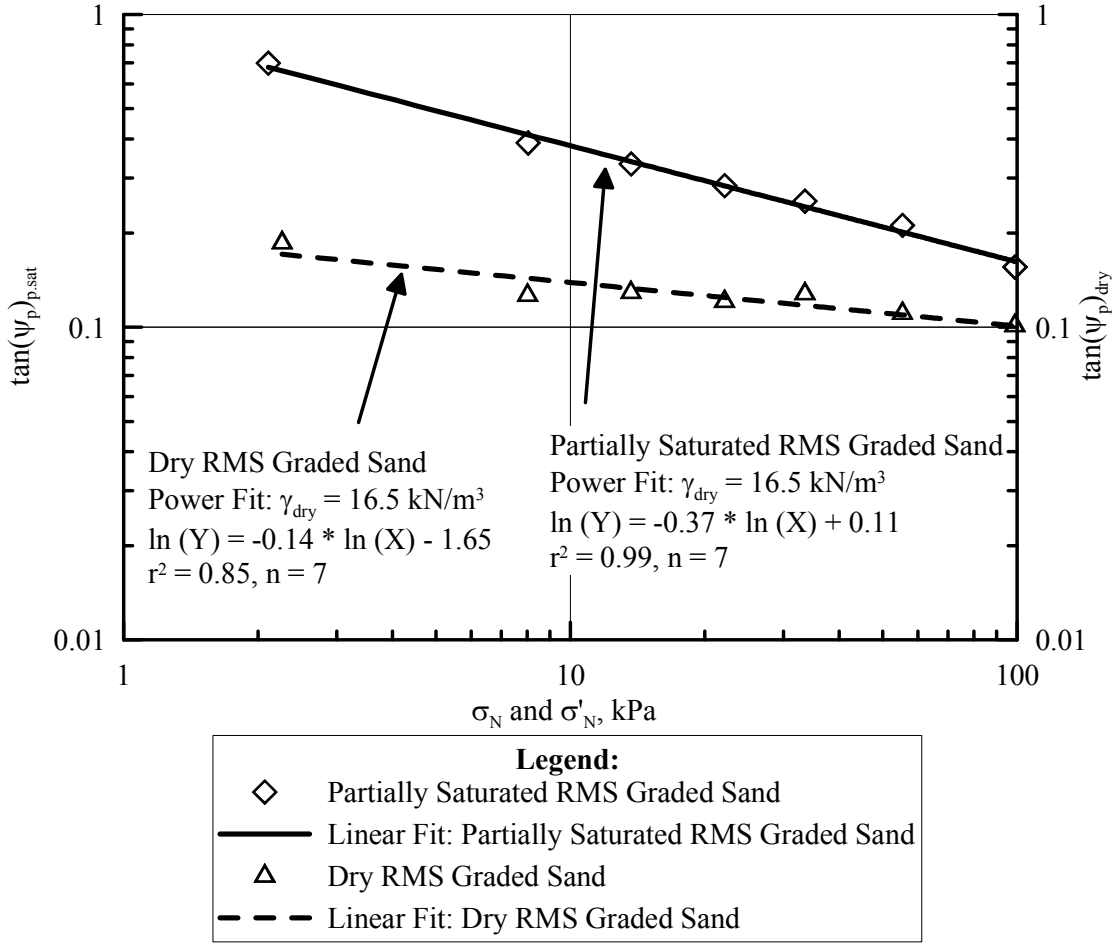

Figure 3.20 $\tan(\psi_p)_{p.sat}$ vs σ_N and $\tan(\psi_p)_{dry}$ vs σ'_N for RMS graded sand at γ_{dry} = 16.5 kN/m³

mechanism for shear strength is identical to the interlocking and critical state concepts for the DS strength of sand advanced by Schofield (2005).

3.8 Indirect Evidence for Cohesion

When large scale tests are performed in partially saturated RMS graded sand, vertical discontinuities commonly form in the soil mass, developing from the pipe to

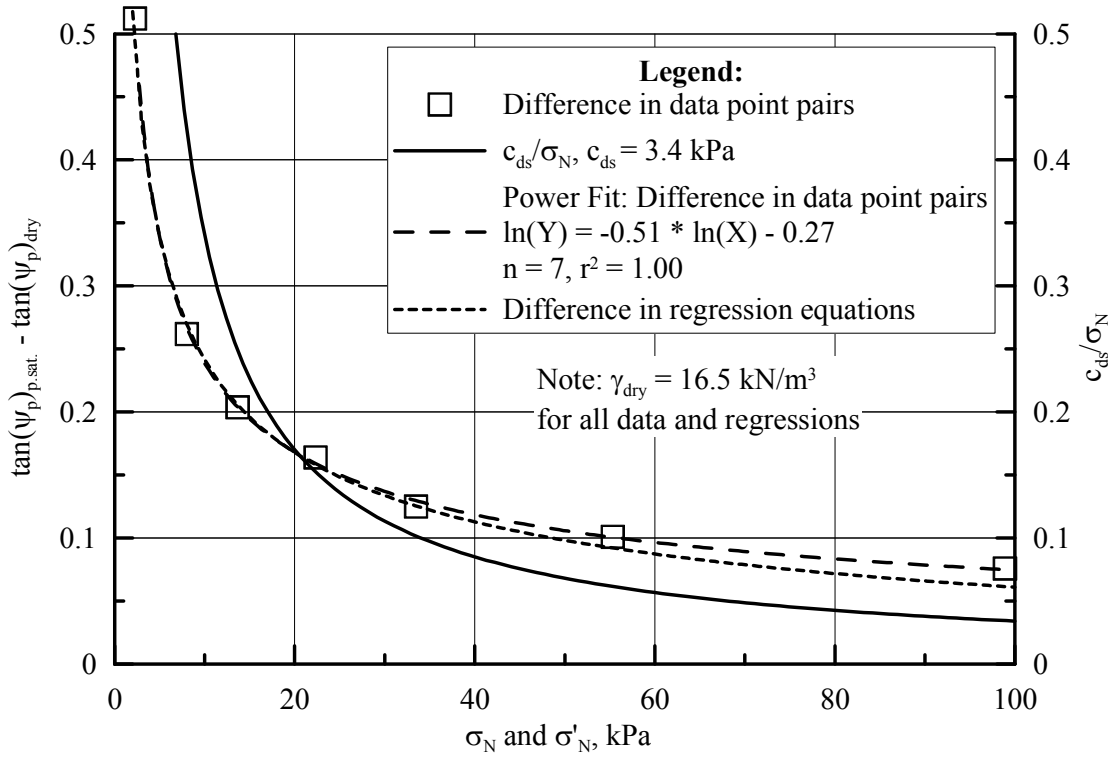

Figure 3.21 $[\tan(\psi_p)_{p.sat} - \tan(\psi_p)_{dry}]$ and c/σ_N vs σ_N and σ'_N for RMS graded sand at γ_{dry} = 16.5 kN/m³

the surface. As the pipe displaces into the soil it creates a passive wedge, as shown in Figure 3.22a. A vertical discontinuity separates the passive wedge from the undisturbed soil behind the pipe, which contains the potential active wedge. In large scale tests, the maximum depth of vertical discontinuity, H_s, was found to be approximately 900 mm. Figure 3.22b shows a schematic of the active soil wedge behind the pipe, where the active wedge is assumed to be a continuous mass of soil.

Figure 3.22c shows a similar active wedge, which is assumed to contain a vertical tension crack of depth $H_s/2$. These conditions are similar to those assumed by Terzaghi (1943) and used to estimate the apparent cohesion of soil standing vertically without support.

In Figs. 3.22b and c, forces consisting of the weight of the soil wedge, W_s, the cohesion of the soil, C_s, and the resultant, R_s, act in the directions shown, and can be resolved to solve for C_s as shown in Figure 3.22d. As can be shown by the derivation in Appendix A, the cohesion associated with an unsupported cut without a tension crack is given as

$$c_{indirect} = \frac{1}{4}\gamma_{dry}(1+w)H_s \cot\left(45° + \frac{\phi_{ds-p}}{2}\right) \tag{3.29}$$

and the cohesion associated with a tension crack is given by

$$c_{indirect} = \frac{3}{8}\gamma_{dry}(1+w)H_s \cot\left(45° + \frac{\phi_{ds-p}}{2}\right) \tag{3.30}$$

It should be noted that Eqn. 3.29 is identical to the equation for an active soil wedge in a c - ϕ material given by Terzaghi (1943), if the active force resultant is equal to zero, and all forces are taken up by soil friction and cohesion.

If the depth of vertically unsupported soil shown in the large scale tests is taken as H_c = 900 mm with typical soil properties (ϕ_{ds-p} = 34.9° for a c - ϕ representation, γ_{dry} = 15.8 kN/m^3, w = 4%), the estimated cohesion with and without a tension crack is $c_{indirect}$ = 2.0 and 2.9 kPa, respectively. These values are consistent with the cohesion measured by the direct shear tests for partially saturated RMS graded sand with γ_{dry} = 15.8 kN/m^3 and w = 4%, which was shown previously in this chapter to be c_{ds} = 2.1 kPa.

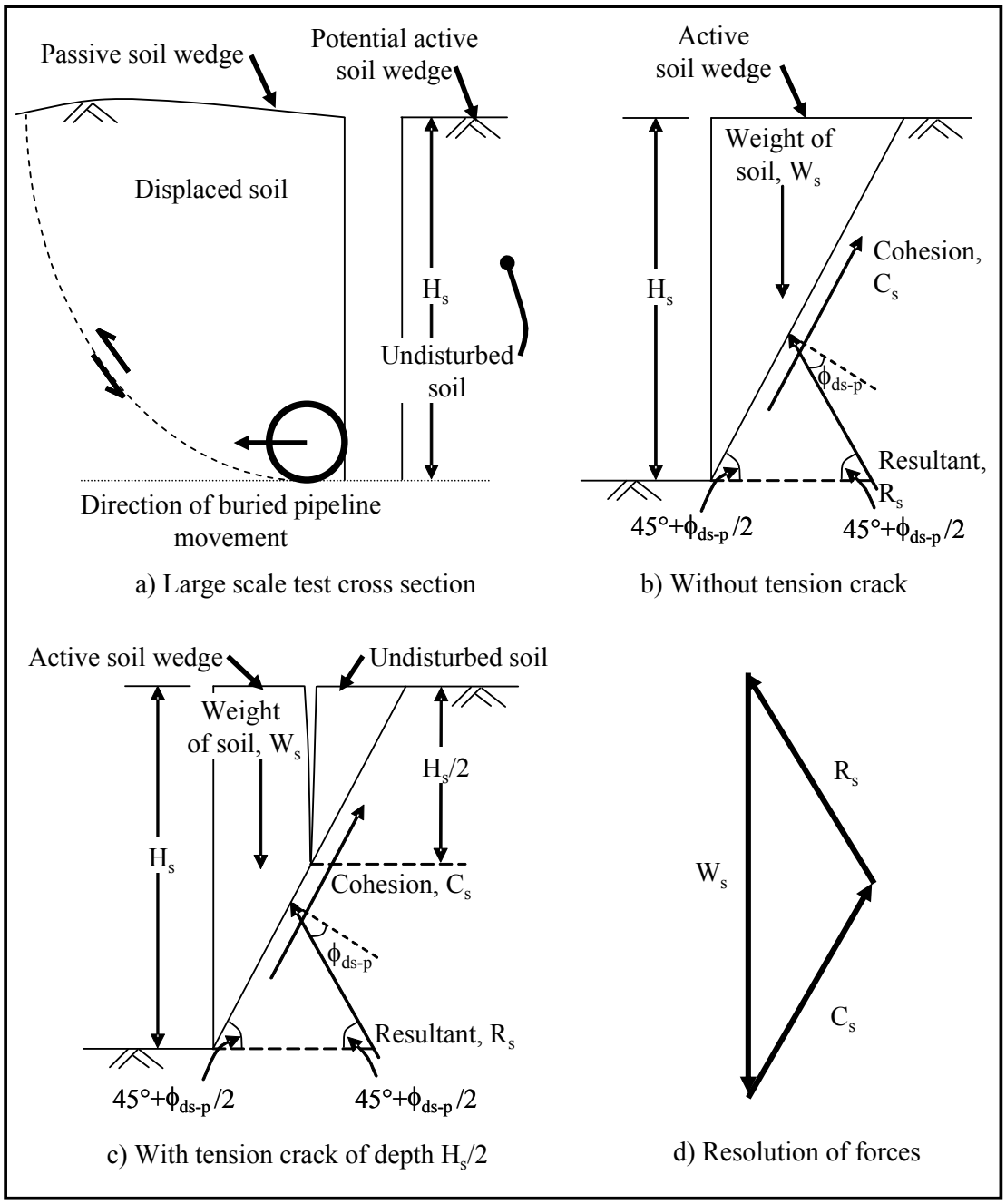

Figure 3.22 Schematic cross section of large scale test and unsupported vertical wall in a c - ϕ material (Not to scale)

3.9 Calculation of Equivalent A-Coefficient for RMS Graded Sand

For the triaxial test, the A-coefficient is defined as

$$A_f = \frac{\Delta u}{\sigma_1 - \sigma_3} \tag{3.31}$$

where Δu is the pore water pressure required to move from the total stress friction angle point of tangency to the effective stress friction angle point of tangency. It does not require the peak shear on the failure surface to be equal for total and effective stress conditions. In fact, there must be a rotation of failure planes between the two conditions. Mohr's circles for the triaxial test on dry and saturated sand specimens are shown in Figure 3.23.

From a DS test, with Mohr's circles for dry and partially saturated sand as shown in Figure 3.24, and equivalent A-coefficient, A_{eq}, can be defined similarly to the triaxial definition. If there is no constraint on rotation of the rupture surface relative to the principal stresses, the A_{eq} is defined purely on the basis of equivalent effective stress conditions to produce the same Mohr's circle at failure for total and effective stresses. Since the rupture plane is fixed, this requires a rotation of principal stresses from total to effective stress conditions, but the plane of zero extension and dilation angle do not change. The classical definition requires that ψ_p be smaller for dry than partially saturated sand, and then assumes that the increased shear strength associated with increased ψ_p and σ'_N is equivalent to the effects of negative pore pressure increase. In other words, increased dilatency and confining stress are lumped under increased effective stress pegged to partially saturated conditions.

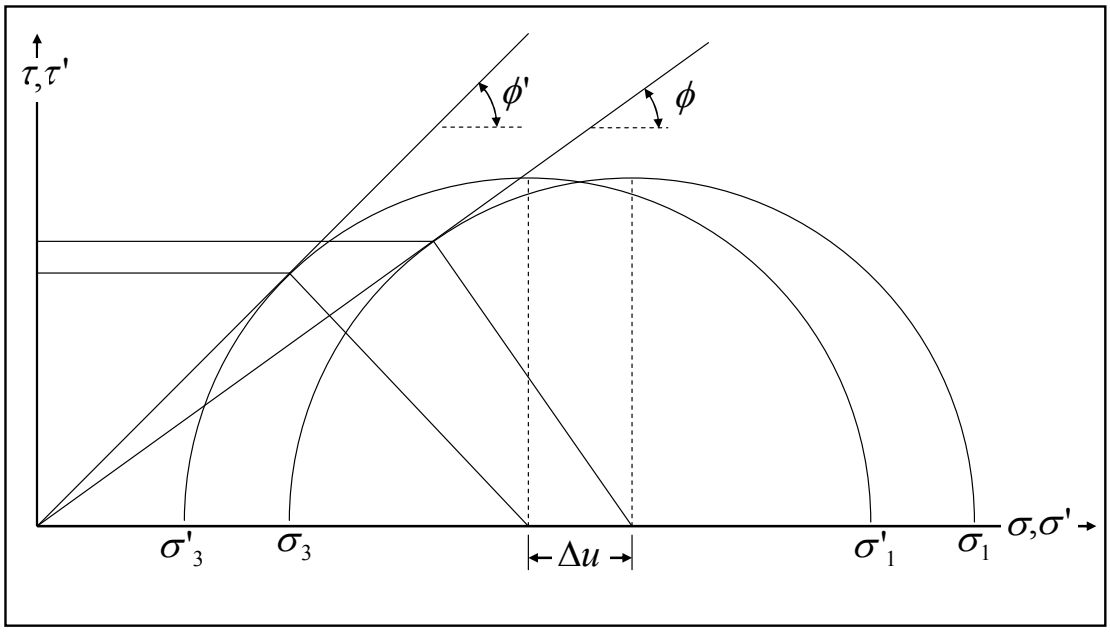

Figure 3.23 Definition of stress parameters for triaxial test on saturated soil specimen

(Not to scale)

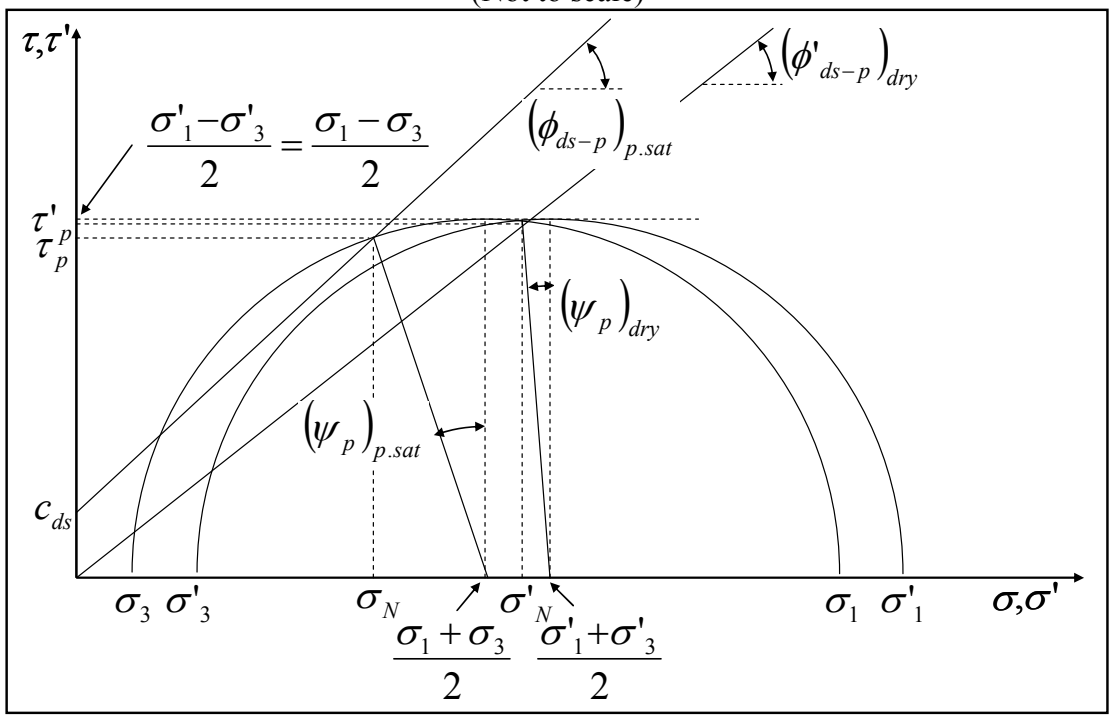

Figure 3.24 Relationships between dry and partially saturated Mohr's circles with the same deviator stress and dry unit weight (Not to scale)

To account properly for suction effects, one must account separately for dilatency and effective confining stresses. Water surface tension increases dilatency of the sand matrix and binds particles together more firmly relative to dry conditions. This is reflected in the measured c_{ds} and increased $\phi_{ds\text{-}p}$. To calculate the difference in negative pore water pressure required to explain the increase in direct shear strength from dry to partially saturated sand for two direct shear tests at the same γ_{dry} with Mohr's circles of equal radius, an equation was derived in Appendix A, taking the form

$$A_{eq} = \frac{u}{\sigma_1 - \sigma_3} = \frac{1}{2}\left[\cos\psi_{dry}\cot\phi'_{ds-dry} + \sin\psi_{dry} - \cos\psi_{p.sat}\cot\phi_{ds-p.sat} - \sin\psi_{p.sat}\right] + \frac{\cos\psi_{p.sat}\cot\phi_{ds-p.sat}}{2\left(\frac{\sigma_N}{c_{ds}}\tan\phi_{ds-p.sat} + 1\right)} \quad (3.32)$$

where parameters are displayed graphically in Figure 3.24. This equation assumes that the ψ_p for dry and partially saturated sand are different, thus the rupture planes in direct shear for total and effective stress are rotated differently with respect to the principal stresses.

To define the range of soil stresses over which to vary A_{eq}, the soil-structure interaction from a large-scale test was considered. Figure 3.25a shows the initial state of stress in the soil, with the major principal stress acting vertically, and the minor principal stress horizontally. Figure 3.25b shows the state of stress during horizontal pipe displacement into the soil. The vertical stress becomes the minor principal stress, and the horizontal stress becomes the major principal stress. Figure 3.25c shows

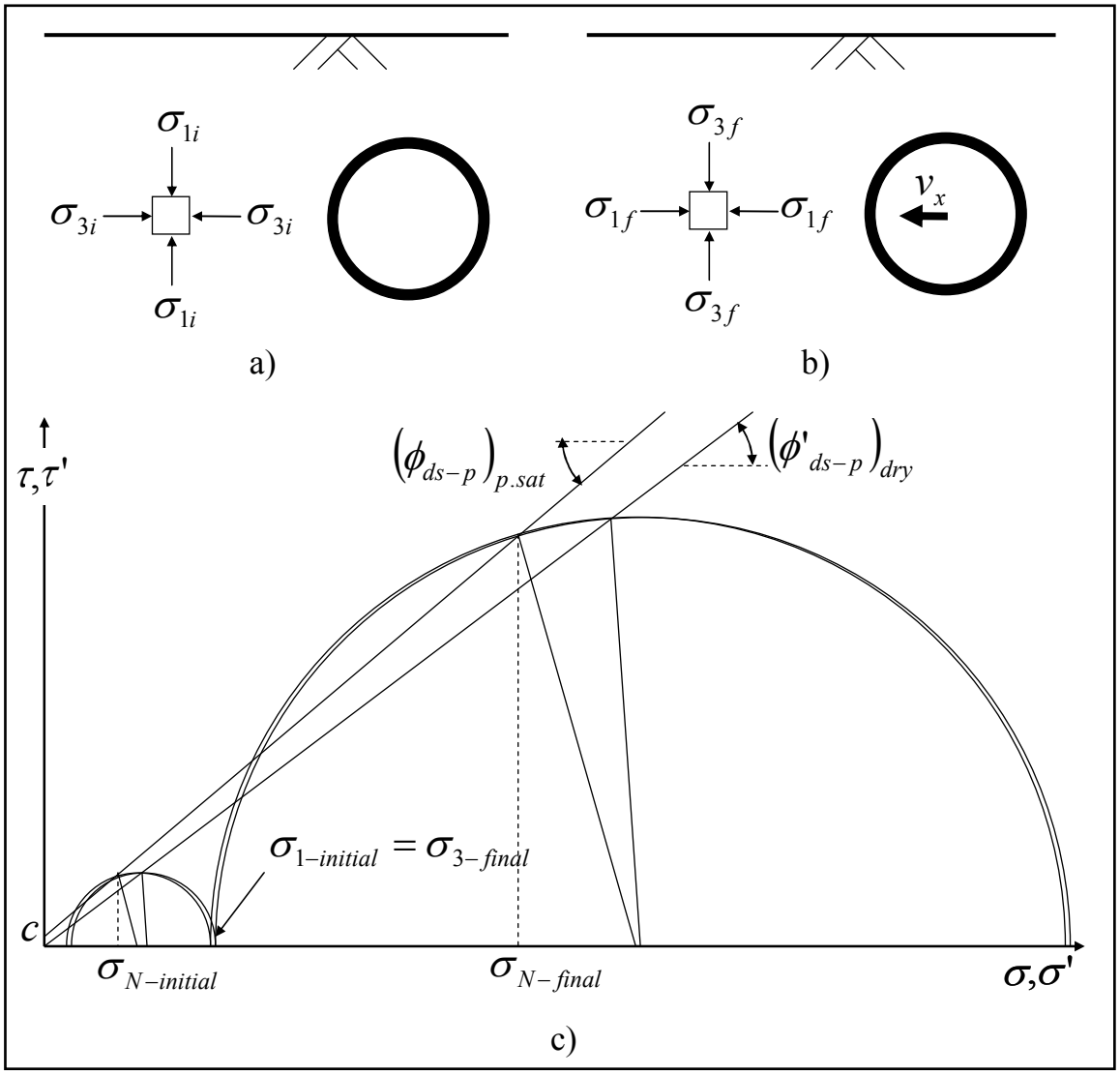

Figure 3.25 Transformation of stresses due to displacement of pipe through soil (not to scale) a) Initial stress state b) Stress state at peak horizontal soil resistance c) Mohr's circles for initial and final stress states

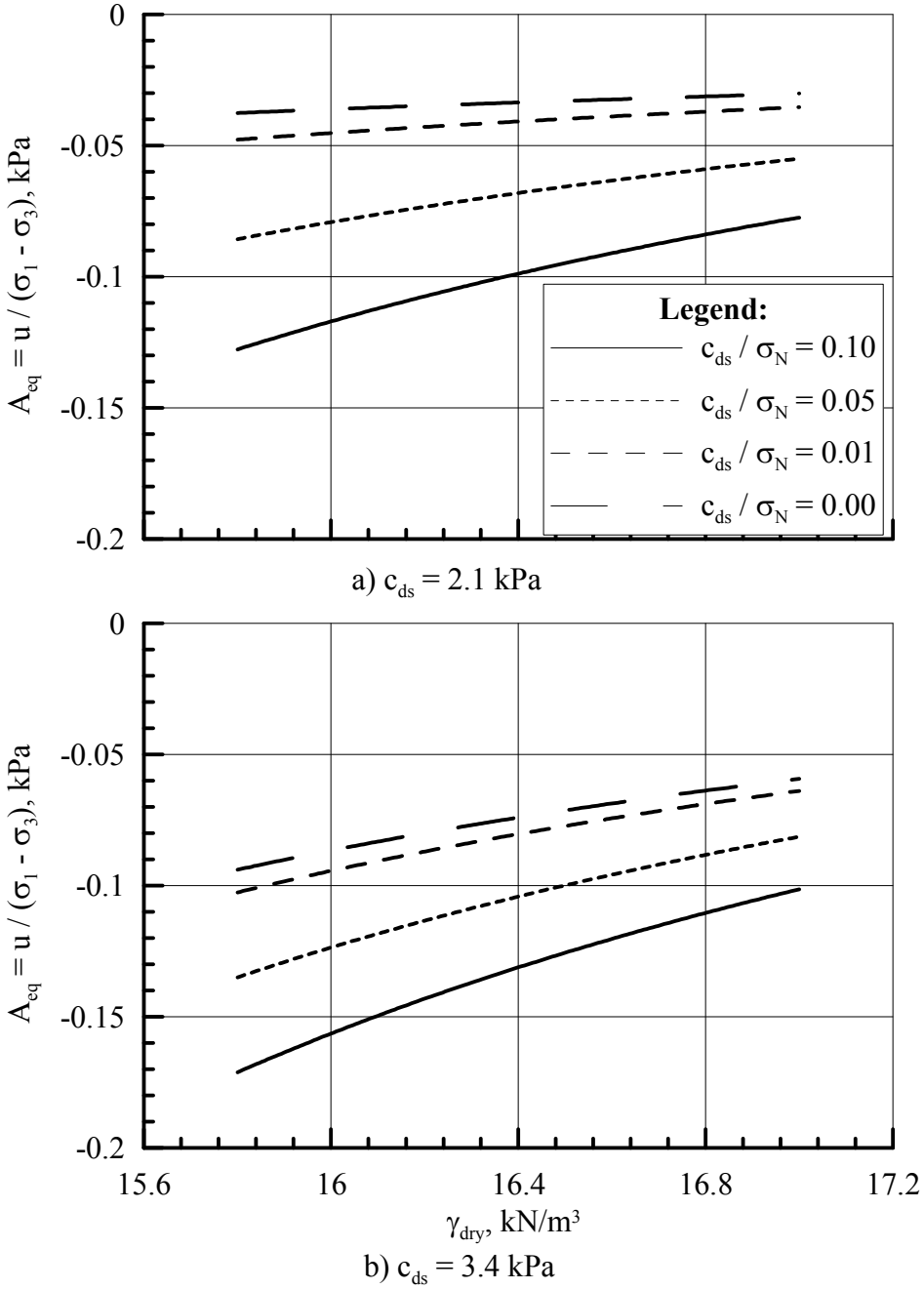

Figure 3.26 Equivalent A-parameter vs γ_{dry} for partially saturated RMS graded sand with variations of c_{ds}/σ_N a) c_{ds} = 2.1 kPa b) c_{ds} = 3.4 kPa

Mohr's circles used to calculate the increase in normal and shear stress associated with the rotation of principal stresses, assuming that the $\phi_{ds\text{-}p}$ and ψ_p remain constant. For a soil with γ_{dry} = 15.8 kN/m^3, initial σ_N is 22 kPa for a pipe burial depth of 1.3 m, while σ_N after rotation of principal stresses = 138 kPa.

Figures 3.26a and b show A_{eq} for a variety of values of c_{ds}/σ_N, keeping c_{ds} constant and varying σ_N from 21 kPa to an infinitely high value. Also shown are lines corresponding to the stress state in the soil before and after the rotation of principal stresses. Figure 3.26a uses c_{ds} = 2.1 kPa, from the Mohr-Coulomb envelopes at γ_{dry} = 15.8 kN/m^3, while Figure 3.26b uses c_{ds} = 3.4 kPa, from the Mohr-Coulomb envelopes at γ_{dry} =16.5 kN/m^3. As c_{ds} increases, the values of σ_N used in the c_{ds}/σ_N calculation increase as well. For Figure 3.26a, the σ_N used are 21 kPa, 42 kPa, 210 kPa, and infinity, corresponding to c_{ds}/σ_N = 0.10, 0.05, 0.01 and 0.00, respectively. For Figure 3.26b, the σ_N used are 34 kPa, 68 kPa, 340 kPa, and infinity, again corresponding to c_{ds}/σ_N = 0.10, 0.05, 0.01 and 0.00, respectively.

The four lines in each figure appear to approach a common value of A_{eq} as γ_{dry} increases, and diverge at low γ_{dry}. A_{eq} is most negative at low σ_N, implying that negative pore water pressure effects increase as σ_N decreases. As the assumed value of c_{ds} increases from 2.1 kPa in Figure 3.26a to 3.4 kPa in Figure 3.26b, A_{eq} becomes more negative, meaning that at the higher γ_{dry}, greater u_m would be generated by a sand at a given deviator stress than at the lower γ_{dry}. This is consistent with the finding from SWRCs that greater u_m are generated for denser sand conditions.

CHAPTER 4

PREPARATION AND MEASUREMENT OF SOIL FOR LARGE SCALE EXPERIMENTS

4.1 Introduction

Soil was placed and measured for six large scale 3-D and eleven large-scale 2-D soil-structure interaction experiments. Up to 900 kN of soil for each large scale test were placed at exacting specifications of water content, w, and dry unit weight, γ_{dry}. Values of w were measured by oven drying according to ASTM D2216 and with the nuclear gage according to ASTM D6938 (ASTM, 2008b). The parameter γ_{dry} was measured using the Selig density scoop (Selig, 1962, Selig and Ladd, 1973) and with the nuclear gage according to ASTM D6938 (ASTM, 2008b).

Density scoop and nuclear gage calibrations were performed on dry and partially saturated RMS graded sand to minimize measurement bias. Statistics are used to evaluate the precision and bias of each measurement device, and are also used to calculate confidence intervals for the mean value of various measured soil properties. Methods of soil placement for large-scale soil-structure interaction tests are described and evaluated on the basis of their efficiency and repeatability in producing soil properties that have tightly controlled precision and no significant bias relative to target values. All large scale tests and calibrations for the current study were performed using either dry or partially saturated RMS graded sand (unless

otherwise noted for previous research), which will be referred to as "dry sand" or "partially saturated sand," respectively, in this chapter.

4.2 Density Scoop

The Selig density scoop (Selig, 1962, Selig and Ladd, 1973) was modified by Trautmann et al. (1985) to increase the base plate dimensions and add scissor arms, as shown in Figure 4.1. It was machined from stainless steel, with threaded connections. The scoop jaws consist of two quarter-cylinders with a radius of 50 mm and length of 80 mm. The jaws are centered within a 200 mm x 280 mm x 6 mm steel baseplate. Initially when the scissor arms are vertical, the scoop jaws are above the plate-soil interface. As the scissor arms are lowered and spread apart, the scoop is forced into the soil, rotating about an axis parallel to the plate as the jaws are closed, thus capturing a sample of soil. The scoop sample is weighed to determine in-situ unit weight of the soil, and then oven dried to calculate w and γ_{dry}.

By comparing the weight of density scoop samples obtained from soils with known γ_{dry}, the density scoop can be calibrated to give reliable measurements of soil properties. To calibrate the density scoop, sand was compacted in a 305 mm x 230 mm x 90 mm wooden box to the desired γ_{dry}, and then leveled to the top of the box and weighed. A density scoop sample was obtained from the compacted soil and weighed, and its w determined by oven drying.

The wooden calibration box was made as small as possible to minimize the effort required to prepare compacted soil specimens for scoop calibration, and to

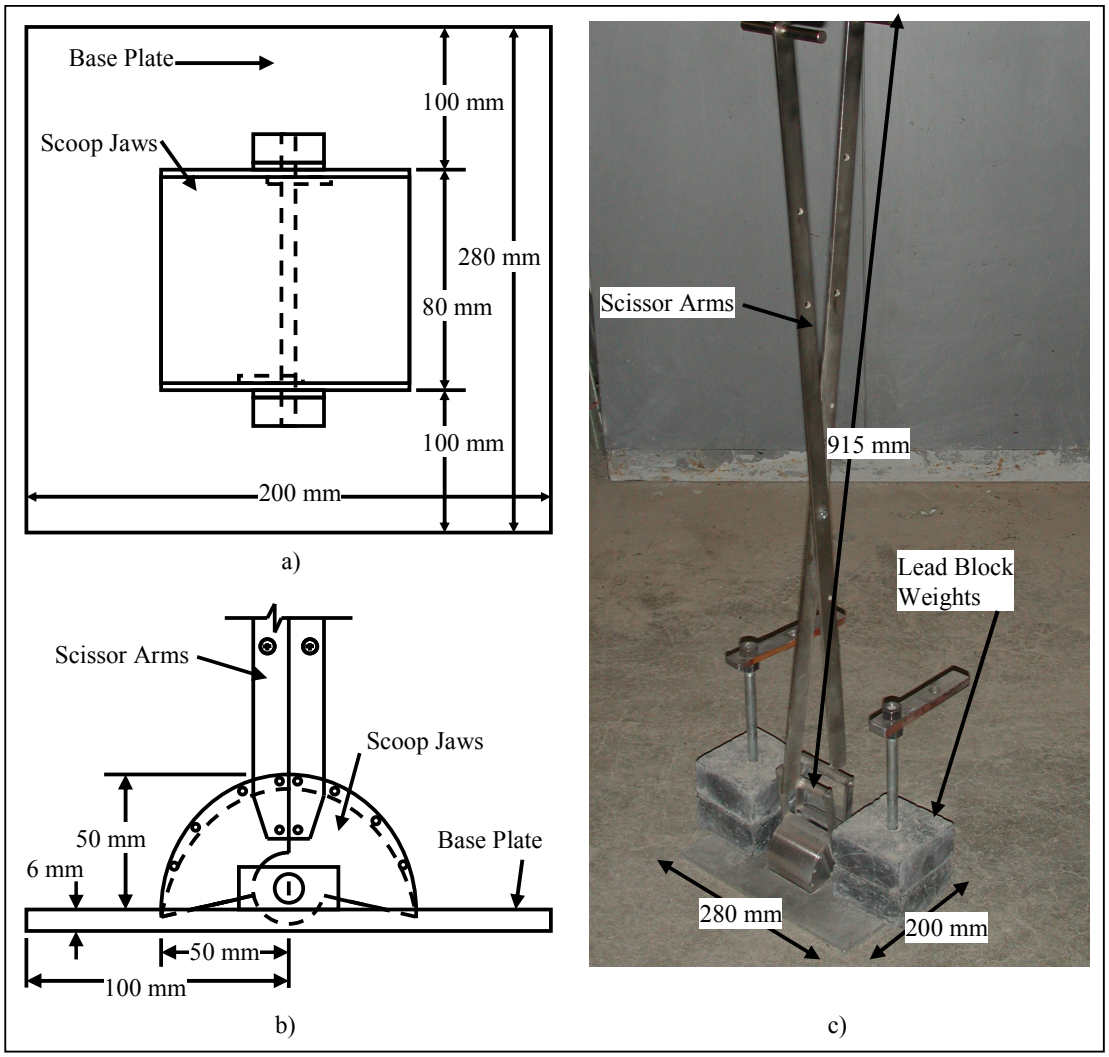

Figure 4.1 a) Schematic of density scoop in plan view b) Schematic in elevation view c) Photo of density scoop with lead block weights

minimize the calibration error associated with non-uniform soil density throughout the box volume. The calibration box interior walls were lined with Formica to minimize side friction during soil compaction, and the edges were sealed with silicone caulking to provide a watertight seal. The box was filled with water and weighed to determine its volume, using water temperature-density relationships as shown by Trautmann et al. (1985).

Trautmann et al. (1985) performed density scoop calibrations with dry CU Filter sand, shown in Fig. 4.2. Also shown in Fig. 4.2 are density scoop calibrations for dry RMS graded sand by Turner (2004) and the current research. It can be seen in the figure that the density scoop calibration is user- and material-sensitive. Although CU Filter sand and RMS graded sands are similar (see particle size distribution comparisons in Fig. 2.1), the Trautmann et al. (1985) calibration for CU Filter sand plots significantly higher than the Turner (2004) calibration for RMS graded sand. The calibrations of RMS graded sand by Turner (2004) and the current study are close to one another, but not statistically indistinguishable. Additionally, the repeatability of a density scoop measurement depends on user technique. Other calibrations of the density scoop for dry CU Filter and RMS graded sands by other researchers at Cornell University are summarized in Table 4.1.

Turner (2004) applied the density scoop to measure γ_{dry} for partially saturated sand, using a mixture of 50% CU Filter sand and 50% RMS graded sand, called RMS graded – CU Filter Mix. Turner (2004) found that density scoop calibration variability occurred because of an unknown volume of the captured soil sample. The scoop tended to rise as the jaws were closed by the operator. Because of enhanced resistance and stiffness of the partially saturated sand relative to dry sand, it was difficult for the user to provide the appropriate force to the scoop that would prevent vertical rise. Turner (2004) used lead block weights placed on top of the steel baseplate to apply a constant vertical force to the scoop that kept the base plate level during sample collection. This modification improved the repeatability of the density scoop and decreased calibration error. The number of weights used varied by soil w and γ_{dry}. As discussed by Turner, more weights are needed for dense sand because of its increased dilatency and tendency for the scoop to rise when sampling from the sand.

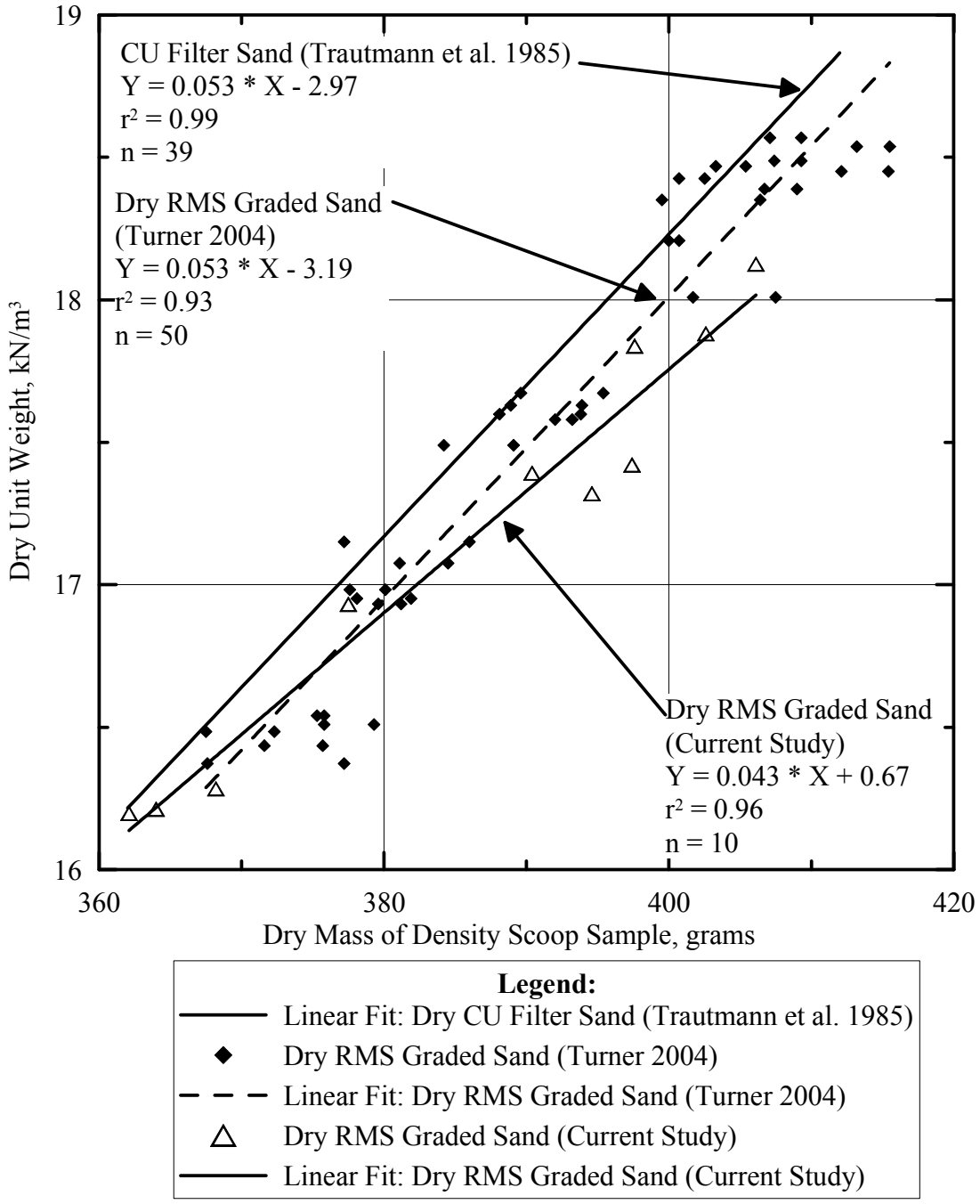

Figure 4.2 Calibrations of density scoop for dry sand

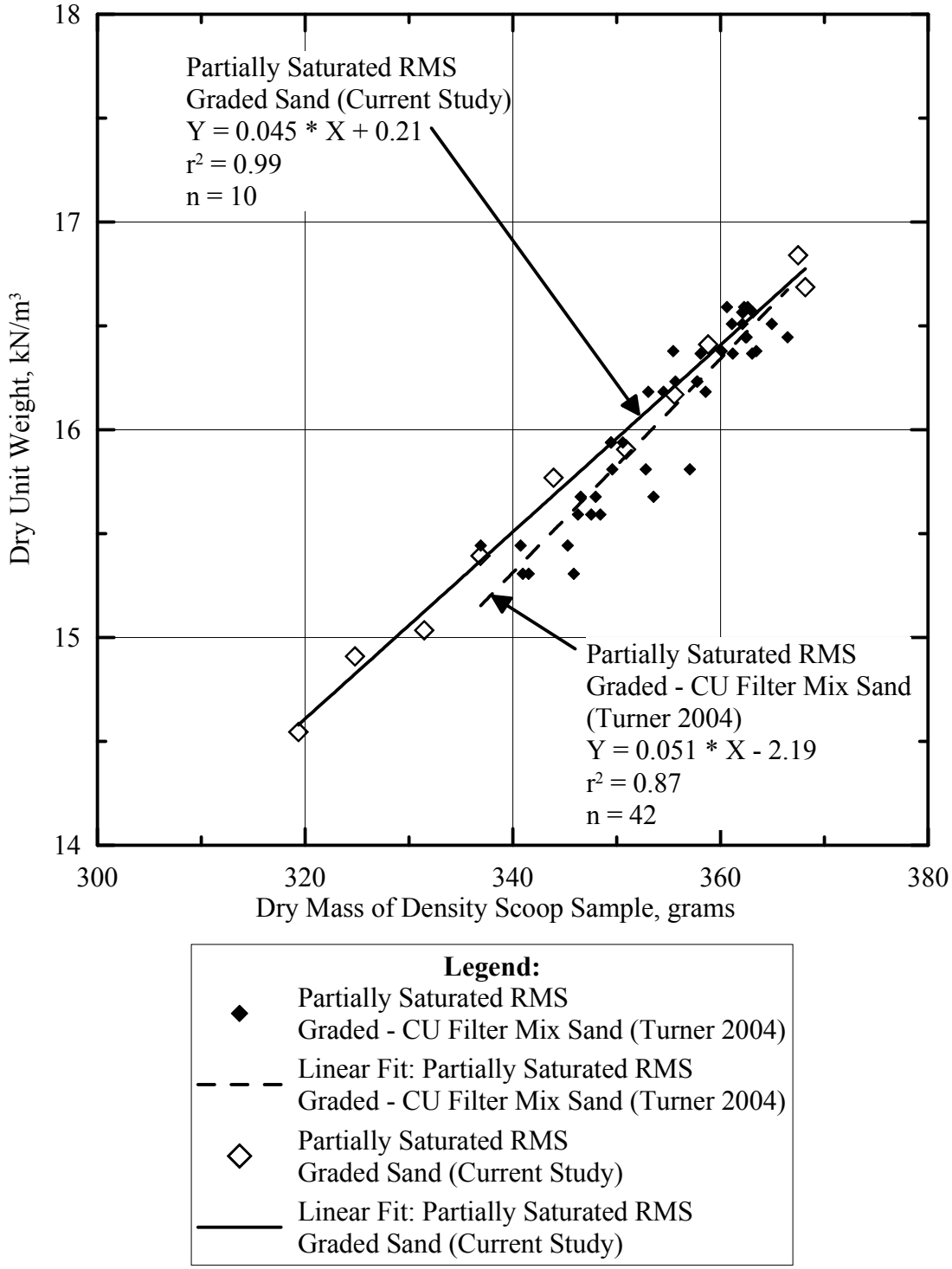

Figure 4.3 Calibrations of density scoop for partially saturated sand

Table 4.1 Comparison of density scoop calibration with previous calibrations

Reference	Sand Type	w	Calibration Equation	r^2	n
Weiler and Kulhawy (1978)	CU Filter	Dry	Y = 0.053 * X - 2.87	N/A	35
Stewart and Kulhawy (1981)	CU Filter	Dry	Y = 0.050 * X - 1.76	N/A	17
Trautmann et al. (1985)	CU Filter	Dry	Y = 0.053 * X - 2.97	0.99	39
Yoshizaki (2002)	RMS Graded	Dry	Y = 0.058 * X - 5.81	0.80	12
Turner (2004)	RMS Graded	Dry	Y = 0.053 * X - 3.19	0.93	50
Turner (2004)	RMS Graded – CU Filter Mix	4%	Y = 0.051 * X – 2.19	0.87	42
Current Study	RMS Graded	Dry	Y = 0.043 * X + 0.67	0.96	10
Current Study	RMS Graded	4%	Y = 0.045 * X + 0.21	0.99	10

As with dry sand, partially saturated sand was prepared to a specified w and compacted to a specified γ_{dry} by striking a steel compaction plate in contact with the soil with a hammer. The steel compaction plate had the same dimensions as the surface area of the wooden calibration box to ensure uniform energy transfer to the entire sand volume. The sand was leveled to the top of the box and weighed. A density scoop sample was obtained using the proper lead block weights, the sample was weighed and a subsample was taken for measurement of w by oven dry methods in accordance with ASTM D2216 (ASTM, 2003d).

The density scoop calibration determined in the current research for partially saturated RMS graded sand (at w = 4%) is compared in Figure 4.3 with the calibration for partially saturated RMS graded – CU Filter mix sand by Turner (2004). The calibration by Turner (2004) has $r^2 = 0.87$, while the current research calibration has $r^2 = 0.99$.

4.3 Nuclear Gage

The nuclear gage is an instrument for measuring the unit weight of water and soil and other materials quickly and repeatably. The gage has long been the industry standard for measurement of asphalt, concrete, and soil backfill unit weight for roadway and geotechnical construction (Mamlouk 1988, NYSDOT, 2007). The Troxler Model 3440 gage (manufactured by Troxler, Inc., Research Triangle Park, NC) used in the current study measures the wet unit weight of soil (γ_{total}) and water present in the soil ($\gamma_{w\text{-}soil}$), both reported in units of kg/m^3. γ_{total} is measured using a different method than $\gamma_{w\text{-}soil}$, and both are reported by the gage. γ_{dry} is calculated by subtracting the water present in the soil (measured either by oven dry methods or using the nuclear gage) from γ_{total}.

There are safety issues associated with the nuclear sources sealed within the gage, and training is required for operators. Moreover, licensing requirements are required for the lab in which the device is used. The operator's manual (Troxler, 2004b) and the ASTM standard test method for nuclear gage testing (ASTM, 2008b) provide procedures for safe handling, operating and storing the nuclear gage. Information about the gage and safety practices are available through the Cornell University Department of Environmental Health and Safety (EHS) (EHS, 2009).

4.3.1 Unit Weight Measurement Theory

The nuclear gage, which is shown in Figure 4.4, contains a cesium-137 source that emits gamma particles measured by the detector after passing through the soil. The source is encapsulated within tungsten shielding in the stainless steel source rod,

which has adjustable depth. Figure 4.4a shows the source rod in safe mode, at the top of its vertical range of travel. The source is located within the body of the gage. When a measurement is not being taken, the nuclear gage is always kept with the source rod in safe mode so that the tungsten shielding within the nuclear gage body minimizes radiation exposure.

To account for decay of the source over time, a standard count is taken every time the nuclear gage is used. The standard count is taken with the gage in safe mode, with the gage placed on a Teflon standard count block, which is located on a flat level surface at least 3 m from large objects, walls, or subsurface voids. The internal calibration of the soil and water unit weight nuclear gage measurements are adjusted according to the standard count.

The source rod can be moved to preset measurement depths below safe mode in 50 mm increments from 0 to 300 mm. At 0 mm depth, or backscatter mode (see Fig. 4.4b), the source rod is lowered so that the source is level with the soil surface. At depths from 50 – 300 mm, called direct transmission mode (see Fig. 4.4c), the source rod is lowered into a prepared hole to the desired depth of measurement.

As shown in Fig. 4.4, detectors in the base of the gage measure gamma particles emitted by the source. As gamma particles collide with electrons in the soil, some are scattered, reducing the number of gamma particles that reach the detector. The number of gamma particles measured by the detector are calibrated relative to soil γ_{total}. Since the gamma particles measured by the detector have passed through the entire distance between the source and detector, the measured unit weight is a true

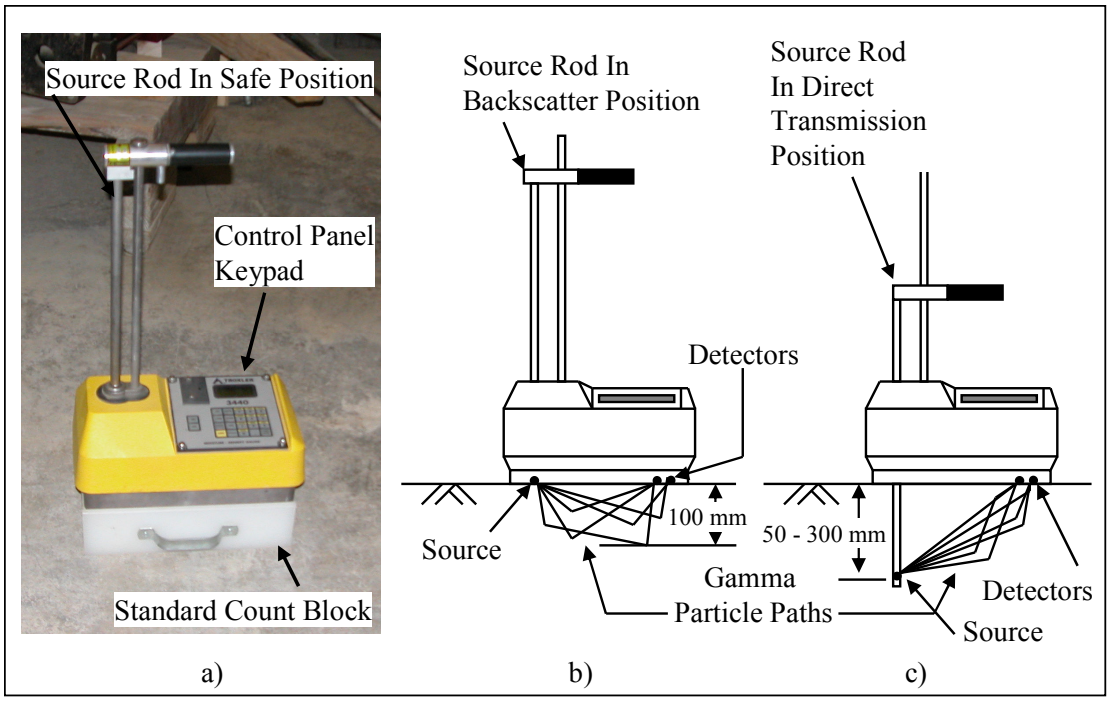

Figure 4.4 a) Photo of nuclear density gage in safe mode on Teflon standard count block b) Schematic of nuclear density gage in backscatter mode c) Schematic of nuclear density gage in direct transmission mode

average for the material between the detector and source. γ_{total} for partially saturated sand is measured in either backscatter or direct transmission mode. γ_{total} for dry sand can only be measured in backscatter, as dry sand does not have sufficient cohesion to support a bored hole in the soil.

According to the manufacturer, the volume of soil measured in direct transmission mode is approximated by a 200 mm diameter cylinder extending from the surface to the source level (Troxler, 2004b). The true volume of measurement depends on the specific material being measured as well as its γ_{dry} and w. In backscatter mode, shown in Figure 4.4b, the source rod is placed directly above the soil surface in the gage, so that gamma particles emitted by the cesium-137 source are

scattered at least once to reach the detector. Since the gamma particles have been scattered at least once on the path from source to detector, the energy of measured gamma particles is less than for direct transmission mode, increasing the variability in measured γ_{total}. Since gamma particles passing through deeper material have to travel a longer distance to reach back to the surface, they are scattered more than gamma particles taking a path closer to the surface, and the measured value of unit weight is more heavily weighted toward the surface unit weight. According to the manufacturer, backscatter mode measures a depth approximately 100 mm below the soil surface (Troxler, 2004b).

4.3.2 Moisture Measurement Theory

A 40mCi americium 241:beryllium source (called the neutron source) is used to measure unit weight of water, yielding 70,000 neutrons per sec. The neutron source is located in the body of the nuclear gage, in contrast with the cesium-137 source, which is within the source rod. The hydrogen atoms present in water in the soil thermalize neutrons released by the source. Thermalization is a process whereby neutrons are slowed by collisions with hydrogen atoms. The neutron detector in the gage is much more sensitive to thermalized (slowed) neutrons than fast neutrons, so the more water in the soil, the more thermalized neutrons that will reach the detector.

In contrast to the gamma source, which is located within the source rod, the neutron source is located within the body of the nuclear gage just above the soil surface. For this reason, unit weight of water is always measured in backscatter mode, whereby neutrons are scattered by the soil and reflected back to the detector (see Figure 4.4b). The true depth of measurement depends on the unit weight of water in

the soil, such that material with greater unit weight of water will have a shallower depth of measurement. According to the manufacturer, the approximate depth of measurement is related to the weight of moisture present in the soil, using the relation

$$D_M = 280 - 27.5M_{water} \quad (4.1)$$

where depth of measurement, D_M, is measured in mm, and weight of water, M_{water}, is measured in kg/m^3.

4.3.3 Unit Weight Calibration of Gage

The nuclear gage was initially calibrated by the manufacturer on calibration blocks of known unit weight and water content, using a method similar to that proposed by Servais (1990). Previous research by Jameson (1985a and 1985b) and Mamlouk (1988) showed that the nuclear gage must be recalibrated for each new material. Cassaro et al. (2000) calibrated a nuclear gage over a range of densities from 9.8 to 18.2 kN/m^3, using a variety of materials, including water, sand, loam, and clay. Cassaro et al. (2000) took 30 sec measurements at depths from backscatter to 300 mm in an iron box with inner dimensions of 450 mm x 350 mm x 500 mm depth. Using blocks of known density, the laboratory calibration was found to be 1 – 16% lower than the manufacturer's calibration at a given γ_{dry}.

Similar to the calibration of the density scoop, the nuclear gage was calibrated using a 900 mm x 450 mm x 250 mm box wooden box. Dry or partially saturated sand was compacted in the box in 50 - 100 mm lifts. The soil surface was leveled to the top of the box, which was then weighed to determine gravimetric unit weight,

$\gamma_{total\text{-}grav}$, of the soil. Eight 15 sec measurements of γ_{dry} were taken at locations around the box in direct transmission mode at a depth of 150 mm for each of 7 prepared soil boxes for partially saturated sand, or 5 prepared soil boxes for dry sand. At each of the eight measurement plots for partially saturated sand, a small sample of sand was removed for determination of w by oven dry methods, in accordance with ASTM D2216 (ASTM, 2003d).

Shown in Figure 4.5 is a plot of gravimetric dry unit weight, $\gamma_{dry\text{-}grav}$, vs dry unit weight measured by the nuclear density gage, $\gamma_{dry\text{-}gage}$, for partially saturated RMS graded sand. $\gamma_{dry\text{-}grav}$ was calculated by dividing soil box dry weight, W_{soil}, by soil box volume, V_{soil}. Soil box dry weight is calculated using the formula

$$W_{soil-dry} = \frac{W_{soil-wet}}{1+w} \tag{4.2}$$

Also shown in Figure 4.5 is a calibration of dry RMS graded sand, measured by the nuclear density gage in backscatter mode. Both dry and partially saturated RMS graded sand show strong relationships between $\gamma_{dry\text{-}grav}$ and $\gamma_{dry\text{-}gage}$, with $r^2 = 0.90$ and 0.93, respectively. Both linear regressions and the majority of the measured data lie below the 1:1 line, also plotted on the figure, and have slopes steeper than 1. The linear regression for partially saturated RMS graded sand falls 1 - 5% below the 1:1 line, while the linear regression for dry RMS graded sand is 3 – 5% below the 1:1 line. This deviation is consistent with the range of deviation found by Cassaro et al. (2000).

The calibration of the neutron source and detector to measure unit weight of water was not investigated by the current study, and measurements of w by the nuclear

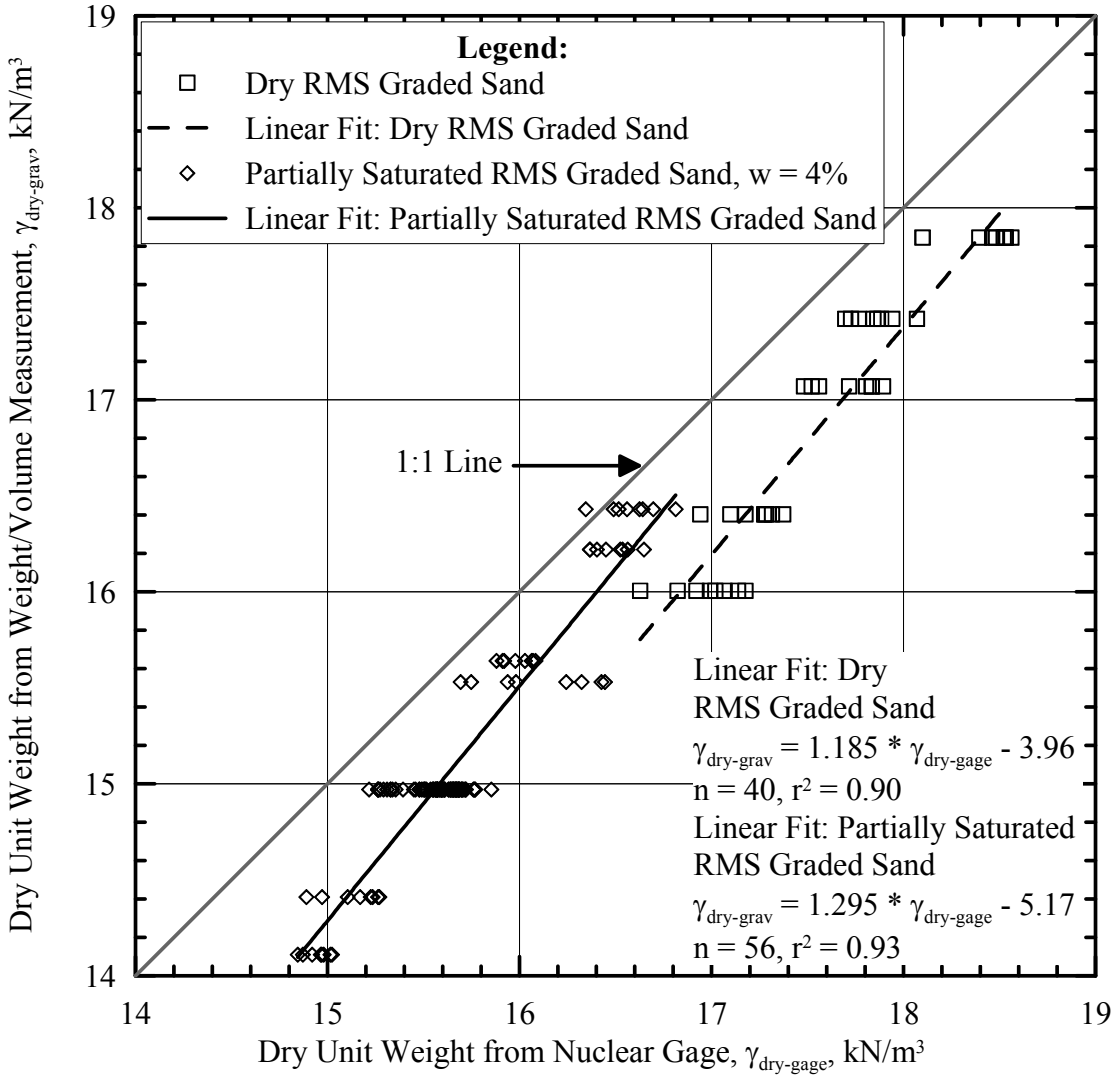

Figure 4.5 Calibration of measured vs true dry unit weight for nuclear density gage using 15 second count for dry and partially saturated RMS graded sand

gage for this study are reported in this chapter using the manufacturer's calibration. It is shown later that within the range of w measured in large scale tests, the precision of measurements of w by oven dry methods is superior to the measurement of w by the nuclear gage.

4.3.4 Wall Influence on Density Measurement

The nuclear gage was designed to measure unit weight of soil and water of an infinite half-space of soil. Deviation from this assumption can cause unknown measurement errors, and it is stated by the owner's manual (Troxler, 2004b) that the measurement of unit weight is affected by proximity to vertical walls. To characterize the influence of wall proximity on the measured value of unit weight, measurements were made in the nuclear gage calibration box at various distances from the wall with the gage oriented with its source facing the wall, its detector facing the wall, and each side facing the wall. It was found that after a separation of 100 mm between the source end or either side of the gage and the wall, there was no influence of wall distance on density measurement. A separation of 300 mm from the detector end of the gage to the wall was necessary to avoid wall influence on density measurement. The difference of wall influence for the detector end wall vs the other walls can be explained by the reflection of gamma particles by the wall back to the detector (see Fig. 4.4). When gamma particles reflect off walls near the source end or the gage sides, there is a longer travel distance for the gamma particles to reach the detector than for reflection off the end wall. The measurement of density will tend to decrease due to wall proximity, as extra gamma particles reaching the detector give the same response as would a looser soil.

For all calibrations of the gage in the 900 mm x 450 mm x 250 mm box and all soil measurements in the large scale test basin, care was taken to orient the gage such that the side of the gage where the detector was located was never less than 300 mm from the wall of the box, the threshold of wall influence. For the other three sides of the gage, the box wall was as close as 100 mm to the gage with no detrimental effects.

4.4 Statistics of Measurement

In the measurement of γ_{dry} and w for sand, the accuracy and precision of reported data depend on the method of measurement, the operator's technique and skill in using a consistent measurement procedure, and the consistency of the sand material being tested. Precision is a measure of the dispersion of values around a mean value, while accuracy, or bias, is the difference between the average of a group of measurements and the true value. By calibrating a measurement device on a specific soil, an operator aims to maximize precision and eliminate bias through consistency of technique.

Trautmann et al. (1985) calibrated and characterized the variability of multiple methods of density measurement for calibrations and large scale tests. By taking a sufficiently large number of measurements with an unbiased technique, density was determined to an arbitrarily high precision. This precision, called the confidence interval, or CI, can be determined by the Central Limit Theorem of statistics, which states that

$$CI = \frac{tS_D}{\sqrt{n}} \tag{4.3}$$

where t is the t-value found in standard statistical tables for (n – 1) degrees of freedom and a given two-tailed probability, S_D is the standard deviation of the measured density, and n is the number of measurements. This relationship shows that the CI decreases as the square root of n increases, while it increases as the standard deviation

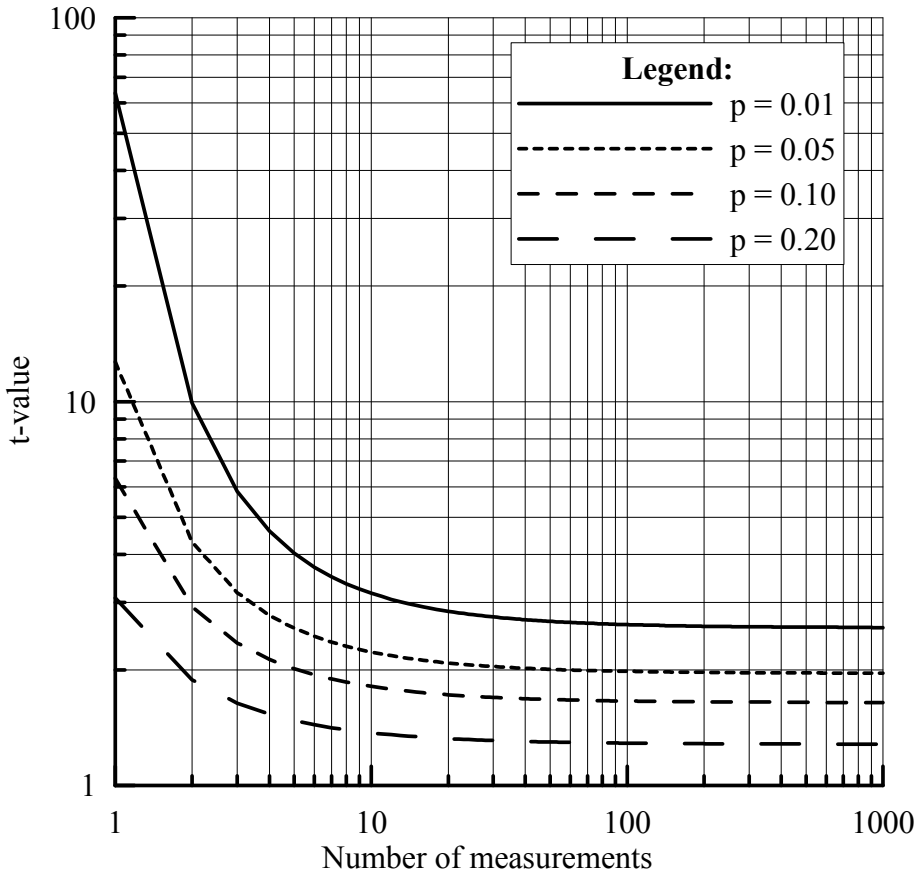

Figure 4.6 t-value vs number of measurements for given probabilities of the two tailed t-distribution

and t-value increase. Figure 4.6, shows that for a given number of measurements, the t-value decreases for increasing probability. At a two-tailed probability of 0.05, as is typically used in this chapter, the t-value is relatively unchanged beyond 20 measurements.

As measured for large scale tests, the standard deviation used in Eqn. 4.3 takes into account both the variance of measurement technique and the variance due to soil inhomogeneity. The variance of a sample of large scale density measurements, or the square of the standard deviation, is equal to the sum of both of these variances.

Trautmann et al. (1985) stated that, while variance due to soil inhomogeneity can never be measured directly, the measurement technique variance can be determined during calibration under controlled conditions.

The density scoop is a destructive test method, in that only a single measurement can be taken at a measurement location. The nuclear gage, on the other hand, is a nondestructive test method. Once a hole is bored in the soil to the desired depth, any number of measurements may be taken at a given depth at the same location without disturbing the soil. By taking a sufficiently large number of measurements at a single location, the variance associated with the nuclear gage can be identified, and the average of the measured data can be assumed to represent the best estimate of the actual value of γ_{dry}.

A series of nuclear gage measurements were performed to characterize variability and precision associated with the determination of γ_{dry} and $\gamma_{w\text{-}soil}$ as a function of measurement duration, location, and depth within the calibration box. Figures 4.7, 4.8 and 4.9 show the effects of the previously mentioned variables on nuclear gage measurements, respectively.

Fig. 4.7a shows precision vs measurement time duration for nuclear gage measurements of $\gamma_{w\text{-}soil}$. The secondary y-axis shows the COV for each set of measurements. Each data point represents the average of 20 nuclear gage measurements of $\gamma_{w\text{-}soil}$. One set of 20 measurements was taken in the same location for a duration of 15 sec, followed by a set of 20 measurements at 60 sec, and 20 measurements at 240 sec. The three sets were all measured at the same location, and it

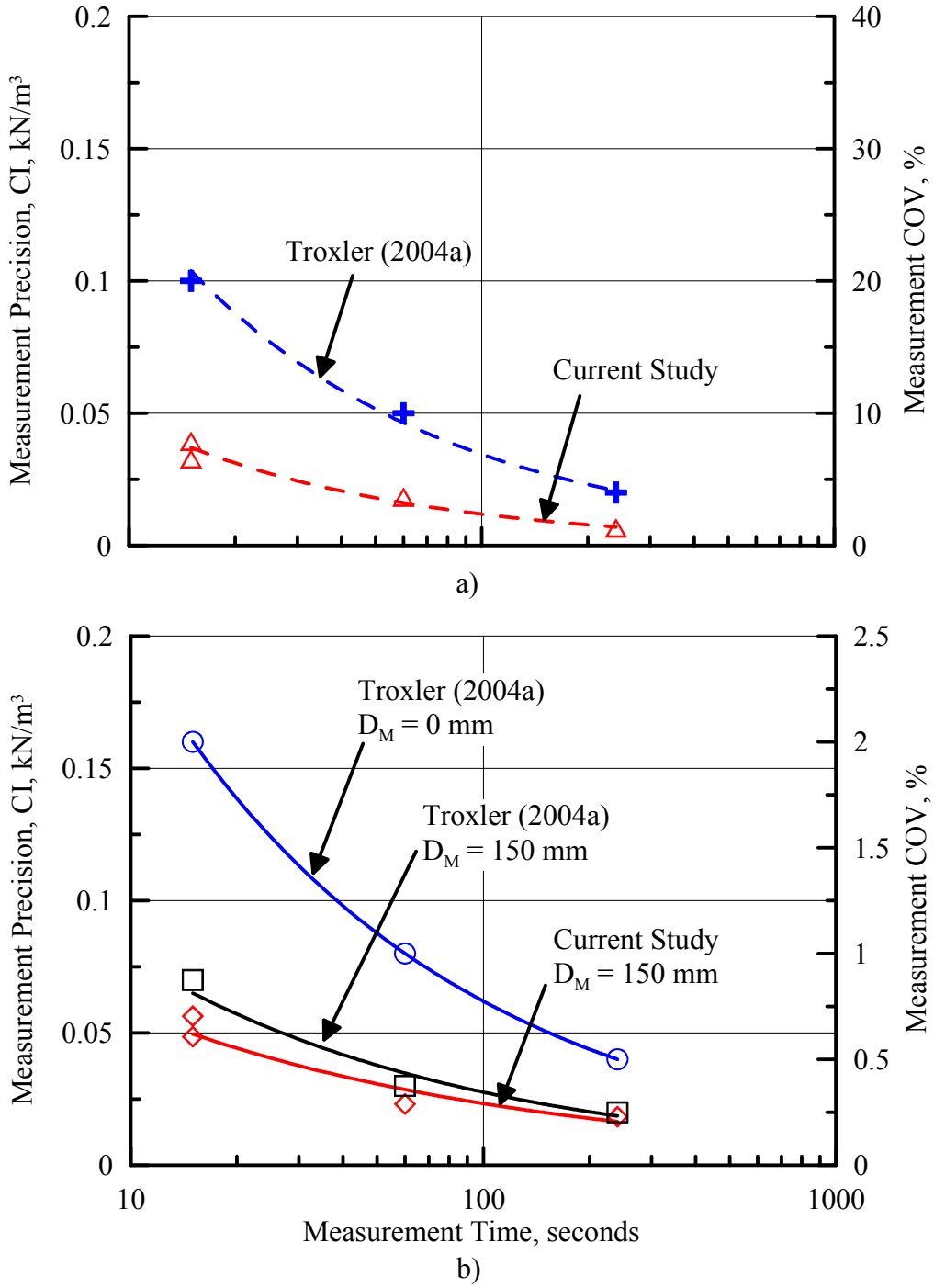

Figure 4.7 Precision and COV vs time of measurement in calibration box for a) $\gamma_{w\text{-}soil}$ b) γ_{dry}

can be seen that the precision of a set of measurements decreases as duration of measurement increases from 15 to 240 sec. Precision of $\gamma_{w\text{-}soil}$ reported by the

manufacturer (Troxler, 2004a) is also plotted in Fig. 4.7a, and shows a similar trend of decreasing precision with increasing duration.

Fig. 4.7b shows precision and COV vs measurement time duration for nuclear gage measurements of γ_{dry}, respectively. Three sets of 20 measurements were taken at a direct transmission depth of 150 mm for the same durations as for Fig. 4.7a. Precision for the same direct transmission depth and the same durations reported by Troxler (2004a) is also shown. Higher precisions for backscatter (depth = 0 mm) measurements at the same time durations are reported by Troxler (2004a) and plotted in the figure. Comparing Fig. 4.7a to 4.7b, the precision of $\gamma_{w\text{-}soil}$ is similar, or slightly smaller than, the precision of γ_{dry}. Because COV is the standard deviation normalized by the mean and S_D is a smaller percentage of γ_{dry} (0.1 kN/m^3 / 16.8 kN/m^3 = 0.7%) than $\gamma_{w\text{-}soil}$ (0.1 kN/m^3 / 1.1 kN/m^3 = 0.8%), the COV values for γ_{dry} are much lower than those for $\gamma_{w\text{-}soil}$.

Fig. 4.8 shows histograms of nuclear gage measurements for different locations within the same calibration box. At each of locations, ten measurements were taken without moving the gage. The histogram for each location shows the distribution of measured values, while the histogram at the top of the figure shows the combined data from all locations. For this particular experiment, the mean γ_{dry} for Location 8 is significantly lower than that of the other locations. As can be seen, the S_D of a measurement set for a given location is between 0.04 – 0.07 kN/m^3, while the S_D for all data is 0.14 kN/m^3. If Location 8 is excluded from the histogram for all data, the S_D for all data decreases to 0.09 kN/m^3, more consistent with the S_D for a single location.

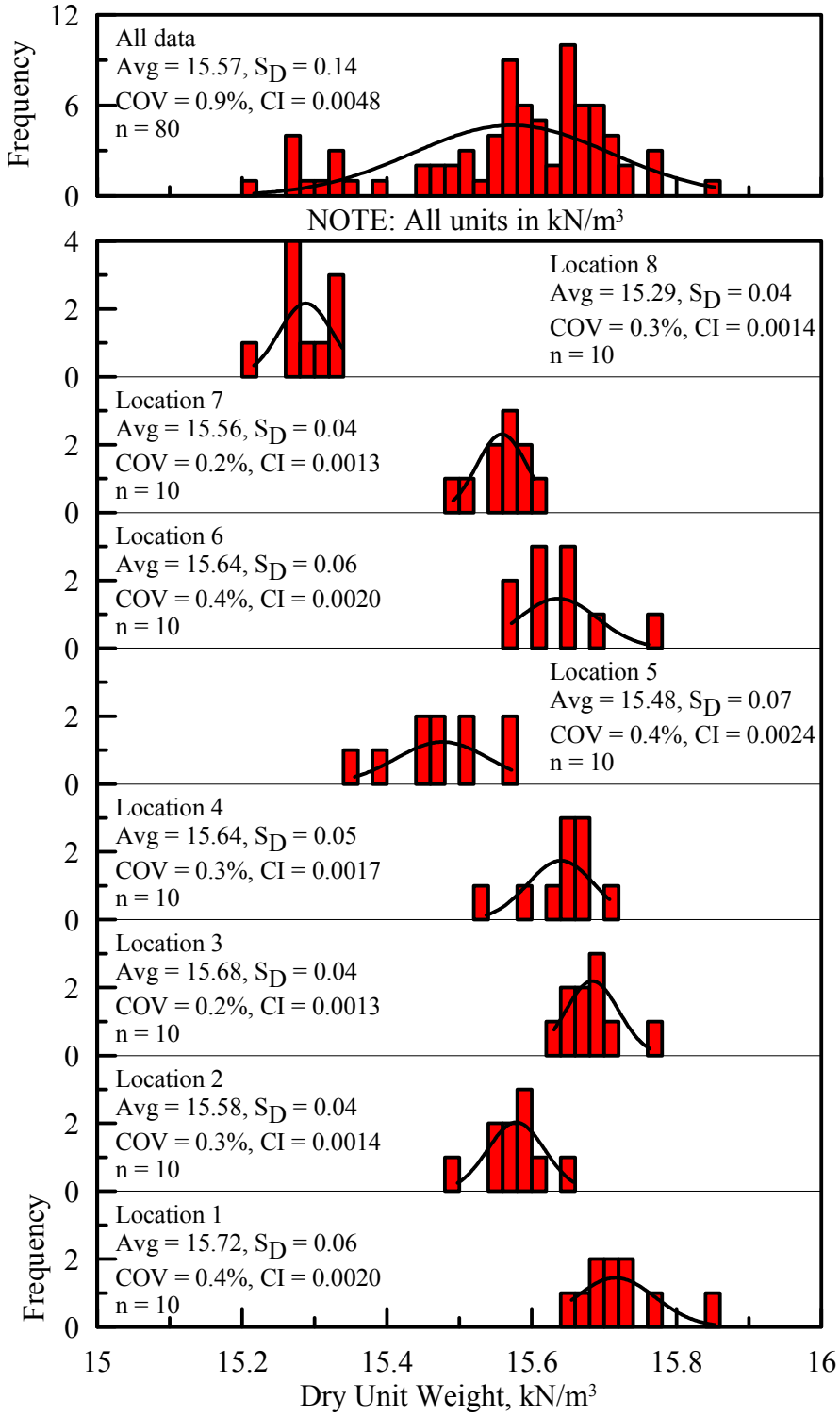

Figure 4.8 Histograms of γ_{dry} for different measurement locations within calibration box

It should be noted that, while Location 8 was the outlier of average γ_{dry}, the measured values for that location all contribute to the actual determination of γ_{dry}. To assess the bias of the eight different locations within the calibration box, boxes prepared to different γ_{dry} were compared. It was found that there was no significant bias for different locations. Because each of the eight measurement locations within the calibration box satisfy the edge distance requirements for unbiased measurements described in previously, it is likely that any bias measured at a given location is due to soil inhomogeneity, rather than instrument measurement error.

Including Location 8, the variance for individual locations and all data are 0.002 – 0.005 $(kN/m^3)^2$ and 0.020 $(kN/m^3)^2$, respectively. If the typical variance of a set of readings at a single location, or the variance related to nuclear gage itself, is 0.004 $(kN/m^3)^2$, then the variance due to soil inhomogeneity within the calibration box can be approximated as 0.016 $(kN/m^3)^2$. This is equivalent to a S_D of soil inhomogeneity in the calibration box of 0.12 kN/m^3, which is consistent with the distribution of measurements around the calibration line as can be seen in the nuclear gage calibration in Fig. 4.5.

Fig. 4.9 shows the precision and COV vs measurement depth for sets of twenty 15 sec measurements taken at the same location at different source rod depths in the calibration box. A single hole was bored into the soil, and 20 measurements were taken at each depth from the backscatter mode to a depth of 200 mm in 50 mm increments, called measurement set A. An additional 20 measurements were then taken at each depth, called measurement set B. There is very little change in precision from set A to set B. There is very little change in precision and COV from the 50 to

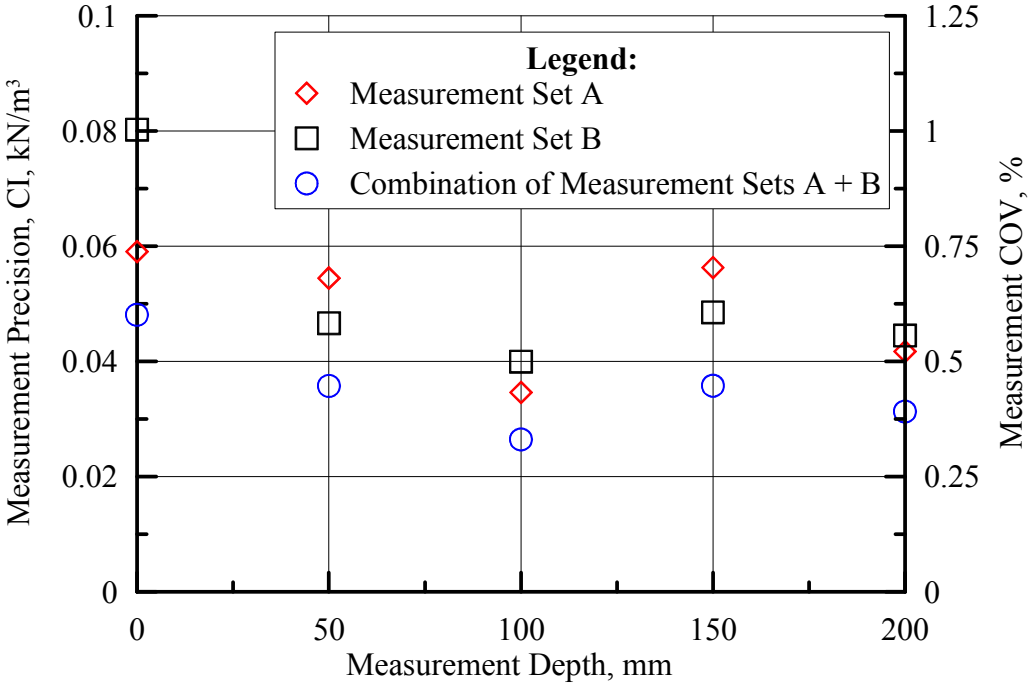

Figure 4.9 Precision and COV vs source rod depth for nuclear gage measurements of γ_{dry} in calibration box

200 mm depth for direct transmission measurements, while backscatter (depth = 0 mm) has a higher precision. Sets A and B were combined to form Set (A + B), which has a smaller precision, showing the influence of a larger sample size on that parameter.

4.5 Soil Placement and Compaction

The most important material property of the soil is shear strength, which is reflected in the value of $\phi_{ds\text{-}p}$. The value of $\phi_{ds\text{-}p}$ is strongly correlated with both γ_{dry} and w, as shown in the previous chapters. Control of γ_{dry} and w for in-place soil is therefore critical for establishing and reporting relatively uniform conditions of soil strength for large scale soil structure interaction tests.

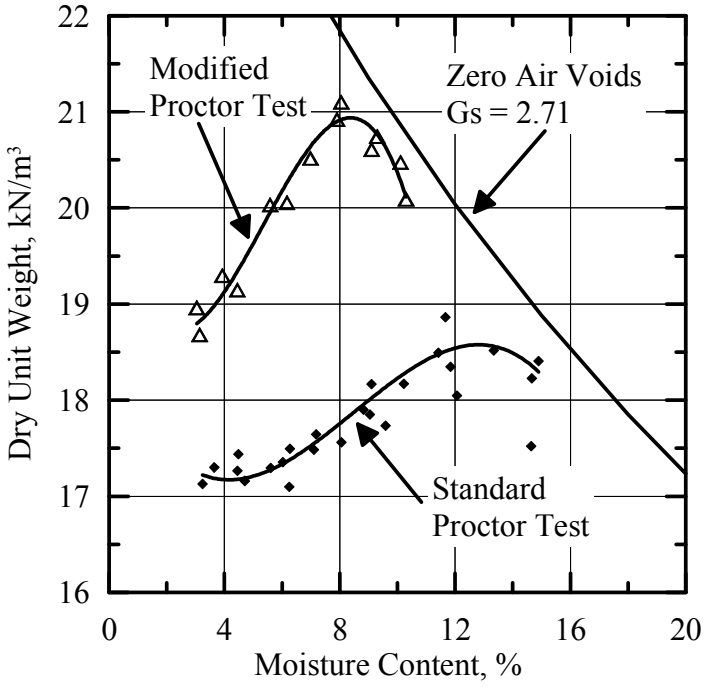

Figure 4.10 Proctor compaction plot of γ_{dry} vs w

4.5.1 Proctor Compaction Tests

The value of γ_{dry} at a given compactive effort depends on w, and an optimum w exists at which the soil will achieve its maximum γ_{dry}. For the Standard Proctor Test, ASTM D698 (ASTM, 2003b), a 24.4 N compaction hammer is dropped 25 times from a height of 305 mm for each of three equal lifts placed in a 943 mm^3 cylindrical mold, and a total energy of 600 kN-m/m^3 is applied to the soil specimen. For the Modified Proctor Test, ASTM D1557 (ASTM, 2003c), a 44.5 N compaction hammer is dropped from a height of 457 mm to compact soil (in the same cylindrical mold as the Standard Proctor Test) and a total energy of 2,700 kN-m/m^3 is applied to the soil specimen. Figure 4.7 shows Proctor compaction curves for partially saturated RMS graded sand using data gathered by Turner (2004) and the current research. The zero air voids line represents the maximum possible γ_{dry} at a given w, and is calculated

using the specific gravity of RMS graded sand, 2.71. Tests using the Modified and Standard methods were performed over a range of w from 3 – 15%, giving optimum w for the two methods of 8 and 13%, respectively. Both of these w, however, are well above the residual w for RMS graded sand, and thus are not practical choices for the target w for large scale tests. Turner (2004) ran large scale tests at w to 8%, and significant water drained from the upper lifts to the lower lifts and bottom of the box. The placement of soil wetter than the residual w can lead to an unknown final distribution of w and γ_{dry}.

4.5.2 Determination of Ideal Lift Thickness and Source Rod Depth

Lift thickness was investigated by performing measurements in a special box with interior dimensions of 2.4 m x 2.4 m x 1.2 m, which was similar in stiffness to the large scale 2-D box. Lift depth was varied from 100 mm, the typical lift thickness for sand placed by Trautmann and O'Rourke (1983) and Turner (2004), to 300 mm, the maximum lift thickness measureable by the nuclear gage. Lift thickness was chosen to be 200 mm. This dimension is consistent with lift thicknesses specified for compacted fill in the field (NYSDOT, 2008), and provides for efficient placement of sand in large-scale tests.

To evaluate the variation of γ_{dry} with measurement depth in the lift, 200 mm lifts were measured, varying source rod measurement depth from 0 mm (using backscatter mode) to 50 - 200 mm (using direct transmission mode). Histograms of γ_{dry} are shown in Figure 4.8 for different measurement depths. Consistent with previously shown data, S_D decreases as measurement depth increases. Average γ_{dry} is

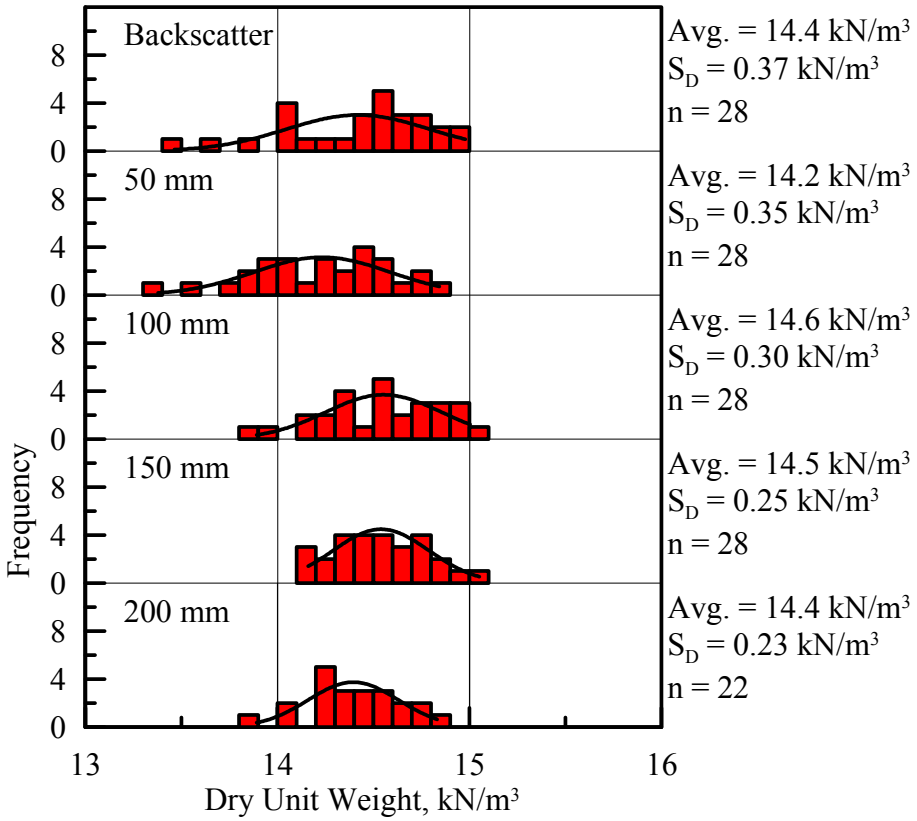

Figure 4.11 Histograms of nuclear gage measurements of γ_{dry} in 2.4 m x 2.4 m x 1.2 m box at different measurement depths for 200 mm lifts

lowest at 50 mm depth, and highest at 100 mm depth, while there is not a significant difference in measurements at backscatter, 150 mm, and 200 mm.

In summary, measurement precision and COV were found to decrease significantly with an increase in time duration from 15 to 240 seconds. Measurement COV at 15 seconds was very good, at 5%, and a sixteen-fold increase in time duration resulted in only a two-fold decrease in COV, to 2.5%. Because efficiency in measuring soil properties for large scale tests is critical, the shorter time duration of 15 seconds was chosen for all measurements taken in the calibrations and large scale tests.

Although it was seen that different locations in the box give different measurements of γ_{dry}, an analysis of different sources of variance showed that the variance of the nuclear gage can be isolated from the variance due to soil inhomogeneity. As long as the edge distance requirements stated previously were followed, there was no significant bias due to location of measurement.

A source rod depth of 150 mm was chosen for partially saturated sand. Since the source rod hole must be pre-bored 50 mm deeper than the source rod measurement depth for a given measurement, a measurement depth of 150 mm allows measurements of the bottom lift to be performed for large scale tests. For dry soil, the backscatter mode was used, as discussed previously.

4.5.3 Preparation of Soil to Target Water Content

For large scale tests, soil was stored prior to testing in permanent wall-mounted soil storage bins, shown in Figure 4.9a. Applying water to in-place soil and mixing the soil manually prior to compaction was found to be labor intensive and led to inconsistent w and γ_{dry} of the compacted material. Spraying the soil as it traveled on conveyors from the soil storage bins to the test box resulted in water covering test equipment, with the potential for damaging the data acquisition systems.

The most effective method was to add water to the sand while it was still in the soil storage bins. A few days prior to placement in the large box, the w of the soil in the storage bins was measured by taking samples at the soil bin doors and at the top of the soil bin, and the amount of water to be added was calculated based on the current

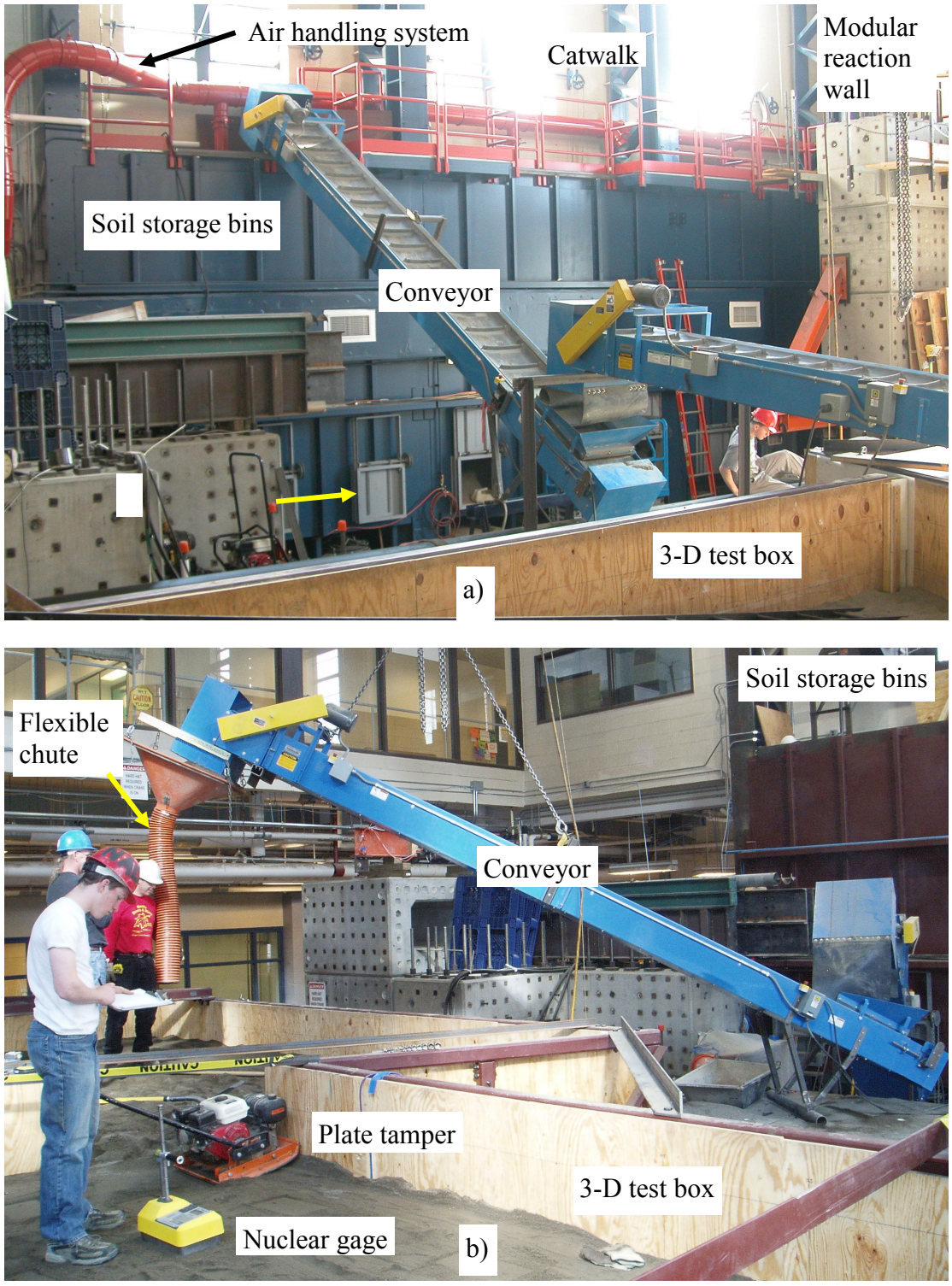

Figure 4.12 Soil conveyors a) Photo of soil storage bins and conveyors for soil removal from 3-D test box b) Photo of conveyor-chute setup for placing soil

and target w of the soil as well as the amount of soil to be prepared. The water was then added in stages over a period of days by a laboratory technician with a garden hose standing on the catwalk above the soil storage bins. Adding the water all at once tended to oversaturate or undersaturate certain regions of the soil and caused excess water to drain from the soil bins. By adding water in stages over a few days the water was able to penetrate the soil with w = 4 – 5%, consistent with the residual state described in Chapter 3. Additionally, if too much water was added and the soil happened to be oversaturated after an individual stage, only a small amount of excess water would flow from the soil storage bins, creating a manageable cleanup situation.

4.5.4 Placement of Soil by Conveyor-Chute Method

The quickest, safest, and most repeatable method of placing 200 mm lifts of soil in the large-scale test boxes was the conveyor-chute system, shown in Figure 4.9b. A 4.3 m long conveyor was placed on the lab floor next to the soil storage bin, and a door at the bottom of the storage bin was partially opened to control soil flow onto the first conveyor. The second 4.3 m long conveyor was placed on the modular reaction wall, and fed soil to the third conveyor. This 6.7 m conveyor was supported at one end by the modular reaction wall and on the other end by the 89 kN capacity overhead crane. Soil flowed from the third conveyor into a hopper attached to the conveyor and out through a wire-ribbed, flexible plastic chute 3.1 m long and 200 mm in diameter. By hoisting the crane to the proper height, the end of the chute was positioned approximately 300 mm above the previous lift, for easy deposition of soil. As soil moved on the conveyors from the storage bins to the test box, the flexible chute was moved around to route soil throughout of the box to place an even 200 mm thick lift. High spots were evened out with a garden rake, and the soil was compacted using a

plate tamper. The plate tamper used was a Honda GX 160 with a 4.1 kilowatt (5.5 horsepower) gasoline powered engine. Two passes of the plate tamper at full throttle were used to compact the soil to a typical γ_{dry} of 15.8 kN/m^3. After the two passes, soil at the corners and edges of the box, as well as any spots missed by the plate tamper, were manually compacted to the target γ_{dry}.

4.5.5 Measurement of Soil Dry Unit Weight and Water Content

Measurements of γ_{dry} and w were taken and recorded for each lift, noting the specific measurement location within the lift. Nuclear gage plots were prepared in a 1.2 m x 0.6 m grid, with 5 rows north-south and 4 columns of measurements east-west. Plots were made by leveling an area of soil 0.4 m x 0.2 m using the steel scraper plate, and boring a hole to a depth of 200 mm (50 mm below the target source rod measurement depth) using a drive pin. At each plot, a 15 sec measurement was taken using the nuclear gage with a source rod depth of 150 mm, and unit weights of soil and water were recorded. After the nuclear gage was used, a sample of soil was obtained for analysis of w by the oven dry method. When all measurements were completed, the next lift of soil was placed. If the next lift was not to be placed until the following day, the soil surface was covered with a plastic sheet to restrict evaporation of water.

After the final lift was placed, compacted and measured, the soil surface was leveled to the desired height using a screed, and a 100 mm x 100 mm square grid was spray painted on the surface using a template. Post-test, the soil was carefully excavated using manual shovels and a 0.55 m^3 capacity clamshell bucket, and returned to the soil bins on conveyors. Figure 4.9a shows the typical conveyor setup for

moving excavated soil from the 3-D test box to the soil storage bins (please note that this photograph shows only two of the available three conveyors).

4.6 2-D Box Soil Preparation

A 2.4 m x 2.4 m x 1.8 m steel framed test box, shown in Figure 4.13a, was fabricated to the same proportions as the 1.2 m x 1.6 m x 1.2 m boxes used by Trautmann and O'Rourke (1983) and Turner (2004). This test box is called the 2-D box because it generates soil-structure interaction under plane strain (2-D) conditions. A pipe was buried in soil, which protruded through the sides of the box. It was pulled laterally through the soil a distance of 250 mm by a pair of hydraulic actuators. A glass side wall allowed viewing of the soil deformation during the test, and a steel slider system prevented soil from leaking from the box at the intersection between the pipe and box wall. For some tests, a smaller version of the 2-D box, identical in dimensions to Turner's box at 1.2 m x 1.6 m x 1.2 m, was constructed within the larger 2-D box, with a similar glass side wall, Formica end walls, floor, and opposite sidewall as the large 2-D box. This box, shown in Figure 4.10b, was used to duplicate the partially saturated sand tests of Turner (2004).

Three tests on dry sand and six tests on partially saturated sand were run using the large 2-D box, and two tests on partially saturated sand were run using the small 2-D box. Dry sand was placed by the conveyor-chute method in 100 mm lifts and compacted using an electric vibrating plate compactor. As described by Trautmann and O'Rourke (1983), the compactor was connected in series through a rheostat and a half-wave rectifier unit. The compactor consisted of a VC-35 electric vibrator,

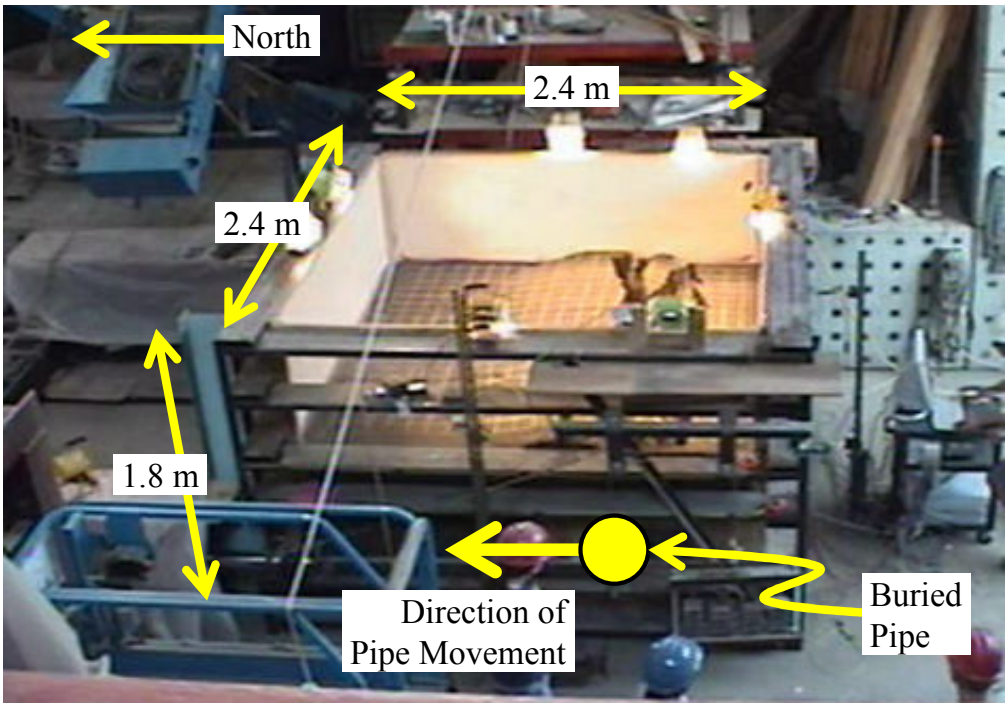

a)

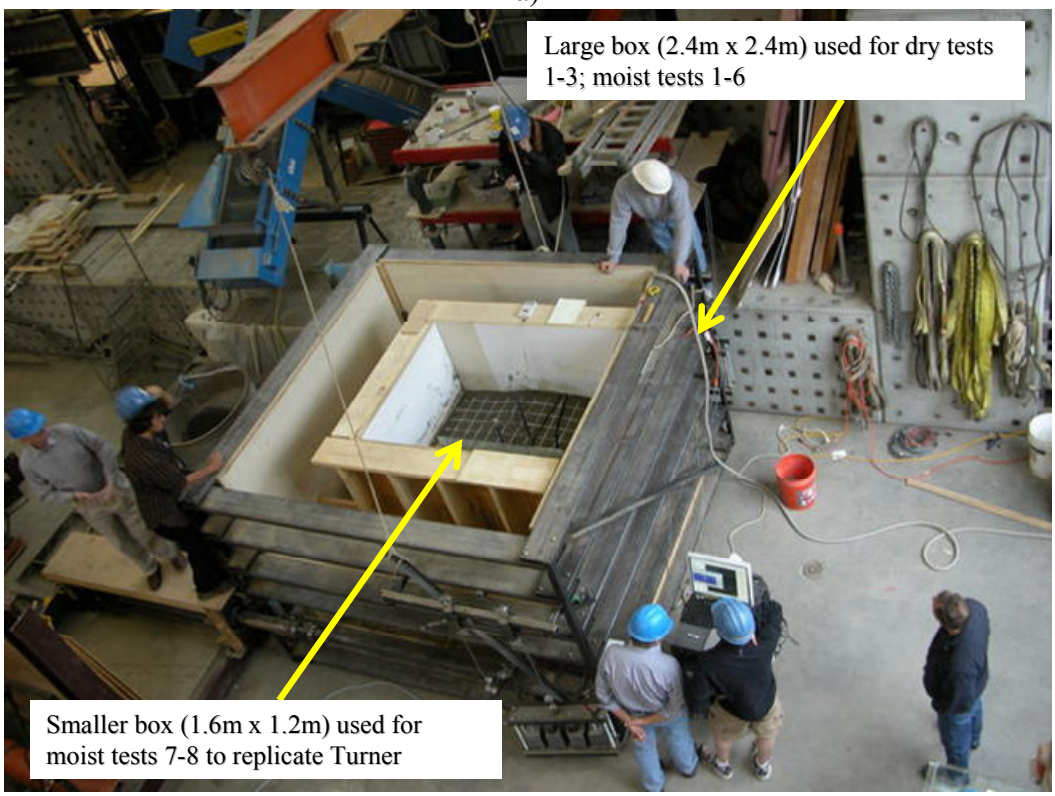

b)

Figure 4.13 Photos of 2-D test box a) Large 2-D test box b) Small 2-D test box

produced by Syntron Division, FMC Corp., Homer City, PA, mounted to a 6-mm x 457 mm x 457 mm steel plate. The compactor vibrated at 60 Hz with amplitude of 1.6 mm (0.06 in.) when loaded by a weight of 650 N (146 lbs) or less, and draws 3 amperes at 110-VAC.

Dry sand γ_{dry} was measured using both the density scoop and nuclear gage. After placing, compacting and leveling the soil, twelve nuclear gage plots were made on the soil surface, with a minimum of 300 mm from the edge of a plot to the nearest wall. After nuclear gage readings were made at each plot using the backscatter mode, density scoop readings were taken, using the leveled, undisturbed area within the existing nuclear gage plot to take the density scoop sample. After the final soil lift was placed, compacted and measured, the surface was leveled to the required height and painted with a 100 mm by 100 mm grid, using red paint for contrast with the light colored dry sand surface.

Partially saturated sand was placed using the conveyor-chute method and compacted using the plate tamper. For γ_{dry} heavier than placed in the 3-D test box, up to 16.5 kN/m^3, different methods were used to compact the soil, such as reduced lift thicknesses, a jackhammer-plate compaction method, or the vibrating plate. It was found that multiple passes of the plate tamper at a reduced lift thickness of 100 mm was the most consistent compaction method for partially saturated sand to achieve higher γ_{dry}. To take nuclear gage measurements for this soil, two 100 mm lifts were compacted, then the resulting 200 mm lift was measured in the same way a typical 200 mm lift was be measured for lower γ_{dry}. While compacting lifts, great care was taken by the operator of the plate tamper to avoid contact with the tactile pressure sensors

installed on the pipe. A vertical layer of Styrofoam was placed at the glass sidewall during compaction to safeguard against damage due to contact with the plate tamper.

Figures 4.14 and 4.15 show histograms of relevant statistics for each lift of 2-D Test 5, which was performed with partially saturated sand. The shaded areas in the figures indicate soil that was placed beneath the invert. The data from these levels are not included in the overall histogram at the top of the figures. The average and statistical spread of the data for each parameter is consistent from lift to lift, indicating that soil placement and compaction methods used were consistent.

Figs. 4.14a and b shows histograms of nuclear gage γ_{dry} and density scoop γ_{dry}, respectively. The COV of nuclear gage measurements on γ_{dry} is 1.1 – 1.5%, in comparison with 1.7 – 2.3% for density scoop measurements of γ_{dry}. Average γ_{dry} is greater for the nuclear gage (16.21 - 16.39 kN/m^3) than the density scoop (15.96 - 16.19 kN/m^3). From visual observation, nuclear gage γ_{dry} is closely clustered about the mean value, while there are more outliers for density scoop γ_{dry}. The distributions showing a collection of all data above the pipe invert show that by either measurement device, γ_{dry} was very consistent from lift to lift, as the COV for the overall distribution is within the range of the COV for individual lifts (1.3% for the nuclear gage, 2.0% for the density scoop).

Figs. 4.15a and b shows histograms of nuclear gage w and oven dry w, respectively. The measurements of oven dry w are consistently more precise (CI = 0.04 – 0.10%) than nuclear gage w (CI = 0.15 – 0.35%), while average oven dry w was consistently higher (4.03 – 4.23%) than average nuclear gage w (3.46 – 3.75%).

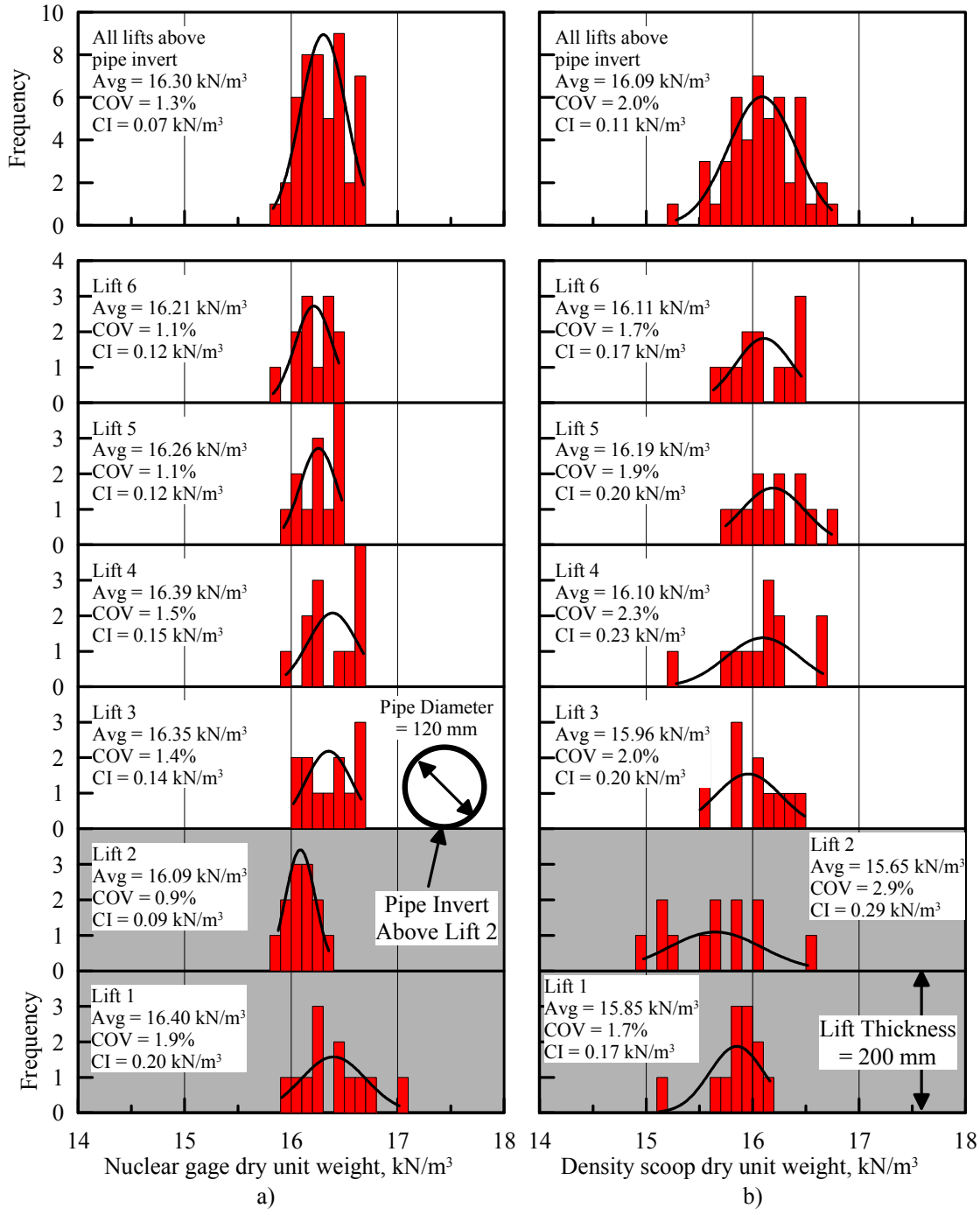

Figure 4.14 Histograms of γ_{dry} for individual lifts and all lifts above pipe invert for 2-D Test 5 measured using a) Nuclear gage b) Density scoop

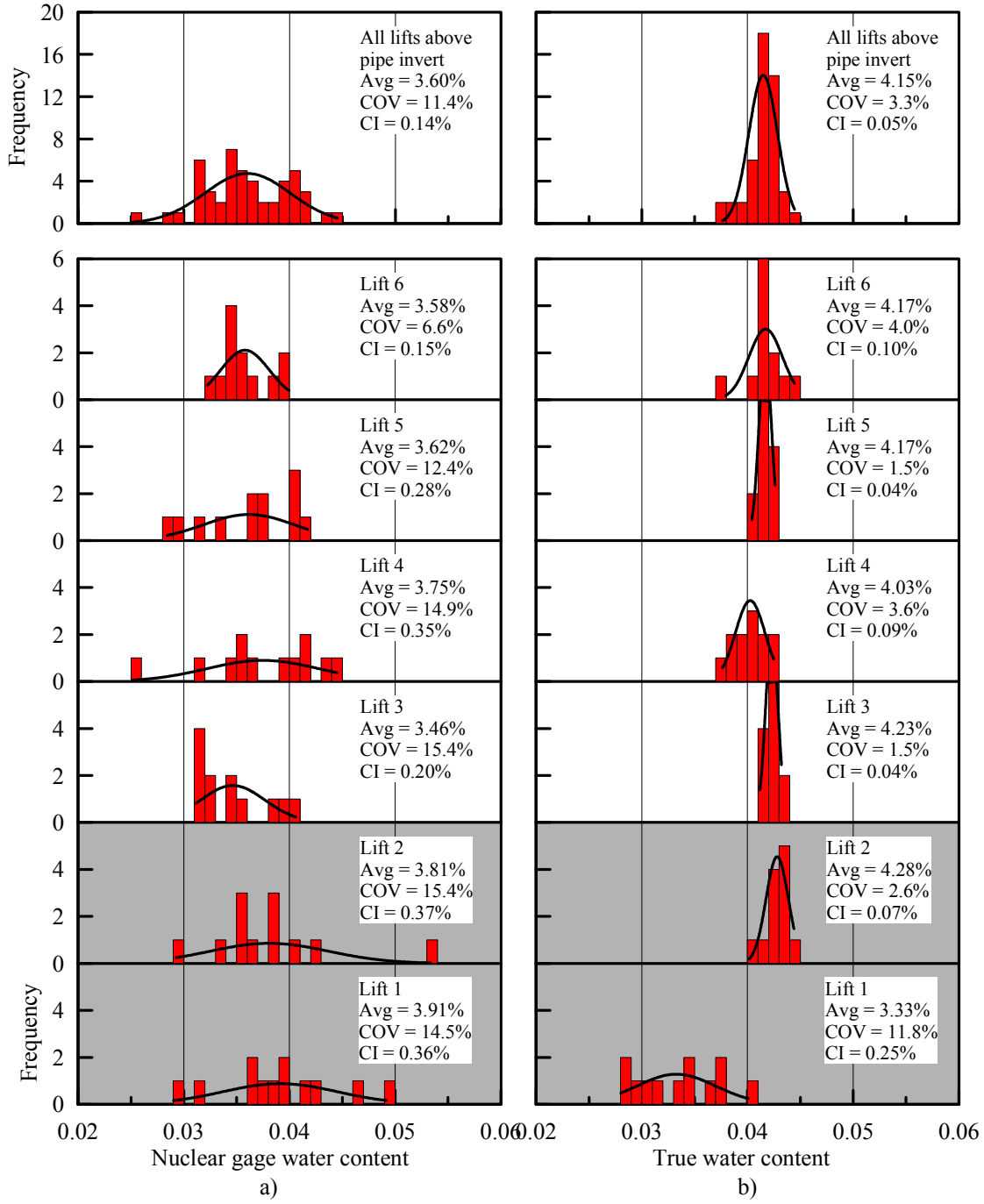

Figure 4.15 Histograms of w for individual lifts and all lifts above pipe invert for 2-D Test 5 measured using a) Nuclear gage b) Oven dry method

Histograms of oven dry w show closely clustered distributions in lifts 2 - 6, indicating that variability of w was very well controlled for soil placed in these lifts. The overall histogram of oven dry w has an average and COV similar to those of the individual lifts, showing good control of average w from lift to lift. On the other hand, distributions of nuclear gage w consistently show greater scatter for lifts 2 – 6. The contrast between the two measurement methods indicates that the variability of nuclear gage distributions is due to the device, and not due to variations of w.

The spatial variability of γ_{dry} in each lift is shown in Fig. 4.16 by gray scale contours of 0.15 kN/m^3. For each lift the contours were developed using twelve measurements, and contours were drawn by Grapher 7.0 (Golden Software, Inc.) using the "Inverse Distance to a Power" method with a $1/r^2$ relationship (Davis, 1986; Franke, 1982). The spatial patterns differ from lift to lift with little or no overlap in easily recognizable zones and aerial distributions of γ_{dry}. These patterns show random variation in which γ_{dry} tends to be independent of fixed location in the test box.

4.7 Direct Comparison of Measurement Devices

Figure 4.17 shows a plot of nuclear gage γ_{dry} vs density scoop γ_{dry} for dry sand. Data were obtained by compacting soil in the calibration box to the desired γ_{dry}, taking nuclear gage measurements at each of eight locations, and taking density scoop measurements at each of the locations. The average value of the eight nuclear gage measurements is plotted vs the average value of the eight density scoop measurements in Fig. 4.17, and a linear regression is fit to the data. Also plotted in Fig. 4.17 are data points for tests 2-D 1 through 2-D 6 representing the average of the twelve

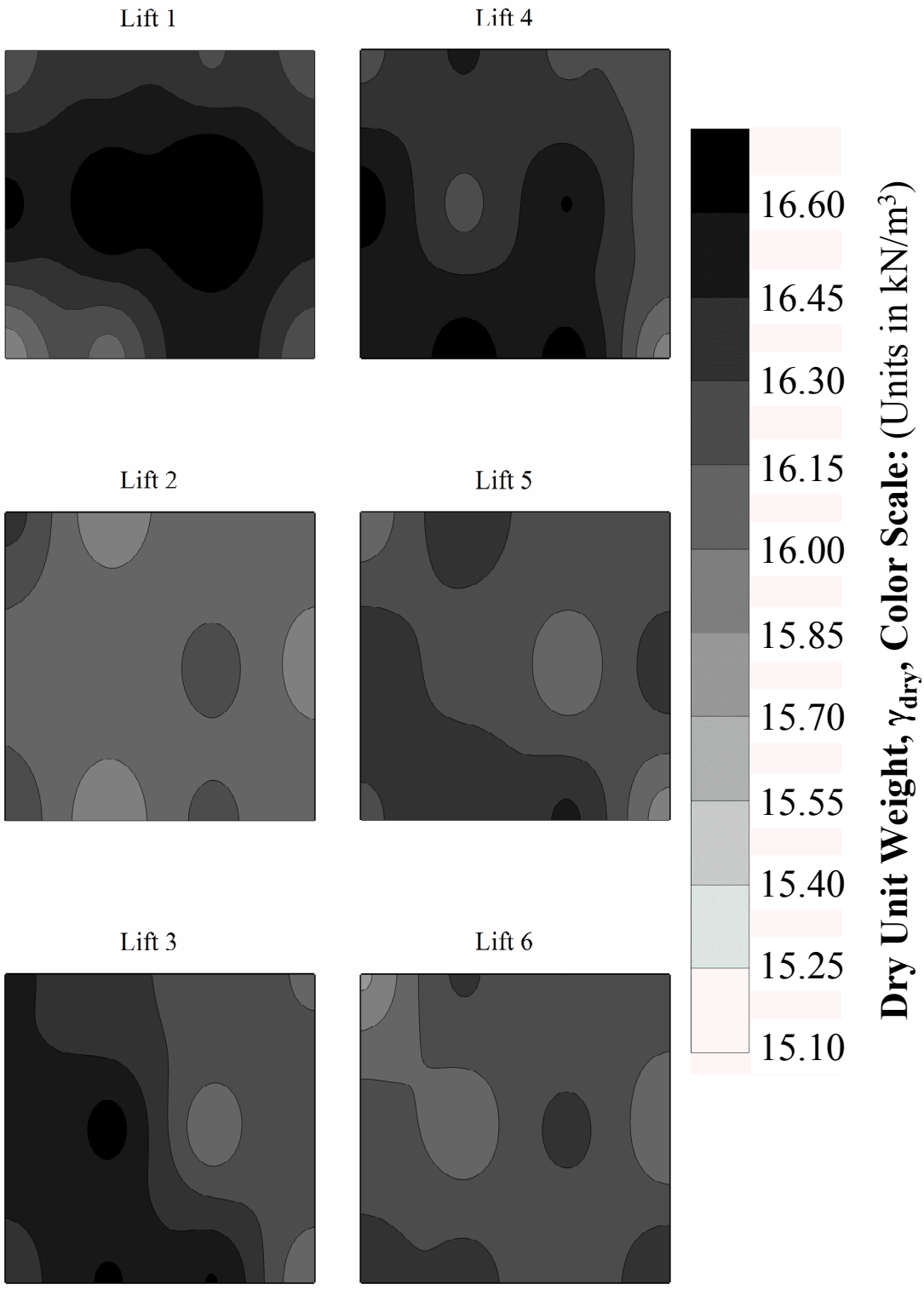

Figure 4.16 Contour plots of γ_{dry} for each lift of 2-D Test 5

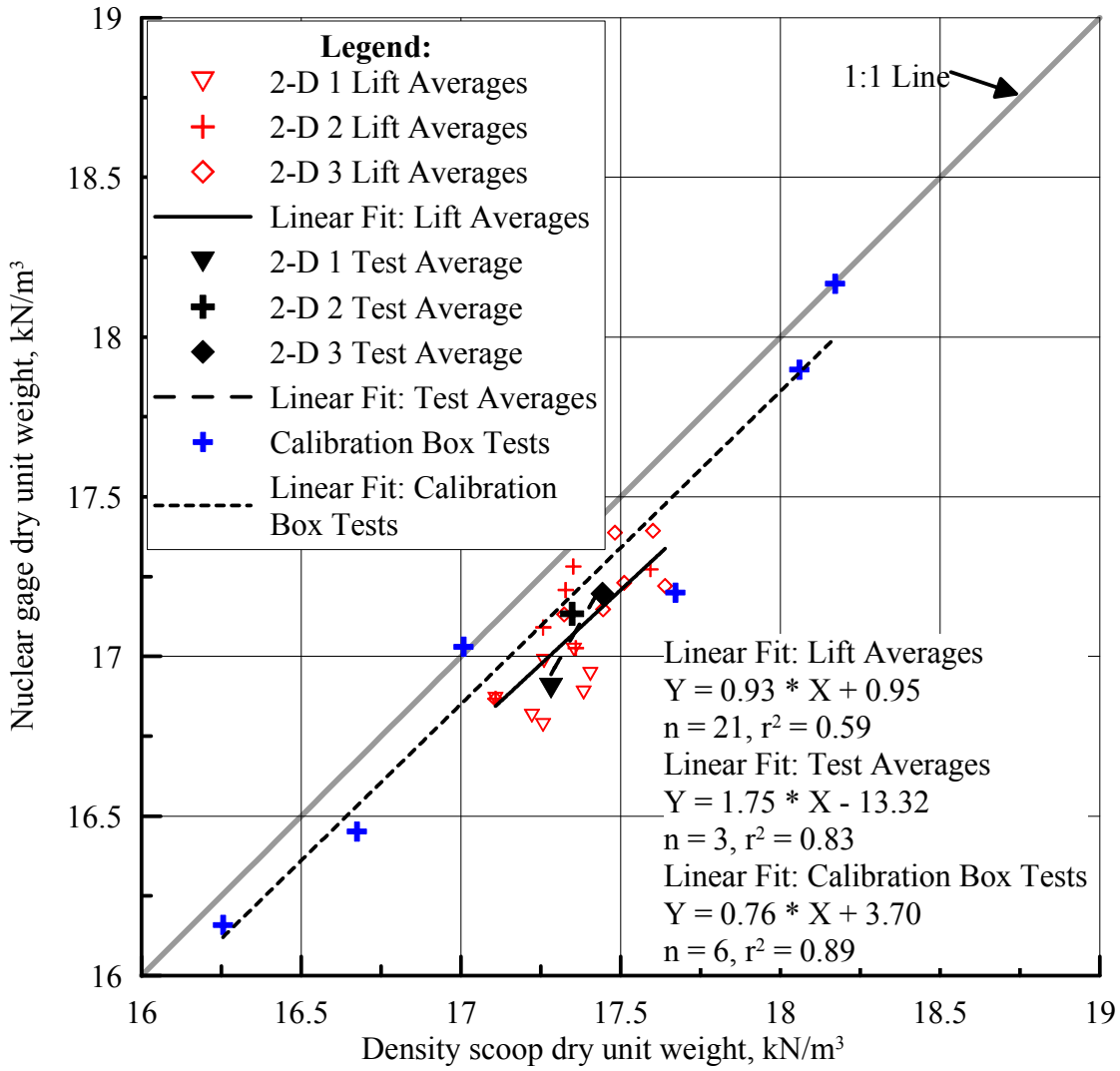

Figure 4.17 Lift averages of nuclear gage dry unit weight vs density scoop dry unit weight for 2-D tests on dry sand

measurements of γ_{dry} taken for each lift by the nuclear gage vs the average of twelve density scoop measurements taken at the same locations. A linear regression is plotted through the lift-by-lift data. The average of all measurements of γ_{dry} for a given test are plotted for the nuclear gage vs the density scoop, and a linear regression is plotted through those data. It can be seen in the figure that the density scoop averages overestimate the average nuclear gage values by about 0.0 – 0.8 kN/m^3.

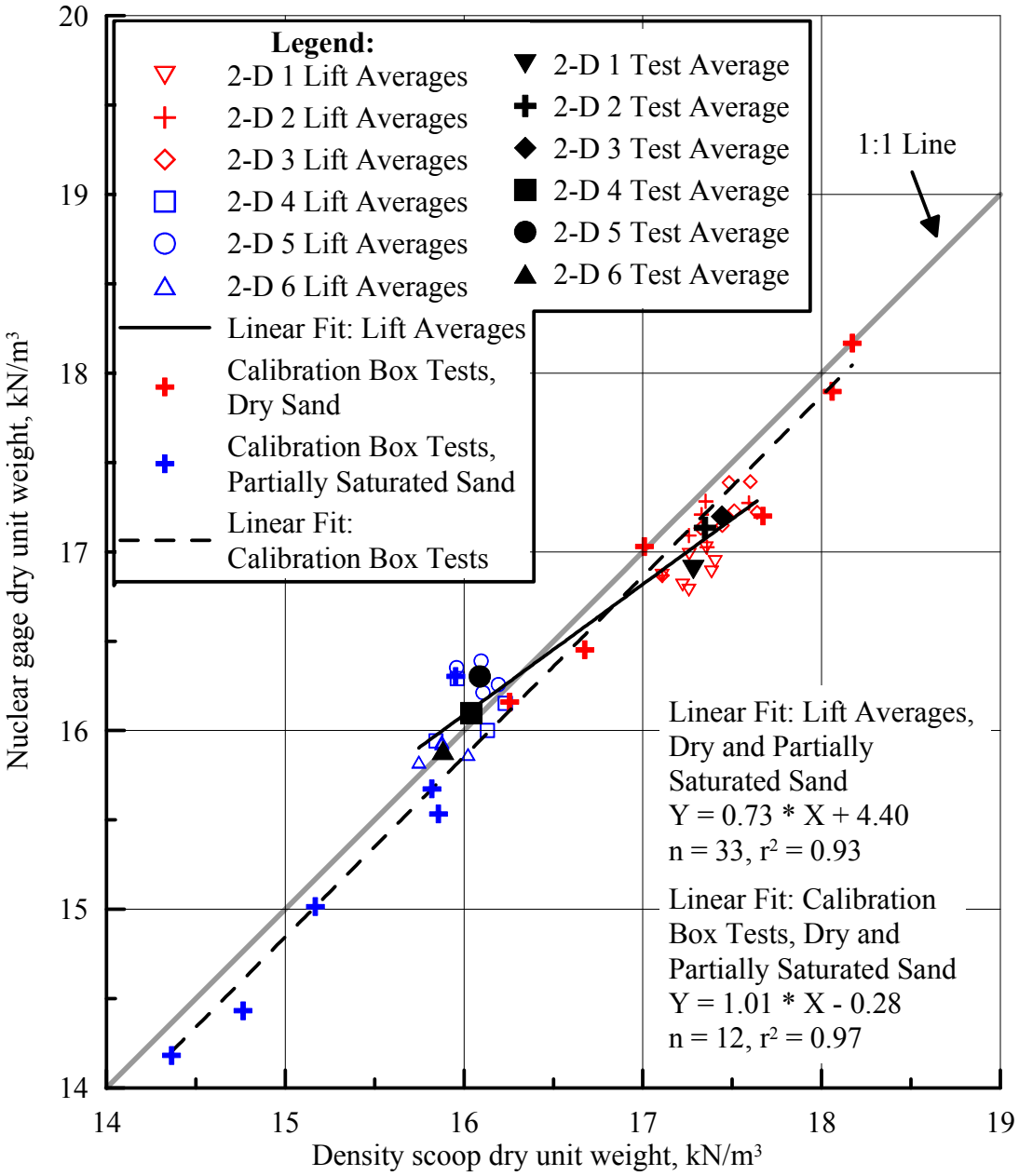

Figure 4.18 Lift averages of nuclear gage dry unit weight vs density scoop dry unit weight for 2-D tests on partially saturated and dry sand

Figure 4.18 shows nuclear gage vs density scoop data for dry and partially saturated sand. Dry sand data are the same as presented in Fig. 4.17, while partially saturated sand data are shown for tests with the calibration box and 2-D test box. As with dry sand, the partially saturated sand lift averages are shown. A linear regression is plotted for dry and partially saturated sand calibration box data, and has a slope close to 1 and a very strong r^2 of 0.97. Lift averages from 2-D tests for partially saturated sand are clustered around the 1:1 line, as are 2-D test averages. A linear regression for 2-D test lifts is plotted for partially saturated and dry sand, with r^2 = 0.93.

Figs. 4.17 and 4.18 show that the γ_{dry} from the nuclear gage and density scoop measurements for partially saturated sand are in favorable agreement. For dry sand, the density scoop measurements provide a γ_{dry} that is approximately 0.4 kN/m^3 larger than the γ_{dry} measured by the nuclear gage in the range of γ_{dry} = 17.0 – 17.7 kN/m^3 as determined by the density scoop.

4.8 3-D Box Soil Preparation

The large-scale test basin is referred to as the 3-D box. Each half basin consisted of a three walled steel framed structure 6.6 m x 3.2 m x 2.3 m, with the two halves separated by a plane of displacement oriented at 65° with respect to test pipelines installed in the basin. Each test pipeline was semi-rigidly fixed at each end wall of the box, and was subjected to complex soil-structure interaction forces by 1.2 m strike slip movement of the fixed box past the movable box. A photo of the 3-D box is shown in Figure 4.19, and a schematic of the initial and final positions of the 3-D box and pipe is presented in Figure 4.20.

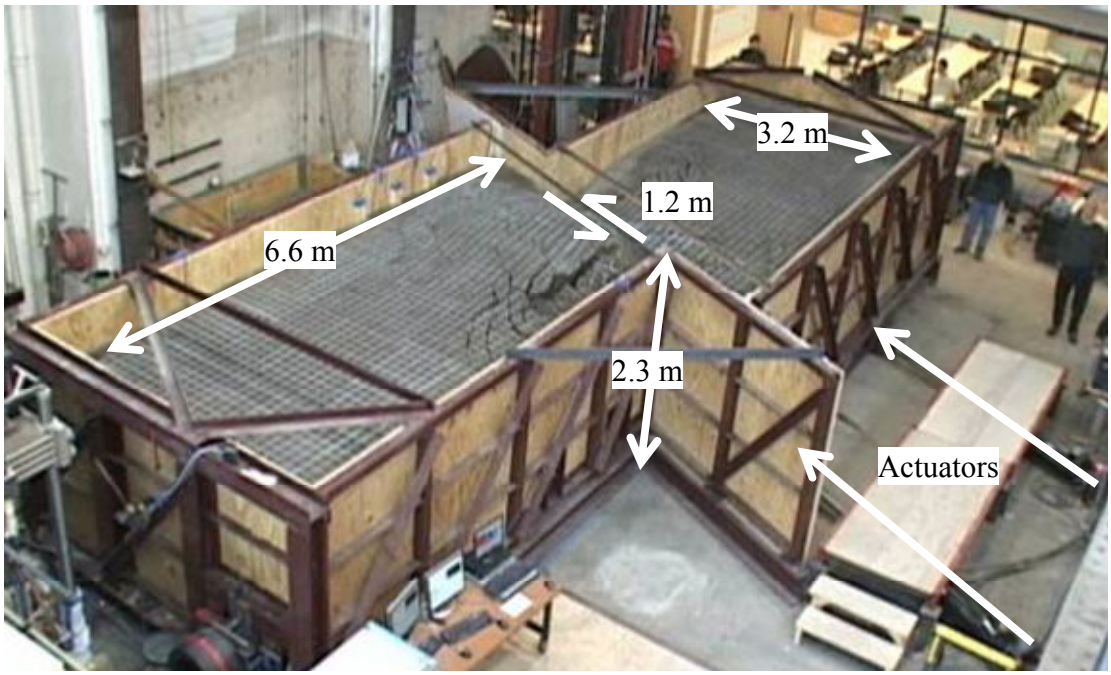

Figure 4.19 Photo of 3-D test basin with key dimensions

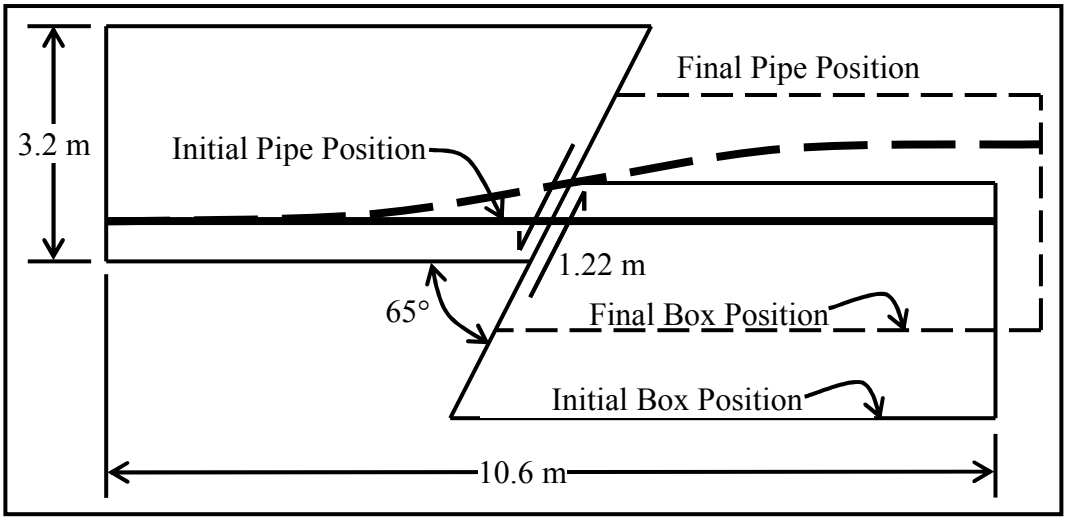

Figure 4.20 Plan view schematic of 3-D box with key dimensions and geometry

Six tests on partially saturated sand were run using the 3-D box. As discussed earlier, partially saturated sand was placed using the conveyor-chute method and compacted by two passes of the plate tamper. After soil placement, the surface was

leveled, painted with a white grid at 100 mm by 100 mm spacing, and covered with plastic to prevent water evaporation.

The target γ_{dry} for the 3-D tests was 15.8 kN/m^3. Figure 4.21 shows depth vs measured soil properties for all 3-D tests. The more darkly shaded area in the figure indicates soil placed beneath the invert of the pipeline, which is not factored into the overall average of the soil properties for a given test. Pipelines installed in the field are placed on existing soil, and backfill is compacted around and above them. The layer of soil underlying the test pipelines is equivalent to existing basal soil in the field.

As can be seen in the Fig. 4.21, γ_{dry} is consistently between 15.6 – 15.9 kN/m^3 for most lifts, and w by oven dry methods is consistently between 3 – 5% for most lifts. The index value of $\phi_{ds\text{-}p}$ was calculated using the relationship of $\phi_{ds\text{-}p}$ vs γ_{dry} that is presented in Fig. 3.12 for partially saturated RMS graded sand. It should be noted that this relationship assumes that a cohesion is present in partially saturated sand at peak shear strength, and the value of cohesion depends on γ_{dry}, where c_{ds} = 2.1 kPa for γ_{dry} < 16 kN/m^3, and c_{ds} = 3.4 kPa for γ_{dry} > 16 kN/m^3.

Outliers of γ_{dry} and w in Fig. 4.21 are associated with random variations in the soil and energy applied, as well as deviations in the method of soil placement. For example, soil was sometimes placed in the test basin by transferring it from 1.2 m x 1.0 m x 0.6 m steel storage containers to the surface of the previous lift. This method gave higher γ_{dry} than the conveyor-chute method because the soil had to be shoveled and leveled manually by lab personnel. The greater amount of handling with this

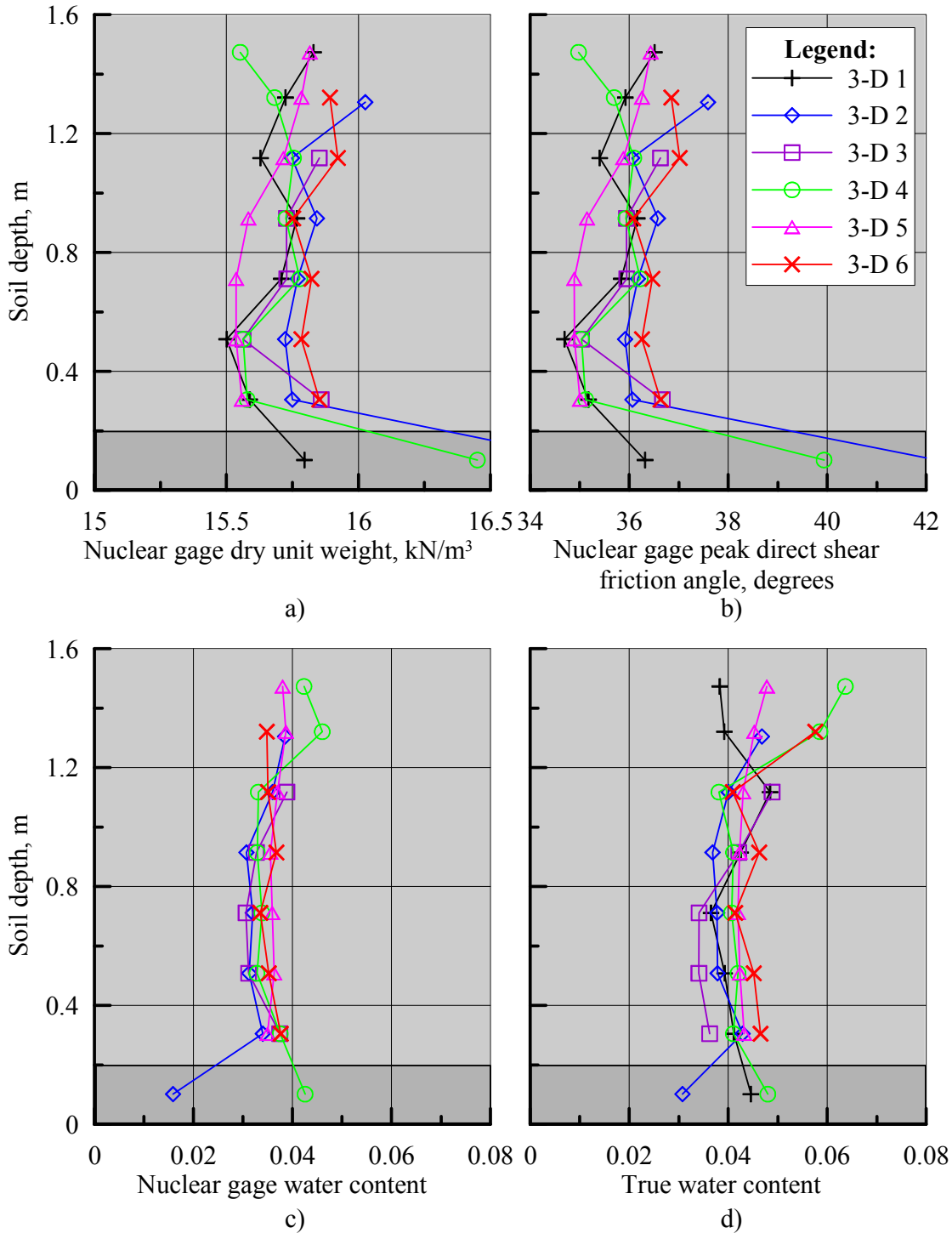

Figure 4.21 Plots of soil material properties vs depth for 3-D tests a) Nuclear gage γ_{dry} b) Nuclear gage ϕ_{ds-p} c) Nuclear gage w d) Oven dry w

method led to increased γ_{dry}. When this method was necessary to place soil, it was used only for the bottom or top lifts, because these lifts had the least effect on soil-pipeline interaction. Because soil placed by transferring from steel containers was not watered with the soil in the storage bins, water was added in-situ, sometimes resulting in a measured w that was higher than the target value.

Figures 4.22 and 4.23 show histograms of soil properties for each lift of 3-D Test 5. . Figs. 4.22a and b show histograms of γ_{dry} and $\phi_{ds\text{-}p}$, respectively, for each lift of 3-D Test 5, as well as histograms showing a summary of all data above the pipe invert. The value of average γ_{dry} is consistent for all lifts, varying from 15.54 – 15.82 kN/m^3. The precision of γ_{dry} for a given lift (as discussed earlier, using a two-tailed probability of 0.05) is between 0.072 – 0.083 kN/m^3 for lifts 2 through 7, while lift 8, where soil was placed by transferring from steel containers, has a precision of 0.118 kN/m^3, showing the greater variability of that method. The value of $\phi_{ds\text{-}p}$ is indexed to γ_{dry} as discussed previously, so trends in one parameter are repeated in the other. Average $\phi_{ds\text{-}p}$ varies from 34.9 – 36.4°. while precision varies from 0.35 – 0.46° for lifts 2 – 7, and 0.65° for lift 8. The range of COV for individual lifts is higher for $\phi_{ds\text{-}p}$ (3.1 – 5.6%) than for γ_{dry} (1.3 – 2.3%), while the values of COV from the histograms of all data above the pipe invert are consistent (1.3% for γ_{dry}, 4.3% for $\phi_{ds\text{-}p}$) with lift COV values, indicating good consistency of soil placement from lift to lift.

Figures 4.23a and b show lift by lift histograms of nuclear gage w and oven dry w, respectively. Also shown are histograms representing all data above the pipe invert. Average nuclear gage w for lifts varies from 3.50 – 3.87%, and precision varies from 0.14 – 0.28%. Average oven dry w varies from 4.20 – 4.78%, and

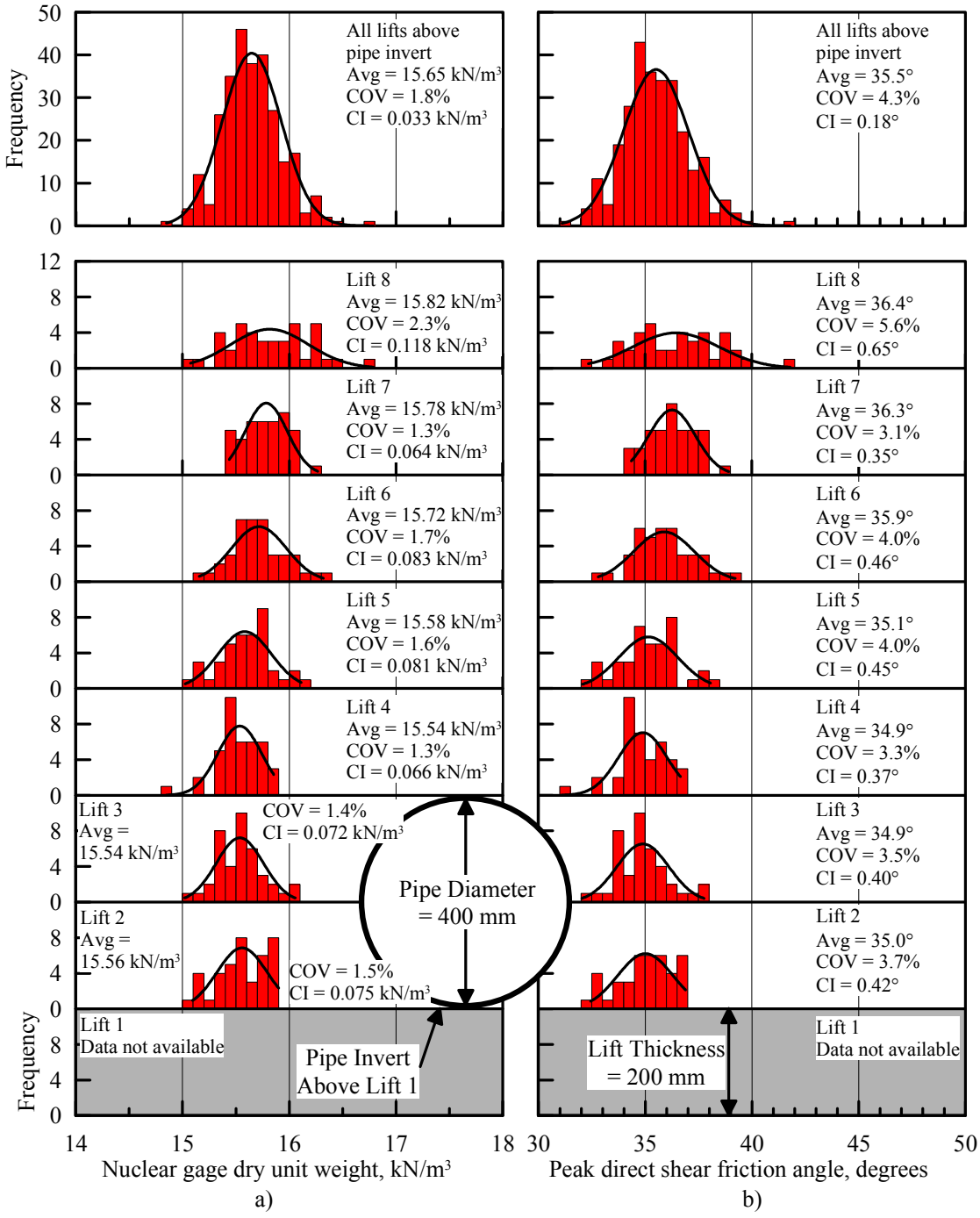

Figure 4.22 Histograms of soil properties by lift for 3-D Test 5 a) Nuclear gage γ_{dry} b) Nuclear gage $\phi_{ds\text{-}p}$

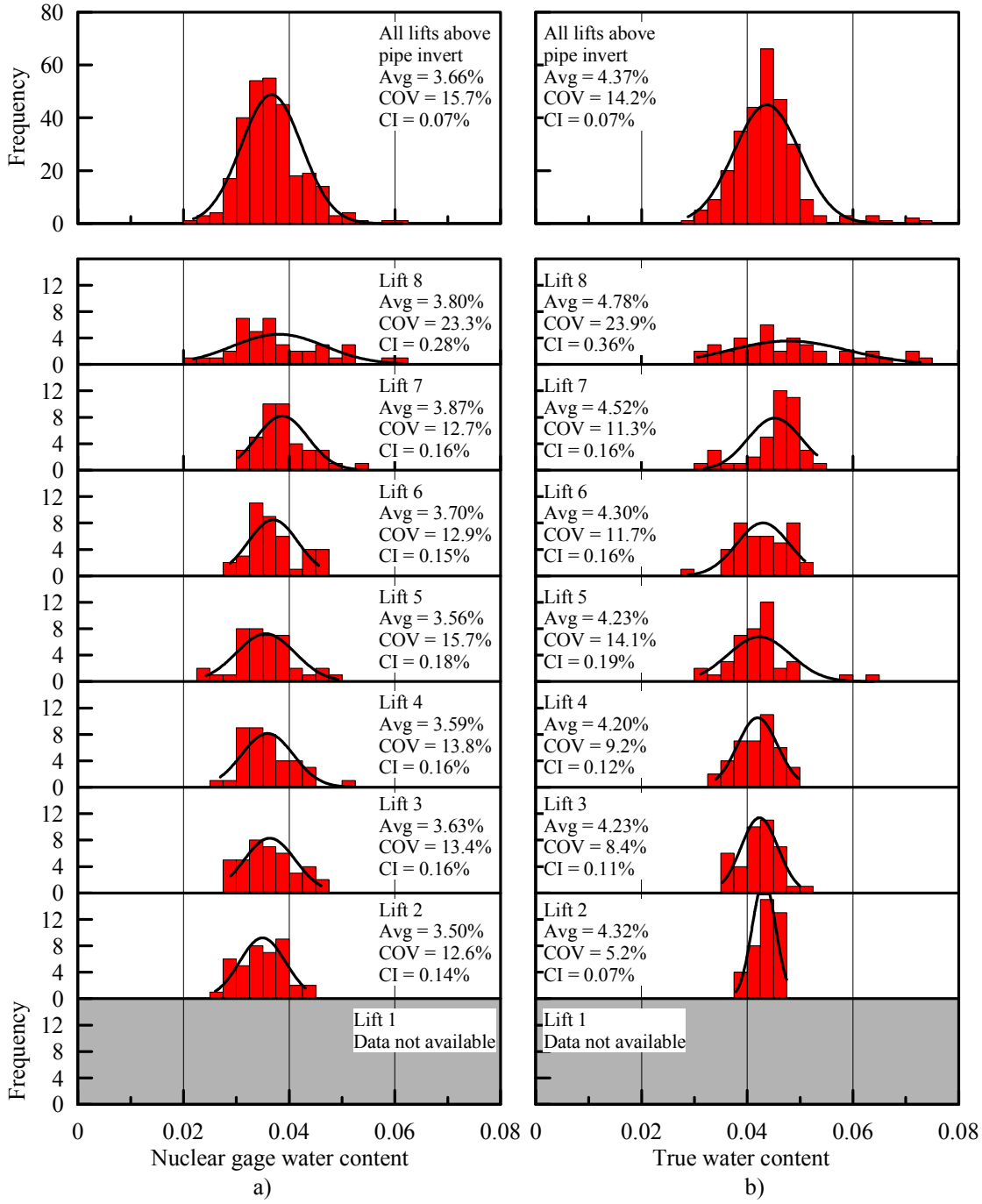

Figure 4.23 Histograms of soil properties by lift for 3-D Test 5 a) Nuclear gage w b) True w by oven dry method

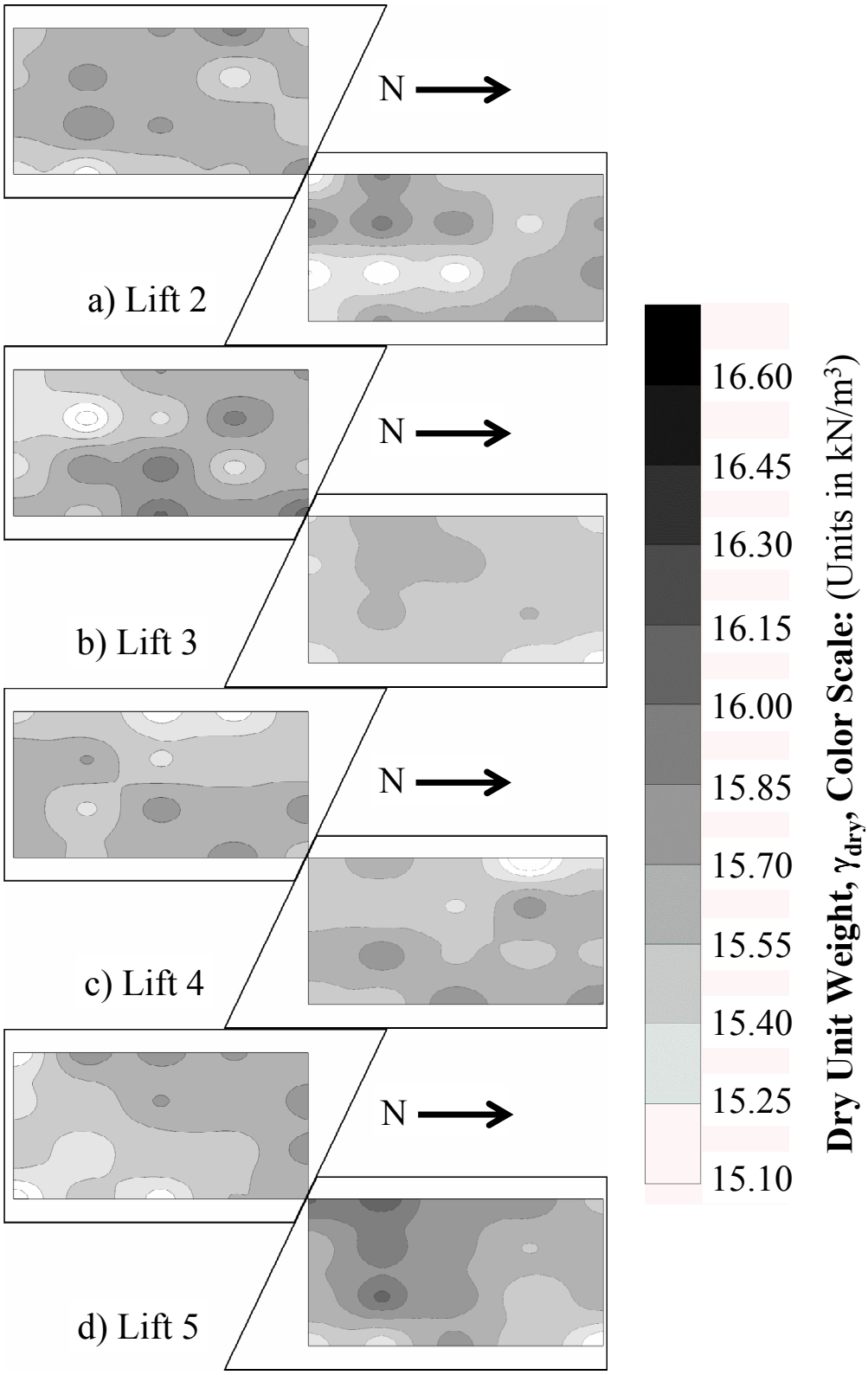

Figure 4.24 Contour plots of γ_{dry} for 3-D Test 5

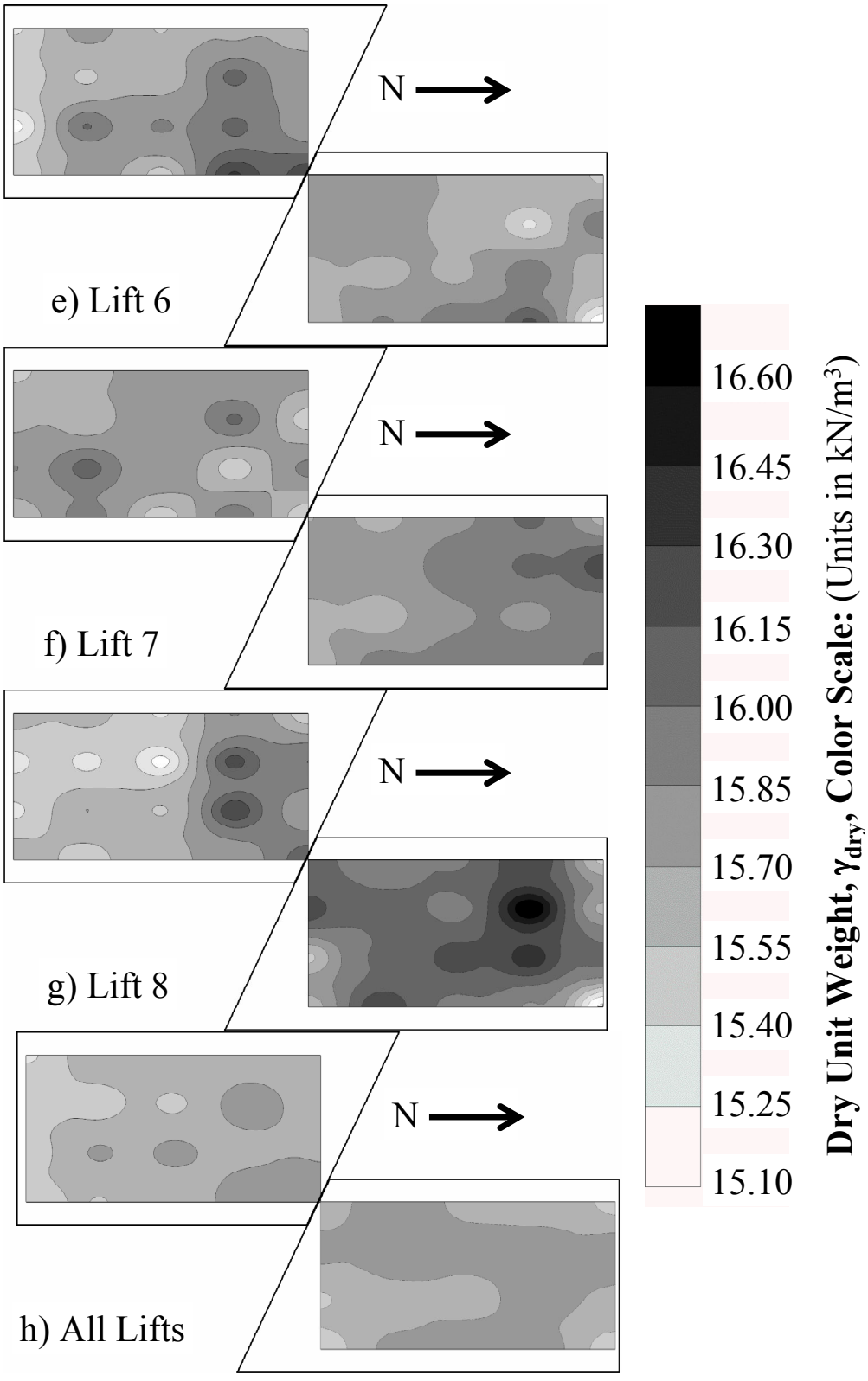

Figure 4.25 Contour plots of γ_{dry} for 3-D Test 5 (continued)

precision is 0.07 – 0.36%. Nuclear gage w generally shows a lower value of average w for a given lift than oven dry w, and also has larger values of COV and precision. Lift 8, placed by the alternate method, is both the wettest and the least precise lift for both methods of measuring w. Aside from lift 8, w by both methods is very consistent from lift to lift.

Contour plots of γ_{dry} for lifts 2 through 8 of 3-D Test 5 are shown in Figure 4.24. The gray scale, in increments of 0.15 kN/m^3, is shaded to indicate γ_{dry} at different locations in the box, with darker shades corresponding to denser materials. Gradients of γ_{dry} are assumed between measurement locations using the "Inverse Distance to a Power" method with a $1/r^2$ relationship, as discussed previously. Figure 4.24h shows a contour plot for the vertical average of γ_{dry} for each location over lifts 2 through 8. It can be seen from Fig. 4.24 that outliers of high and low γ_{dry} are generally randomly distributed both within a lift and throughout the soil mass, indicating that there are no areas which are consistently being over- or under-compacted. It can also be seen that the contour plot for lift 8 shows greater variability than the other lifts, as was shown by the histograms and statistics discussed previously. Again, this increased variability can be pegged to a deviation from the more consistent conveyor-chute method, which requires little handling of the soil, to the more variable container transfer method, which involves substantial manual labor and handling of the soil.

CHAPTER 5

TACTILE PRESSURE SENSORS FOR SOIL-STRUCTURE INTERACTION ASSESSMENT

5.1 Introduction

A tactile pressure sensor is an array of small sensors, referred to as sensels, embedded in a polymeric sheet or pad, that measure the distribution of normal stresses associated with externally applied loads. They were originally developed to support artificial intelligence, but have since been used in industrial and ergonomic applications, including the design of automotive seats and brake pads (e.g., Paikowsky and Hajduk, 1997; Tekscan, 2003).

Important research on tactile pressure sensors has been performed by Paikowsky and co-workers (Paikowsky and Hajduk, 1997; Paikowsky et al., 2000; Paikowsky et al., 2003; Paikowsky et al., 2006), who were the first to investigate their application for geotechnical purposes. Paikowsky and Hajduk (1997) report on a comprehensive series of sensor tests in granular media. They conclude that the tactile pressure sensor system provides normal stress measurements in granular soil to a good degree of accuracy. They also show that sensor measurements are sensitive to load rate, creep, and hysteresis upon unloading, and provide experimental data that help quantify these effects. Tactile pressure sensors have been applied to measure the vertical stress under model strip footings (Paikowsky et al., 2000), vertical stress distribution due to arching during trap door experiments in granular material

(Paikowsky et al., 2003), vertical stress distribution beneath a conical pile of sand (Paikowsky et al., 2006) and vertical pressures transmitted by railroad tracks (Stith, 2005). Paikowsky and coworkers developed a calibration device for applying controlled granular material pressure to tactile pressure sensors (Paikowsky and Hajduk, 1997) and investigated the effects of soil grain size relative to sensel dimensions on sensor measurements (Paikowsky et al., 2006).

Conventional soil stress cells typically register stresses that are either low or high relative to actual soil stresses as a function of stress cell stiffness, size and aspect ratio (thickness-to-length ratio), cell placement procedures, and other factors (e.g., Kohl et al., 1989; Dunnicliff, 1988; Weiler and Kulhawy, 1982; Selig, 1964). Because tactile pressure sensors are thin, wide and flexible, they possess favorable characteristics with respect to aspect ratio and stiffness. The sensors can be adapted to a variety of surface geometries not possible with soil stress cells, and will conform to the curved surfaces of piles, drilled shafts, pipelines, and culverts. They are also affected, however, by limitations related to their construction and material properties. Shear stresses may cause relative slip between polymeric sheets, generating perturbations in the registered voltage. The polymers within the sensor possess visco-elastic characteristics that require an understanding of time dependent response for calibration and interpretation of measurements.

This chapter presents laboratory measurements to help clarify the effects of external shear and creep on sensor performance. Various techniques for minimizing the effects of shear are investigated, and a method for isolating the sensor from external shear effects is proposed. Time-dependent characteristics of sensor response are investigated, and a measurement process that accounts for time-dependent

performance is presented. Tactile pressure sensor measurements in response to vertical loading and unloading and to lateral loads on full-scale pipelines caused by large horizontal ground movement are compared with independent measurements of the loads. Tactile pressure sensors are used to show the distribution of normal stress on pipelines subject to large lateral soil movement.

5.2 Tactile Pressure Sensors

The sensors rely on changes in either resistance or capacitance to applied load. They are commercially available from various manufacturers (e.g., Pressure Profile Systems, Inc., Sensor Products, Inc., and Tekscan, Inc.) in many sizes and shapes, with sensel density of 0.3 to over 200 sensels per cm^2.

Tactile pressure sensors manufactured by Tekscan, Inc. were used in this study. A schematic of the sensor system is shown in Figure 5.1. The tactile pressure sensor consists of two 0.1 mm thick polymer sheets, with opposing, interior faces that contain rows and columns of resistive ink. The rows and columns of ink overlap at grid points, or sensels, where applied forces are measured. Figure 5.2 is a photograph of the tactile pressure sensor (Tekscan Model 5315). The sensor sheets measure 622 x 530 mm with a sensing region dimension of 488 x 427 mm. The sensor contains 48 columns and 42 rows resulting in 2016 sensels spaced at 10 mm on center in each direction. It uses proprietary hardware and software to record, convert, and display the sensor readings.

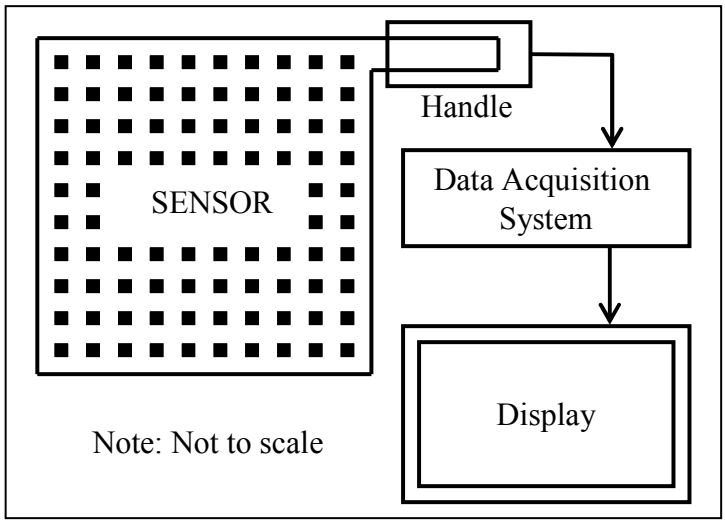

Figure 5.1 Schematic of tactile pressure sensor measurement system

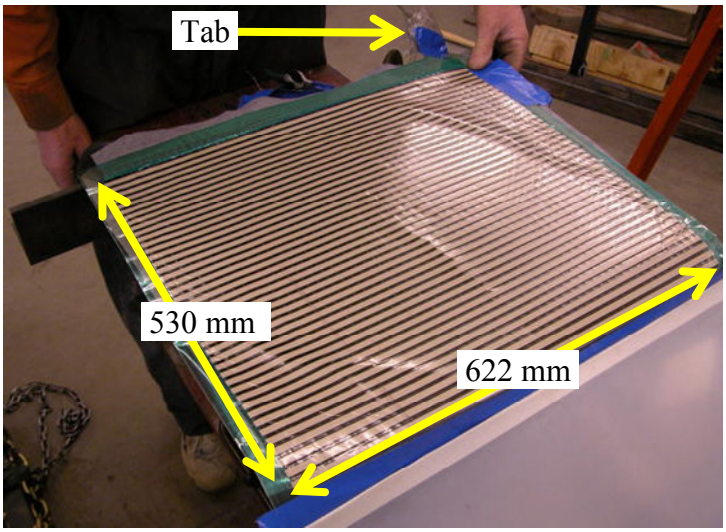

Figure 5.2 Photo of tactile pressure sensor

When normal pressures are applied to the sensor, changes in resistance at the loaded sensels are read sequentially. Resistance change is measured as an analog voltage and then converted to an 8 bit digital number that is transmitted to a data acquisition board. Proprietary software converts the number to pressure in accordance with the sensor calibration. The resulting array of numbers is converted to a colorized distribution of pressure.

5.3 Calibration of Sensors

The sensors used in this study require conditioning, equilibration, and calibration before use. Conditioning involves loading the sensor to a level at or above the anticipated test load several times. It reduces the magnitude of drift and hysteresis in the sensor readings and improves repeatability. Typically, the conditioning load is applied as a uniform pressure either with pneumatic or hydrostatic devices.

After conditioning, equilibration is performed. Equilibration involves applying a uniform pressure to the entire active area of the sensor. The software determines a gain or scale factor for each sensel such that the digital output of that sensel is equal to the average digital output of all the loaded sensels. Sensels with a lower original output have their gain increased while those with a higher original output have their gain decreased. This equilibration compensates for differences in sensitivity between sensels due to manufacturing or repeated use of the sensor. Equilibration can be performed using a single- or multi-load application.

Calibration of the sensor is performed after equilibration is complete. During calibration, uniform pressures are applied to the sensor that cause changes in the resistance of the loaded sensels. During calibration the analog reading from the sensel is converted to a digital value, referred to as Raw (Raw sensor data units). This value is then correlated to engineering units based on the magnitude of the applied pressure.

Sensors are typically calibrated using a 1-load or 2-load calibration. During a 1-load calibration, it is assumed the sensor has zero output under zero applied load. A known load then is applied to the sensor to obtain a single calibration point. A

calibration line is obtained by connecting the zero point to the calibration point on a sensor output vs load graph. A 2-load calibration uses an initial load and a second higher load. The calibration points are then connected using a power law equation.

Conditioning, equilibration, and calibration were performed in this study by a pneumatic device with an internal urethane bladder that fills with air to apply uniform pressure. The unit includes an analog pressure gage to monitor applied pressure, a dial valve regulator to apply pressure, and a toggle switch pressure regulator. Each operation using this device can be performed in minutes.

Figure 5.3 presents calibration plots for a typical sensor with an inset plot showing the response vs time for various levels of applied pressure. The manufacturer's recommended calibration procedure is to 1) condition the sensor by loading and unloading three to five times to 120% of the expected peak load, 2) equilibrate at midrange of the expected peak load, and 3) calibrate at either one (1-load calibration) or two applied pressures (2-load calibration). Typically, the calibration pressures are held for about one minute or until the pressure appears to stabilize as viewed with the visualization software.

The inset plot of Fig. 5.3 shows data for a detailed calibration of a sensor at five different levels of applied pressure. The measured sensor response in Raw/mm^2 with respect to time is nonlinear, and yields a different pressure calibration depending on the time chosen for holding the load. Frequently, times between 60 and 120 sec are selected for calibration because there is very little change in measured load during this interval. In this study, it was found that the sensor response is well characterized by a conventional creep model for load duration beyond 120 sec.

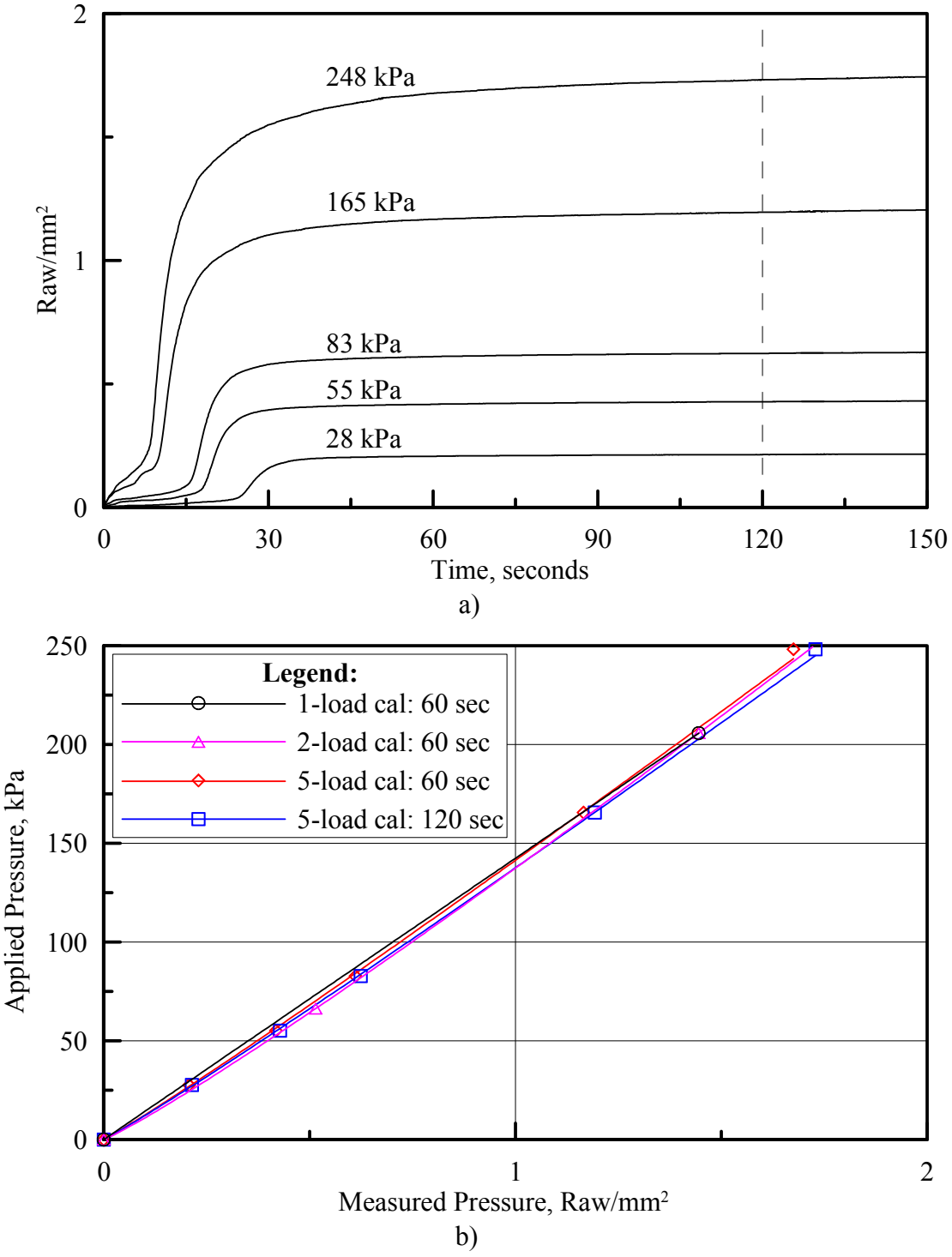

Figure 5.3 Tactile pressure sensor calibrations a) Tactile pressure sensor response vs time at five load levels b) Comparison of tactile pressure sensor calibrations

Four calibration curves are plotted in Fig. 5.3 corresponding to four different calibration techniques. Curves for 1-load and 2-load calibrations determined according to the manufacturer's recommendations are plotted relative to 5-load calibrations in which the sensor was calibrated more rigorously at five different pressure levels. After each equilibration and calibration, the pressure was reduced to zero for one hour to allow for relaxation, then pressurized higher for the next level of equilibration and pressurization. Two 5-load calibrations were performed by holding the applied load for 60 sec and 120 sec.

Figure 5.3 shows that the 2- and 5-load regression plots are statistically indistinguishable from each other at a 95% confidence level. The 1-load plot overestimates at all applied pressure, especially at pressures less than or equal to 25 kPa where the 1-load pressure may exceed the 2- and 5-load calibration pressures by as much as 25%.

5.4 Shear Stress Effects

Tactile pressure sensors are designed to measure normal stress only. Sensor manufacturers do not provide methods to account for or quantify shear effects, and user manuals typically recommend reducing or eliminating shear transferred to the sensor. Shear stresses can displace one sheet of the sensor relative to the other, damage the sensor, and result in inaccurate normal stress readings.

To evaluate the effects of shear stresses on sensor measurements, direct shear tests were performed on the sensors. Before testing, the sensors were conditioned,

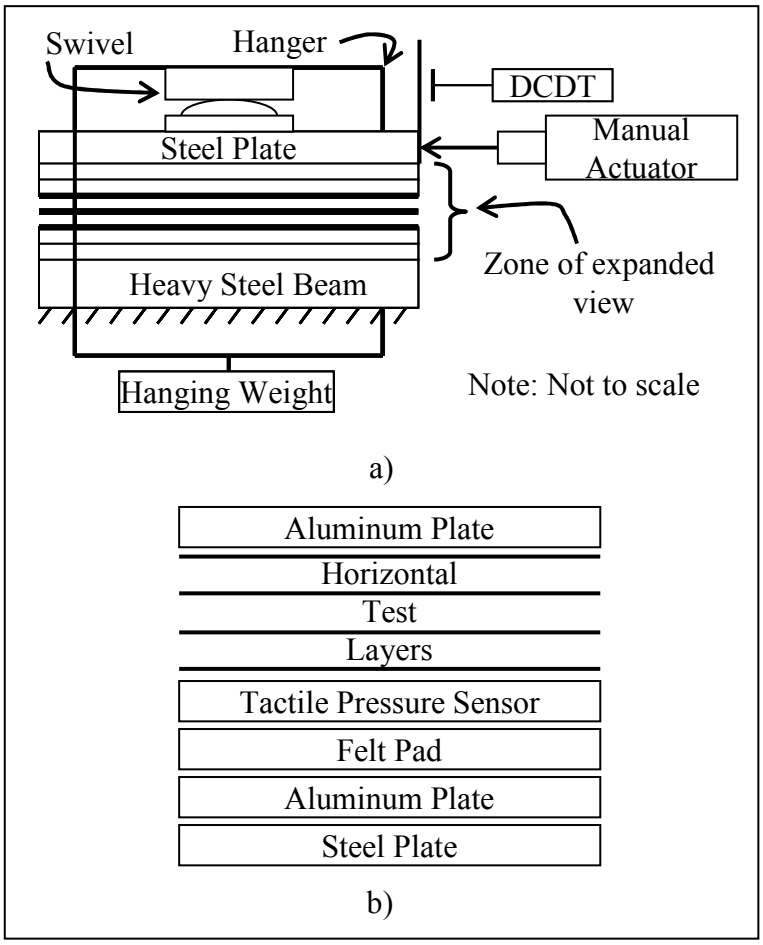

Figure 5.4 a) Schematic of apparatus to evaluate shear stress effects on tactile pressure sensor measurements b) Expanded view of horizontal layers and plates

equilibrated, and then calibrated using a 2-load method. Figure 5.4 shows a schematic of the testing apparatus. The direct shear tests were designed for normal stresses of 43 to 161 kPa. As illustrated in the figure, iron weights were suspended on a steel hanger to convey normal force to the sensor. A motorized or hand operated jack was placed in contact with the upper steel plate, and displaced horizontally until it caused movement. The jack displacement, applied horizontal force, and force measured by the tactile pressure sensor were monitored continuously.

Table 5.1 Summary of shear test results on tactile pressure sensors

Horizontal Test Layers	No. of Tests	Observed Response
Single 0.5 mm thick sheet of LDPE	10	27 - 41% reduction in measured normal force during shear
0.5 mm thick sheet of LDPE underlying a 6 mm thick sheet of rubber	1	13% reduction in measured normal force
Two 0.5 mm thick sheets of LDPE	4	29 - 35% reduction in measured normal force during shear
Two 0.5 mm thick sheets of LDPE with Teflon spray lubricant between the sheets	8	2% reduction in measured normal force during shear, accompanied by increased shear effects over time
0.5 mm thick sheet of LDPE overlying a 0.5 mm sheet of Teflon	2	27 - 41% reduction in measured normal force during shear
Two 0.5 mm thick sheets of Teflon	2	2% reduction in measured normal force during shear

The expanded view in Fig. 5.4 shows the horizons of plates and sheets that were tested. In all cases, there were two 12-mm-thick aluminum plates positioned at the top and bottom of the layers. Also, a 3-mm-thick sheet of felt was positioned on the bottom aluminum plate, on top of which was the tactile pressure sensor sheet. The horizontal test layers refer to the horizontal polymer sheets that were located on top of the tactile pressure sensor. Table 5.1 summarizes the different test layers that were investigated and number of tests associated with each layered system. It also provides a brief description of the measured normal force during the application of shear. Six different layered systems were evaluated, including a single sheet of low density polyethylene (LDPE), LDPE sheet in combination with a rubber sheet, two LDPE sheets, two LDPE sheets with an intervening layer of Teflon spray lubricant, two sheets of LDPE, one sheet of LDPE overlying one sheet of Teflon, and two sheets of Teflon.

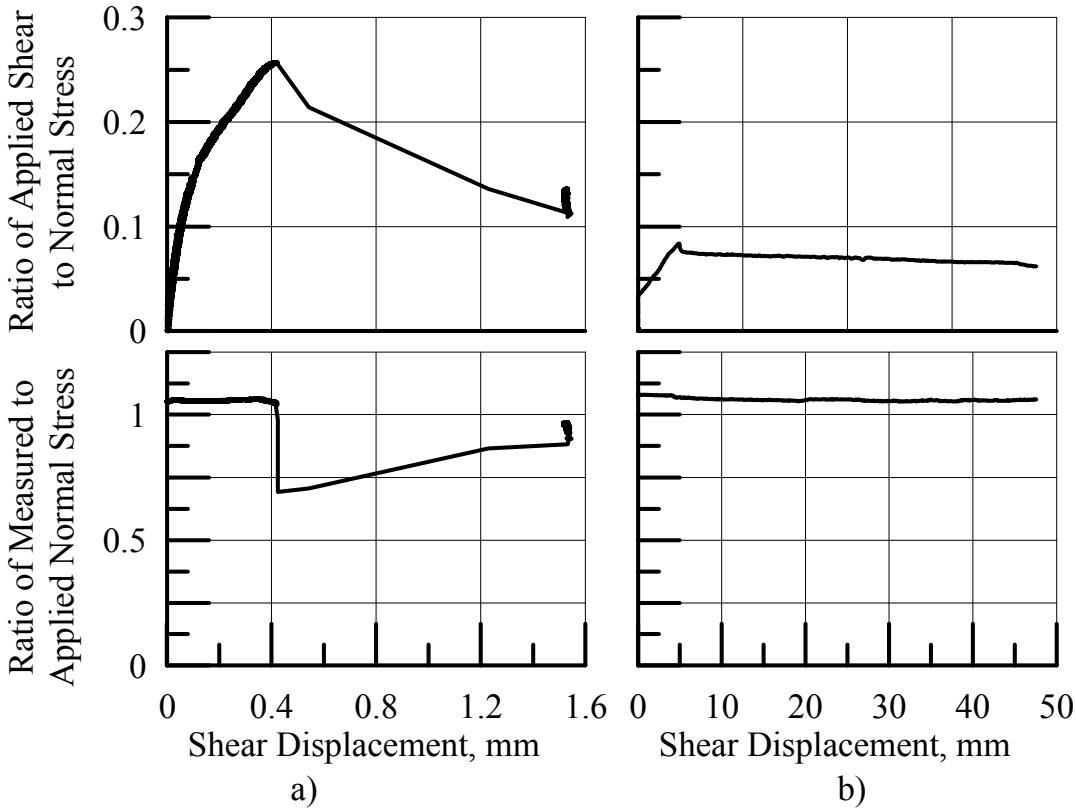

Figure 5.5 Plots of the ratio of applied shear to normal stress and the ratio of measured to applied normal stress vs displacement for a tactile pressure sensor protected by a) A single sheet of LDPE b) Two sheets of Teflon

Figure 5.5 presents representative results for two layered systems. Two plots of data are shown for each test. The upper plot shows the ratio of the applied shear stress to applied normal stress vs horizontal displacement. The lower plot shows the ratio of the measured normal stress to applied normal stress vs shear displacement. Figure 5.5a shows the effects of shear stress for a single sheet of LDPE above the sensor. The normalized normal force, which should equal one with no shear effects, drops rapidly to 0.7 when shear displacement occurs, and then slowly rises back towards one.

Figure 5.5b shows the results for two layers of Teflon sheets placed above the sensor to create a low-friction sliding plane. The normal force was basically unchanged during shear, demonstrating the success of this method in providing protection against shear effects. As indicated in Table 5.1, Teflon spray lubricant between two sheets of LDPE was also effective in reducing shear effects. However, the thixotropic properties of the lubricant led to increased shear resistance over time, and prevented it from being useful in applications with significant time delays (several hrs.) between lubricant application and initiation of shear.

5.5 Time Dependent Effects

Tactile pressure sensors are known to experience drift or creep when measuring an applied load. Drift is reported to vary from 0 - 3% of applied load per log time (Tekscan, 2003). To evaluate the time dependent effects, sustained loading tests were performed. Before testing, the sensors were conditioned, equilibrated, and calibrated using the 2-load method described earlier. Weights, which were hung from a crane with a load cell attached, were applied to the sensor by means of a loading assembly similar to that in Fig. 5.4. Load cell measurements were taken continuously during and after load application. Loads were held constant for more than 1200 sec. to acquire measurements for several log cycles of time.

Fig. 5.6 shows the results of five tests plotted as the ratio of measured to applied pressure vs log time for applied pressures of 15 to 151 kPa. The application of pressure to about 2 sec is followed by a transition to creep at 120 sec. For applied pressures of 49 – 151 kPa the pressure ratio vs log time plots are tightly grouped,

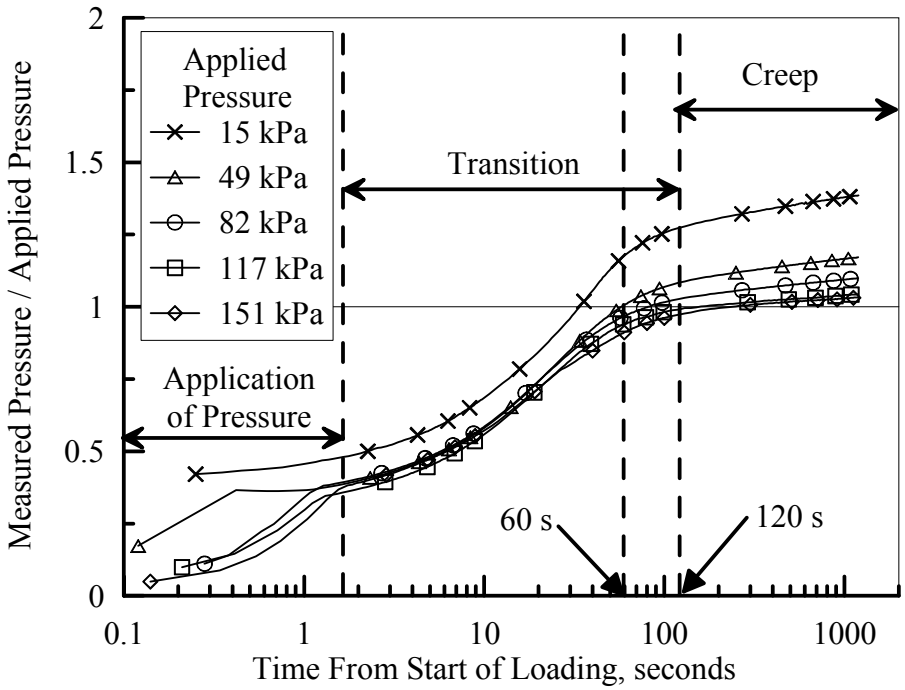

Figure 5.6 Normalized pressure vs time tests at five different pressure levels

especially at times less than 120 sec. At 60 and 120 sec the pressure ratios plot at or slightly below and at or slightly above 1.0, respectively. The maximum difference in the pressure ratios at 60 and 120 sec is about 10%.

It should be noted that the pressure ratio vs log time plot at a low pressure of 15 kPa is significantly above the trends at higher applied pressures. This type of behavior was observed for many sensors in this study and is consistent with observations by Paikowsky and Hajduk (1997), who report inaccurate measurements at low applied pressures. In general, it was found that pressure exceeding 15% of the upper range of the sensor is required for the most reliable and consistent measurements.

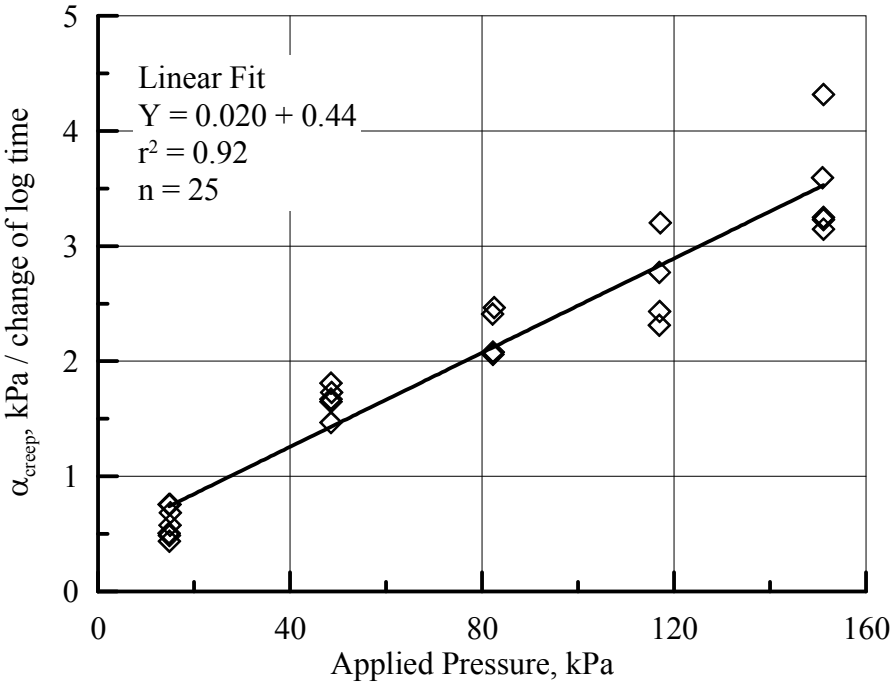

Figure 5.7. Creep response vs applied pressure

The change in measured pressure, Δp_1, after 120 sec. can be expressed as

$$\Delta p_1 = \alpha_{creep} \log \frac{t_2}{t_1} \tag{5.1}$$

in which α_{creep} is the coefficient of creep, reported in units of kPa per change in log time, and t_1 and t_2 are times during creep where $t_2 > t_1$.

Figure 5.7 shows a plot of the creep coefficient, α_{creep}, determined at 120 – 1200 sec. after loading vs the applied pressure. The plot was developed with data from 25 tests performed as described above using two different sensors with applied pressures between 15 - 151 kPa. The creep coefficient increased from about 0.8 to 3.5 kPa per change of log time as the applied pressure increased from 15 kPa to 150 kPa.

The data in Figs. 5.6 and 5.7 illustrate two important characteristics. First, sensor measurements are within 10% of applied pressure 60 to 120 sec. after loading for pressure exceeding 15% of the upper sensor range. Second, the onset of creep begins at approximately 120 sec. after loading. Sensors calibrated at 120 sec. provide reasonably accurate measurements at an equal time following load application, after which Eqn. 5.1 can be used to characterize sensor response in terms of creep. The pressure change, Δp, from Eqn. 5.1 should be subtracted from the measured pressure over time to correct for sensor creep and estimate the actual applied stress.

5.6 Measurement of Vertical Loading and Unloading

Tactile pressure sensors were loaded and unloaded using the procedure illustrated in Fig. 5.8 in which lower and upper pallets holding lead blocks were placed in contact with the sensors. The load was applied for 120 sec, after which the upper pallet and blocks were removed to reduce part of the load. The sensors were positioned in a layered assembly of protective felt and aluminum plates similar to the arrangement depicted in Fig. 5.4.

The measured and applied pressures for two different sensors (A and B) are plotted vs time in Fig. 5.9. Measured pressures using both 2- and 5-load (at 120 sec) calibration plots are presented. Consistent with the calibration plots in Fig. 5.3, there is no clear difference in the tactile pressure sensor response for 2- and 5-load calibrations. The measured pressures increased nonlinearly with time and at 120 sec. were between 4 and 9% below the applied pressure. After partial unloading, the measured pressures fell rapidly until they were ± 2% of the applied pressure after 120 sec.

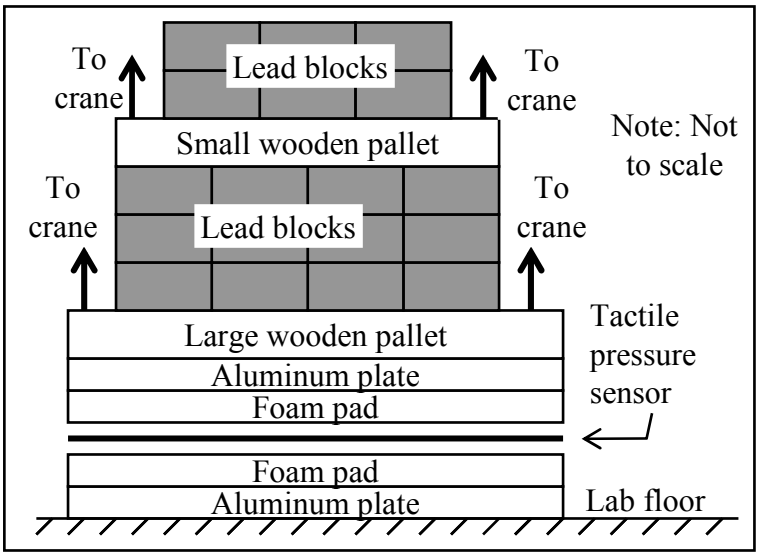

Figure 5.8 Schematic of test for vertical loading and unloading of tactile pressure sensors

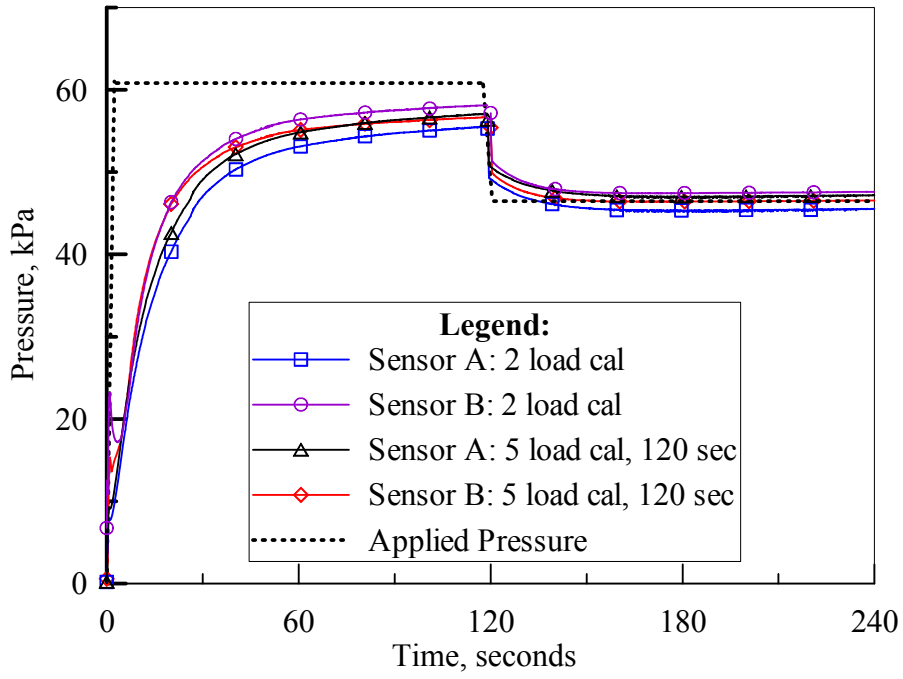

Figure 5.9 Applied and measured pressure vs time for vertical loading and unloading of tactile pressure sensors

These measurements corroborate performance demonstrated earlier in the paper, and show a favorable comparison between measured and applied pressure, provided the comparison is made at a time after loading consistent with that used in the calibration of the sensor. Moreover, the measured vs applied pressures compare favorably after partial unloading, showing that the sensors can provide reliable measurements for simple unloading stress paths.

5.7 Measured vs Applied Loading During Large-Scale Tests

Tactile pressure sensors have been used in full-scale three-dimensional (3-D) tests of ground rupture effects on buried pipelines and two-dimensional (2-D) tests of pipelines under horizontal ground displacements at full-scale and in the centrifuge (Ha et al., 2008; O'Rourke and Bonneau, 2007; O'Rourke et al., 2008). The combined tests were part of a research program using the experimental facilities of the George E. Brown, Jr., Network for Earthquake Engineering Simulation [NEES] (O'Rourke et al., 2008; Palmer et al., 2006) to improve design for soil-pipeline interaction under large ground deformation.

Measurements by Paikowsky and Hajduk (1997) of tactile pressure sensor response as a function of loading rate in granular media provide valuable insight about sensor performance. Paikowsky and Hajduk compared applied pressure and sensor output at loading rates between 1 and 10 kPa/sec. They developed calibration procedures, based on linear regressions of applied stress and sensor output vs time for various loading rates, and showed that the calibration procedures produce measurements to within ± 10% of the applied pressure for monotonically increasing load and applied pressure exceeding 100 kPa.

The soil-pipeline interaction tests for large ground deformation at the NEES sites provided the opportunity to explore further sensor response under variable loading rates. A constant rate of horizontal movement of 2.5 mm/sec was imposed in large-scale 2-D tests of buried pipelines instrumented with tactile pressure sensors. Lateral forces on the pipes were measured independently of the sensors. No special sensor calibrations were performed to account for load rate effects. The intention was to compare directly the loads taken independently with those measured by the sensors using the 2-load calibrations described previously. A favorable comparison between the two measurements would allow for easier and more expeditious use of the sensors. Moreover, the opportunity would still exist for more detailed calibrations, such as those described by Paikowsky and Hajduk (1997), to further improve accuracy with respect to load rate effects.

Figure 5.10 presents a schematic of the large-scale 2-D test basin, which was filled with RMS graded sand placed in both dry and partially saturated conditions and compacted in 200 mm lifts. As discussed in chapter 2, the median grain size was 0.7 mm, which is over one order of magnitude smaller than the 10 x 10 mm sensels. Detailed information about the grain size characteristics, mineralogy, and strength properties of the sand are described in chapters 2 and 3 of this work. Multiple soil-structure interaction tests were performed using the test basin and sand with different dry densities and water contents, different peak angle of shear resistance as determined by direct shear tests, $\phi'_{ds\text{-}p}$, and different ratios of pipe centerline depth to external pipe diameter, H_c/D.

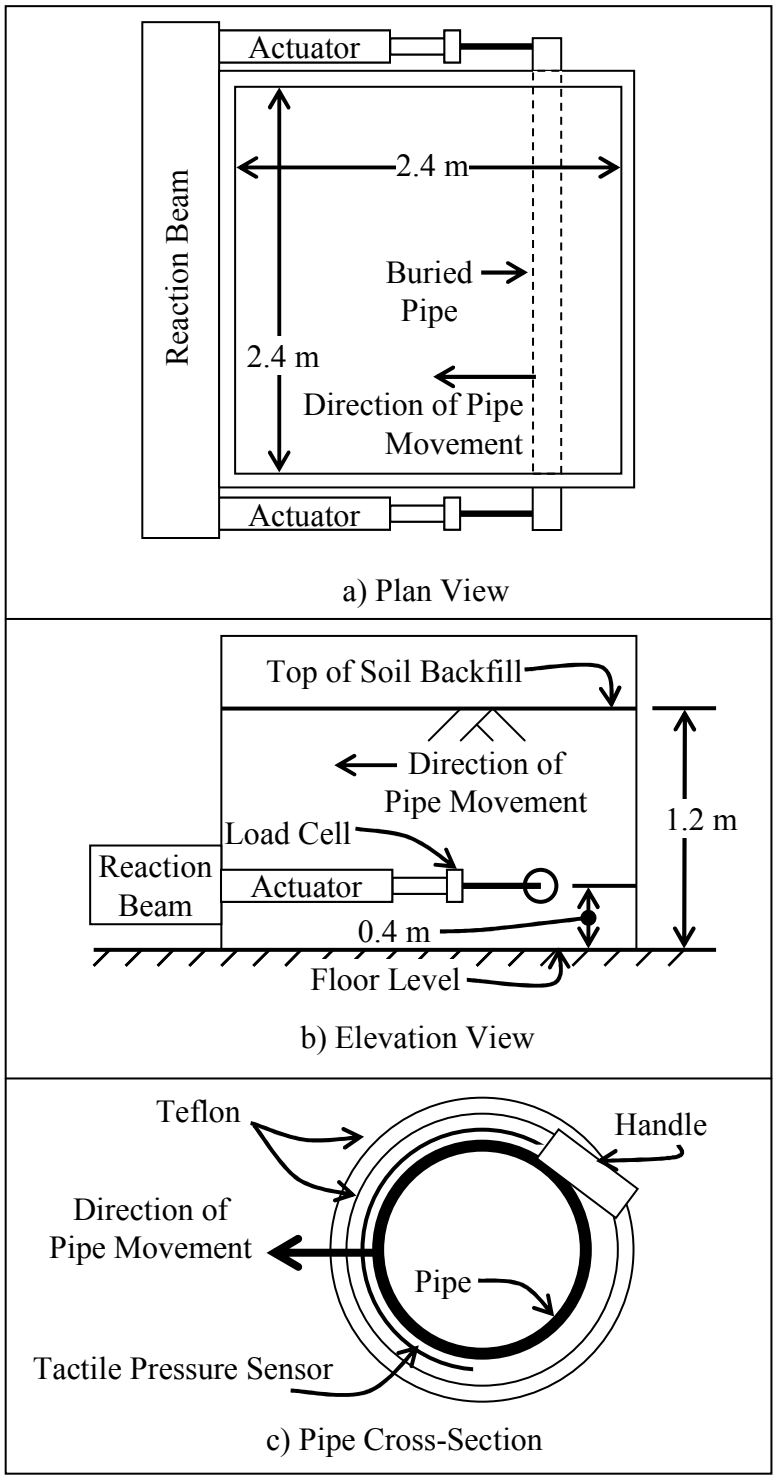

Figure 5.10 Schematic of 2-D test basin for soil-structure interaction of underground pipelines (Not to scale)

The basin was designed to measure the lateral force vs displacement of pipelines through the application of horizontal force with the two long-stroke (1.2 m in one direction) hydraulic actuators as shown in the figure. Horizontal force was measured on each side of the box with a load cell, and lateral movement was measured with Temposonic displacement transducers that provide a voltage output that corresponds to displacement. The loading arm was designed so that the test pipe could rise without vertical restraint as it was displaced laterally though the soil. The rate of pipe displacement was 2.4 mm/sec. The test basin and loading conditions were similar to those used in previous full-scale tests (e.g., Trautmann and O'Rourke, 1985: O'Rourke et al., 2004) with the main exception being size. The internal dimensions of the test basin were 2.44 m x 2.44 m in plan and 1.82 m in depth. The end effects of wall friction were minimized by the relatively large width of the test basin and by lining the interior of the box with Formica and glass, both of which provide for relatively low angles of interface friction.

Tests were performed on pipelines 120 mm and 150 mm in nominal diameter, buried at a pipe centerline depth to diameter ratio, H_c/D, between 3.5 and 7.5. The test pipes had a 2.5-mm-thick high density polyethylene (HDPE) external coating, which is a typical coating used for pipelines in the field. Soil density was strictly controlled with over 100 nuclear density gage measurements per test and a similar number of oven dried water content measurements when partially saturated sand was used.

As illustrated in the pipe section view of Fig. 5.10c, tactile pressure sensors were placed on the pipe and covered with a double layer of 0.5-mm-thick Teflon sheets. The outer layer of Teflon was wrapped around the pipe, but not secured, to allow rotation and sliding during the test. As described previously, the sensor sheets

had a 488 x 427 mm sensing region with 2016 sensels spaced at 10 mm on center in each direction. Prior to installation the sensors were conditioned and calibrated at load rates similar to the rate of loading during full-scale tests. A two-load calibration was used, and sensor readings were continuously recorded during the tests.

Figure 5.11 shows that the stress applied to the sensor has varying magnitude and direction. Measurements of soil movement relative to the pipe in large-scale tests show soil displacement along the pipe surface that mobilizes surface shear stresses consistent with the pattern illustrated in Fig. 5.11a (O'Rourke et al., 2008). Letting p_1 denote the soil pressure per unit length along the pipe and f denote the frictional force between soil and pipe per unit length, the total force per unit length acting on the pipe is obtained by combining p_1 and f appropriately. The frictional force per unit length is given by $f(\theta) = p_1(\theta)\tan\delta_{SI}\sin\theta$, where δ_{SI} is the interface friction angle between the pipe and soil, and θ is the circumferential angle around the pipe. The net force acting on the pipe surface in the transverse horizontal direction, P_h, is given by

$$P_h = \int_0^{2\pi} R_1 p_1(\theta)\cos\theta d\theta + \int_0^{2\pi} R_1 p_1(\theta)\tan\delta_{SI}\sin\theta d\theta \qquad (5.2)$$

The net force per unit length can also be obtained from the experimental data using the following relation

$$P_h = \sum_{j=1}^{J}(p_m)_j S_j \cos\theta_j + \sum_{j=1}^{J}(p_m)_j \tan\delta_{SI} S_j \sin\theta_j \qquad (5.3)$$

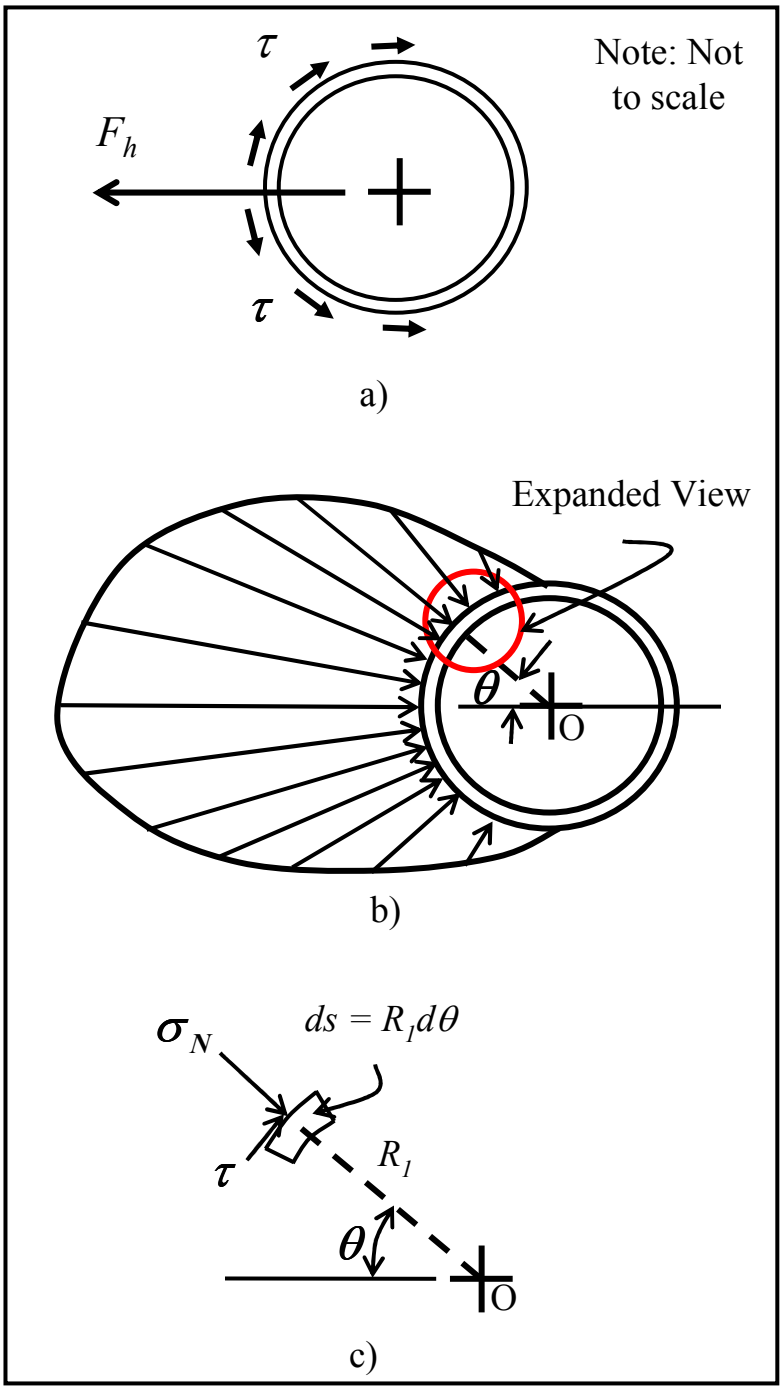

Figure 5.11 Soil-pipe interaction model for underground pipeline under horizontal displacement a) Shear stress orientation b) Normal stress distribution c) Expanded view

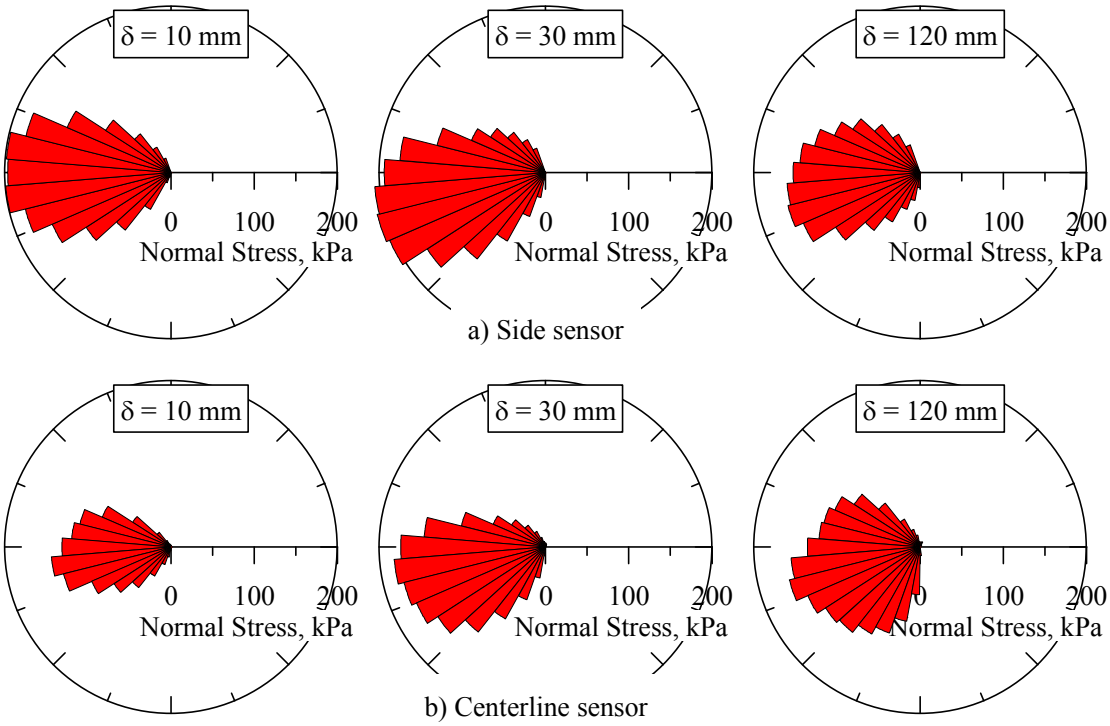

Figure 5.12 Distribution of normal pressure on underground pipeline from tactile pressure sensors during 2-D test 5

where $(p_m)_j$ is the measured pressure at the j-th pressure sensor node, S_j is the arc length associated with the j-th pressure sensor node ($S_j = 2\pi R / J$), θ_j is the angle defining the orientation of $(p_m)_j$, and J is the total number of pressure sensor nodes around the pipe surface per unit length.

Figure 5.12 shows the normal stress distribution measured by tactile pressure sensors at various stages during lateral loading for a test using dry sand with unit weight of 17.2 kN/m^3, D = 120 mm, and H_c/D = 5.5. The peak friction angle of the sand, $\phi'_{ds\text{-}p}$, measured in a conventional 60 x 60 mm direct shear testing device in accordance with ASTM D 3080-04 (ASTM, 2003e), was 44°. Two tactile pressure

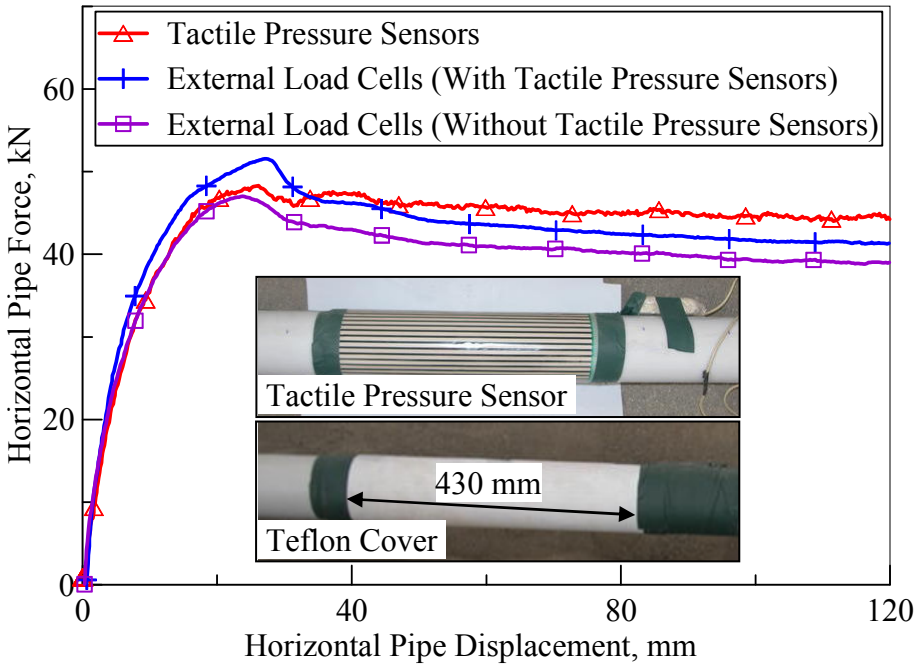

Figure 5.13 Horizontal pipe force vs horizontal pipe displacement for underground pipeline with inset photos of tactile pressure sensor and Teflon cover during 2-D test 5

sensors were used during the test. One was positioned between 90 - 520 mm from the end of the pipe, and is referred to as the side sensor. The other, positioned between 1000 – 1430 mm from the end of the pipe, is referred to as the centerline sensor. The measured pressure distributions are shown at lateral displacements of the test pipe of 15, 25, and 120 mm, corresponding to a pre-peak, peak, and post-peak load on the pipe. For the 120 mm diameter pipe, the sensel width of 10 mm corresponds to about 9° of arc length. Thus, the pressure distribution is shown as 19 discrete measurements around the pipe. Virtually all pressure was confined to the front half circumference of the pipe.

Figure 5.13 shows the lateral force vs displacement plot developed from the tactile pressure sensor measurements in comparison with that developed from the load cell measurements external to the test basin, as described above. Inset photos show

the tactile pressure sensor on the pipe and Teflon protective cover. Also shown is the lateral force vs displacement plot for the same pipe with HDPE coating, but without sensors, as measured by the external load cells. This plot was developed for the same sand and H_c/D. The sand unit weight was 16.9 kN/m^3, with $\phi'_{ds-p} = 42°$, which is very close to the corresponding unit weight and friction angle of sand used to test the pipe with tactile pressure sensors and protective Teflon covers.

There is only a small difference of 10% in peak horizontal force for the pipes with and without sensors, and that difference is well explained by the difference in unit weight and friction angle. It appears therefore that the sensors and protective covers did not alter the horizontal force with respect to the pipe without sensors. All horizontal force measurements using pipe with sensors were compared in dimensionless charts with data acquired in other 2-D tests using pipe without sensors (O'Rourke et al., 2008). No significant variation in force or deviations from the trends of the data have been observed for pipe with and without sensors.

The horizontal force for each sensor at each increment of lateral displacement was calculated from the measured pressure distribution using Eqn. 5.3. The angle of interface shear, δ_{SI}, for sand on Teflon was determined from direct shear tests and the correlation between δ_{SI}/ϕ'_{ds-p} and Shore D hardness established by O'Rourke et al. (1990) for smooth polymers in contact with granular soil. The value of δ_{SI} so determined is 29°. The measured forces from the two sensors were averaged at each movement increment to produce the horizontal force vs lateral displacement plot for the tactile pressure sensors.

Frictional forces generated along the side walls of the test basin were carefully evaluated by special tests in which the sliding mechanism for lateral movement of the test pipe was subjected to measured horizontal loads while the lateral resistance to sliding was measured. During these tests, tactile pressure sensors were used to measure the forces normal to the interior sides of the box. Those forces were converted to horizontal resisting forces by multiplying the normal force by tan $\delta_{SB,}$ where δ_{SB} is the interface friction angle between the soil and the Formica and glass surfaces of the box interior. Tests with the 60 x 60 mm direct shear apparatus indicate that δ_{SB} is about 25° for the interface between the test sand and both Formica and glass. The wall friction force was subtracted from the horizontal force measured by the external load cells to provide the actual lateral force on the pipe. In general, the correction for end shear effects at peak horizontal load was less than 6% of the measured lateral load.

CHAPTER 6

SUMMARY AND CONCLUSIONS

6.1 Introduction

This chapter provides a summary of the major research findings of this work. The sections that follow summarize the research findings according to the four objectives of the research: 1) characterization of direct shear strength for dry sand; 2) characterization of partially saturated sand; 3) control and measurement of soil placement for large scale tests; and 4) assessment of soil-structure interaction forces. The final section provides a discussion of research needs and future research directions.

6.2 Direct Shear Characteristics of Dry Glacio-Fluvial Sand

The conventional 60 mm direct shear (DS) box has been shown by many researchers (Cerato and Lutenegger, 2006; Dietz, 2000; Wu et al., 2008) to have significant limitations for characterizing the strength and dilation of sands with particle sizes larger than approximately 1 - 2 mm. To explore the difference in DS behavior as a function of DS test apparatus dimension, the box length (L) was varied from 60 mm, associated with the conventional apparatus, to 100 mm and 300 mm in modified DS test equipment. The modified DS test equipment was fabricated in accordance with several design improvements based on recommendations by Lings and Dietz (2004) and Dietz (2000).

Improvements used in the modified DS apparatus include dimensions selected to be length (L) = width (B) = 100 mm, and height (H) = 39 mm (consisting of upper and lower frames with H = 19 mm and a 1 mm gap). The load pad was secured to the upper frame before the start of displacement to eliminate counter-rotation between the two elements. Disturbance to the sample was minimized by setting a 1 mm opening with Teflon strips between the upper and lower frames before deposition, and then removing the strips immediately before displacement. To avoid the out of balance force often applied to the DS box by way of a bulky swan neck and to bring the point of shear load transmission to the center of the sample, a pair of "wings" were attached to the mid points of the side-walls on the upper frame, allowing shear force to be applied in line with the central plane of the DS specimen. At the intersection of the wings and the shear load cell rams, rollers were used to allow vertical displacement of the upper frame during shearing of the sample, and to minimize unknown vertical forces applied to the sample and load cells.

For RMS graded sand, the maximum particle size, D_{max}, and median particle size, D_{50}, were approximately 6 mm and 0.7 mm, respectively. The American DS standard, ASTM D 3080 (ASTM, 2003e), recommends a minimum L/D_{max} ratio of ten and H/D_{max} ratio of 6, both of which were satisfied for RMS graded sand in the 60 mm conventional DS apparatus. Nevertheless, it was found that peak DS angle of shear resistance, $\phi'_{ds\text{-}p}$, and peak dilation angle, ψ_p, in the 60 mm apparatus were systematically greater by 4 – 6° and 3 – 7°, respectively, than the corresponding $\phi'_{ds\text{-}p}$ and ψ_p with the 100 mm apparatus. Moreover, the values of $\phi'_{ds\text{-}p}$ and ψ_p obtained for RMS uniform sand with the 60 mm apparatus were very close to those measured with the 100 mm apparatus, being on average 2 – 3° larger. The scatter in the 60 mm data

for RMS uniform sand, however, made them statistically indistinguishable from the 100 mm data at a 95% confidence level.

The gap, or separation, between the upper and lower frames of the DS apparatus was investigated, and a linear relationship was found between gap separation and direct shear strength and dilation parameters. As gap size increases, $\phi'_{ds\text{-}p}$, $\phi'_{ds\text{-}ld}$ and ψ_p all decrease. A 1 mm gap was chosen for tests performed in this study. The optimum gap configuration found by Dietz was a 4 mm gap with split rubber edging, which was found to give nearly the same strength and dilation values as a gap of 1 mm with no edging. A 1 mm gap is close to D_{50} for RMS graded sand, 0.59 mm, and to the ASTM recommended value of 0.64 mm (ASTM, 2003e). A 1 mm gap is sufficiently small that soil loosening and deterioration does not occur in the separation between the upper and lower boxes, and sufficiently large that measurements of peak shear strength and dilation are not amplified by constraints imposed by the testing apparatus.

Of critical importance for soil-structure interaction modeling is the conversion of the DS peak angle of shear resistance to the plane strain peak shear resistance angle, $\phi'_{ps\text{-}p}$. Conversion of DS to plane strain strength parameters allows the results of DS tests to be used in soil-structure interaction modeling for 2-D conditions. Conversion of DS to plane strain conditions was accomplished through the relationship derived by Davis (1968), as follows:

$$\tan\phi'_{ds} = \frac{\cos\psi \sin\phi'_{ps}}{1 - \sin\psi \sin\phi_{ps}} \tag{2.4}$$

For all sands investigated in this work, including RMS graded, RMS uniform, and CU Filter sand, the validity of the above relationship was explored through the use of flow rules proposed by Taylor (1948), Rowe (1962, 1969), and Bolton (1986) for expressing the relationship between strength, critical state conditions, and dilatency. Values of ϕ'_{crit} and ψ determined by DS tests were used in conjunction with the relationship proposed by Davis (1968) and aforementioned flow rules to compare the measured values of $\phi'_{ds\text{-}p}$ and ψ_p with flow rule predictions of $\phi'_{ps\text{-}p}$ and ψ_p. In all cases, the comparisons were favorable. The conversion of direct shear to plane strain peak shear resistance using the above equation provides a procedure for 2-D strength characterization that is consistent with existing flow rules and the test data acquired in this work, and thus suitable for 2-D simulations of soil-structure interaction.

Critical state angles of shear resistance, ϕ'_{crit}, were estimated from the results of DS and sand cone tests, and flow rules reflecting the estimated values of ϕ'_{crit} were then compared with DS measurements of $\phi'_{ds\text{-}p}$ and ψ_p. Using this two-fold approach, the ϕ'_{crit} for RMS graded, RMS uniform, and CU Filter sands are estimated as 41°, 38°, and 39°, respectively. The test results also help to quantify the variability associated with ϕ'_{crit} evaluation. The standard deviation of ϕ'_{crit}, as assessed by DS and sand cone test results for the three different sands, vary from 0.8° to 2.5°. A reasonable range for ϕ'_{crit} is 41° ± 2° and 38° ± 2° for RMS graded and RMS uniform sand, respectively. For CU Filter sand, ϕ'_{crit} = 39° ± 1°. The ϕ'_{crit} for the glacio-fluvial sands of this investigation are relatively high when compared with uniform sand composed of quartz and feldspars (Bolton, 1986). The ϕ'_{crit} values, however, are consistent with those reported for glacio-fluvial sand elsewhere (Koerner, 1970; Lee, 1966).

6.3 Direct Shear and Matric Suction Characteristics of Partially Saturated Glacio-Fluvial Sand

Soil water retention curves for desorption conditions (SWRCs) were developed for RMS graded sand using Tempe cells. The SWRCs determined in this work are in favorable agreement with SWRCs reported by Singh et al. (2006) for sand similar in grain size distribution to RMS graded sand. The water content, w, at residual state shown by the SWRCs is 5.6%. This value is close to w = 4 – 5%, which is the range of w to which the sand drained for large scale tests. Knowledge of the residual w led to an important part of the large scale test preparation process in which partially saturated RMS graded sand was prepared and placed at residual w, thereby allowing for statistically tight controls on w and in situ γ_{dry}.

Matric suction was measured in situ for RMS sand in the large scale 2-D and 3-D tests using tensiometers fabricated by the Cornell University Department of Crop and Soil Sciences. The tensiometer measurements show matric suctions of 2.5 – 5.1 kPa for partially saturated RMS graded sand with γ_{dry} = 15.8 – 16.5 kN/m^3 and w = 3.7 – 4.9%. Tempe cell measurements were plotted according to curve fitting rules proposed by Feng and Fredlund (1994) to develop SWRCs for RMS graded sand. The resulting SWRCs were used in hysteresis relationships proposed by Pham et al. (2005) to define an adsorption SWRC. When plotted on SWRCs for adsorption, the tensiometer measured matric suctions follow closely the adsorption trends. The favorable comparison of data and adsorption trends occurs because the water is drawn from the tensiometer thus generating adsorption into the soil from the tensiometer.

The DS failure envelope for partially saturated RMS graded sand shows clearly a cohesive intercept, c_{ds}, and direct shear angle of shear resistance, $\phi_{ds\text{-}p}$, both of which increase as the γ_{dry} increases. Both the c_{ds} and $\phi_{ds\text{-}p}$ values are total stress parameters because the negative pore water pressure was not directly measured in the direct shear specimens during testing, thus eliminating the ability to calculate the effective normal stress conditions. Cohesion at peak state was found to be dependent on γ_{dry} for partially saturated RMS graded sand, varying from c_{ds} = 2.1 kPa at γ_{dry} = 15.8 kN/m^3 to c_{ds} = 3.4 kPa at γ_{dry} = 16.5 kN/m^3. In contrast, no cohesive intercept was measured for dry RMS graded sand at equivalent γ_{dry}. Additionally, Mohr Coulomb envelopes for partially saturated RMS graded sand at critical state showed no cohesion.

A relationship was derived between c_{ds} and $\phi_{ds\text{-}p}$ determined by DS testing and c_{ps} and $\phi_{ps\text{-}p}$ for plane strain conditions under the assumptions that the coaxiality of incremental strain and stress applies for the partially saturated sand of this study. Given the low values of suction measured for the test sand, it is likely that the relative orientations of stress and incremental strain are not materially different than those for dry sand. Moreover, strength and volume change characteristics evaluated on the premise of coaxiality provide results that support a rational mechanics-based explanation of observed behavior and are consistent on a comparative basis with the properties of dry sand.

Plane strain c_{ps} and $\phi_{ps\text{-}p}$ were evaluated directly from DS measurements of c_{ds} and $\phi_{ds\text{-}p}$ by calculating the centers and tops of the Mohr Circle at failure from the DS data and using the linear regression of these data. Eqns. 3.14 through 3.18 in Chapter 3 were derived from the Mohr Circle constructed with measured DS data. These equations are satisfied if and only if

$$c_{ps} = \frac{c}{\cos \phi_{ps-p}} \tag{6.1}$$

$$\phi_{ps-p} = \sin^{-1}\left(\tan \alpha\right) \tag{6.2}$$

where c and α are the intercept and slope, respectively, of a linear regression of the $(\sigma_1 + \sigma_3)/2$ vs $(\sigma_1 - \sigma_3)/2$ data.

A linear relationship was found between $\phi_{ds\text{-}p}$ and ψ_p vs γ_{dry} for partially saturated sand. Moreover, the ratio of τ_p/σ_N, when plotted as a function of ψ_p, was shown to agree favorably with the relationships between τ_p/σ_N vs ψ_p given by the flow rules of by Taylor (1948), Rowe (1962, 1969), and Bolton (1986) modified to include cohesion.

Experimental data for dry and partially saturated RMS graded sand were plotted as peak shear strength vs normal stress for the two different γ_{dry} values representative of soil used in the large scale tests. Direct comparison of these data sets show an increase in DS strength and dilation from dry to partially saturated sand. At a given γ_{dry}, partially saturated RMS graded sand has an approximate 10° and 5° increase in $\phi_{ds\text{-}p}$ and ψ_p, respectively, in comparison to dry RMS graded sand. To define a relationship between dry and partially saturated sand, the Taylor (1948) flow rule was considered. The Taylor (1948) flow rules for dry and partially saturated sand were combined to give the relationship

$$\frac{c_{ds}}{\sigma_N} = \tan\left(\psi_p\right)_{p.sat} - \tan\left(\psi_p\right)_{dry} \tag{6.3}$$

which shows that the increase in dilatency between dry and partially saturated sand is equal to the normalized cohesion, c_{ds}/σ_N.

The difference in $\tan(\psi_p)$ for dry and partially saturated RMS sand is equal to the c_{ds}/σ_N ratio at both γ_{dry} = 15.8 and 16.5 kN/m^3. It can be concluded therefore that the cohesion associated with partially saturated RMS graded sand is related to increased dilatency. It appears that suction increases the interference among the sand particles, thus increasing the work against volumetric expansion during shear failure. This mechanism for shear strength is identical to the interlocking and critical state concepts for the DS strength of sand advanced by Schofield (2005).

There was not a clear relationship found between compaction energy and DS soil specimen strength for dry sand, because vibration energy has a much greater effect on the compaction of dry sand than does tamping. For partially saturated sand, however, compaction effort controlled by tamping is a good predictor of γ_{dry}, and thus of DS strength and dilation parameters. Loose sand (15.0 kN/m^3) was prepared with 50 kN-m/m^3 of compaction energy, medium sand (15.8 kN/m^3) required 150 kN-m/m3, and dense sand (16.5 kN/m^3) required 250 kN-m/m^3. With the 100 mm box, these values of γ_{dry} correspond to values of $\phi_{ds\text{-}p}$ = 32, 36, and 40°, and ψ_p = 5, 11, and 16°, respectively.

The interface angle of frictional shear resistance, δ_{SI}, between partially saturated RMS graded sand and Teflon and HDPE was found to be 22° at γ_{dry} = 14.9 kN/m^3, increasing linearly to 30° at γ_{dry} = 16.6 kN/m^3. Values of Shore D hardness, H_D, between 58 and 60 were measured for Teflon and HDPE. These δ_{SI} values

compare favorably with those predicted from H_D using the relationship proposed by O'Rourke et al. (1990) for a dry sand polymer interface.

6.4 Preparation and Measurement of Soil for Large Scale Experiments

Soil was placed and measured for six large scale 3-D and eleven large-scale 2-D soil-structure interaction experiments. Up to 900 kN of soil, occupying 55 m^3 for each large scale 3-D test, were placed at exacting specifications of water content, w, and dry unit weight, γ_{dry}. The soil preparation and measurement procedures that were developed and shown to provide consistent results are described as follows:

For large scale tests, soil was stored before testing in permanent wall-mounted soil storage bins. Water was applied to the sand while it was still in the soil storage bins. A few days before placement in the large scale test basin, the w of the soil in the storage bins was measured by taking samples at the soil bin doors and at the top of the soil bin, and the amount of water to be added was calculated based on the current and target w of the soil as well as the amount of soil to be prepared. The water was then applied in stages over a period of days by a laboratory technician with a garden hose standing on the catwalk above the soil storage bins. By adding water in stages over a few days the water content reached 4 – 5%, consistent with the residual state found by Tempe cell measurements.

The sand was transported to the test basin on a series of three conveyors into a hopper and deposited through a flexible plastic chute. As soil moved on the conveyors from the storage bins to the test box, the flexible chute was moved around to distribute soil throughout the box and place an even 200 mm thick lift, consistent with

specifications for compacted fill in the field (NYSDOT, 2008). Compaction was typically performed with two passes of a gasoline powered plate tamper, and locations missed were manually compacted to the target γ_{dry}.

Forty measurements of γ_{dry} and w were taken and recorded for each lift in a defined grid. Nuclear gage plots were prepared with a bored hole to a depth of 200 mm, and 15 sec measurements of soil unit weight and water weight were taken using the nuclear gage with a source rod depth of 150 mm at each location. A sample of soil was obtained at each plot for analysis of w by the oven dry method. It took 3 - 5 days to bring soil to residual water content, and the placement, compaction and measurement of each lift of soil took 1 – 2 hours. Placement, compaction, and measurement of all lifts, as well as leveling soil and painting a grid on the surface took 3 – 5 days. To prevent evaporation, the soil was covered with plastic sheets that were removed before testing.

6.5 Nuclear Gage and Density Scoop Measurements

The nuclear gage, an instrument for measuring the unit weight of water and soil and other materials, was used to measure the wet unit weight of soil (γ_{total}) and water present in the soil ($\gamma_{w\text{-}soil}$) for large scale tests in accordance with ASTM D6938 (ASTM, 2008b). The Troxler Model 3440 gage (manufactured by Troxler, Inc., Research Triangle Park, NC) was used in the current study. Nuclear gage measurements were performed to characterize variability and precision associated with the determination of γ_{dry} and $\gamma_{w\text{-}soil}$ as a function of measurement duration, location, and depth within the calibration box.

In the measurement of γ_{dry} and w for sand, the accuracy and precision of the reported data depend on the method of measurement, the operator's technique and skill in using a consistent measurement procedure, and the consistency of the sand material being tested. Precision is a measure of the dispersion of values around a mean value, while accuracy, or bias, is the difference between the average of a group of measurements and the true value. After Trautmann et al. (1985), density was determined to an arbitrarily high precision by taking a sufficiently large number of measurements with an unbiased technique. This precision, or CI, is determined by the Central Limit Theorem of statistics, as

$$CI = \frac{tS_D}{\sqrt{n}} \tag{6.4}$$

where parameters are as defined in Chapter 4. A two-tailed probability of 0.05 was used to calculate values of CI.

To evaluate the variation of γ_{dry} with measurement depth in a 200 mm lift, the source rod measurement depth was varied from 0 mm (using backscatter mode) to 50 - 200 mm (using the direct transmission mode). It was found that standard deviation, S_D, decreases as measurement depth increases. Average γ_{dry} is lowest at the 50 mm depth, and highest at the 100 mm depth, while there is not a significant difference in measurements at backscatter, 150 mm, and 200 mm depths.

As measured in the calibration box, measurement precision and COV were found to decrease significantly with an increase in the time of measurement from 15 to 240 sec. Measurement COV at 15 sec was very good, at 5%, and a sixteen-fold

increase in time duration resulted in only a two-fold decrease in COV, to 2.5%. Because efficiency in measuring soil properties for large scale tests is critical, the shorter time duration of 15 sec was chosen for all measurements taken in the calibrations and large scale tests.

The nuclear gage was found to be sensitive to vertical discontinuities in the soil mass, as discussed by the manufacturer (Troxler, 2004a). After testing in the calibration box, minimum edge distance from the gage to the nearest vertical discontinuity was found to be 300 mm on the side of the gage corresponding to the detector, and 100 mm on the other three sides of the gage. These requirements were strictly followed for all measurements in the calibration box and for large scale tests.

Although it was seen that different locations in the calibration box give different measurements of γ_{dry}, an analysis of different sources of variance showed that the variance of the nuclear gage measurements can be isolated from the variance due to soil inhomogeneity at different locations in the calibration box. As long as the edge distance requirements stated previously were followed, there was no significant bias due to location of measurement.

The nuclear gage measurements of γ_{dry} were compared directly to those of the Selig Density Scoop (Selig, 1962; Selig and Ladd, 1973). Comparative data were obtained by compacting soil in the calibration box to a desired γ_{dry}, and taking both nuclear gage and density scoop measurements at each of eight locations. The average value of the eight nuclear gage measurements was plotted vs the average value of the eight density scoop measurements, along with data for six 2-D tests representing the

average of the twelve measurements of γ_{dry} taken for each lift by the nuclear gage vs the average of twelve density scoop measurements taken at the same locations.

It is shown that the density scoop average γ_{dry} overestimated the average nuclear gage γ_{dry} by about 0.0 – 0.8 kN/m^3 for dry RMS graded sand. Measurements of γ_{dry} from the nuclear gage and density scoop for partially saturated RMS graded sand are in favorable agreement. For dry sand, the density scoop measurements provide a γ_{dry} that is approximately 0.4 kN/m^3 larger than the γ_{dry} measured by the nuclear gage in the range of γ_{dry} = 17.0 – 17.7 kN/m^3 as determined by the density scoop. As seen in histograms of measured values for 2-D tests, the COV and CI of nuclear gage measurements on γ_{dry} are systematically smaller than those of the density scoop measurements of γ_{dry}. From visual observation, the nuclear gage γ_{dry} is closely clustered about the mean value, while there are more outliers for density scoop γ_{dry}.

Values of water content, w, were measured by oven drying according to ASTM D2216 (ASTM, 2003d) and with the nuclear gage according to ASTM D6938 (ASTM, 2008b). Comparisons of the two methods of measurement of w are shown with lift by lift histograms from large scale 2-D tests. The measurements of oven dry w are consistently more precise (CI = 0.04 – 0.10%) than nuclear gage w (CI = 0.15 – 0.35%), while average oven dry w was consistently higher (4.03 – 4.23%) than average nuclear gage w (3.46 – 3.75%). Histograms of oven dry w for individual lifts show closely clustered distributions, indicating that variability of w was very well controlled for soil placed in these lifts. On the other hand, distributions of nuclear gage w consistently show greater scatter for the same locations. Lift by lift histograms of nuclear gage w and oven dry w for 3-D tests repeat the trends observed for 2-D

tests, as nuclear gage w generally shows a lower value of average w for a given lift than oven dry w, and also has larger values of COV and precision.

Lift by lift histograms for 3-D Test 5 show that average γ_{dry} is consistent for all lifts, varying from 15.54 – 15.82 kN/m^3. The precision of γ_{dry} for a given lift is between 0.072 – 0.083 kN/m^3 for lifts 2 through 7, while lift 8, where soil was placed by transferring from steel containers, has a precision of 0.118 kN/m^3, showing the greater variability of that method. The 95% confidence interval of the mean of all data (0.033 kN/m^3) is much smaller than that for individual lifts (0.072 – 0.118 kN/m^3), demonstrating the influence of a large number of measurements on statistical confidence.

6.6 Tactile Pressure Sensors for Soil-Structure Interaction Assessment

The use of tactile pressure sensors for soil-structure interaction in the presence of shear stresses will result in damage to the sensor or inaccurate readings of normal stress. To develop a system for protection against shear stress, an investigation was performed with a large DS apparatus capable of applying 161 kPa normal stress to the tactile pressure sensor. Shear displacement was applied between the sensor and various protective layers, and shear stresses were measured with load cells. Six different layered systems were evaluated, including a single sheet of low density polyethylene (LDPE), LDPE sheet in combination with a rubber sheet, two LDPE sheets, two LDPE sheets with an intervening layer of Teflon spray lubricant, two sheets of LDPE, one sheet of LDPE overlying one sheet of Teflon, and two sheets of Teflon.

With a single sheet of LDPE, the normalized normal force, which should equal one with no shear effects, drops rapidly to 0.7 when shear displacement occurs, and then slowly rises back towards one. For two layers of Teflon sheets, the normal force was basically unchanged during shear, demonstrating the success of this method. Teflon spray lubricant between two sheets of LDPE was also effective in reducing shear effects. However, the thixotropic properties of the lubricant led to increased shear resistance over time, and prevented it from being useful in applications with significant time delays (several hrs.) between lubricant application and initiation of shear. A protective system that includes two layers of Teflon was chosen as the best protection against the effects of shear stress on sensor measurements.

Tactile pressure sensors were calibrated using 1- 2-, and 5-load calibrations. While the 1-load calibration overestimated the applied pressure by as much as 25%, the 2- and 5-load calibrations were statistically indistinguishable at a two-tailed probability level of 95%. The 2-load calibration was chosen for its efficiency and compatibility with the proprietary software.

Test results show that sensor measurements are within 10% of applied pressure 60 to 120 sec after loading for pressure exceeding 15% of the upper bound sensor pressure. Test results for applied pressures below 15% of the upper bound pressure are not reliable, consistent with the observations of Paikowsky and Hajduk (1997), who report inaccurate measurements at low applied pressures. The accuracy of measurements with tactile pressure sensors compares favorably with that of conventional soil stress cells. Tactile pressure sensors have additional benefits by providing distributed stress measurements over relatively large surfaces and adapting to various surface geometries not possible with conventional stress cells.

Creep of the sensor measurements begins at approximately 120 sec after loading. Sensor response for longer durations of measurement is characterized by a conventional creep equation in which the increment in measured pressure is equal to the product of a creep coefficient and the change in log time. This apparent pressure should be subtracted over time from the measured pressure to estimate the actual applied pressure.

Two-dimensional soil-structure interaction tests were performed with tactile pressure sensors wrapped around a pipe that was buried in sand and displaced laterally. Force-displacement curves generated from sensor data compare well with those derived from independent measurements of the applied loads. Methods are provided herein for resolving normal stresses on the pipe from sensor measurements and for determining the horizontal force on the pipe.

On the basis of the test results acquired in this study, tactile pressure sensors are suitably accurate and versatile for reliable measurement of normal stresses in large-scale laboratory and centrifuge tests of soil-structure interaction. Care, however, must be taken to eliminate or mitigate shear stresses transmitted to the sensor surface and to account for time-dependent sensor response to applied pressure.

6.7 Future Research Directions

In this section, specific topics are identified for further investigation. These recommendations are summarized in four sections: 1) characterization of dry sand, 2) characterization of partially saturated sand, 3) measurement of soil properties for large scale tests, and 4) measurement of soil-structure interaction pressure.

6.7.1 Characterization of Dry Sand

A number of investigators (Cerato and Lutenegger, 2006; Dietz, 2000; Jewell and Wroth, 1987; Scarpelli and Wood, 1982) have sought to evaluate the influence of box length on direct shear parameters for soils with various particle size distributions. This work measured a 3 – 7° decrease in $\phi'_{ds\text{-}p}$ and ψ_p for dry RMS graded sand for an increase in box length from 60 to 100 mm, while a further increase in length did not result in a significant decrease in measured parameters. It would be useful to investigate comprehensively the influence of box length on the measured strength and dilation parameters of sands. It would be useful to include both uniform and graded sands to investigate the influence of length for soils of various particle size distributions.

Trautmann and O'Rourke (1983) tested interfaces between dry sand and Formica and glass using a conventional DS apparatus. O'Rourke et al. (1990) investigated interface direct shear behavior between dry sand and polymers using the conventional DS apparatus, while Lings and Dietz (2005) and Dietz and Lings (2006) used the modified DS apparatus to test dry sand-steel interfaces. The current study tested partially saturated sand-polymer interfaces using the conventional DS apparatus, finding good correspondence with trends set forth by O'Rourke et al. (1990). There was not time in this work to test dry and partially saturated sand-polymer interfaces using the modified DS apparatus, but further work in this area would be helpful.

Dry and partially saturated sand for the current study was compacted primarily by tamping in three lifts. Although pluviation was used by Dietz (2000) to prepare DS

specimens with uniform sands, it was found that sample deposition by pluviation resulted in particle segregation for the sands of this study, even though they are classified as poorly graded sands according to standard classification methods (Lambe and Whitman, 1969). Experimental comparison of pluviation, tamping, and vibratory compaction methods would be valuable for dry sand.

Various sand cone tests have been proposed (Miura et al. 1997; Santamarina and Cho, 2001) and were used in the current research. It should be recognized that the angles of repose measured for sands are dependent on the dimension of the cone or device. It would be useful to assess the value of the critical state friction angle by various sand cone tests in comparison to the large-displacement friction angle measured by the DS apparatus. These tests should be performed with uniform and well graded particle size distributions. Well graded material is often specified in the field, whereas uniform sand is not commonly used (NYSDOT, 2008).

6.7.2 Characterization of Partially Saturated Sand

An interesting finding of the current study is the measurement of cohesion and the increased strength and dilation of partially saturated RMS graded sand at w = 4% relative to the same material in a dry state. It would be useful to test this material and other sands at a variety of water contents to determine the effect that partial saturation has on the dilation and the Mohr Coulomb strength parameters of various materials as a function of particle size distribution, unit weight, and mineralogy. It would be especially useful to investigate the relationship between the normalized cohesion and increased dilation ratio for other materials and water contents. At w higher than residual w, cohesion will decrease as matric suction decreases. At w lower than

residual w, however, increase in cohesion and friction angle due to higher matric suction may be offset by the reduced number of water-soil surface bonds. The relationship between w and shear strength parameters as w declines from residual to hygroscopic should be explored.

Large scale tests were performed on partially saturated sand at residual w of 4 – 6%, showing low values of matric suction from 2.5 – 5.1 kPa. Suction will increase as the void sizes in the specimen decrease. Hence, the introduction of finer-grained soil constituents will increase matric suction and cohesion. It would be very helpful to perform a series of DS tests for dry and partially saturated sand specimens containing increasingly greater percentages of fine grained material so that the interrelationships among matric suction, cohesion, and friction angle can be explored. Moreover, by performing DS tests on dry and partially saturated soil at the same γ_{dry} with coarse and fine materials, one can explore relationships between dilation and cohesion. Tests run with fine grained constituents would include fine grained materials that are nominally inert, such as rock flour or pond silt. The fine grained materials should also include those that have active physio-chemical characteristics, such as clays with varying plasticity indexes.

Models for characterizing partially saturated soils have been proposed by various researchers (Bishop et al., 1960; Fredlund, 2006; Alonso et al., 1990). It would be useful to compare the predicted strength relationships to the degree of saturation or w predicted by these models with the data presented in this work. Models proposed by Fredlund are combined in specialized software (Soilvision, Soilvision Systems Ltd.), and application of the software would be necessary to provide an appropriate comparison.

6.7.3 Measurement of Soil Properties for Large Scale Tests

When compared with alternative measurements of γ_{dry}, the nuclear gage performed favorably with respect to precision and bias. For measurement of water content, the nuclear gage was not as reliable as the ASTM standard oven dry method (ASTM, 2003d), systematically underpredicting oven dry measurements of w in large scale tests. It would be valuable to explore the reasons for the lack of a more favorable comparison between the two methods of water content measurement, and to develop a more reliable nuclear gage measurement of w.

6.7.4 Measurement of Soil-Structure Interaction Pressure

Creep effects on tactile pressure sensor response were investigated in this work, focusing on times of 120 to 1200 sec after the initiation of loading. Paikowsky and Hajduk (1997) dealt with rate of loading effects on calibration of tactile pressure sensors in a special calibration device using glass spheres. They found that the slope of a calibration curve was reasonably constant over a wide range of load rates, while the intercept was more sensitive to the rate of loading. However, the use of glass spheres in their calibration device makes the work by Paikowsky and Hajduk (1997) less applicable to real sands commonly used in the field. It would be valuable to develop a calibration and validation method using a standardized sand (such as Ottawa sand) rather than glass spheres, or to develop a consistent process for calibrating sensors with any given sand material. One option is to explore the device used by Paikowsky and Hajduk (1997), using different sands. Another possibility would be to use a tactile pressure sensor initially calibrated in a pressure chamber and subsequently loaded in carefully run plate load tests.

APPENDIX A

DERIVATION OF KEY EQUATIONS FOR PARTIALLY SATURATED SAND

A.1 Introduction

This appendix uses basic soil mechanics principles and algebraic manipulation to derive key equations for a soil which has both cohesive and frictional strength components. Derivations presented in this appendix are 1) the conversion from direct shear (DS) to plane strain parameters, 2) calculation of the indirect cohesion for a vertical discontinuity of depth H_s, 3) calculation of the indirect cohesion for the same vertical discontinuity with a tension crack of depth $H_s/2$ within the active soil wedge, and 4) the derivation of an equivalent A-coefficient for the DS test.

A.2 Conversion from Direct Shear to Plane Strain Parameters

Figure 3.6a shows DS and plane strain Mohr-Coulomb stress parameters for partially saturated sand. As defined in Chapter 3, the DS and plane strain friction angles at peak state, ϕ_{ds-p} and ϕ_{ps-p}, are given by

$$\tan\phi_{ds-p} = \frac{\tau_p - c_{ds}}{\sigma_N} \tag{A.1}$$

$$\tan\phi_{ps-p} = \frac{\tau_{ps} - c_{ps}}{\sigma_{ps}} \tag{A.2}$$

where other parameters are as defined in Chapter 3.

Given that the DS test failure plane coincides with zero extension and that stress and incremental strain are co-axial, an equation can be derived that is similar to Eqn. 2.4 in Chapter 2. As can be seen in Fig. 3.6a,

$$R = \frac{\tau_p}{\cos\psi} \tag{A.3}$$

$$\tau_{ps} = R\cos\phi_{ps} = \tau_{ds}\frac{\cos\phi_{ps}}{\cos\psi} \tag{A.4}$$

$$\tau_p = \tau_{ps} + \left[2R\sin\left(\frac{\phi_{ps}-\psi}{2}\right)\right]\sin\left(\frac{\phi_{ps}+\psi}{2}\right) \tag{A.5}$$

By algebraic manipulation, we get

$$\tau_p = \tau_p\frac{\cos\phi_{ps}}{\cos\psi} + 2\frac{\tau_p}{\cos\psi}\sin\left(\frac{\phi_{ps}-\psi}{2}\right)\sin\left(\frac{\phi_{ps}+\psi}{2}\right) \tag{A.6}$$

$$\cos\psi = \cos\phi_{ps} + 2\sin\left(\frac{\phi_{ps}-\psi}{2}\right)\sin\left(\frac{\phi_{ps}+\psi}{2}\right) \tag{A.7}$$

By trigonometric identity, it can be shown that

$$2R\sin\left(\frac{\phi_{ps}-\psi}{2}\right)\cos\left(\frac{\phi_{ps}+\psi}{2}\right) = R\left(\sin\phi_{ps} - \sin\psi\right) \tag{A.8}$$

Further algebraic manipulation leads to

$$\sigma_N\tan\phi_{ps} = \tan\phi_{ps}R\left(\sin\phi_{ps} - \sin\psi\right) + R\cos\phi_{ps} - c_{ds} \tag{A.9}$$

Combining A.3 with A.9 gives

$$\sigma_N \tan\phi_{ps} = \tan\phi_{ps} \frac{\tau_p}{\cos\psi}\left(\sin\phi_{ps} - \sin\psi\right) + \frac{\tau_p}{\cos\psi}\cos\phi_{ps} - c_{ds} \qquad \text{(A.10)}$$

Dividing by σ_N gives

$$\tan\phi_{ps} = \tan\phi_{ps} \frac{\tau_p}{\sigma_N}\frac{1}{\cos\psi}\left(\sin\phi_{ps} - \sin\psi\right) + \frac{\tau_p}{\sigma_N}\frac{1}{\cos\psi}\cos\phi_{ps} - \frac{c_{ds}}{\sigma_N} \qquad \text{(A.11)}$$

Multiplying by $\cos\phi_{ps}$ gives

$$\sin\phi_{ps} = \sin\phi_{ps} \frac{\tau_p}{\sigma_N}\frac{1}{\cos\psi}\left(\sin\phi_{ps} - \sin\psi\right) + \frac{\tau_p}{\sigma_N}\frac{1}{\cos\psi}\cos^2\phi_{ps} - \frac{c_{ds}\cos\phi_{ps}}{\sigma_N} \qquad \text{(A.12)}$$

$$\sin\phi_{ps} = \frac{\tau_p}{\sigma_N}\frac{1}{\cos\psi}\left[\left(\sin^2\phi_{ps} + \cos^2\phi_{ps}\right) - \sin\phi_{ps}\sin\psi\right] - \frac{c_{ds}\cos\phi_{ps}}{\sigma_N} \qquad \text{(A.13)}$$

By trigonometric identity, it can be shown that

$$\sin\phi_{ps} = \frac{\tau_p}{\sigma_N}\frac{1}{\cos\psi}\left[1 - \sin\phi_{ps}\sin\psi\right] - \frac{c_{ds}\cos\phi_{ps}}{\sigma_N} \qquad \text{(A.14)}$$

$$\sin\phi_{ps}\left[1 + \frac{\tau_p}{\sigma_N}\tan\psi\right] = \frac{\tau_p}{\sigma_N}\frac{1}{\cos\psi} - \frac{c_{ds}\cos\phi_{ps}}{\sigma_N} \qquad \text{(A.15)}$$

$$\sin\phi_{ps} = \frac{\dfrac{\tau_p}{\sigma_N}\dfrac{1}{\cos\psi} - \dfrac{c_{ds}\cos\phi_{ps}}{\sigma_N}}{1 + \dfrac{\tau_p}{\sigma_N}\tan\psi} \qquad \text{(3.16)}$$

which is equivalent to Eqn. 3.14 in Chapter 3. However, this is a transcendental equation, which must be solved iteratively. If c_{ds} is set to zero, as is the case for dry sand, this equation reduces to

$$\sin\phi_{ps} = \frac{\tan\phi_{ds}}{\cos\psi + \tan\phi_{ds}\sin\psi} \tag{3.17}$$

which is equivalent to Eqn. 2.4 in Chapter 2.

A.3 Cohesion for a Wedge Failure in a c-ϕ Material

In Chapter 3, Figs. 3.22a and b show the geometry of an vertical soil surface, such as commonly results from large scale tests. Forces consisting of the weight of the soil wedge, W_s, the cohesion of the soil, C_s, and the resultant, R_s, act in the directions shown, and can be resolved to solve for C_s as shown in Figure 3.22d. The cohesion, $c_{indirect}$, associated with an unsupported cut in the soil is given as

$$c_{indirect} = \frac{1}{4}\gamma_{dry}(1+w)H_s \cot\left(45° + \frac{\phi_{ds-p}}{2}\right) \tag{A.18}$$

The following derivation shows how this formula is reached. From the geometry of Fig. 3.22b,

$$W_s = 2C_s \sin\left(45° + \frac{\phi_{ds-p}}{2}\right) \tag{A.19}$$

$$C_s = \frac{H_s c_{indirect}}{\sin\left(45° + \frac{\phi_{ds-p}}{2}\right)} \tag{A.20}$$

$$W_s = 2H_s c_{indirect} \tag{A.21}$$

Combining A.19 with A.20,

$$W_s = 2\left(\frac{H_s c_{indirect}}{\sin\left(45° + \frac{\phi_{ds-p}}{2}\right)}\right)\sin\left(45° + \frac{\phi_{ds-p}}{2}\right) \tag{A.22}$$

Combining A.21 with A.22,

$$\frac{1}{2}\gamma_{dry}(1+w)H_s{}^2\cot\left(45° + \frac{\phi_{ds-p}}{2}\right) = 2H_s c_{indirect} \tag{A.23}$$

By algebraic manipulation, we get

$$c_{indirect} = \frac{1}{4}\gamma_{dry}(1+w)H_s\cot\left(45° + \frac{\phi_{ds-p}}{2}\right) \tag{A.24}$$

As can be seen, Eqn. A.19 is identical to Eqn. 3.29.

A.4 Cohesion for a Wedge Failure in a c-ϕ Material with Tension Crack

The cohesion, $c_{indirect}$, associated with an unsupported cut in the soil with a tension crack of depth $H_s/2$ within the active wedge is given as

$$c_{indirect} = \frac{3}{8}\gamma_{dry}(1+w)H_s\cot\left(45° + \frac{\phi_{ds-p}}{2}\right) \tag{A.25}$$

From the geometry of Fig. 3.22c,

$$W_s = \frac{1}{2}\gamma_{dry}(1+w)H_s{}^2 \cot\left(45° + \frac{\phi_{ds-p}}{2}\right) - \frac{1}{2}\gamma_{dry}(1+w)\left(\frac{H_s}{2}\right)^2 \cot\left(45° + \frac{\phi_{ds-p}}{2}\right) \quad \text{(A.26)}$$

$$W_s = \frac{1}{2}\gamma_{dry}(1+w)H_s{}^2 \cot\left(45° + \frac{\phi_{ds-p}}{2}\right) - \frac{1}{8}\gamma_{dry}(1+w)H_s{}^2 \cot\left(45° + \frac{\phi_{ds-p}}{2}\right) \quad \text{(A.27)}$$

$$W_s = \frac{3}{8}\gamma_{dry}(1+w)H_s{}^2 \cot\left(45° + \frac{\phi_{ds-p}}{2}\right) \quad \text{(A.28)}$$

$$W_s = 2C_s \sin\left(45° + \frac{\phi_{ds-p}}{2}\right) \quad \text{(A.29)}$$

$$C_s = \frac{H_s c_{indirect}}{2\sin\left(45° + \frac{\phi_{ds-p}}{2}\right)} \quad \text{(A.30)}$$

$$W_s = 2\left(\frac{H_s c_{indirect}}{2\sin\left(45° + \frac{\phi_{ds-p}}{2}\right)}\right)\sin\left(45° + \frac{\phi_{ds-p}}{2}\right) \quad \text{(A.31)}$$

$$W_s = H_s c_{indirect} \quad \text{(A.32)}$$

Combining A.31 with A.32,

$$\frac{3}{8}\gamma_{dry}(1+w)H_s{}^2 \cot\left(45° + \frac{\phi_{ds-p}}{2}\right) = H_s c_{indirect} \quad \text{(A.33)}$$

By algebraic manipulation, we get

$$c_{indirect} = \frac{3}{8}\gamma_{dry}(1+w)H_s \cot\left(45° + \frac{\phi_{ds-p}}{2}\right) \quad \text{(A.34)}$$

As can be seen, Eqn. A.34 is identical to Eqn. 3.30.

A.5 Derivation of A – Coefficient for Direct Shear Test

As discussed in Chapter 3, Figure 3.24 shows Mohr circles of equal radius for dry and partially saturated sand. To calculate the difference in negative pore water pressure required to explain the increase in direct shear strength between the two direct shear tests at the same γ_{dry}, Eqn. 3.22 was derived.

$$\frac{u}{\sigma_1 - \sigma_3} = \frac{1}{2}\left[\cos\psi_{dry}\cot\phi'_{ds-dry} + \sin\psi_{dry} - \cos\psi_{p.sat}\cot\phi_{ds-p.sat} - \sin\psi_{p.sat}\right] + \frac{\cos\psi_{p.sat}\cot\phi_{ds-p.sat}}{2\left(\frac{\sigma_N}{c_{ds}}\tan\phi_{ds-p.sat} + 1\right)} \quad \text{(A.35)}$$

This equation assumes that the ψ_p for dry and partially saturated sand are different, thus the rupture planes in direct shear for total and effective stress are rotated differently with respect to the principal stresses. From Fig. 3.24, it can be seen that

$$\tau'_{p-dry} = \sigma'_N \tan\phi'_{ds-dry} \quad \text{(A.36)}$$

$$R = \frac{\sigma'_N \tan\phi'_{ds-dry}}{\cos\psi_{dry}} \quad \text{(A.37)}$$

$$\tau_{p-p.sat.} = \sigma_N \tan\phi_{ds-p.sat.} + c_{ds} \quad \text{(A.38)}$$

$$R = \frac{\sigma_N \tan\phi_{ds-p.sat.} + c_{ds}}{\cos\psi_{p.sat}}, \text{ or } \sigma_N = \frac{R\cos\psi_{p.sat.} - c_{ds}}{\tan\phi_{ds-p.sat.}} \quad \text{(A.39)}$$

Combining A.36 with A.39,

$$\sigma'_N = \left[\frac{\sigma_N \tan\phi_{ds-p.sat.} + c_{ds}}{\cos\psi_{p.sat.}}\right]\frac{\cos\psi_{dry}}{\tan\phi'_{ds-dry}} \quad \text{(A.40)}$$

From Fig. 3.24,

$$u = \left[\frac{\sigma_1' + \sigma_3'}{2}\right] - \left[\frac{\sigma_1 + \sigma_3}{2}\right] \tag{A.41}$$

$$\left[\frac{\sigma_1' + \sigma_3'}{2}\right] = \sigma'_N \left(1 + \tan\phi'_{ds-dry} \tan\psi_{dry}\right) \tag{A.42}$$

Combining A.40 with A.42,

$$\left[\frac{\sigma_1' + \sigma_3'}{2}\right] = \left[\frac{\sigma_N \tan\phi_{ds-p.sat} \cos\psi_{dry}}{\cos\psi_{p.sat.} \tan\phi'_{ds-dry}} + \frac{c\cos\psi_{dry}}{\tan\phi'_{ds-dry}}\right]\left(1 + \tan\phi'_{ds-dry} \tan\psi_{dry}\right) \tag{A.43}$$

$$\left[\frac{\sigma_1' + \sigma_3'}{2}\right] = \left(\sigma_N \tan\phi_{ds-p.sat.} + c_{ds}\right)\frac{\cos\psi_{dry} + \tan\phi'_{ds-dry} \sin\psi_{dry}}{\cos\psi_{p.sat.} \tan\phi'_{ds-dry}} \tag{A.44}$$

From Fig. 3.24,

$$\left[\frac{\sigma_1 + \sigma_3}{2}\right] = \sigma_N + \tau_{p.sat.} \tan\psi_{p.sat.} \tag{A.45}$$

Combining A.38 with A.45,

$$\left[\frac{\sigma_1 + \sigma_3}{2}\right] = \sigma_N + \left(\sigma_N \tan\phi_{ds-p.sat.} + c_{ds}\right)\tan\psi_{p.sat.} \tag{A.46}$$

Combining A.44 with A.46,

$$u = \left(\sigma_N \tan\phi_{ds-p.sat.} + c_{ds}\right)\left[\frac{\cos\psi_{dry} + \tan\phi'_{ds-dry} \sin\psi_{dry}}{\cos\psi_{p.sat.} \tan\phi'_{ds-dry}} - \tan\psi_{p.sat.}\right] - \sigma_N \tag{A.47}$$

By algebraic manipulation, we get

$$u = \left(\sigma_N \tan\phi_{ds-p.sat.} + c_{ds}\right)\times$$
$$\left[\frac{\cos\psi_{dry} + \tan\phi'_{ds-dry}\sin\psi_{dry}}{\cos\psi_{p.sat.}\tan\phi'_{ds-dry}} - \frac{\sin\psi_{p.sat.}}{\cos\psi_{p.sat}}\frac{\tan\phi'_{ds-dry}}{\tan\phi'_{ds-dry}}\right] - \sigma_N \qquad \text{(A.48)}$$

Combining A.39 with A.48,

$$u = \frac{\left(\sigma_N \tan\phi_{ds-p.sat.} + c_{ds}\right)}{\cos\psi_{p.sat.}}\times$$
$$\left[\cos\psi_{dry}\cot\phi'_{ds-dry} + \sin\psi_{dry} - \sin\psi_{p.sat.}\right] - \frac{R\cos\psi_{p.sat.} - c_{ds}}{\tan\phi_{ds-p.sat.}} \qquad \text{(A.49)}$$

By algebraic manipulation, we get

$$u = \frac{\left(\sigma_N \tan\phi_{ds-p.sat.} + c_{ds}\right)}{\cos\psi_{p.sat.}}\left[\cos\psi_{dry}\cot\phi'_{ds-dry} + \sin\psi_{dry} - \sin\psi_{p.sat.}\right] -$$
$$R\cos\psi_{p.sat.}\cot\phi_{ds-p.sat.} + c\cot\phi_{ds-p.sat.} \qquad \text{(A.50)}$$

From Fig. 3.24,

$$2R = \left(\sigma_1 - \sigma_3\right) = \frac{2}{\cos\psi_{p.sat.}}\left(\sigma_N \tan\phi_{ds-p.sat.} + c_{ds}\right) \qquad \text{(A.51)}$$

Combining A.50 with A.51,

$$\frac{u}{2R} = \frac{u}{\sigma_1 - \sigma_3} = \frac{1}{2}\left[\cos\psi_{dry}\cot\phi'_{ds-dry} + \sin\psi_{dry} - \sin\psi_{p.sat.}\right] -$$
$$\frac{1}{2}\cos\psi_{p.sat.}\cot\phi_{ds-p,sat,} + \frac{c_{ds}\cot\phi_{ds-p,sat,}}{2R} \qquad \text{(A.52)}$$

By algebraic manipulation, we get

$$\frac{u}{\sigma_1-\sigma_3}=\frac{1}{2}\left[\cos\psi_{dry}\cot\phi'_{ds-dry}+\sin\psi_{dry}-\sin\psi_{p.sat.}\right]-$$
$$\frac{1}{2}\cos\psi_{p.sat.}\cot\phi_{ds-p.sat.}+\frac{c_{ds}\cos\psi_{p.sat.}\cot\phi_{ds-p.sat.}}{2\left(\sigma_N\tan\phi_{ds-p.sat.}+c_{ds}\right)} \quad (A.53)$$

$$\frac{u}{\sigma_1-\sigma_3}=\frac{1}{2}\left[\cos\psi_{dry}\cot\phi'_{ds-dry}+\sin\psi_{dry}-\cos\psi_{p.sat.}\cot\phi_{ds-p.sat.}-\sin\psi_{p.sat.}\right]+$$
$$\frac{\cos\psi_{p.sat.}\cot\phi_{ds-p.sat.}}{2\left(\frac{\sigma_N}{c_{ds}}\tan\phi_{ds-p.sat.}+1\right)} \quad (A.54)$$

As can be seen, Eqn. A.54 is identical to Eqn. 3.32. If c_{ds} is set to zero,

$$\frac{u}{\sigma_1-\sigma_3}=\frac{1}{2}\left[\cos\psi_{dry}\cot\phi'_{ds-dry}+\sin\psi_{dry}-\cos\psi_{p.sat.}\cot\phi_{ds-p.sat.}-\sin\psi_{p.sat.}\right] \quad (A.55)$$

If $\phi_{ds\text{-}p.sat.}$ and $\psi_{p.sat.}$ are set to zero,

$$\frac{u}{\sigma_1-\sigma_3}=\frac{1}{2}\left[\cos\psi_{dry}\cot\phi'_{ds-dry}+\sin\psi_{dry}-1\right] \quad (A.56)$$

APPENDIX B

SUMMARY OF ARCHIVED DATA

B.1 Introduction

Data presented in this work are contained in the NEES central data repository. A document identifying the locations of all data used in this thesis can be found by starting at <https://central.nees.org/>, selecting the "Publicly Available Projects" tab, and choosing the project called "NEESR-SG: Evaluation of Ground Rupture Effects on Critical Lifelines". In the subfolder for this project, select the "Documentation" tab, and the "Cornell Research Papers" folder. The specific files that are stored in the data repository are listed in a file called <Nathaniel Olson Research Summary.pdf>.

The data stored in the NEES central data repository are organized according to the structure of this thesis, and include in part the information listed below. Also shown in the repository are research papers published by Cornell University and Rensselaer Polytechnic Institute, and specific information concerning each large scale and centrifuge scale test run by the two partner schools.

B.2 Characteristics of Dry Glacio-Fluvial Sand

Data summarized in the NEES central data repository include:

- Digital photographs of three glacio-fluvial sands
- Particle size distribution numerical data

- Direct shear (DS) test procedures
- DS test data for dry sand with summary spreadsheet
- Digital photographs of sand cone tests

B.3 Characteristics of Partially Saturated Sand

Data summarized in the NEES central data repository include:

- Tempe cell and tensiometer procedures and data
- DS test data for partially saturated sand

B.4 Preparation and Measurement of Soil for Large Scale Tests

Data summarized in the NEES central data repository include:

- Density scoop calibrations
- Nuclear gage calibrations
- Results for all large scale tests
- Soil placement, compaction and measurement procedure

B.5 Measurement of Soil-Pipeline Stresses

Data summarized in the NEES central data repository include:

- Tactile pressure sensor calibrations
- DS test data on tactile pressure sensors
- Creep test results
- Tactile pressure sensor installation and data analysis procedure

B.6 Force-Displacement Results from Large Scale Soil-Pipeline Tests

Data summarized in the NEES central data repository include:

- Force-displacement results for each large scale test
- Large scale test procedure
- Large scale test instrumentation maps
- Dimensionless design curves for soil-pipeline tests

REFERENCES

Alonso, E.E., Gens, A, & Josa, A (1990). "A Constitutive Model for Partly Saturated Soils." *Geotechnique*. 40(3), 405-430.

ASTM. (1953). Symposium on Direct Shear Testing of Soils; Fifty-Fifth Annual Meeting (Fiftieth Anniversary Meeting) American Society for Testing Materials, New York City, N. Y., June 26, 1952. American Society for Testing Materials, Philadelphia.

ASTM. (2003a). D422-63: "Standard Test Method for Particle-Size Analysis of Soils." *Annual Book of ASTM Standards*, *Vol. 4.08*. ASTM International, West Conshohocken, PA, 10-17.

ASTM. (2003b). D698-00aa: "Standard Test Methods for Laboratory Compaction Characteristics of Soil Using Standard Effort (12 400 ft-lbf/ft^3 (600 kN-m/m^3))." *Annual Book of ASTM Standards*, *Vol. 4.08.* ASTM International, West Conshohocken, PA, 78-87.

ASTM. (2003c). D1557-00: "Standard Test Methods for Laboratory Compaction Characteristics of Soil Using Modified Effort (56,000 ft-lbf/ft^3 (2,700 kN-m/m^3))." *Annual Book of ASTM Standards*, *Vol. 4.08*. ASTM International, West Conshohocken, PA, 133-141.

ASTM. (2003d). D2216-98: "Standard Test Methods for Laboratory Determination of Water (Moisture) Content of Soil and Rock by Mass." *Annual Book of ASTM Standards*, *Vol. 4.08.* ASTM International, West Conshohocken, PA, 219-223.

ASTM. (2003e). D3080-04: "Standard Test Methods for Direct Shear Test of Soils Under Consolidated Drained Conditions." *Annual Book of ASTM Standards*, *Vol. 4.08.* ASTM International, West Conshohocken, PA, 347-352.

ASTM. (2003f). D4318-00: "Standard Test Methods for Liquid Limit, Plastic Limit, and Plasticity Index of Soils." *Annual Book of ASTM Standards, Vol. 4.08*. ASTM International, West Conshohocken, PA, 582-594.

ASTM. (2008a). D6836 - 02: "Standard Test Methods for Determination of the Soil Water Chararcteristic Curve for Desorption Using a Hanging Column, Pressure Extractor, Chilled Mirror Hygrometer, and/or Centrifuge." *Annual Book of ASTM Standards, Vol. 4.08*. ASTM International, West Conshohocken, PA, www.astm.org.

ASTM. (2008b). D6838 – 08a: "Standard Test Method for In-Place Density and Water Content of Soil and Soil-Aggregate by Nuclear Methods (Shallow Depth)." *Annual Book of ASTM Standards Vol. 4.08*. ASTM International, West Conshohocken, PA, www.astm.org.

Bishop, A. W. (1950). "Discussion on the Measurement of the Shear Strength of Soils in Relation to Practice." *Geotechnique,* 2(2), 113-116.

Bishop, A. W., Alphan, I., Blight, G. E., and Donald, I. B. (1960). "Factors Controlling the Shear Strength of Partly Saturated Cohesive Soils." *ASCE Research Conf. on Shear Strength of Cohesive Soils,* Boulder, CO, 503–532.

Blatz, J. A., and Graham, J. (2003). "Elastic-Plastic Modeling of Unsaturated Soil Using Results from a New Triaxial Test with Controlled Suction." *Geotechnique*, 53(1), 113–122.

Bray, J.D., Seed, R.B., Cluff, L.S., and Seed, H.B. (1994). "Earthquake Fault Rupture Propagation Through Soil." *Journal of Geotechnical Engineering*, ASCE, 120(3), 543-561.

Bolton, M.D. (1986). "The Strength and Dilatancy of Sands." *Geotechnique* 36(1), 65-78.

Brooks, R. H., and Corey, A. T. (1964). "Hydraulic Properties of Porous Media." *Hydrology Paper No. 3*, Colorado State Univ., Fort Collins, CO.

BSI, (1990), BS 1377: Part 7: 4: "Determination of Shear Strength by Direct Shear." British Standards Institute, Milton Keynes, UK.

Buckingham, E. (1907). "Studies on the Movement of Soil Moisture." *US Dept Agr. Bur. Soils Bulletin 38*.

Cássaro, F.A.M, Tominaga, T.T., Bacchi, O.O.S., Reichardt, K., Oliveira, J.C.M., and Timm, L. C. (2000). "Improved Laboratory Calibration of a Single-Probe Surface Gamma-Neutron Gauge." *Aust. J. Soil Res*., (38), 937–946.

Cerato, A.B., and Lutenegger, A.J. (2006). "Specimen Size and Scale Effects of Direct Shear Box Tests on Sands." *Geotechnical Testing Journal*, 29(6), 507-516.

Cole, E.R. (1967). "The Behaviour of Soil in the Simple Shear Apparatus." PhD Thesis, University of Cambridge.

Cornell University Department of Environmental Health and Safety (2009). http://www.ehs.cornell.edu/rad/rad_safety.cfm.

Dane, J.H., and Topp, G.C. (2002). *Methods of Soil Analysis: Part 4, Physical Methods*. Soil Science Society of America.

Davis, E. H. (1968). "Theories of Plasticity and the Failure of Soil Masses." *Soil Mechanics, Selected Topics,* I. K. Lee, ed., Buterworth, London.

Davis, J.C. (1986), *Statistics and Data Analysis in Geology*. John Wiley and Sons, New York.

Dietz, M. S. (2000). "Developing an Holistic Understanding of Interface Friction using Sand within the Direct Shear Apparatus." PhD Thesis, University of Bristol.

Dietz, M.S., and Lings, M.L., (2006). "Postpeak Strength of Interfaces in a Stress-Dilatancy Framework." *ASCE Journal of Geotechnical and Geoenvironmental Engineering*, 132(11), 1474-1484.

Dunnicliff, J., (1988). *Geotechnical Instrumentation for Monitoring Field Performance*. John Wiley & Sons, Toronto, Canada.

Dyer, M. R. (1986). "Observation of the Stress Distribution in Crushed Glass with Applications to Soil Reinforcement." PhD Thesis, University of Oxford.

Everett, D.H. (1954). "A General Approach to Hysteresis – Part 3: A Formal Treatment of the Independent Domain Model of Hysteresis." *Transactions of the Faraday Society*, 50, 1077-1096.

Everett, D.H. (1955). "A General Approach to Hysteresis – Part 4: An Alternative Formulation of the Domain Model." *Transactions of the Faraday Society*, 51, 1551-1557.

Feng, M., and Fredlund, D. G. (1999). "Hysteretic Influence Associated with Thermal Conductivity Sensor Measurements." *Proc.*, 52nd Canadian Geotechnical Conf., Regina, Sask., Canada, 651–657.

Franke, R. (1982). "Scattered Data Interpolation: Test of Some Methods." *Mathematics of Computations*, 33(157), 181-200.

Fredlund, D. G. (2000). "The Implementation of Unsaturated Soil Mechanics into Geotechnical Engineering." *Can. Geotech. J.*, 37(5), 963–986.

Fredlund, D. G. (2002). "Use of the Soil-Water Characteristic Curve in the Implementation of Unsaturated Soil Mechanics." *Proc.,* 3rd Int. Conf. on Unsaturated Soils, UNSAT 2002, Keynote Address, Vol. 3, Balkema, Recife, Brazil, 887–902.

Fredlund, D.G. (2006). "Unsaturated Soil Mechanics in Engineering Practice." *ASCE Journal of Geotechnical and Geoenvironmental Engineering*, 132(3), 286-321.

Fredlund, D. G., and Morgenstern, N. R. (1976). "Constitutive Relations for Volume Change in Unsaturated Soils." *Can. Geotech. J.*, 13(3), 261–276.

Fredlund, D. G., and Xing, A. (1994). "Equations for the Soil-Water Characteristic Curve." *Can. Geotech. J.*, 31(3), 521–532.

Fredlund, M. D., Fredlund, D. G., and Wilson, G. W. (1997). "Prediction of the Soil–Water Characteristic Curve from Grain-Size Distribution and Volume-Mass Properties." *Proc*., 3rd Brazilian Symp. on Unsaturated Soils, NSAT '97, Vol. 1, Rio de Janeiro, Brazil, 13–23.

Fredlund, M. D., Fredlund, D. G., and Wilson, G. W. (2000). "An Equation to Represent Grain-Size Distribution." *Can. Geotech. J.*, 37(4), 817-827.

Gardner, W., Israelsen, O.W., Edlefsen, N.F., and Clyde, D. (1922). "The Capillary Potential Function and its Relation to Irrigation Practice." (Abstract) *Phys. Rev. 20*, 196.

Ha, D., Abdoun, T., O'Rourke, M.J., Symans, M.D., O'Rourke, T.D., Palmer, M.C. and Stewart, H.E. (2008). "Centrifuge Modeling of Earthquake Faulting Effects on Buried HDPE Pipelines crossing Fault Zones." *Journal of Geotechnical and Geoenvironmental Engineering*, ASCE, 134(10), 1501-1515.

Haines, W.B. (1930). "Studies in the Physical Properties of Soil: The Hysteresis Effect in Capillary Properties and the Modes of Water Distribution Associated Therewith." *Journal of Agricultural Science*. 20, 97-116.

Hamada, M. and O'Rourke, T.D. Eds. (1992). "Case Studies of Liquefaction and Lifeline Performance during Past Earthquakes." *NCEER-92-0001*, 1, National Center for Earthquake Engineering Research, Buffalo, NY, April 1992.

Houlsby, G.T. (1991). "How the Dilatancy of Soils Affects their Behaviour." *Proc.* 10th ECSMFE 4, Florence, Italy, 1189-1202.

Hvorslev, J. (1939). "Torsion Shear Tests and their Place in the Determination of the Shearing Resistance of Soils." *Proc*. ASCE, Vol. 39, pp 999-1022.

Jameson, G.W. (1985a). "A Field Evaluation of Nuclear Gage Calibration Methods: Part 1: Manufacturer's Calibration." *Australian Road Research Board*, 15(1), 20-29.

Jameson, G.W. (1985b). "A Field Evaluation of Nuclear Gage Calibration Methods: Part 1: Field and Blocks-Field Calibrations." *Australian Road Research Board*, 15(2), 83-89.

Jewell, R.A. & Wroth, C.P. (1987). "Direct Shear Tests on Reinforced Sand." *Geotechnique,* 37(1), 53-68.

Jewell, R.A. (1989). "Direct Shear Tests on Sand." *Geotechnique,* 39 (2), 309-322.

Klausner, Y. (1991). *Fundamentals of Continuum Mechanics of Soils*. Springer-Verlag, New York.

Koerner, R. M. (1970). "Behaviour of Single Mineral Soils in Triaxial Shear." *J. Soil Mech. Fdns Div. Am. Sot. Civ. Engrs* 96(4), 1373-1390.

Kohl, K.M., New, B.M., and O'Rourke, T.D. (1989). "Stress Cell Measurements for the Investigation of Soil-Pipeline Interactions during Vehicular Loading." *Proc.* Geotechnical Instrumentation in Civil Engineering Projects, University of Nottingham, UK, Apr., 17 p.

Lambe, T.W. & Whitman, R.V. (1969). *Soil Mechanics*. J. Wiley and Sons, New York.

Lazarte, C.A., Bray J.D., Johnson, A.M., and Lemmer, R.E. (1994). "Surface Breakage of the 1992 Landers Earthquake and its Effect on Structures." *Bulletin of the Seismological Society of America*, 84(3): 547-561.

Lebedeff, A.F. (1927). "The Movement of Ground and Soil Waters." *Proc.* 1st Int. Cong. Soil Sci. Vol. 1, 459-494.

Lee, I. K. (1966). "Stress-Dilatancy Performance of Feldspar." *J. Soil Mech. Fdns Div. Am. Sot. Civ. Engrs* 92(2), 79-103.

Lings, M. L., and Dietz, M. S. (2004). "An Improved Direct Shear Apparatus for Sand." *Geotechnique*, 54(4), 245–256.

Lings, M. L., and Dietz, M. S. (2005). "The Peak Strength of Sand-Steel Interfaces and the Role of Dilation." *Soils Found.*, 45(6), 1–14.

Livingston, B.E. (1908). "A Method for Controlling Plant Moisture." *Plant World 11*, 39-40.

Mamlouk, M.S. (1988). "Nuclear Density Testing of Granular Materials: State of the Art." *report to Arizona Department of Transportation*, FHWA-AZ88-839.

Matthews, M. C. (1988). “The Engineering Application of Direct and Simple Shear Testing.” *Ground Engng* 21(2), 13–21.

Miura, K., Maeda, K. & Toki, S. (1997). “Method of Measurement for the Angle of Repose of Sands.” *Soils Fnds* 37(2), 89-96.

Morgenstern, N. R. & Tchalenko, J. S. (1967). “Microscopic Structures in Kaolin Subjected to Direct Shear.” *Geotechnique* 17(4), 309-328.

New York State Department of Transportation. (2007). “Geotechnical Test Method for Earthwork Compaction Control by Nuclear Gage.” New York State Department of Transportation: Geotechnical Engineering Bureau, from www.nysdot.gov.

New York State Department of Transportation. (2008). “Standard Specifications, Section 200: Earthwork.” New York State Department of Transportation, from www.nysdot.gov.

Nitao, J. and Bear, J. (1996). “Potentials and their Role in Transport in Porous Media.” *Water Resour. Res.* 32, 225-250.

O’Rourke, M.J. and Liu, X. (1999). “Response of Buried Pipelines Subject to Earthquake Effects.” *Monograph No. 3*, MCEER, Buffalo, NY: 248 p.

O'Rourke, T.D., Druschel, S.J., and Netravali, A.N. (1990). “Shear Strength Characteristics of Sand-Polymer Interfaces.” *Journal of Geotechnical Engineering*, ASCE, 116(3), 451-469.

O’Rourke, T.D. (1998). “An Overview of Geotechnical and Lifeline Earthquake Engineering.” *Proc.* Geotechnical Earthquake Engineering and Soil Dynamics Conference, Seattle, WA, Aug., GSP No. 75, ASCE, Reston, VA, 1392-1426.

O’Rourke, T.D. and Bonneau, A. (2007). “Lifeline Performance under Extreme Loading during Earthquakes.” *Earthquake Geotechnical Engineering*, K.D. Pitilakis, ed., Springer, Dordrecht, Netherlands, 407-432.

O'Rourke, T. D., and Druschel, S. J. (1989). “Improved Anchoring Practices for Plastic Gas Pipelines.” *Geotechnical Engineering Report 89-2*, School of Civ. and Envir. Engrg., Cornell Univ., Ithaca, N.Y.

O’Rourke, T.D., Jezerski, J.M., Olson, N.A, Bonneau, A., Palmer, M.C., Abdoun, T., and O’Rourke, M. (2008). “Geotechnics of Pipeline System Response to Earthquakes.” *Proc.* 4th Decennial Geotechnical Earthquake Engineering and Soil Dynamics Conference (GEESD IV), ASCE, Sacramento, CA., May, paper 193.

Paikowsky, S.G., Player, C. M. & Connors, P.J. (1996). "Closure." *Geotech. Test. Jrnl* 19(4), 447-451.

Paikowsky, S.G. and Hajduk, E.L. (1997). "Calibration and Use of Grid-Based Tactile Pressure Sensors in Granular Material." *Geotechnical Testing Journal*, ASTM, 20(2), 218-241.

Paikowsky, S.G., Palmer, C.J., and Dimillio, A.F. (2000). "Visual Observation and Measurement of Aerial Stress Distribution under a Rigid Strip Footing." *Geotechnical Special Publication No. 94*, ASCE, April, 148 – 169.

Paikowsky, S.G., Rowles, L.E., and Tien, H.S. (2003). "Visualization Measurements of Stress around a Trap Door." *Proc.* 12th Pan American Conference and 39th Rock Mechanics Symposium, Cambridge, MA, VGE Publications, June, 1171 – 1177.

Paikowsky, S.G., Palmer, C.J., and Rowles, L.E. (2006). "The Use of Tactile Sensor Technology for Measuring Soil Stress Distribution." *Proc.* GeoCongress 2006-Geotechnical Engineering in the Information Technology Age, Atlanta, GA, ASCE, February-March, 6p.

Palmer, M.C., O'Rourke, T.D. Stewart, H.E., O'Rourke, M.J., and Symans, M (2006). "Large Displacement Soil-Structure Interaction Test Facility for Lifelines." *Proc.* 8th US National Conference on Earthquake Engineering and 100th Anniversary Earthquake Conference Commemorating the 1906 San Francisco Earthquake, EERI, San Francisco, CA. April, paper 1257.

Palmeira, E. M. & Milligan G. W. E. (1989). "Scale Effects in Direct Shear Tests on Sand." *Proc.* 12th ICSMFE (Rio), Vol. 1, Ses. 8, No. 17, 739-742.

Parsons, J.D. (1936). "Progress Report on an Investigation of the Shearing Resistance of Cohesionless Soils." *Proceedings:* 1st International Conference on Soil Mechanics and Foundation Engineering, Vol. 2, 133-138.

Pham, H. Q., Fredlund, D. G., and Barbour, S. L. (2005). "A Study of Hysteresis Models for Soil Water Characteristic Curves." *Can. Geotech. J.*, 42(6), 1548-1568.

Rowe, P.W. (1962). "The Stress Dilatancy Relation for Static Equilibrium of an Assembly of Particles in Contact." *Proc. Roy. Soc. A269*, pp. 500-527.

Rowe, P.W. (1969). "The Relation between the Shear Strength of Sands in Triaxial Compression, Plane Strain and Direct Shear." *Geotechnique,* 19(1), 75-86.

Santamarina, J.C., Cho, G.C. (2001). "Determination of Critical State Parameters in Sandy Soils--Simple Procedure." *Geotechnical Testing Journal* 24(2), 185 – 192.

Scarpelli, G. & Wood, D. M. (1982). "Experimental Observations of Shear Band Patterns in Direct Shear Tests." *Proc.* IUTAM Symp. Deformation and Failure of Granular Materials (eds P.A. Vermeer & H. J. Luger), Balkema, Rotterdam, 473-484.

Schofield, R. K. (1935). "The pF of Water in Soil." *Trans. 3rd Int. Cong. Soil Science*, Oxford, UK, 2, 37–48.

Schofield, A.N. (2005). *Disturbed Soil Properties and Geotechnical Design*. Thomas Telford Publications.

Selig, E.T., (1962). "Fixed-Volume Soil Density Measuring Device." *U.S. Patent No. 3,038,341*, U.S. Patent Office, Washington, DC.

Selig, E.T. (1964). "A Review of Stress and Strain Measurement in Soil." *Proc.* Symposium on Soil-Structure Interaction, Univ. of Arizona, Tucson, AZ, 172-186.

Selig, E.T. and Ladd, R.S., (1973), "Evaluation of Relative Density Measurements and Applications." *Evaluation of Relative Density and its Role in Geotechnical Projects Involving Cohesionless Soils, STP 523*, ASTM, Philadelphia, PA, 487-504.

Servais, S.G.C (1990). "A Comparison of Field and Blocks Calibration of Nuclear Density/Moisture Gauges." *Australian Journal of Road Research* 20(3), 3-9.

Shibuya, S., Mitachi, T. & Tamate, S. (1997). "Interpretation of Direct Shear Box Testing of Sands as Quasisimple Shear." *Geotechnique* 47(4), 769-790.

Sillers, W.S. (1997). "The Mathematical Representation of the Soil-Water Characteristic Curve." M.Sc. Thesis, Department of Civil Engineering, University of Saskatchewan, Saskatoon, Sask.

Singh, A., Roberson, R., Ranaivoson, A., Siekmeir, J. and Gupta, S. (2006). "Water Retention Characteristics of Aggregate and Granular Materials." *Unsaturated Soils 2006 (GSP 147)*, 1326-1377.

Skempton, A. W. (1949). "Alexandre Collin: A Note on his Pioneer Work in Soil Mechanics." *Geotechnique*, 1(4), 216-221.

SSSA. (1997). *Glossary of Soil Science Terms*. SSSA, Madison, WI.

Stith, J.C. (2005). “Railroad Track Pressure Measurements at the Rail/Tie Interface using Tekscan Sensors.” MS Thesis, University of Kentucky, Lexington, KY, 151p.

Stewart, J.P., and Kulhawy, F.H., (1981). “Experimental Investigation of the Uplift Capacity of Drilled Shaft Foundations in Cohesionless Soil.” *Contract Report B-49(6), to Niagra Mohawk Power Corporation*, School of Civil and Environmental Engineering, Cornell University, Ithaca, NY, May 1981, 136 p.

Stroud, M. A. (1971). “Sand at Low Stress Levels in the S.S.A.” PhD Thesis, Cambridge University.

Takada, N. (1993). “Mikasa's Direct Shear Apparatus, Test Procedure and Results.” *Geotech. Test. Jrnl.,GTJODJ*, 16(3), 314-322.

Taylor, D. W. (1948). *Fundamentals of Soil Mechanics*. Wiley, New York.

Tekscan (2003). *Tekscan I-Scan Equilibration and Calibration Practical Suggestions*. Tekscan, Inc, South Boston, MA.

Terzaghi, K. (1943). *Theoretical Soil Mechanics*. Wiley, New York.

Tokimatsu, K. and Suzuki, H. (2004). “Pore Water Pressure Response around Piles and its Effects on p-y Behavior during Soil Liquefaction.” *Soils and Foundations*, JGS, 44(6), 101-110.

Trautmann, C.H., and O’Rourke, T.D., (1983). “Behavior of Pipe in Dry Sand Under Lateral and Uplift Loading.” *Geotechnical Engineering Report 83-7*, Cornell University, Ithaca, New York.

Trautmann, C.H., Kulhawy, F.H., and O’Rourke, T.D. (1985). “Sand Density Measurement for Laboratory Studies.” *Geotechnical Testing Journal*. 8(4), 159-165.

Troxler Electronic Laboratories (2004a) *Brochure: Troxler Models 3430 and 3440*, http://www.troxlerlabs.com.

Troxler Electronic Laboratories (2004b) *Manual of Operation and Instruction: Model 3440 Surface Moisture-Density Gauge*, http://www.troxlerlabs.com.

Turner, J. (2004). “Lateral Force-Displacement Behavior of Pipes in Partially Saturated Sand.” M.S. Thesis, Cornell University.

Vanapalli, S.K., Sillers, W.S. and Fredlund, M.D. (1998). "The Meaning and Relevance of Residual State to Unsaturated Soils." *51st Canadian Geotechnical Conference*. Edmonton, Albera, October 4-7, 1-8.

van Genuchten, M. Th., Leij, F. and Yates, S. (1991). "The RETC Code for Quantifying the Hydraulic Functions of Unsaturated Soils." *EPA Research Document* EPA/600/2-91/065.

van Genuchten, M. Th. (1980). "A Closed-Form Equation for Predicting the Hydraulic Conductivity of Unsaturated Soils." *Soil Sci. Soc. Am. J.*, 44(5), 892–898.

Weiler, W.A., Jr., and Kulhawy, F.H., (1978), "Accuracy of the Density Scoop for Unit Weight Determinations in Cohesionless Soils." *Geotechnical Testing Journal*, ASTM, 1(4), 234-236.

Weiler, W.A. and Kulhawy, F.H. (1982). "Factors Affecting Stress Cell Measurements in Soil." *Journal of Geotechnical Engineering*, ASCE, 108(12), 1529-1548.

Wernick, E. (1977). "Stresses and Strains on the Surface of Anchors." *Proc.* 9th ICSMFE (Tokyo), Spec. Sess. No. 4, 113-119.

Wernick, E. (1979). "A True Direct Shear Apparatus to Measure Soil Parameters of Shear Bands." *Proc*. 7th ECSMFE (Brighton), Vol. 2, 175-182.

Wheeler, S. J., and Sivakumar, V. (1995). "An Elasto-Plastic Critical State Framework for Unsaturated Soil." *Geotechnique*, 45(1), 35–53.

Wroth, C. P. (1958). "The Behaviour of Soils and Other Granular Media when Subjected to Shear." PhD Thesis, University of Cambridge.

Wu, P., Matsushima, K., and Tatsuoka, F. (2008). "Effects of Specimen Size and Some Other Factors on the Shear Strength and Deformation of Granular Soils in Direct Shear Tests." *Geotechnical Testing Journal*, 31(1), 45-64.

Yoshisaki, K., O'Rourke, T.D., and Hamada, M. (2001). "Large Deformation Behavior of Buried Pipelines with Low-Angle Elbows Subjected to Permanent Ground Deformation." *Journal of Structural Mechanics and Earthquake Engineering*, JSME, 4(50), 215-228.

Yoshizaki, K. (2002). "Study on Large Deformation Behavior of Buried Pipelines with Elbows Subjected to Permanent Ground Deformation." Ph.D. Thesis, Waseda University, Tokyo, Japan.